

DECOMPOSITION KINETICS OF DIETHYLZINC AND DIMETHYLCADMIUM AND  
THEIR REACTIONS WITH WATER BY *IN SITU* RAMAN SPECTROSCOPY AND  
DENSITY FUNCTIONAL THEORY CALCULATION

By

YOUNG SEOK KIM

A DISSERTATION PRESENTED TO THE GRADUATE SCHOOL  
OF THE UNIVERSITY OF FLORIDA IN PARTIAL FULFILLMENT  
OF THE REQUIREMENTS FOR THE DEGREE OF  
DOCTOR OF PHILOSOPHY

UNIVERSITY OF FLORIDA

2007

© 2007 Young Seok Kim

To my parents and much-loved wife

## ACKNOWLEDGMENTS

First of all, I would like to pray to God. The Lord, thanks for giving me an opportunity to study in University of Florida. You have showed me a right way to go every moment and I know you will keep guiding me to a bright future. My study couldn't be accomplished without your love and willing. Please stay with me and my family forever. I pray this in the name of Jesus. Amen.

I was pleased to work in Dr. Tim Anderson's research group. He has kept his eyes on my research and always tried to listen, understand, and support me. Under his academic philosophy, I had the opportunity to learn from various fields, such as chemistry, physics and engineering. I am very proud with the fact that I am a member of Dr. Anderson's research group.

I also give my sincere thanks to all my committee members. Dr. Nicoló Omenetto taught me the spectroscopy-related theory and practical experiments. He showed me a real relationship between a teacher and a student. I also want to thank Dr. Valerie Kleiman. I was afraid of her class because she picked a student randomly to let him solve a problem on the blackboard. However, I realized that her efforts made it possible for me to think and apply my knowledge to actual research calculations. Dr. Helena Hagelin-Weaver always encouraged me during my study. She inspired me to elevate my research to a higher level through communications about our papers. I definitely owe many things to all of them.

I also appreciate Dr. Jennifer Curtis for thoughtful concerns on me and sincere prayers for my father's health. I believe that God led me to many coincidences to meet God's people. In addition, my colleagues were also good teachers and friends. Especially, I appreciate Dr. Jang Yeon Hwang, Dr. Taewoong Kim, Dr. Yong Sun Won, Dr. Byoung Jin Chun, and Matthew Monroe. It was really nice to work with them. Particularly, I enjoyed a lot of discussions over 'Two Regular Grande Coffees' with Dr. Yong Sun Won at Starbucks. He is such a good friend.

Every morning, I could be refreshed with hearing ‘good morning, my favorite student’ from Shirley Kelly and Deborah Sandoval. I feel that they are my aunts. I am so lucky to know them. I also appreciate Sherrie Jenkins for her kindness and deep consideration. It was also nice to have friends in Gainesville; the Doocho family (Hae Young and Soo Bin), Younghwan Namkoong, Benoit Lauly and Joy Guingab. I pray for their bright future. I also want to thank my academic mentors in Korea; Dr. Sung Hyun Kim, Dr. Do Young Yoon, and Dr. Dong Shik Kim for their support.

My special thanks go to my gorgeous wife, Hae Kyung. Whenever I was in slump, she made me happy and encouraged me to achieve a goal. I appreciate her love and dedication. I wish that we always love and take care of each other to build faithful family and to make our life flourish. I also would like to thank my parents-in-law for their love.

My parents are so strongly dedicated to me so that I can feel their love at any time and any place. I love them so much. I hope that my graduation makes my father happy to help him improve his health. I also appreciate all the support from all my family; Min Jung, Johannes, Young Jin, Young Joo, Hyun Jung, Ji Yeon and my aunts. This work is dedicated to all of them.

Finally, I would like share God’s word in my mind with everybody; we know that all things work together for good to them that love God, to them who are the called according to his purpose (Romans 8:28).

## TABLE OF CONTENTS

	<u>page</u>
ACKNOWLEDGMENTS .....	4
LIST OF TABLES .....	9
LIST OF FIGURES .....	11
LIST OF SYMBOLS .....	15
GLOSSARY .....	18
ABSTRACT .....	20
 CHAPTER	
1 INTRODUCTION .....	22
2 RAMAN SCATTERING DIAGNOSTICS .....	27
2.1 Introduction.....	27
2.2 Theoretical Background.....	28
2.2.1 Characteristics of Scattered Light .....	30
2.2.2 Selection Rules .....	33
2.2.3 Raman Cross-Section .....	34
2.2.3.1 Absolute cross-section of nitrogen .....	35
2.2.3.2 Relative cross-section of nitrogen .....	36
2.3 Experimental Methods.....	38
2.3.1 Inverted Impinging Jet MOCVD Reactor .....	38
2.3.2 Spectroscopy System.....	40
2.3.3 System Characteristics.....	42
2.3.3.1 Wavelength selection .....	42
2.3.3.2 Signal to noise ratio .....	44
2.3.3.3 Delivery of metal organic sources.....	45
2.3.4 Calibrations.....	46
2.3.4.1 Monochromator .....	46
2.3.4.2 Detector .....	47
2.3.4.3 Reactor .....	48
2.4 Applications.....	49
2.4.1 Temperature Measurement.....	49
2.4.2 Concentration Measurement.....	53
2.4.3 Electronic Raman Scattering.....	55
2.5 Summary.....	56

3	FIRST PRINCIPLES CALCULATIONS .....	66
3.1	Introduction.....	66
3.2	Estimation of Vibrational Frequency.....	67
3.2.1	Numerical Estimation .....	67
3.2.2	Analytical Estimation .....	68
3.2.3	Hot-band Transition Estimation .....	69
3.3	Thermodynamic Properties.....	72
3.4	Rate Constant Estimation .....	74
3.4.1	Unimolecular Reaction.....	75
3.4.2	Bimolecular Reaction .....	84
3.5	Equilibrium Constant Estimation .....	85
3.6	Summary.....	88
4	REACTOR MODELING AND PARAMETER EXTRACTION.....	97
4.1	Introduction.....	97
4.2	Mathematical Description.....	98
4.2.1	Boundary Conditions.....	99
4.2.2	Encoding.....	99
4.3	Physical Property Estimation.....	100
4.4	Optimization for Parameter Extraction.....	102
4.5	Applications.....	103
4.5.1	Gas Phase MOCVD Simulation .....	104
4.5.2	Transient Study.....	105
4.6	Summary.....	106
5	DIETHYLZINC DECOMPOSITION KINETICS AND REACTION CHEMISTRY WITH WATER.....	113
5.1	Introduction.....	113
5.2	Experimental and Calculation Details .....	115
5.3	Decomposition Mechanism of Diethylzinc .....	118
5.3.1	Laser-Induced Decomposition of $\text{Zn}(\text{C}_2\text{H}_5)_2$ in a Flow Cell.....	119
5.3.2	Diethylzinc Decomposition in an Inverted Impinging Jet Reactor .....	121
5.3.3	Reaction Intermediates .....	125
5.4	Zinc Oxide Film Formation from Diethylzinc and Water Reactions .....	128
5.4.1	Calculation Methods.....	129
5.4.2	Computational Reaction Pathways.....	130
5.4.2.1	Diethylzinc with water .....	130
5.4.2.2	Ethyl Hydrido zinc with water .....	131
5.4.2.3	Dimer with water.....	131
5.4.3	Zinc Oxide Film Deposition.....	133
5.5	Reaction Intermediate Identification from the Diethylzinc/Water System .....	137
5.6	Surface Adsorption .....	139
5.6.1	System Description.....	140

5.6.2 Statistics for Unbound (Ideal Gas) and Bound (Fermi-Dirac Statistics) Molecules.....	141
5.6.3 Equilibrium Analysis.....	142
5.6.4 Vibrational Energy Calculations .....	143
5.7 Summary.....	146
6 DIMETHYLCADMIUM DECOMPOSITION KINETICS AND PARAMETER EXTRACTION.....	161
6.1 Introduction.....	161
6.2 Decomposition Mechanisms of Dimethylcadmium .....	163
6.2.1 Bond Dissociation Energy .....	163
6.2.2 Raman-Active Frequency .....	165
6.2.3 Reaction Intermediates .....	168
6.3 Kinetics Parameter Extraction .....	171
6.4 Homogeneous Reactions with Water.....	172
6.5 Summary.....	173
7 CONCLUSIONS AND RECOMMENDATIONS .....	186
REFERENCES .....	190
BIOGRAPHICAL SKETCH .....	197



## LIST OF TABLES

<u>Table</u>	<u>page</u>
2-1 Absolute Raman cross-section of N <sub>2</sub> measured at different wavelength of incident light. ....	57
2-2 Examples of relative normalized differential Raman scattering cross-sections obtained using the Q-branch of N <sub>2</sub> .....	58
2-3 Dispersions of the monochromator (Å/mm). ....	61
2-4 Selected properties of some metal organic precursors.....	62
2-5 Expected emission wavelengths of Zn atom and their lifetime. ....	65
3-1 Calculated Raman shift between various vibrational states.....	89
3-2 Calculated vibrational temperatures regarding to possible frequencies between Zn-C.....	89
3-3 Contributions of hot band transition for overall peak shift with temperature increase. ....	90
3-4 Probability changes of existing photons at each excited state with respect to temperature increase. ....	91
3-5 Thermodynamic properties and according rate constants calculated from B3LYP/6-311G(d) model chemistry. ....	92
3-6 Thermodynamic properties and estimated rate constants calculated from B3LYP/6-311G(d) model chemistry (Unit: kcal/mol). 10 Å bond length with triplet multiplicity could reproduce plausible reaction rate. ....	93
3-7 Decomposition mechanisms of DMCD and their calculated rate information.....	93
3-8 Reported kinetics data for TMIn decomposition with various carrier gases. ....	94
3-9 Calculated ΔH and ΔG with different basis-set combinations (kcal/mol). ....	96
4-1 Estimated Lennard-Jones potential parameters for N <sub>2</sub> carrier and the Zn- and Cd-molecules. ....	108
5-1 Reported activation energy for the homogeneous dissociation of the first Zn-C bond of diethylzinc. ....	148
5-2 Calculated Raman shift (cm <sup>-1</sup> ) of ν[Zn-C] and ν[Zn-H] for selected Zn-containing molecules. ....	148
5-3 Calculated reaction rate constants.....	150

5-4	Favorable reactions involving intermediates calculated from B3LYP/6-311G(d) model chemistry. Thermodynamic properties are derived from the same theory level...	151
5-5	Symmetrical Raman-active Zn-C stretching of Zn-containing intermediates and estimated Raman shifts (cm <sup>-1</sup> ) with a scaling factor applied. ....	152
5-6	Structural information of reaction species shown in Figure 5-7, 9, and 11 calculated by B3LYP/6-311G(d) theory level. ....	155
5-7	Gibbs energy and enthalpy of reactions shown in Figure 5-14 along with the computed dipole moments calculated by B3LYP/6-311G(d) theory model chemistry...	156
5-8	Vibrational normal modes of dihydroxozinc. Each motion was assigned to proper irrepresentative of C <sub>2h</sub> point group, and subsidiary information was obtained. ....	159
6-1	Reported activation energies for the homogeneous dissociations of the first and second Cd-C bonds of dimethylcadmium. ....	175
6-2	Calculated thermodynamic properties of first Cd-C homolytic fission in DMCd. (1) ECP for Cd and higher accuracy basis set for ligands as specified, (2) ECP for Cd and lower accuracy basis set for ligands as specified. ....	175
6-3	Reported $\nu[\text{Cd-C}]_{\text{sym}}$ vibrational frequencies (cm <sup>-1</sup> ). ....	176
6-4	The calculated frequencies for the symmetric Cd-C stretching motion in Cd(CH <sub>3</sub> ) <sub>2</sub> and CdCH <sub>3</sub> using the B3LYP model chemistry. ....	177
6-5	The calculated frequencies for the symmetric Cd-C stretching motion in Cd(CH <sub>3</sub> ) <sub>2</sub> and CdCH <sub>3</sub> using the HF model chemistry. ....	178
6-6	Molecular orbitals of Cd(CH <sub>3</sub> ) <sub>2</sub> and their energy values in Hartree obtained by (A) B3LYP and (B) HF level theory calculations. ....	180
6-7	Molecular orbitals of CdCH <sub>3</sub> and their energy values in Hartree obtained by (A) B3LYP and (B) HF level theory calculations. ....	181
6-8	The Cd-C symmetric frequency calculated from different basis-set combinations. ....	182
6-9	Expected Raman active frequency for the dimer, (CdCH <sub>3</sub> ) <sub>2</sub> . ....	183
6-10	Partition functions for monomer and dimer species (Equation 6-3). The B3LYP/6-311G(d) level theory calculation was performed for each molecule. ....	184
6-11	Calculated equilibrium constants for Equation 6-3. ....	184

## LIST OF FIGURES

<u>Figure</u>	<u>page</u>
1-1 Methodology used in this study (T: temperature, C: concentration). .....	26
2-1 Principles of Raman scattering illustrated for a diethylzinc molecule with Zn-C vibrational frequency. ....	57
2-2 Rayleigh and Raman scattering as a two-photon process. The broken line represents virtual levels at some energy above the ground state level.....	57
2-3 MOCVD reactor along with a photograph of the experiments (a) and a schematic diagram of the reactor (b). ....	58
2-4 Photograph of experimental system (a) and schematic of optical path (b).....	59
2-5 Photograph of double additive monochromator (a) and schematic of the inside (b).....	59
2-6 Photographs of detectors used in the experiments, PMT (a) and CCD (b).....	59
2-7 Schematic of circuit diagram for a photomultiplier tube (PMT). ....	60
2-8 Czerny-Turner plane grating monochromator. The grating spatially disperses the spectral components of the incident radiation. ....	60
2-9 Photographs of the delivery system showing the three inlets (center, annulus, and outer). The precursor molecule is introduced via carrier gas through the center line, a second reactant (i.e., H <sub>2</sub> O) through the annulus inlet, and an inert ‘sweep’ gas through the outer inlet. ....	61
2-10 Pure room temperature rotational spectrum of N <sub>2</sub> . ....	62
2-11 Measurement positions for temperature determination. ....	63
2-12 The N <sub>2</sub> rotational spectra taken at the three different in Fig. 2-11. ....	63
2-13 Temperature extraction at a single position using Equation 2-36.....	64
2-14 The measured temperature profile in the MOCVD reactor. The heater temperature was set at 200°C. The points were obtained by experiments and the line was simulated from the detailed model.....	64
2-15 Emission lines of Zn atoms with respect to its electronic energy state. ....	65
3-1 Potential surface scan along with Zn-C distance in diethylzinc. ....	89
3-2 Energy difference between ground state and excited states explaining equal energy split. Hot band transition can be analytically calculated based on this concept. ....	90

3-3	Peak shift of Zn-C stretch due to population changes at each vibrational excited state. ...	91
3-4	Reaction scheme of homolytic fission in Zn-C bond.....	92
3-5	Suggested calculation domain with an imaginary bond between Zn-C to correct entropy calculation.....	92
3-6	Comparison of reaction rates for Zn-C homolytic bond fission. The calculated rate seems reasonable the same with the result from Dumont at 550°C.....	93
3-7	Comparison of reaction rates for Cd-C homolytic bond fission. The calculated rate matched well with Laurie and Long at the temperature 300 °C and with Price and Dickenson at 150 °C. However, it should be noted that actual reaction temperature should be around 500 °C.....	94
3-8	Comparison of reaction rates for In-C homolytic bond fission of TMin with carrier gas, N <sub>2</sub> . Numbered references were reported with different carrier gases: (1) D <sub>2</sub> , (2) H <sub>2</sub> , (3) H <sub>2</sub> and (4) He. ....	95
3-9	Electron density contour for TMin, DMin, and Methyl radical. A combination of basis set was used (LanL2DZ for TMin and 6-311++G(2d,2p) for C and H) with B3LYP calculation method. (a) TMin, (b) DMin, (c) Methyl.....	95
3-11	Elongated molecular geometries for TMin decomposition. Two products were connected by an imaginary bond, which has length of (d) 5 Å and (e) 10 Å. ....	96
3-12	The comparison of reaction rates for In-C homolytic bond fission of TMin. ....	96
4-1	The schematic of the axisymmetric reactor model and boundary conditions used in detailed model.....	108
4-2	Calculated streamlines and isotherms in the reactor with N <sub>2</sub> carrier gas: (a) streamlines and (b) temperature isotherms [°C] for the gas velocity at 0.1 cm/s. ....	109
4-3	Simulated isotherm (horizontal) [°C] and concentration streamline of dimethylcadmium (vertical with arrow). Reaction was not considered. The heater temperature was set at 500 °C and flow rate at 2.5 cm/s. ....	109
4-4	Streamlines of N <sub>2</sub> gas at room temperatures (25 °C) after (a) 0.05 (b) 0.5 (c) 5 and (d) 30 sec. (Next page) The flow patterns of N <sub>2</sub> gas at (e) 60 (f) 120 (g) 360 sec and (h) time-independent solution. The gas flow rate was set at 2.5 cm/s.....	110
4-5	Streamlines of N <sub>2</sub> gas at room temperatures (25 °C) after (i) 60 (j) 120 (k) 360 sec and (l) time-independent solution. The gas flow rate was set at 10.0 cm/s. ....	112
5-1	Laser induced Raman shifts of DEZn at room temperature. The lower spectrum was obtained at 1.3 W incident laser power and upper line was obtained at 3.3 W incident laser power.....	148

5-2	Measured DEZn centerline profile along with simulated profile assuming only homolytic fission using rate constants: -----, Koski <i>et al.</i> , — — —, Dumont et al. and solid line, computational calculation in this study. The simulated temperature profile is also shown. ....	149
5-3	The potential energy surface for DEZn along the Zn-C bond length for two multiplicities. The solid line represents a Morse potential fit.....	149
5-4	Comparison of measured DEZn centerline profile (symbol) to simulated profile assuming only $\beta$ -hydride elimination (dash line(1)) or only homolysis (dash line(2)) using the rate constants shown in Table 5-3. The solid line includes both reactions. The computed profiles of $\text{ZnC}_2\text{H}_5$ and $\text{HZnC}_2\text{H}_5$ are also shown with both pathways included.....	150
5-5	Raman spectra at two positions in the reactor (1 and 2 mm above the inlet) indicating presence ( $\text{ZnC}_2\text{H}_5$ ) <sub>2</sub> .....	152
5-6	Schematic diagram of two suggested competing reactions with reaction enthalpies [kcal/mol] listed. ....	152
5-7	Possible reaction pathway of diethylzinc reaction with one mole of water.....	153
5-8	Enthalpy changes [kcal/mol] in reactions of diethylzinc and water represented in Fig. 5-7. ....	153
5-9	Likely reaction pathways of ethyl hydrido zinc with water. Dashed arrow indicate relatively unfavorable reaction pathway.....	153
5-10	Enthalpy changes [kcal/mol] in reaction of ethyl hydrido zinc and water shown in Fig. 5-9. ....	154
5-11	Likely reaction pathways of ethyl hydrido zinc with water. Dashed arrow indicate relatively unfavorable reaction pathway.....	154
5-12	Enthalpy changes [kcal/mol] in reactions of ethyl hydrido zinc and water given in Fig. 5-11. ....	154
5-13	Proposed reaction pathways between three Zn-containing molecules and water.....	155
5-14	Proposed reaction pathways of dihydroxozinc (a) dimerization from two molecules and (b) trimerization from three molecules. In energetic comparison, trimerization reaction (b) is more likely feasible. However, this reaction seems not likely continuously happening in gas-phase but on solid surface. ....	156
5-15	Measured Raman shifts for water (upper) and diethylzinc (lower). The peaks labeled with a star are plasma peaks from Ar <sup>+</sup> laser probe.....	156

5-16	Raman spectra taken at various positions (temperatures) along the centerline of the reactor. The heater temperature was set at 600 °C.....	157
5-17	Possible peak assignments of the four detected peaks in Fig. 5-16.....	158
5-18	Two different adsorption mechanisms according to molecular orientation onto the surface. The first case, <i>a</i> , Zn atom was bound with a dangling bond on Si substrate; on the other hand, lone pair of oxygen participated in bond formation in the case of <i>b</i> . Harmonic oscillation was assumed in frequency estimations for both cases. ....	158
5-19	Zn-Si or O-Si vibrational frequency estimation ( <i>a</i> and <i>b</i> motions in Fig 5-18). Structure optimization and frequency calculation were carried out using B3LYP/6-311G(d) model chemistry to keep the consistency. The mass of Si was arbitrary increased to realize the solid surface and it turned out that the vibrational motions converged to certain wavenumber of frequency. ....	159
5-20	The adsorption behavior of dihydroxozinc on Si surface. The adsorbed portion of gas molecules is a function of the site density, and it was examined from $10^{31}$ to $10^{34}$ with assumption of one mole of adsorbent ( $10^{23}$ ). ....	160
5-21	The $\text{Si}_9\text{H}_{12}$ silicon substrate model. 12 H atoms were used for each Si atoms on second and third row to terminate the available bond formation and strong enough force constants in Si-H vibration were assumed to keep proper geometry. The geometry optimization was carried out using B3LYP/6-311G(d). ....	160
5-22	$\text{HZnC}_2\text{H}_5$ adsorption on Si cluster. Due to strong interaction between Zn and Si, original Zn-H bond was broken and the fragment migrated to neighbor Si site.....	160
6-1	Raman shift of $\text{Cd}(\text{CH}_3)_2$ and its first dissociated product, $\text{CdCH}_3$ , observed at different positions using the inverted, impinging-jet reactor. ....	179
6-2	Molecular orbital contours of $\text{Cd}(\text{CH}_3)_2$ . The energy values are listed in Table 6-6.....	179
6-3	Molecular orbital contours of $\text{CdCH}_3$ . The energy values are listed in Table 6-7.....	181
6-4	Detection of reaction intermediate during dimethylcadmium decomposition. The bottom spectrum was taken at room temperature and the most upper spectrum was scanned at around 500 °C, while the middle spectrum was taken around 300 °C.....	183
6-5	Convergence of rate constant and relative Raman cross-section for dimethylcadmium using Genetic and Simplex algorithms. ....	184
6-6	Enthalpy of reactions. A) Between one mole dimethylcadmium and water. B) With additional water molecule. The unit of heat of reaction is kcal/mol.....	185

## LIST OF SYMBOLS

•	$q_{elec}$	Electronic partition function
•	$D_0$	Ionization energy [Kcal/mol]
•	$T_m$	Mean temperature of measurement [K]
•	$I_j$	Measured intensity of component j
•	$P$	Nominal pressure
•	$R$	Residual from the exact solution
•	$\chi_j$	Anisotropic Raman scattering fraction
•	$\alpha_0$	Static polarizability at equilibrium state
•	$\mu$	Viscosity [Pa·s]
•	$\varphi_i$	Wavefunction explaining the electronic and vibrational states at $i$ stage
•	$g_k$	Degeneracy
•	$\omega_{el}$	Degeneracy of the electronic partition function
•	$\rho$	Density [g/cm <sup>3</sup> ]
•	$r_e$	Equilibrium distance [Å]
•	$R$	Gas constant [J/K·mol]
•	$\bar{g}$	Gravitational constant
•	$C_p$	Heat capacity [Kcal/°C]
•	$M$	Molecular weight of the gas mixture [g]
•	$N$	Number density
•	$\alpha$	Polarizability
•	$\hbar$	Reduced Plank constant [J·s]

- $\Sigma_j$  Relative Raman cross-section
- $\Theta_{A,B,C}$  Rotational temperatures [K]
- $R(\tilde{\nu})$  Spectral response of the spectrometer
- $\nu$  Stoichiometric coefficient
- $\gamma_0^2$  Anisotropy of the polarizability tensor
- $D_0$  Centrifugal distortion constant [ $\text{cm}^{-1}$ ]
- $K_c$  Equilibrium constant of the reaction
- $\hat{H}$  Hamiltonian operator of the molecule
- $Q_{TS}^*$  Partition function of the activated complex
- $\mu$  Reduced mass [g]
- $B_0$  Rotational constant [ $\text{cm}^{-1}$ ]
- $\sigma$  Symmetry number of rotational motion
- $k$  Thermal conductivity [ $\text{J/m}\cdot\text{s}\cdot\text{K}$ ]
- $[\mu_0]_{fi}$  Transition moment between  $i$  and  $f$  stages
- $t(\lambda)$  Triangular shaped function
- $\vec{v}$  Velocity vector
- $\Theta_{vj}$  Vibrational temperature [K]
- $\tilde{\nu}$  Wavenumber ( $\equiv 1/\lambda$ ) [ $\text{cm}^{-1}$ ]
- $(\partial\sigma/\partial\Omega)_j$  Differential scattering cross-section for the  $j^{\text{th}}$  vibrational band [ $\text{cm}^2/\text{Sr}$ ]
- $\sigma, \sigma^2$  Standard deviation and variance
- $\tilde{\nu}_0, \tilde{\nu}_j, \tilde{\nu}_Q$  Wave number of the incident light, molecule, and Q-branch of  $\text{N}_2$  [ $\text{cm}^{-1}$ ]
- $\omega, \omega_s$  Frequency of the incident and the scattered [ $\text{cm}^{-1}$ ]



- $\Theta_r, \Theta_v$  Rotational and vibrational temperatures [K]
- $\Omega$  Appropriate collision potentials
- $\Psi$  Eigen function (wave function)
- $\sigma$  Collision diameter [ $\text{\AA}$ ]
- $E$  Eigen value (energy) [Kcal/mol]
- $f(J)$  Correction to the anisotropy ( $\gamma_0^2$ ) of the polarizability
- $F(J)$  Rotational term [ $\text{cm}^{-1}$ ]
- $I$  Moment of inertia
- $I_0$  Intensity of the incident light [ $\text{W}/\text{cm}^2$ ]
- $n$  Refractive index
- $r$  Distance between the molecule and scattered photon [cm]
- $R_d$  Reciprocal linear dispersion [nm/mm]
- $s_g$  Geometric spectral bandpass [ $\text{cm}^{-1}$ ]
- $T$  Temperature [K]
- $V$  Molecular volume [ $\text{cm}^3$ ]
- $V_C, V_A, V_S$  Flow velocity of the center, annuls, and sweep inlets [cm/s]
- $W_s$  Slit width [ $\mu\text{m}$ ]

## GLOSSARY

- **ALD:** Atomic layer deposition. ALD film growth is self-limited and based on surface reactions, which makes achieving atomic scale deposition control possible.
- **B3LYP:** A density functional theory calculation. It is Becke's three parameters hybrid exchange functional combined with the Lee-Yang-Parr gradient-corrected correlation functionals.
- **Basis set:** The set of mathematical functions from which the wave function is constructed. For example, 6-311G(d), 6-311++G(2d,2p), LanL2DZ, and SDD are used in this study. 6-311G means that the core consists of 6 Gaussian Type Orbitals (GTO) which are not split, while the valence orbitals are described by one orbital constructed from 3 primitive GTOs and two orbitals that are single GTOs. 6-311++G(2d,2p) includes the diffused and polarized functions. LanL2DZ and SDD are ECP basis sets developed by Los Alamos Laboratory and Stuttgart Laboratory, respectively.
- **BSSE:** Basis set superposition error. In quantum chemistry, if the total energy is minimized as a function of the system geometry, the short-range energies from the mixed basis sets must be compared with the long-range energies from the unmixed sets, and this mismatch can be corrected using BSSE calculation.
- **CARS:** Coherent anti-Stokes Raman scattering. It is very similar to Raman spectroscopy but involves a lasing process that dramatically improves the signal. CARS is a third-order nonlinear optical process involving a pump and a Stokes frequency laser beam that interacts with the sample and generates a coherent anti-Stokes frequency beam.
- **CCD:** Charge coupled device. An image sensor, consisting of an integrated circuit containing an array of linked, or coupled, light-sensitive capacitors.
- **CVD:** Chemical vapor deposition. The production of thin layers of materials in the fabrication of integrated circuits by means of specific chemical reactions.
- **DFT:** Density functional theory. Quantum mechanical method used in physics and chemistry to investigate the electronic structure of many-body systems, in particular molecules and the condensed phases.
- **ECP:** Effective core potential. A potential model having a radical solution which replaces the electrons with analytical functions that would reasonably accurately, and much more efficiently, represent the combined nuclear-electron core to the remaining electrons.
- **FEM:** Finite element method. A method to find approximate solution of partial differential equations as well as of integral equations such as the heat transport equation.
- **HF:** Hartree-Fock. An approximate method for the determination of the ground-state wavefunction and ground-state energy of a quantum many-body system.

- **II-VI compound:** Chemical compound between a metallic element in group II and a nonmetallic element in group VI of the periodic table. Many of these compounds are semiconducting.
- **ITO:** Indium tin oxide. A mixture of indium(III) oxide ( $\text{In}_2\text{O}_3$ ) and tin(IV) oxide ( $\text{SnO}_2$ ), typically 90%  $\text{In}_2\text{O}_3$ , 10%  $\text{SnO}_2$  by weight. It is transparent and colorless in thin layers.
- **Laser:** Coherent light source based on light amplification by stimulated emission of radiation.
- **LED:** Light emitting diodes. A semiconductor device that emits incoherent narrow-spectrum light when electrically biased in the forward direction of the P-n junction. This effect is a form of electroluminescence.
- **LIF:** Laser induced fluorescence. A spectroscopic method used for studying structure of molecules, detection of selective species and flow visualization and measurements. The species to be examined is excited with help of a laser. The wavelength is often selected to be the one at which the species has its largest cross section. The excited species will after some time, usually in the order of few nanoseconds to microseconds, de-excite and emit light at a wavelength larger than the excitation wavelength. This light, fluorescence, is measured.
- **MOCVD:** Metal organic chemical vapor deposition. A CVD process using metal organic precursors.
- **PMT:** Photomultiplier. An extremely sensitive detector of light in the ultraviolet, visible and near infrared.
- **PVD:** Physical vapor deposition. A technique used to deposit thin films of various materials onto various surfaces (e.g., of semiconductor wafers) by physical means, as compared to chemical vapor deposition.
- **Refractive index:** The ratio of the velocity of light in a vacuum to the velocity of light in some medium.
- **TCO:** Transparent conducting oxide materials, such as ITO.

Abstract of Dissertation Presented to the Graduate School  
of the University of Florida in Partial Fulfillment of the  
Requirements for the Degree of Doctor of Philosophy

DECOMPOSITION KINETICS OF DIETHYLZINC AND DIMETHYLCADMIUM AND  
THEIR REACTIONS WITH WATER BY *IN SITU* RAMAN SPECTROSCOPY AND  
DENSITY FUNCTIONAL THEORY CALCULATION

By

Young Seok Kim

May 2007

Chair: Timothy James Anderson  
Major: Chemical Engineering

The gas phase decomposition of diethylzinc and dimethylcadmium as well as their gas phase reactions with H<sub>2</sub>O were studied to better understand the deposition of transparent conducting ZnO or CdO. Heterogeneous reactions of the likely species (Zn(OH)<sub>2</sub>) on Si was also examined computationally. Composition and temperature profiles were measured using Raman scattering in an inverted, impinging-jet, pedestal reactor that was x-y-z translatable. Density functional theory was used to describe the bond dissociation behavior and vibrational frequencies of reaction intermediates and products along with metal-carbon symmetrical motions.

The decomposition kinetics of diethylzinc (DEZn) was first studied to resolve the discrepancy in the literature as to the dominant decomposition mechanism,  $\beta$ -hydride elimination or homolytic fission of the Zn-C bond. Although photolysis produced the  $\beta$ -hydride elimination product ZnH<sub>2</sub> and thermal decomposition probing also detected this molecule, the dominant pathway was homolytic fission of the Zn-C bond. This was ascertained from the analysis of composition profiles of DEZn and computational chemistry results. Computational chemistry calculations suggested the dimer ((ZnC<sub>2</sub>H<sub>5</sub>)<sub>2</sub>) should be produced, and this species was detected for the first time. Next, the reaction of DEZn with water was studied both computationally and

experimentally. Various Zn-containing molecules and water were studied computationally based on the B3LYP/6-311G(d) model chemistry. Based on these limited calculations the most probable reaction intermediate near the substrate was dihydroxozinc. The most plausible reaction pathway was trimerization to complete the Wurtzite structure of solid ZnO films.

The decomposition kinetics of dimethylcadmium was also examined. For the computational component of this study, the B3LYP theory level calculation with the SDD/STO-3G/3-21G basis set combination for Cd, C, and H atoms was found to reproduce the experimentally reported Cd-C vibrational stretching of  $\text{Cd}(\text{CH}_3)_2$  and  $\text{CdCH}_3$ . This basis set was used to find out if additional reaction intermediates existed. Based on selected model chemistry, the Raman-active frequency shift was calculated for most likely reaction intermediate  $(\text{CdCH}_3)_2$  and this species was detected experimentally. Finally, the obtained experimental data were compared to simulations. The decomposition kinetic parameters of dimethylcadmium were successfully extracted using a parameter estimation procedure that incorporated both Genetic and Simplex algorithms. The relative Raman cross-section was estimated as 20.97 and the rate constants for the first Cd-C bond breaking as  $k_0=5.01 \times 10^{13} \text{ s}^{-1}$  and  $E_a=56.0 \text{ kcal/mol}$ .

## CHAPTER 1 INTRODUCTION

Most research to develop highly transparent and conductive thin films has focused on n-type semiconducting metal oxides, such as indium tin oxide and zinc oxide [Bus96, Min00, Gor00]. These transparent conducting oxide (TCO) films have excellent optical transmittance across the visible range of wavelengths as well as outstanding electrical conductivity. Thus TCO films are used as transparent current electroheaters, antistatic layers, and in a number of optoelectronic devices, such as highly sensitive photodetectors and indicator devices based on electrochromic materials. Moreover, these films are widely applied in the energy industry as transparent electrodes, n-type semiconductors hetero-junction, devices and spectral selective coatings. At some point in the near future, improved TCO coatings are certain to be required for several important applications, including liquid crystal displays [All01].

TCO films are typically prepared in practice by physical vapor deposition (PVD) methods such as vacuum evaporation, RF sputtering, DC sputtering, and RF ion plating [Cha01, Bre02]. Excellent coatings can be produced by PVD but in commercial applications it has the severe disadvantages of high equipment cost and relatively low production rate. Therefore, more economic techniques, including spray hydrolysis of halides [Zho01, Saw02], reactive evaporation of metals [Tom01, Tsa03], pulsed laser deposition [Suz02, Cho03, Mor03, Liu03] and chemical vapor deposition (CVD) [Nak91, All98, Aki99] have been tried with varying degrees of success. Among these methods, CVD has attracted attention since it is relatively easy to perform and inexpensive. TCO deposition techniques have undergone many changes in the last several years with CVD being one of the most promising techniques. Surprisingly, not too many CVD studies have been reported in spite of the fact that CVD does not require high vacuum and accordingly has the advantage of relative ease for large-scale applications while

suitable for coating complicated shapes. One of the difficulties in depositing films by thermal CVD is the lack of volatile and thermally stable precursors. It is anticipated that CVD of TCOs would attract more attention if suitable chemical reactants and knowledge of their decomposition pathway were known [Kan75, Rya82, Mar90, Mar91, Aki99, Zho01, Zen03]. Therefore, elucidation of kinetics, including gas phase decomposition of metal organics and surface heterogeneous reactions to form TCO films, is of interest for establishing growth conditions and improving reactor designs [Kol98, Min00, Gor00, Par02a, Par02c].

Kinetic data on the decomposition of metal organic precursors are often obtained using a simple flow cell or flow tube experiment that incorporate gas chromatography or mass spectrometry [Maz89, Syw91, Tho96] to measure reactant and product concentrations. Establishing homogeneous reaction conditions, minimizing the influence of the sampling probe, and identifying reaction intermediates with these approaches, however, can make the data analysis difficult. Another approach for following the reaction chemistry is to use a reactor model to analyze data obtained from actual MOCVD growth runs since the film represents a record of the growth process (e.g., measurements of film composition, thickness, and impurity profiles). The modeling of real deposition reactors is certainly complicated (e.g., complex view factors, time dependent surface reactivity and emissivity, moving susceptors, flow instabilities) and inconsistent film quality, such as film thickness, makes the modeling more difficult. These constraints limit the ability of a model to distinguish reaction pathways and estimate reaction rate constants. For these reasons, several researchers have used reactors specifically designed for kinetic studies and effectively used optical probes such as Raman scattering, IR absorption, laser induced fluorescence (LIF), and coherent anti-Stokes Raman scattering (CARS) [Ric91] to detect reaction species. As an example, a study of the decomposition of phosphine ( $\text{PH}_3$ ) by several

analysis methods [Abr91, Luc88, Lar87], revealed that *in situ* probing is necessary to follow the process more closely. In fact, optical methods are well suited to probe the reactive boundary layer above a heated susceptor in a MOCVD reactor.

In this study, the integration of a Raman spectrometer into a versatile reactor designed to quantitatively measure rate constants was employed to better understand the chemistry of relevant MOCVD reactions. To assist in the interpretation of the result, the increasingly realistic predictions from computational chemistry are used. Quantitative estimation of rate parameters can then be addressed with measured temperature and composition profiles. This approach is presented in Figure 1-1. This methodology has been applied to the group II-VI reactions to extract kinetic information. The methodology consists of developing a measurement reactor system, modeling the heat, mass and momentum transport in the reactor, and extracting physical parameters from experimental data. Computational chemistry is used to estimate Raman scattering cross-section and vibrational frequencies to assist in the interpretation of data. Furthermore, computational chemistry combined with statistical thermodynamics allowed assessment of the probability of various reaction pathways.

Based on motivations stated above, specific objectives of this research are summarized. The first objective is to understand the homogeneous gas-phase reactions of  $\text{Zn}(\text{C}_2\text{H}_5)_2\text{-H}_2\text{O}$  and  $\text{Cd}(\text{CH}_3)_2\text{-H}_2\text{O}$  deposition chemistry, determining rate constants warranted by experimental data. The second objective is to extend understanding of the chemistry using the density functional theory (DFT) and model chemistries. The third objective is to develop and validate a methodology to extract and estimate reaction rate constants and physical parameters in binary compound deposition systems using the ZnO and CdO as test case. With this background



established, the fourth objective is to applying the results to reactor optimization studies for the deposition of more complex compound semiconductors, such as Zn-rich  $\text{Zn}_x\text{Cd}_{1-x}\text{O}$ .

This work is composed of five main chapters. In Chapter 2, the fundamental background of Raman scattering is introduced and its applications, such as temperature and concentration determinations are discussed. In Chapter 3, applications of the first principles calculations are examined and the importance of basis set selection (for rate and equilibrium constant calculations) is emphasized. In Chapter 4, numerical reactor modeling procedures are described and a parameter extraction procedure is briefly explained. As a test molecule, diethylzinc decomposition mechanisms and film deposition from diethylzinc and water molecules are introduced in Chapter 5. As another example, dimethylcadmium, is discussed in Chapter 6. In this chapter, the basis set selection for Raman frequency estimation is discussed.

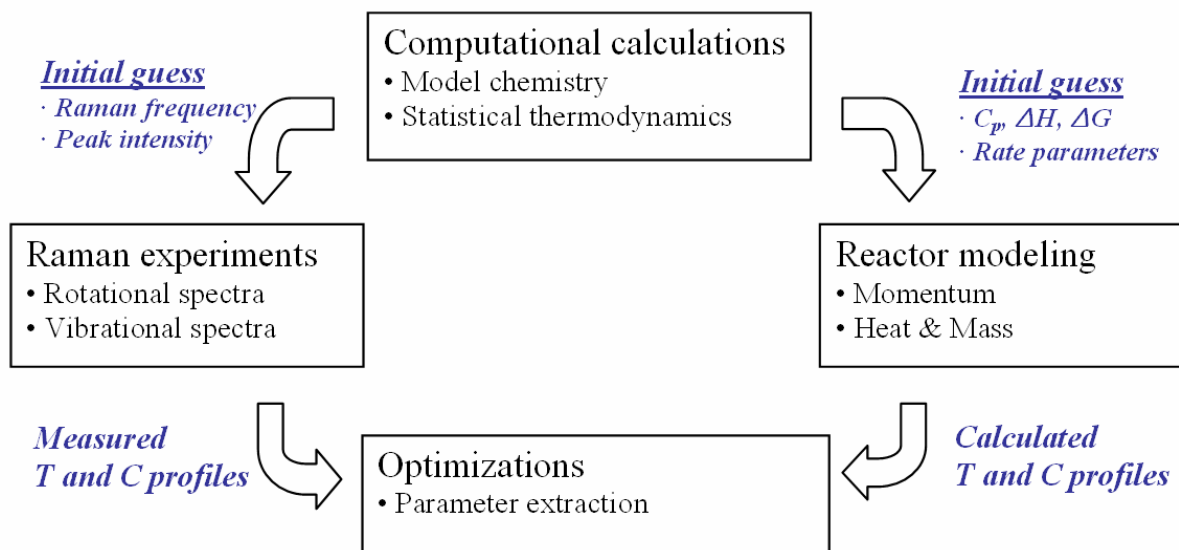


Figure 1-1. Methodology used in this study (T: temperature, C: concentration).

## CHAPTER 2 RAMAN SCATTERING DIAGNOSTICS

### 2.1 Introduction

Molecules possess translational, vibrational, and rotational degrees of freedom. They consist of atoms that have a certain mass and that are connected by elastic bonds. As a result, they can perform periodic motions at a number of fundamental frequencies. Infrared (IR) and Raman spectrometers are the most important tools for observing rotational and/or vibrational spectra. Depending on the nature of the motions, which is determined by the symmetry of the molecular structure, a specific vibrational motion may be IR active and Raman inactive or vice versa. The following characteristics are the most relevant advantages [Sch79, Sue95, Tho99] of Raman spectroscopy compared to the infrared absorption method:

- Raman requires a single excitation source, which is independent of the molecular vibration  $\bar{\nu}_m$ . For example, an incident light source at 632.8 nm allows scanning Raman shifts in the range 200~4000  $\text{cm}^{-1}$ . On the other hand, to record an IR absorption spectrum in the same range, an incident light source continuously tunable from 2.5 to 50  $\mu\text{m}$  is needed.
- Raman takes advantages of the unique characteristics of the laser source. In particular, the most beneficial advantage is that the laser can be focused to a narrow waist (confocal), thus providing high spatial resolution. This is difficult, however, to achieve in IR absorption due to the line-of-sight nature of the measurement.
- Pulsed lasers can be used in Raman spectroscopy. For example, nano, pico, or femto second lasers can be used to give high temporal resolution. IR absorption spectroscopy, however, cannot take advantage of this.
- IR spectroscopy is not suitable for totally symmetric molecules, such as  $\text{N}_2$  or  $\text{O}_2$ . In fact, these molecules are IR-inactive since there is no change in the dipole moment during the vibration (selection rules).
- Depolarization studies in Raman spectroscopy provide additional information. For example, molecular symmetry or asymmetry information can be elucidated using polarizers in the excitation and detection paths.

On the other hand, compared to IR, Raman spectroscopy has the disadvantage that its signal intensity is rather weak. Despite this, it is a suitable technique to study the kinetics within a MOCVD reactor. Many approaches to study of reactions of interest to MOCVD extract a small amount of the reacting material from the reactor through a sampling tube for *ex situ* analysis. Reactions can occur during the sample transfer or analysis to confound the results of the study. As an example, the decomposition kinetics of trimethylindium (TMIn) were investigated by several probing methods, and large differences in the values of frequency factors and activation energies were reported [Hwa04, Jac64, Lar86] (see section 3.4.1). Therefore, more reliable kinetic information on a MOCVD process is obtainable if *in situ* probing is used with a reliable probe. As with *ex situ* methods, analysis of *in situ* observations is complex and requires a detailed reactor model since MOCVD processes are influenced by factors such as carrier gas, properties of the reactor wall, flow patterns inside the reactor, and thermal conditions. In addition, temperature variations within a MOCVD reactor are generally steep and therefore chemical changes of reactants occur very rapidly. As a consequence, high spatial resolution is necessary. The combination of *in-situ* Raman spectroscopy with its high spatial resolution on reliable reactor models should be an appropriate approach to study the reaction kinetics and chemistry occurring during MOCVD.

## 2.2 Theoretical Background

“The much admired dark blue of the deep sea has nothing to do with the color of water, but is simply the blue of the sky seen by reflection”, this was stated by Lord Rayleigh, who had successfully explained the blue color of the sky as due to the scattering of sunlight by molecules constituting the gaseous atmosphere [Alm92]. Raman later explained this as arising from the scattering of light by water molecules. The effect is based on the change in the energy of the radiation during scattering [Mih98]. During irradiation, some of the photons are scattered as a

result of the dipole moments induced through the static polarizability of the electrons. This is referred to as Rayleigh or elastic scattering. On the other hand, a small fraction of the photons is scattered through the modulation of the electronic, rotational, and vibrational motions leading to Raman or inelastic scattering, this process being much more informative (Figure 2-1). The vibrational and rotational structure of such molecules can be investigated by means of Raman spectroscopy. Raman scattering is closely related to Rayleigh scattering, which is described below.

Molecules with no permanent dipole moment (homonuclear diatomic molecules and also certain types of polyatomic molecules) do not have pure vibrational or rotational spectra. As said before, when molecules (or atoms) interact with light whose frequency is away from their natural absorption frequency, a certain fraction of the radiation is scattered elastically, i.e., the wavelength remains unchanged. This process is Rayleigh scattering. The Rayleigh scattering cross-section depends on the polarizability of the molecule and on the wavelength of the radiation. Classically, the bound electrons in the molecule can be seen as executing forced vibrations under the electric field  $\varepsilon e^{i\omega t}$  (i.e.,  $e^{i\omega t}$  is a wave equation and  $\varepsilon$  is the amplitude) of the electromagnetic wave, with an amplitude proportional to  $\varepsilon$  and to the polarizability. As a result of this interaction, they radiate perpendicular to their direction of motion at the frequency  $\omega$  of the driving field. In a perfectly homogeneous medium, the contributions to sideways scattering cancel out and it is the statistical fluctuations about the mean density that are responsible for Rayleigh scattering. Its close connection with the refractive index,  $n$ , is brought out by the fact that the Rayleigh scattering cross-section is proportional to  $(n-1)^2$ .

In addition to elastic scattering (Rayleigh), there is a much smaller probability for the molecules to scatter the radiation inelastically (Raman). The difference in energy between the

incident and scattered photons is accounted for by a change in excitation energy (rotational, vibrational, or even electronic) of the molecule. This is Raman scattering, and the relation between the frequencies of the incident,  $\omega$ , and scattered,  $\omega_s$ , radiation is given by

$$\hbar\omega - \hbar\omega_s = \Delta E \quad (2-1)$$

where  $\hbar$  is the reduced Plank constant and  $\Delta E$  is specific to the molecule. Raman scattering evidently gives information on the energy levels of the molecule. For a red shift or  $\Delta E$  positive, the molecule ends up to a higher energy state; for a blue shift or  $\Delta E$  negative, into a lower state. These two cases are known as Stokes and anti-Stokes scattering, respectively.

### 2.2.1 Characteristics of Scattered Light

Assume an incident light source with intensity  $I_0$  [W/cm<sup>2</sup>] at frequency  $\nu_0$  to be incident on a sample. The scattered intensity,  $I_{\text{scat}}$ , can be defined as a function of several parameters, e.g.,

$$I_{\text{scat}} = f(V, r, \lambda, n, n_0) I_0 \quad (2-2)$$

where  $V$ ,  $r$ ,  $\lambda$ ,  $n$  and  $n_0$  are the molecular volume, the distance between the molecule and scattered photon, the wavelength, and the refractive index of molecular system and the surroundings, respectively. Light is scattered in all directions, which gives a  $1/r^2$  dependence. Moreover, it is known that the electric field,  $\bar{E}_{\text{scat}}$ , is proportional to the dipole moment,  $P_0$ , which is again proportional to the molecular volume  $V$ . Since the scattered intensity is proportional to square of the amplitude of the electric field, it can be summarized as follows:

$$I_{\text{scat}} \propto |\bar{E}_{\text{scat}}|^2 \quad \text{and} \quad \bar{E}_{\text{scat}} \propto P_0 \propto V \quad (2-3)$$

Therefore, it is clear that the intensity of scattered light is proportional to  $V^2$ . As a result, Equation 2-2 can be more conveniently expressed as

$$I_{\text{scat}} = f(n, n_0) \cdot f\left(\frac{V^2}{r^2}\right) \cdot f(\lambda) \cdot I_0 \quad (2-4)$$

where  $n, n_0$  are dimensionless. Since  $V^2$  has the units of  $cm^6$  and  $r^2$  has units of  $cm^2$ ,  $f(\frac{V^2}{r^2})$  has units of  $cm^4$  and, hence,  $f(\lambda)$  has the units of  $cm^{-4}$ . Therefore, the intensity of the scattered light is proportional of  $1/\lambda^4$ .

$$I_{\text{scat}} \propto \frac{1}{\lambda^4} \quad (2-5)$$

From the above statement, the radiation intensity,  $I$ , due to the transition moment  $[\mu_0]_{fi}$ , where the subscripts  $f$  and  $i$  refer to the final and initial states of the transition, can be rewritten as

$$I = k'_v \tilde{\nu}^4 [\mu_0]_{fi}^2 \sin^2 \theta \quad (2-6)$$

where  $k'_v = \pi^2 c / 2\varepsilon_0$  and  $\mu_0$  is the transition moment amplitude.  $\tilde{\nu}$  is the wavenumber ( $\equiv 1/\lambda$ ) of the scattered radiation and  $\varepsilon_0$  is the vacuum permittivity, respectively. The angle  $\theta$  represents the angle of observation (or detection) relative to the incident light. Suppose that the illumination, characterized only by its  $z$ -component ( $E_z \neq 0$  only) propagates along the  $y$ -axis and the scattered light is observed along the positive  $x$ -axis. For this experimental setup, the scattering plane is the  $xy$ -plane and the relevant components of the polarizability tensor are  $\alpha_{yz}$  and  $\alpha_{zz}$  only. Therefore, the observed intensity can be divided into two parts related to each of these polarizability components. For the Stokes scattering case:

$$I_{\parallel}^{\perp} = k'_v \tilde{\nu}^4 (v_k^i + 1) b_{v_k}^2 \overline{(\alpha'_{yz})_k^2} E_{z0}^2 \quad (2-7a)$$

$$I_{\perp}^{\perp} = k'_v \tilde{\nu}^4 (v_k^i + 1) b_{v_k}^2 \overline{(\alpha'_{zz})_k^2} E_{z0}^2 \quad (2-7b)$$

where the subscripts // and  $\perp$  specify the directions of the scattered electric fields relative to the scattering plane and the bar above  $\alpha$  denotes space average. If there are  $N$  randomly oriented molecules, the following term needs to be considered:

$$N \sum_i (v_k^i + 1) f_{v_k^i} = \frac{N}{1 - \exp(-hc \tilde{\nu}_k / k_B T)} \quad (2-8)$$

where  $f_{v_k^i}$  is the fraction of molecules in the vibrational state  $v_k^i$ . Then,

$$^{\perp} \mathbf{I}_{//} = N \frac{\tilde{\nu}^4 h k_{\tilde{\nu}}' \overline{(\alpha'_{yz})_k^2} E_{z0}^2}{8\pi^2 c \tilde{\nu}_k [1 - \exp(-hc \tilde{\nu}_k / k_B T)]} \quad (2-9a)$$

$$^{\perp} \mathbf{I}_{\perp} = N \frac{\tilde{\nu}^4 h k_{\tilde{\nu}}' \overline{(\alpha'_{zz})_k^2} E_{z0}^2}{8\pi^2 c \tilde{\nu}_k [1 - \exp(-hc \tilde{\nu}_k / k_B T)]} \quad (2-9b)$$

Degeneracy has not been considered during the derivation of Equations 2-9. If a vibration mode  $k$  has a degeneracy  $g_k$ , the observed intensity will be  $g_k$  times as intense as that given by Equations 2-9. The sum of the two terms in the left hand side of Equations 2-9 is the experimentally observed signal intensity and their ratio gives information about the molecular geometry.

The scattering intensity for the rotational case is calculated in a similar way. In the rotational case, the energy spacing is not constant (as in the harmonic oscillator assumption) and therefore a summation similar to that given in Equation 2-8 is not necessary. The pertinent relations are:

$$^{\perp} \mathbf{I}_{//} = k_{\tilde{\nu}}' \tilde{\nu}^4 N_{v'',J''} \overline{[\alpha'_{yz}]_{v'',J''}^2} E_{z0}^2 \quad (2-10a)$$

$$^{\perp} \mathbf{I}_{\perp} = k_{\tilde{\nu}}' \tilde{\nu}^4 N_{v'',J''} \overline{[\alpha'_{zz}]_{v'',J''}^2} E_{z0}^2 \quad (2-10b)$$

where  $v''$  and  $J''$  are the initial vibrational and rotational states, respectively, and the terms with a bar represent again space-averaged squares of the transition polarizability components. For



diatomic molecules, the space-averaged squares are reported.  $N_{v,J}$  is the number of molecules in state  $(v, J)$ . For initial state  $(0, J)$ ,

$$N_J = N \frac{g_J (2J+1) \exp[-F(J)hc / k_B T]}{\sum_J g_J (2J+1) \exp[-F(J)hc / k_B T]} \quad (2-11)$$

where  $F(J)$  is the rotational term.  $g_J$  is degeneracy due to the nuclear spin statistics and should be considered when the molecule has a center of symmetry. The term  $(2J+1)$  is the degeneracy for rotational state  $J$ . For the ground vibrational state, the rotational term  $F(J)$  is given by the following expression:

$$F(J) = B_0 J(J+1) - D_0 J^2 (J+1)^2 + \dots \quad (2-12)$$

where  $B_0$  is the rotational constant and  $D_0$  the centrifugal distortion constant. The subscript '0' implies that the vibrational quantum number is zero. In Equation 2-12, the first term derives from the rigid rotor approximation, while the second and higher order terms account for non-rigidity. For nitrogen, the values of  $B_0$  and  $D_0$  are 1.989574 and  $5.76 \times 10^{-6} \text{ cm}^{-1}$ , respectively, indicating that, in this case, the rigid rotor approximation is valid.

### 2.2.2 Selection Rules

Using a simple classical model, it is easy to demonstrate that when a chemical species is irradiated at the frequency  $\nu_s$  and its polarizability is modulated at the vibrational frequency  $\nu_0$ , the time dependence of the induced dipole moment  $\mu$  is given by:

$$\mu(t) = \alpha_0 E_0 \cos 2\pi \nu_0 t + \frac{1}{2} \left( \frac{\partial \alpha}{\partial Q} \right)_0 Q_0 E_0 \cos 2\pi (\nu_0 + \nu_s) t + \frac{1}{2} \left( \frac{\partial \alpha}{\partial Q} \right)_0 Q_0 E_0 \cos 2\pi (\nu_0 - \nu_s) t \quad (2-13)$$

where  $\alpha$ ,  $\alpha_0$  and  $E_0$  are the polarizability, the static polarizability at equilibrium state, and the amplitude of the radiation, respectively. The three terms in Equation 2-13 correspond to the

Rayleigh scattering (with  $\nu = \nu_0$ ), to the anti-Stokes Raman scattering (with  $\nu = \nu_0 + \nu_s$ ) and to the Stokes Raman scattering (with  $\nu = \nu_0 - \nu_s$ ). The selection rules for Raman scattering are determined by evaluating the transition moment  $R$ , which is given by:

$$R = \int \varphi_i^* \mu \varphi_j d\tau \quad (2-14)$$

where  $\varphi_i^*$  and  $\varphi_j$  denote the wavefunctions explaining the electronic and vibrational states at initial and final stages, respectively. Using Equation 2-13, one obtains that

$$R = \int \varphi_i^* [(r - r_e) \left( \frac{\partial \alpha}{\partial r} \right)_e] \varphi_j d\tau \quad (2-15)$$

From Equation 2-15, it is clear that there must be a change in polarizability during a vibration for Raman scattering to occur. Therefore, Raman scattering occurs only if the following conditions hold:

$$\Delta \nu = \pm 1 \quad (2-16)$$

$$\left( \frac{\partial \alpha}{\partial Q} \right)_0 \neq 0 \quad (2-17)$$

As in IR spectroscopy, overtone transitions, which are much weaker, appear at  $\Delta \nu = \pm 2$ .

### 2.2.3 Raman Cross-Section

The Raman cross-section is one of the most important factors in experimental measurements since the intensity of a vibrational Raman transition is directly proportional to the number of molecules and to the differential cross-section [Sch79].

$$I_j = I_0 N_j \left( \frac{\partial \sigma}{\partial \Omega} \right)_j \quad (2-18)$$

where  $(\partial \sigma / \partial \Omega)_j$  is the differential scattering cross-section for the  $j^{\text{th}}$  vibrational band and  $N_j$  is the number of scattered molecules. The direct evaluation of the Raman cross-sectional area of a

stable gas such as N<sub>2</sub> at mild temperature has been attempted unsuccessfully [Sch79]. It soon turned out that, for gases, the most reliable values are obtained by comparison of the scattering cross-section with that of a rotational Raman line of N<sub>2</sub>. This method was first applied by Golden *et al.* [Gol62]. Once the absolute scattering cross-section for nitrogen is firmly established, only measurements relative to N<sub>2</sub> as standard are necessary for all other gases.

### 2.2.3.1 Absolute cross-section of nitrogen

Relative Raman scattering cross-sections of gases measured with laser excitation are determined relative to that of the Q-branch of the vibrational Raman band of nitrogen. The advantage of using N<sub>2</sub> as an internal standard is that, on one hand, it is non-reactive and can easily be mixed with other gases, and on the other hand, no resonance enhancement is expected, except in the far *UV*. Therefore, it is very important to determine the absolute scattering cross-section for nitrogen as accurately as possible. Hyatt *et al.* [Hya73] reported a measurement using the pure rotational Raman line (J=1→3) of H<sub>2</sub> at 587 cm<sup>-1</sup> as reference and they established that the nitrogen cross-section closely follows the  $(\bar{\nu}_0 - \bar{\nu}_j)^4$  dependence for the visible exciting lines of an argon ion laser from 458 to 514 nm [Hya73, Gol62]. The scattering cross-section of the rotational lines of H<sub>2</sub> was chosen as reference because its optical anisotropy and wavelength dependence are well known both experimentally and theoretically. To check the results, a measurement of the cross-section of the Q-branch of the vibrational band relative to the strongest pure rotational line (J=6→8) of nitrogen was also made. The differential scattering cross-section of a Stokes shifted pure rotational Raman line in the S-branch ( $\Delta J=+2$ ) of a linear molecule is given by the following relationship [Sch79]:

$$\frac{d\sigma_{rot}}{d\Omega}(\nu_0, J) = \frac{2^4 \pi^4}{45} (\nu_0 - \nu_{rot})^4 \cdot \frac{3(J+1)(J+2)}{2(2J+3)(2J+1)} \cdot 7\gamma_0^2 \quad (2-19)$$

where  $\nu_{rot}$  is the wavenumber shift of the rotational line and  $\gamma_0^2$  the anisotropy of the polarizability tensor. Taking into account the thermal population of the initial level, the statistical weight factor  $g_s$  due to the nuclear spin, and using Equation 2-19 for the intensity of a rotational line (Equation 2-20), where  $B$  denotes the rotational constant, gives

$$I_{rot} = N \cdot \frac{d\sigma_{rot}}{d\Omega} \cdot I_0$$

$$= \frac{2^4 \pi^4}{45} \cdot g_s \cdot N \cdot (\nu_0 - \nu_{rot})^4 \cdot e^{\frac{-J(J+1)hcB}{kT}} \cdot \frac{3(J+1)(J+2)}{2(2J+3)(2J+1)} \cdot 7\gamma_0^2 \cdot I_0 \quad (2-20)$$

Spectroscopic temperature can be determined from the intensity ratio of a Stokes and an anti-Stokes rotational Raman line, as can be seen from the following expression:

$$\frac{I(J)_{Stokes}}{I(J)_{anti-Stokes}} = \frac{(\nu_0 - \nu_{rot})^4}{(\nu_0 + \nu_{rot})^4} \cdot e^{\frac{4(J+\frac{3}{2})hcB}{kT}} \quad (2-21)$$

and was found to be  $299 \pm 1$  K for hydrogen at a room temperature of  $296 \pm 2$  K [Sch95]. Table 2-1 shows the results of the measurements of the absolute differential Raman scattering cross-section of the Q-branch of  $N_2$  at  $2333 \text{ cm}^{-1}$  [Sch79]. The normalized absolute differential scattering cross-sections are also presented as a function of  $(\nu_0 - \nu_{rot})^4$ . Therefore it appears well justified to calculate a weighted average from all the available data. The following result is then obtained:

$$\left(\frac{d\sigma_{rot}}{d\Omega}\right)_{Q,N_2} = (5.05 \pm 0.1) \cdot 10^{-48} \cdot (\nu_0 - 2331 \text{ cm}^{-1})^4 \quad [cm^6 / Sr] \quad (2-22)$$

This value can be used throughout the visible and into *UV* to about 330 nm.

### 2.2.3.2 Relative cross-section of nitrogen

Most of the differential Raman scattering cross-sections in the literature are given relative to the cross-section of the Q-branch of  $N_2$  measured at the same excitation wavelength and can

therefore be readily converted into absolute values [Sch79]. The relative differential scattering cross-section shows a slight dependence on the excitation wavelength, i.e.,

$$\frac{\frac{d\sigma_j}{d\Omega}}{\left(\frac{d\sigma_{rot}}{d\Omega}\right)_{Q,N_2}} = \frac{(\nu_0 - \nu_j)^4}{(\nu_0 - 2331)^4} \cdot \frac{2331}{\nu_j [1 - \exp(-hc\nu_j/kT)]} \cdot \frac{g_j \cdot (45a_j^2 + 7\chi_j\gamma_j^2)}{(45a_{N_2}^2 + 7\chi_{N_2}\gamma_{N_2}^2)} \quad (2-23)$$

especially when the Raman shift  $\nu_j$  is very different from  $2331 \text{ cm}^{-1}$ . In Equation 2-23, the exponential Boltzmann factor for  $N_2$  has been omitted because it is negligible at ambient temperature, and  $\chi_j$  denotes the fraction of anisotropic Raman scattering which is concentrated in the Q-branch. To compare results obtained at different wavelengths, one usually needs to recalculate the results for one particular wavelength. This procedure can be avoided by defining the so-called “relative normalized differential Raman scattering cross-section”, given as follows:

$$\Sigma_j \equiv \frac{\frac{d\sigma_j}{d\Omega}}{\left(\frac{d\sigma_{rot}}{d\Omega}\right)_{Q,N_2}} \cdot \frac{(\nu_0 - 2331)^{-4}}{(\nu_0 - \nu_j)^{-4}} \cdot [1 - \exp(-\frac{hc\nu_j}{kT})] = \frac{2331}{\nu_j} \cdot \frac{g_j \cdot (45a_j^2 + 7\chi_j\gamma_j^2)}{(45a_{N_2}^2 + 7\chi_{N_2}\gamma_{N_2}^2)} \quad (2-24)$$

This differential cross-section is now independent of  $\nu_0$ , as long as  $a_j^2$  and  $\gamma_j^2$  can be regarded as constant and independent of the temperature. It is also obvious that the quantity  $\Sigma_j$  is closely related to the scattering activity  $g_j \cdot (45a_j^2 + 7\chi_j\gamma_j^2)$ .

Some examples for the relative normalized differential scattering cross-section,  $\Sigma_j$ , are presented in Table 2-2 [Sch79]. The accuracy of the data shown is  $\pm 10 \%$  for the visible excitation lines and  $\pm 15 \%$  in the near *UV*. Within these limits most of the values agree quite well.

## 2.3 Experimental Methods

Chemical vapor deposition consists of gas phase reactions involving one or more gaseous reacting species and surface reactions at a heated substrate that lead to film deposition. Compound semiconductors are usually deposited by the volatilization of a suitable metal-bearing compound into a carrier gas, which is then transported to the deposition zone. The precursor molecule should be thermally stable at a temperature sufficiently high to produce an adequate vapor pressure yet thermally unstable at the higher deposition temperature. These criteria are generally fulfilled by metal organic compounds. The main control parameters are the gas flows, gas composition, substrate temperature, and the geometry of the deposition apparatus (reactor design). Optimizing the reactor design and operating conditions for a particular application can be long and expensive if performed experimentally. If quantitative information is available about the reaction pathways, reactor models are now sufficiently sophisticated to allow many of the optimizations to be performed computationally. Unfortunately there have been very few kinetic studies of the MOCVD reaction chemistry [Dav90, Kel69, Mes98, Liu78]. For the reaction noted in the previous section, Raman spectroscopy is expected to be a good approach to such studies. Detailed information on the system and the experimental methodology are described below.

### 2.3.1 Inverted Impinging Jet MOCVD Reactor

It is important to design an experimental reactor that give a strong signal and is able to be accurately modeled. An inverted stagnation flow reactor (Figure 2-3) was used to investigate *in situ* gas phase reaction kinetics. Gas flow is directly introduced from the bottom inlets toward a quartz envelope where ceramic heaters are placed. This inverted geometry allows a significant suppression of natural convection effects due to the existing vertical temperature gradient. The reactor was designed to be axisymmetric to simplify its modeling.

**Reactor Body:** Since quartz is transparent to visible light, the main reactor body was constructed with quartz to simplify the interpretation of Raman measurements (Figure 2-3). The reactor body consisted of a cylindrical inner reactor chamber to mimic CVD reactions and an outer rectangular enclosure to minimize loss of optical signals during the experiments. The inner reactor consisted of a quartz cylinder (ID = 70 mm) with four longitudinal slots positioned to allow to admission of the probing source or collection of the scattered light. This cylindrical envelope shape ensured uniformity of the flow pattern inside. This arrangement allowed the gas phase dynamics to be monitored through the main body of the reactor.

**Reactor Exit:** The reactor outlet assembly that sealed to the reactor body (o-ring) consisted of a stainless steel cylindrical chamber equipped with two symmetrical exhaust lines and an electric heating unit. The heating unit consisted two stacked heaters connected in parallel to provide sufficient energy to maintain the high working temperature of the proposed experiments ( $\sim 900^{\circ}\text{C}$ ). Temperature has measured with a Ni-Cr thermocouple that was placed underneath the heaters to control the current supply. In addition, a porous ceramic cap was placed over the heating unit to reduce heat loss from the heater and to enhance the signal to noise ratio when Raman scattering data were collected near the heater. The actual MOCVD substrate was not installed during the measurements, rather the bottom surface of the quartz envelope served as the susceptor.

**Reactor Inlet:** The reactor base was equipped with three gas inlets, named center, annular and outer positions. Each inlet was filled with glass beads and equipped with a screen to produce a paralleled flow condition at exit of the packed bed gas distribution (Figure 2-9). The center and annulus inlet channels supplied the metal organic precursor and inert or  $\text{H}_2\text{O}$  gas, respectively,

while an inert gas was supplied through the outer inlet channel to sweep the reaction gases away to prevent wall deposition and thus signal attenuation.

### 2.3.2 Spectroscopy System

The MOCVD reactor is interfaced with a Raman spectrometer (Jobin Yvon U-1000). 488 nm or 514 nm lines of the argon-ion laser and the 532 nm line of solid-state laser were available as excitation light sources. The Raman signal is collected at a right angle with respect to the excitation axis, directed into a double monochromator, and detected by a photomultiplier (PMT) or by a charge coupled device (CCD). The entire reactor is mounted on an x-y-z translation stage to allow spatial probing of the gas phase. With this design, the temperature and concentration of species at a specific point within the reactor can be measured without disturbing the flow system. A schematic diagram of the Raman system used in this work is depicted in Figure 2-4. This system is also capable of solid-state Raman micro probing using a microscope attached to the system.

**Lasers:** Laser radiation has significantly different properties from the radiation emitted by conventional light sources since it is highly directional, spectrally pure and very intense. The solid-state laser (Verdi-8, Coherent) and an argon ion laser (Innova 90, Coherent) were used in this work. The solid-state laser has a single line emission at 532.08 nm and the argon ion laser produces several lines, but the intense 488 or 514 nm lines, which could be independently selected, were used in this work. The laser beam is optically steered and focused by a lens (focal length = 110 mm) into the macro chamber where either a transparent reactor or a gas flow cell is located. Raman scattering signals from the sample are collected at a right angle and focused into the entrance slit of the spectrometer (Jobin Yvon, U-1000).

**Monochromator:** Monochromators are the most widely used dispersive instruments. The spectrometer was equipped with two gratings, which have a groove density of 1800 lines/mm.



This spectrometer covers the spectral range 320 to 910 nm and its focal length is 1 m. An exit slit, set to approximately the same size as the entrance slit, is used to isolate a small spectral range from all the wavelengths that strike the focal plane. This range is the monochromator spectral bandpass. Different spectral bandpasses can be selected sequentially by rotating the dispersion element to bring a new band into the proper orientation so that it passes through the exit slit (see Section 2.3.3.1). Figure 2-5 shows the double-additive monochromator used in the experiments.

**Detector:** Scattered light is dispersed and then observed with either a PMT or CCD detector (Figure 2-6). The PMT contains a photosensitive cathode and a collection anode. The cathode and anode are separated by several electrodes called dynodes to provide electron multiplication or gain. Figure 2-7 shows a schematic circuit diagram of a typical PMT. The cathode is negatively biased in the range 400 to 2500 V with respect to the anode. A photoelectron ejected by the photocathode strikes the first dynode and releases two to five secondary electrons. Each secondary electron is accelerated by the field between the first and second dynode and strikes the next dynode with sufficient energy to release another two to five electrons. Since each dynode down the chain is biased  $\sim 100$  V more positive than the preceding dynode, this multiplication process continues until the anode is reached. The result is a large charge packet generated in a few *ns* for each photoelectron collected by the first dynode. Finally, the number of anode pulses per unit time or per unit event is counted (photon counting).

Like photodiode arrays, a CCD is a solid-state sensor and is constructed with integrated circuit technology. The charges generated by the incident photons are collected and stored in metal oxide semiconductor (MOS) capacitors. The MOS capacitors are initially reversed biased by a positive voltage applied to the metallic electrode; this creates a depletion region in the

silicon below the electrode. Photons striking the array give rise to electron-hole pairs, and the electrons can be stored temporarily in the wells. An array of these devices can be scanned for the stored charges.

**Recorder:** Finally, photon signals from either of the detectors are converted into electric signals which are acquired and processed in the personal computer.

### **2.3.3 System Characteristics**

#### **2.3.3.1 Wavelength selection**

Monochromators consist of a dispersive element (prism or grating) and an image transfer system (entrance slit, mirrors or lenses, and exit slit). Within the monochromator an image of the rectangular entrance slit is transferred to the exit slit after dispersion of the wavelength components of the incident radiation. The grating monochromator used in this study is based on the Czerny-Turner configuration shown in Figure 2-8. The slits play an important role in determining the resolution and the light throughput of the monochromator. Incident radiation passes through the entrance slit  $S_1$  and strikes the parabolic, collimating mirror  $M_1$ . The entrance slit, at the focal point of  $M_1$ , acts as a point source to produce parallel radiation for the dispersion element, a grating. The grating spatially disperses the spectral components of the incident radiation. Collimated rays of diffracted radiation strike the parabolic focusing or camera mirror  $M_2$ . The dispersed radiation is focused in the focal plane producing entrance slit images in that plane. Because the parallel rays of a given wavelength are incident on the focusing element at a specific angle, each wavelength is focused to a slit image at a different center position on the focal plane. The exit slit  $S_2$  placed in the focal plane isolates a particular wavelength interval. To change the wavelength selected by the monochromator, the dispersive element is rotated to bring a different wavelength band through the exit slit. The characteristic of dispersion is summarized in Table 2-3. Then, the desired signals are selected through the exit slit and passed

into the detector. The spectral bandpass (nm) is the half-width of the wavelength distribution passed by the exit slit. The spectral bandpass can be calculated as the product of geometrical entrance slit width and the reciprocal linear dispersion of the grating [Ing88]. The geometric spectral bandpass is given by

$$s_g = R_d W_s \quad (2-25)$$

where  $R_d$  and  $W_s$  are the reciprocal linear dispersion and slit width, respectively. The reciprocal linear dispersion is determined by the specific design of the spectrometer. For the U-1000,  $R_d=0.243$  nm/mm at 514.5 nm. As a typical example by setting the slit width to 100  $\mu\text{m}$ , a spectral band pass of 0.024 nm is obtained. The spectral resolution, hence, is given by  $0.9 \text{ cm}^{-1}$ .

The geometrical width of both the entrance and exit slits determine the spectral profiles of the output observed at the exit slit, since the entrance slit image is swept across the exit slit. The resulting convolution of the entrance and exit slit images is a triangular shaped function,  $t(\lambda)$ , called the slit function. Mathematically, the slit function can be described as

$$\begin{aligned} t(\lambda) &= \{1 - |(\lambda - \lambda_0)/s_g|\} & \text{for } \lambda_0 - s_g \leq \lambda \leq \lambda_0 + s_g \\ t(\lambda) &= 0 & \text{elsewhere} \end{aligned} \quad (2-26)$$

where  $\lambda_0$  is the wavelength setting of the monochromator and  $\lambda$  is the incident wavelength.

Depending upon the relative values of the slit function and the width of the spectral source to be measured, the result of the convolution will vary. This is especially important when one has to measure the true profile of a line. Thus, for a monochromatic source,  $t(\lambda)$  indicates the fraction of the image on the image on the focal plane at a given wavelength that is passed by the exit slit. In other words, the slit function indicates the shape of a narrow spectral line recorded on a spectrometer during a spectral scan.

### 2.3.3.2 Signal to noise ratio

Because noise affects the quality and precision of spectroscopic measurements, the optimization of experimental variables is based on increasing the signal to noise ratio (S/N). Noise can be divided into two categories: predictable and unpredictable. Unpredictable noise is referred to as random noise and it can be further divided into two categories. Firstly, there is fundamental random noise. Because of the discrete characteristics of light and matter, this noise cannot be eliminated (and is sometimes called intrinsic noise). Secondly, there is non-fundamental random noise coming from imperfect instrumental components or poorly devised experiments. In principle, this can be eliminated, and it is sometimes called extrinsic noise.

On the other hand, there is predictable noise. This noise can be found from many sources, such as spectrometer with photomultiplier tube or focal length adjustment from the MOCVD reactor to monochromator. Therefore, the system calibration for the optimum S/N ratio should be performed in advance and then lenses or mirrors in the MOCVD reactor unit should be adjusted. Once the limiting noise sources are identified, the conditions for highest S/N can be determined. The detail calibration method is described in section 2.4. The S/N can be expressed using the information provided by the signal, as well as of knowledge of the predictable, and unpredictable noise (Equation 2-27) [Ing88].

$$S / N = \frac{E_s}{(\sigma_s^2 + \sigma_B^2 + \sigma_{dt}^2)^{\frac{1}{2}}} \quad (2-27)$$

where  $E_s$  is the signal intensity (for example, voltage or counts), and each noise is defined as follows:

- $\sigma_s = [(\sigma_s)_s^2 + (\sigma_s)_f^2]^{\frac{1}{2}}$  Shot and flicker noise contributions
- $\sigma_B = [(\sigma_B)_s^2 + (\sigma_B)_f^2]^{\frac{1}{2}}$  Background shot and flicker contributions

- $\sigma_{dt} = (\sigma_d^2 + \sigma_{ar}^2)^{\frac{1}{2}}$  Dark and amplifier-readout contributions

- $\sigma_d = [(\sigma_d)_s^2 + (\sigma_d)_{ex}^2]^{\frac{1}{2}}$  Dark shot and excess noise contributions

where  $\sigma$  and  $\sigma^2$  are the standard deviation and the variance of the various contributions and the noises are considered to be independent so that they add quadratically. It should be noted that the shot and flicker contributions show a different behavior as a function of signal intensity, namely the shot noise increases with the square root of the signal, while flicker noise increases linearly with the signal.

### 2.3.3.3 Delivery of metal organic sources

A gas handling assembly was used to supply gases to the reactor. The system can supply three gases simultaneously to the reactor through the center, annulus and sweep (outer) inlets depicted in Figure 2-9. A bubbler containing a metal organics can be connected to each inlet and the flow rates are controlled by mass flow controllers. The mass flow controllers were calibrated with bubble flow meters by flowing nitrogen in 20 to 80 % of the control range.

Metal organic chemicals are normally provided with bubblers to separate chemicals from air since these chemicals are often pyrophoric and maybe toxic. A carrier gas, typically  $N_2$  or  $H_2$ , is, therefore, introduced into the bubbler. For experimentalist, the metal organic precursor is allowed to saturate the carrier gas and subsequently delivered into the MOCVD reactor. The main body of the bubbler is immersed into a heat bath, where the temperature is controlled. Thus, the partial pressure of metal organics saturated in the carrier is adjusted by changing the bath temperature. The amount of material delivered is adjusted by both the bath temperatures and carrier gas flow rates. Some typical metal organic chemicals, for transporting Zn and Cd, along with selected properties are listed in Table 2-4.

### 2.3.4 Calibrations

To obtain the most reliable experimental data, each part of the apparatus must be carefully calibrated to minimize system error or uncertainty. In particular, a Raman system is very sensitive to temperature and humidity since variation in the shape and surface featuring properties of the mirrors in the monochromator can distort the optical image. Especially in fluids, water vapor condensed on mirrors to change the reflective index, with the consequence that a peak shift may occur and the signal to noise ratio would decrease. In fact, optimum signal to noise ratio is essential in the experiments to recognize the low-intensity peaks at the expected spectral positions. Moreover, well-calibrated conditions help to recognize reaction intermediates or products. Therefore, calibrations must always be carried out before undertaking a measurement.

#### 2.3.4.1 Monochromator

Calibration of the monochromator is the first step. Generally, the wavelength accuracy is calibrated using the strong mercury emission at 546.074 nm. Therefore, a mercury lamp or even room light from a fluorescent bulb can be used as the light source. After placing the lamp in front of the entrance slit, the calibration procedure is as follows:

Since the Raman shift of mercury appears at  $1122.6\text{ cm}^{-1}$  (for wavelength of 514.5319 nm incident light and mercury emission at 546.074 nm), the first step is to place the proper information into the controlling software. Next, the four slits should be adjusted as discussed later. Finally, the first and second slits of the spectrometer should be narrow ( $\sim 15\text{ }\mu\text{m}$  each) while the third and fourth slits are relatively wide (50 and  $100\text{ }\mu\text{m}$ , respectively). The first and second slits are then adjusted to maximizing the wavenumber shift intensity. Then, the incident light should be scanned in the approximate range  $500\text{ to }520\text{ cm}^{-1}$  to detect mercury Raman shift

position. This step is usually easy since the intensity is sufficiently strong and distinctly lies in the wavenumber range. These conditions are selected to give a strong mercury signal using very sensitive conditions (i.e. at 15  $\mu\text{m}$  width for all slits). Therefore, this rough scan would indicate how much the spectrometer was affected by the environment (i.e., temperature, humidity) and it can be corrected by adjusting the mirror placed behind of the spectrometer to maximize the observed peak position. The spectrometer position is moved to the observed peak position and the real-time scanning procedure is performed to optimize the resolution while decreasing the third and fourth slit widths, and limit is 15  $\mu\text{m}$ . This calibration can be performed with fine-tuning of the mirror knob placed behind of the spectrometer. Therefore, the real time calibration of observed mercury emission line gives the clue for best condition of the spectrometer. Once the above procedure is done, the wavelength counter on the spectrometer is adjusted to indicate real mercury position at 546.074 nm and subsequently the detector is then calibrated.

#### **2.3.4.2 Detector**

The PMT device consists of a photomultiplier tube and its socket. A high voltage of -1750 V is supplied to the cathode and with the counted photon signal outputted through the anode. The signal is then sent to the amplifier and discriminator (Jobin Yvon, DM302) where the real signal is selected and amplified. Since the amplifier and discriminator play an important role on the signal to noise ratio, it must be fine-tuned. It is noted that this step should be done after monochromator calibration has been completed.

To tune this instrument all light sources (such as the Mercury lamps, room lights, and lasers) should be turned off to allow checking the background level of the PMT. Then, the light source (a Mercury lamp) is turned on and another scan is taken to detect the Mercury signal. The maximum signal level of the PMT response is recorded. To improve the signal to noise ratio, the

amplifier and discriminator level should be adjusted by adjusting a screw bolt in the device using an insulated screw driver while at the same time monitoring the signal level of PMT to determine the change in the signal to noise ratio. The dark and Hg lamp signal maximization step should be repeated until a maximum signal is attained under Hg lamp illumination and with less than 25 counts of dark background signal. If the signal to noise ratio deteriorates or the background rises above 25 counts, the adjustment should be repeated in the opposite direction. This fine-tuning of the amplifier settings should enable the experimentalist to achieve a high signal to noise ratio.

#### **2.3.4.3 Reactor**

Once the light source interacts with gas flows inside of the reactor, scattered light is emitted in all directions. The lenses, which are located outside the reactor and perpendicular to the excitation axis, collect scattered photons and transfer them to the entrance slit of the monochromator. Therefore, distances of the lenses from the reactor wall and their vertical position are important to maximize collection of photons. Since the monochromator and the detector are assumed to be calibrated, the reactor calibration is the last step before taking an actual measurement. Since carrier gas of  $N_2$  is stable at typical reaction conditions, it is recommended to use this gas for reactor calibration. First, establish a  $N_2$  flow through the gas center line with the other 2 lines. Next scan in real time the strongest intensity of rotational Raman shift, i.e., the 6<sup>th</sup> excitation motion at  $60\text{ cm}^{-1}$ . Adjust the vertical position of the lenses as well as their focusing distance from the monochromator to maximize the peak intensity. After this procedure is satisfied completely, the gas supply can be switched to the metal organics for the experimental measurements.



## 2.4 Applications

### 2.4.1 Temperature Measurement

As mentioned in section 2.2.2, for diatomic molecules, such as  $H_2$ , the selection rule  $\Delta \nu = +1$  refers to Stokes Raman scattering and  $\Delta \nu = -1$  to anti-Stokes Raman scattering. When  $\Delta \nu \neq 0$ , there is a change in the vibrational energy, there is also a change in the rotational energy. This allows  $\Delta J = -2$  ( $J' < J''$ ) to arise as well as  $\Delta J = +2$  ( $J' > J''$ ), since a rotational level in the higher vibrational state will necessarily have a higher energy than a rotational level in the lower vibrational state, irrespective of the relative  $J$  values. The rotational energy,  $E_R$ , of a diatomic molecule is most conveniently expressed in wavenumber, using the rotational term  $F(J)$ , where  $F(J) = E_R / hc$ . In the *rigid rotor* approximation, which assumes the moment of inertia about the bond axis is zero,  $F(J)$  is given by;

$$F(J) = BJ(J+1) \quad (2-28)$$

where  $B = \frac{h}{8\pi^2 Ic}$ , where  $I$  is the moment of inertia about an axis through the center of gravity and perpendicular to the bond axis,  $h$  is the Planck constant, and  $c$  is the light velocity. If the masses of the two atoms are  $m_1$  and  $m_2$ , and their distance apart is  $r$ , then it is easily shown that

$$I = \mu r^2 \quad (2-29)$$

where  $\mu$  is termed the reduced mass and is given by the expression

$$\mu = \frac{m_1 m_2}{m_1 + m_2} \quad (2-30)$$

It should be noted that in real molecules the rigid rotor approximation does not apply, and centrifugal stretching arises because of the non-rigidity of the bond. Also, because of anharmonicity, the distance  $r$ , and hence  $I$  and  $B$ , become functions of the vibrational quantum number. Proceeding with the rigid rotor approximation, and combining the selection rule

$\Delta J = +2$  with  $F(J)$  as defined in Equation 2-29, the magnitude of the wavenumber shift associated with a rotational transition can be expressed as follows:

$$\begin{aligned} |\Delta \tilde{\nu}_s| &= F(J+2) - F(J) \\ &= B(J+2)(J+3) - BJ(J+1) \\ &= 4B(J + \frac{3}{2}) \end{aligned} \quad (2-31)$$

where  $J = 0, 1, 2, \dots$ . The series of lines arising from transitions with  $\Delta J = +2$  is termed the  $S$  branch, hence the designation of the wavenumber shift as  $|\Delta \tilde{\nu}_s|$ . In addition,  $\Delta J = 0$  is termed the  $Q$  branch,  $\Delta J = +1$  the  $R$  branch,  $\Delta J = -1$  the  $P$  branch and  $\Delta J = -2$  the  $O$  branch. Thus, provided the rotational levels are reasonably populated, a pure rotational Raman spectrum will consist of two series of lines or  $S$  branches, one on each side of the exciting line of wavenumber  $\tilde{\nu}_0$ . One series will be the Stokes lines (involving transitions of the type  $J+2 \leftarrow J$ , for which  $\Delta J = +2$ ), with absolute wavenumber  $\tilde{\nu}_0 - |\Delta \tilde{\nu}_s|$ . The pattern of spacing is now easily deduced. When  $J=0$ ,  $|\Delta \tilde{\nu}_s| = 6B$ , when  $J=1$ ,  $|\Delta \tilde{\nu}_s| = 10B$ , when  $J=2$ ,  $|\Delta \tilde{\nu}_s| = 14B$  and so on. Thus in each  $S$  branch the first rotational line has a wavenumber shift of  $6B$  from the excitation line and successive rotational lines have equal interline spacing of  $4B$ .

In general, the pure rotation of a molecule will give rise to a pure rotational Raman spectrum if the polarizability of the molecule varies in different directions at right angles to the axis of rotation. Therefore, even symmetrical molecules such as  $H_2$  and  $CO_2$  have pure rotational Raman spectra. The selection rule for pure rotational Raman energy changes for linear molecules is  $\Delta J = 0, \pm 2$ . This selection rule differs from that for infrared transitions ( $\Delta J = \pm 1$ ). One way to rationalize this is that in a nonsymmetrical diatomic molecule the permanent dipole moment rotates with the molecule but, because of its symmetry, the polarizability ellipsoid after only one-half a molecular revolution is indistinguishable from the original ellipsoid. Applying

this selection rule to the rotational energy equation, one obtains the wavenumber of the Stokes lines ( $J+2 \leftarrow J$ ),

$$\tilde{\nu} = \frac{\Delta E_{rot}}{hc} = B(4J + 6) \quad J = 0, 1, 2, \dots \quad (2-32)$$

and of the anti-Stokes ( $J \rightarrow J-2$ ),

$$\tilde{\nu} = \frac{\Delta E_{rot}}{hc} = B(4J - 2) \quad J = 2, 3, 4, \dots \quad (2-33)$$

Figure 2-10 shows a rotational Raman spectrum of  $N_2$  taken on the system described in this section. The frequencies in  $\text{cm}^{-1}$  of  $N_2$  can be reproduced by Equation 2-32.

Taking advantage of Raman scattering, there have been several studies to determine temperature profiles in MOCVD reactors [Kop84, Mon86]. A given rotational state distribution of a molecule is related to a given temperature (Equation 2-9). Conversely, by measuring the distribution spectroscopically, the temperature information can be obtained. It was reported that this temperature measurement technique could be accurate with less than 5 % of uncertainty at typical MOCVD conditions [Dri82]. The measured intensity of a rotational transition is the sum of two parts as shown Equations 2-9. Rotational transitions at the ground state of vibration are generally used for temperature measurement and therefore vibration quantum numbers are dropped. For Stokes Raman scattering, the observed intensity **I** is

$$\mathbf{I} = (\tilde{\nu}_0 - \tilde{\nu}_{J+2,J})^4 \frac{g_J (2J+1) \exp[-F(J)hc / k_B T]}{\sum_J g_J (2J+1) \exp[-F(J)hc / k_B T]} N \frac{7}{45} \frac{3(J+1)(J+2)}{2(2J+1)(2J+3)} C_0 \quad (2-34)$$

where  $\tilde{\nu}_0$  is the wave number of the incident light and  $C_0$  is a constant ( $= k'_v \gamma_0^2 E_{z_0}^2$ ) under given experimental conditions. A few correction factors to this equation are needed to account for non-ideality. Every spectroscopy system has its own spectral response as a function of wavelength.

In addition, the anisotropy  $\gamma_0^2$  is influenced by the centrifugal distortion. With these considerations, the observed intensity is finally expressed as:

$$\mathbf{I} = (\tilde{\nu}_0 - \tilde{\nu}_{J+2,J})^4 \frac{g_J \cdot (2J+1) \cdot \exp[-F(J)hc/k_B T]}{\sum_J g_J \cdot (2J+1) \cdot \exp[-F(J)hc/k_B T]} N \frac{7}{45} \frac{3(J+1)(J+2)}{2(2J+1)(2J+3)} C_0 \times R(J; \tilde{\nu}_0) \cdot f(J) \quad (2-35)$$

where  $R(J; \tilde{\nu}_0)$  is the spectral response of the spectrometer and  $f(J)$  is the correction to the anisotropy ( $\gamma_0^2$ ) of the polarizability.  $R(\tilde{\nu})$  is an equipment-specific quantity and it is determined experimentally with a well-known light source such as a tungsten strip lamp. An expression for  $f(J)$  is theoretically given in the following form:

$$f(J) = 4 \chi^{-1} (B_e/\omega_e)^2 [J(J+1) + (J+2)(J+3)] \quad (2-36)$$

where  $\chi$  and  $B_e/\omega_e$  are respectively 0.45 and  $8.476 \times 10^{-4}$  for nitrogen. Rearranging Equation 2-35 and taking the natural logarithm results in the following equation:

$$\ln \left\{ \frac{(2J+3)\mathbf{I}}{(\tilde{\nu}_0 - \tilde{\nu}_{J+2,J})^4 g_J (J+1)(J+2) R(J; \tilde{\nu}_0) f(J)} \right\} = C_1 - \frac{F(J)hc}{k_B T} \quad (2-37)$$

where  $C_1 = \ln \left\{ 7NC_0 / 30 \sum_J g_J (2J+1) \exp[-F(J)hc/k_B T] \right\}$  and this is a constant at each experimental condition. Therefore, the temperature can be extracted from the Boltzmann distribution expression in Equation 2-37 by linear regression if the spectral response  $R(\tilde{\nu})$  and the correction to the anisotropy  $f(J)$  are known. At high temperature, the population of the next excited vibrational state increases and another correction should then be included: this holds for  $R(\tilde{\nu})$  and  $f(J)$  as well. For nitrogen, this correction is not necessary for  $T$  below  $10^3$  K [Dra82], due to its high vibration frequency ( $2331 \text{ cm}^{-1}$ ). Therefore, the rotational spectra of  $N_2$  can be easily utilized for temperature determination under typical MOCVD reaction conditions.

The results of temperature measurement in the MOCVD system used in this work are presented below. It was found that this method was very accurate in extracting the local temperature. For example, the test temperature obtained from this procedure was  $23.7 \pm 0.8$  °C, which was in very good agreement with the value of 23.6 °C obtained from a measurement. Figure 2-11 shows a photograph of the reactor with arrow points to the three different axial positions at which measurements were taken. The temperature at each point was then determined using Equation 2-37. It should be noted that the actual height of the reactor is adjustable along the vertical z-axis while the probing light beam is at fixed position (Figure 2-11). Since the actual measurements could be carried out with fine adjustments of reactor height, this probing method provides the most reliable temperature profiles in MOCVD reactor, which is characterized by rapid changes in temperature along the vertical axis. Figure 2-12 shows the rotational spectra of N<sub>2</sub> taken at the 3 positions. At room temperature, the most populated N<sub>2</sub> rotational state is placed at 6<sup>th</sup> rotational excited state; therefore, this peak at 60 cm<sup>-1</sup> can be distinguished clearly at position ③. Using the procedure outlined in this section using Equation 2-37, a linear relationship was obtained (Figure 2-13). This measurement was repeated to obtain the temperature profile in MOCVD reactor (Figure 2-14) along the entire axis for a set point of 200°C. The intercept in Figure 2-14 is the temperature predicted at the substrate surface, a parameter which is not easily amenable to experimental evaluation. This requires, however, a quantitative determination of C<sub>1</sub>, which is specific to a given experimental setup, while the slope does not contain any setup-specific information.

#### 2.4.2 Concentration Measurement

Equations 2-8 and 9 share a common term, i.e.,  $I \propto N(\partial\sigma/\partial\Omega)$  where the term in the parentheses is the differential cross-section at a specified observation angle (90 ° in this study)

and is a function of the incident light and temperature. For the vibrational case, the differential cross-section is deduced from Equation 2-8 as follows:

$$\left( \frac{\partial \sigma}{\partial \Omega} \right)_k = C_k \frac{(\tilde{\nu}_0 - \tilde{\nu}_k)^4}{\tilde{\nu}_k [1 - \exp(-hc \tilde{\nu}_k / k_B T)]} \quad (2-38)$$

where  $C_k$  is a constant, which contains specific information of the  $k^{\text{th}}$  vibrational mode. The value of  $C_k$  is determined experimentally and the absolute cross-section for the vibration is then obtained. In practice, cross-sections are usually reported relative to that of the Q-branch of nitrogen at  $2331 \text{ cm}^{-1}$  because nitrogen is sufficiently stable enough to be an internal standard and its cross-section closely follows the  $(\tilde{\nu}_0 - \tilde{\nu}_k)^4$  dependence in the visible range [Sch79]. In the ultraviolet, however, a resonance enhancement effect ordinarily takes place and Equation 2-38 is no longer valid. With the nitrogen Q-branch standard, the relative cross-section for vibration mode  $k$ ,  $\Sigma_k$ , is defined as

$$\Sigma_k = \frac{C_k \tilde{\nu}_Q}{C_Q \tilde{\nu}_k} = \frac{(\partial \sigma / \partial \Omega)_k (\tilde{\nu}_0 - \tilde{\nu}_Q)^4}{(\partial \sigma / \partial \Omega)_Q (\tilde{\nu}_0 - \tilde{\nu}_k)^4} \frac{1 - \exp(-hc \tilde{\nu}_k / k_B T)}{1 - \exp(-hc \tilde{\nu}_Q / k_B T)} \quad (2-39)$$

The relative cross-section defined in Equation 2-39 is independent of experimental conditions such as temperature and wavelength of the incident light. The spectral response,  $R(\tilde{\nu})$ , of the spectrometer must be incorporated in the calculations involving measured intensities, because  $\tilde{\nu}_k$  and  $\tilde{\nu}_Q$  are usually apart from each other.

When reaction kinetics is studied with Raman spectroscopy, a relationship between the intensity ratio and the density ratio of two constituents is easily derived. One of the two constituents is conveniently taken as an internal standard. From Equations 2-8 and 39, the density ratio of components  $j$  and  $q$  is related to their intensity ratio by

$$\frac{N_q}{N_j} = \frac{(\tilde{\nu}_0 - \tilde{\nu}_j)^4}{(\tilde{\nu}_0 - \tilde{\nu}_q)^4} \frac{1 - \exp(-hc \tilde{\nu}_q/k_B T)}{1 - \exp(-hc \tilde{\nu}_j/k_B T)} \frac{\mathbf{I}_q}{\mathbf{I}_j} \Sigma_j \quad (2-40)$$

where  $N$  is the number density and  $\mathbf{I}_j$  a measured intensity of component  $j$ . Then, for a binary system, the mole fraction of component  $j$  is given by

$$x_j = \frac{N_j}{N_j + N_q} \quad (2-41)$$

### 2.4.3 Electronic Raman Scattering

Atomic metals such as Zn or Cd can be produced by sequential fragmentation of metal organic precursors. Electrons at ground state can be excited to higher energy states by the probing light source and then relax to the original level. If degenerated ground states are available, transitions between ground states and the first excited state can show Raman-like effects called “electronic” Raman. For example, the ground states of group III atoms, such as Ga, In, and Al are commonly  $^2P_{1/2}$  and  $^2P_{3/2}$  and the first allowed excited electronic state is  $^2S_{1/2}$ . Since two different ground states exist, a typical three level Raman scheme exists, i.e., excitation from  $^2P_{1/2}$  to  $^2S_{1/2}$  and emission from  $^2S_{1/2}$  to  $^2P_{3/2}$ . Splittings for the group III atoms are 16, 113, 826, and 2213  $\text{cm}^{-1}$  for B, Al, Ga, and In atoms, respectively.

The above argument does not apply, however, to atoms in the group II column of the periodic table since their atomic orbital is a closed s orbital. For example, Zn and Cd have  $3d^{10}4s^2$  and  $4d^{10}5s^2$  configurations in their outermost shells. Therefore, electronic Raman cannot be present and, as a result, electronic Raman detection is not possible during the experiment. This, for example, detection of metal Zn atom is not considered in the diethylzinc decomposition study. The Zn atom configuration ground state  $^1S_0$  and its most probable emission lines are shown in Figure 2-15 and Table 2-5. Among them, the emission line of ① is the most likely;

however, radiation from the excited state ( $^1P_1$ ) to the ground state ( $^1S_0$ ) has a spontaneous lifetime of 1.6 ns, which is too short to be detected. It is conceivable that other techniques, such as atomic absorption and fluorescence, may be much better suitable than electronic Raman to follow the concentration profiles of these atoms in the MOCVD reactor. These measurements can be performed with tunable laser sources since the excitation wavelength needs to be resonant with the atomic transition from the ground state to the excited state.

## 2.5 Summary

The advantages of Raman scattering experiments on gas-phase MOCVD reaction kinetics have been described. The principles of Raman scattering were explained, with emphasis on the characteristic features that are relevant to *in situ* measurements in the MOCVD reactor of this study. Therefore, the system characteristics, including spectrometer, detectors, and MOCVD reactor, and even the associated calibration procedures were discussed in detail. The calibration details for each part are expected to be useful to maintain the system properly.

The important physical properties, such as relative Raman cross-section, were introduced and mathematical expressions for temperature and concentration measurements were derived. As an example, sample measurements and calculations for  $N_2$  carrier gas were presented and the concept of electronic Raman effects was introduced.



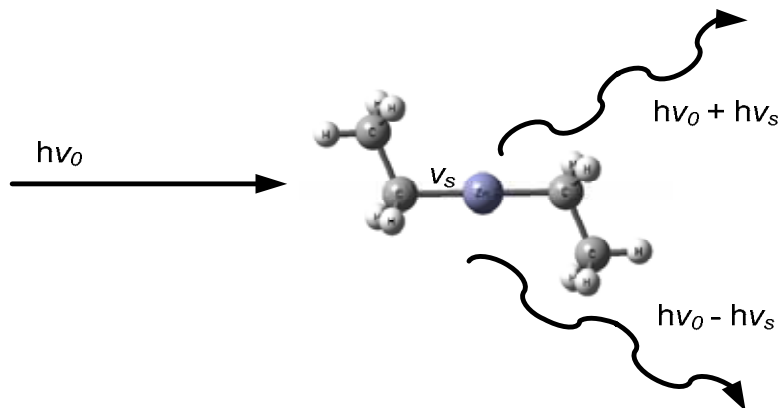


Figure 2-1. Principles of Raman scattering illustrated for a diethylzinc molecule with Zn-C vibrational frequency.

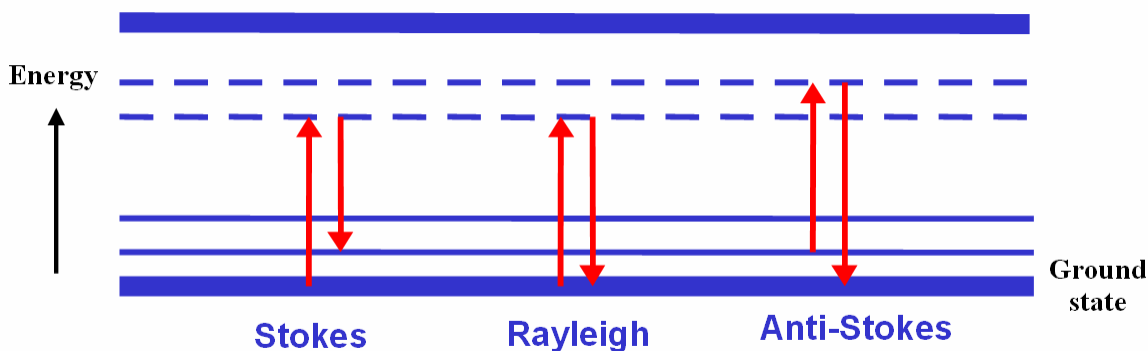


Figure 2-2. Rayleigh and Raman scattering as a two-photon process. The broken line represents virtual levels at some energy above the ground state level.

Table 2-1. Absolute Raman cross-section of N<sub>2</sub> measured at different wavelength of incident light.

Exciting line $\lambda_0$ [nm]	$\frac{d\sigma}{d\Omega}$ [ $10^{-32} \frac{cm^2}{Sr}$ ]	$\frac{d\sigma}{d\Omega} (\nu_0 - 2331)^{-4}$ [ $10^{-48} \frac{cm^6}{Sr}$ ]
632.8	21±3	6.4±1
514.5	44±17	5.1±2
488.0	33±11	3.0±1
457.9	76±5	5.2±0.4
435.8	92±10	5.1±0.5
363.8	204±25	5.1±0.6
351.1	243±30	5.2±0.7
Weighted average		5.05±0.08

Table 2-2. Examples of relative normalized differential Raman scattering cross-sections obtained using the Q-branch of  $N_2$ .

Molecule	$\nu_j$ [cm <sup>-1</sup> ]	Exciting wavelength $\lambda_0$ [nm]									
		287	337	347	351	364	436	458	488	515	633
N <sub>2</sub>	2331	1	1	1	1	1	1	1	1	1	1
O <sub>2</sub>	1555		1.2	1.0	1.0	1.0	1.0	1.0	1.0	1.0	0.9
H <sub>2</sub>	4156		4.2				4.1		3.6	3.4	
H <sub>2</sub> O	3652		3.1	3.9					2.5	3.4	
NH <sub>3</sub>	3334			4.6	6.0	6.4	4.5	6.2	6.2	6.4	
C <sub>2</sub> H <sub>4</sub>	1623		1.8				1.7			1.5	
	1342		2.8				2.8				
C <sub>2</sub> H <sub>6</sub>	993						2.2		1.2		
C <sub>3</sub> H <sub>8</sub>	1451		2.8								
	867						1.8			1.7	
C <sub>6</sub> H <sub>6</sub>	992		9.7			10.9	12.5	10.8	6.8	12.7	
C <sub>6</sub> H <sub>12</sub>	802		4.7				3.7		3.6	4.1	

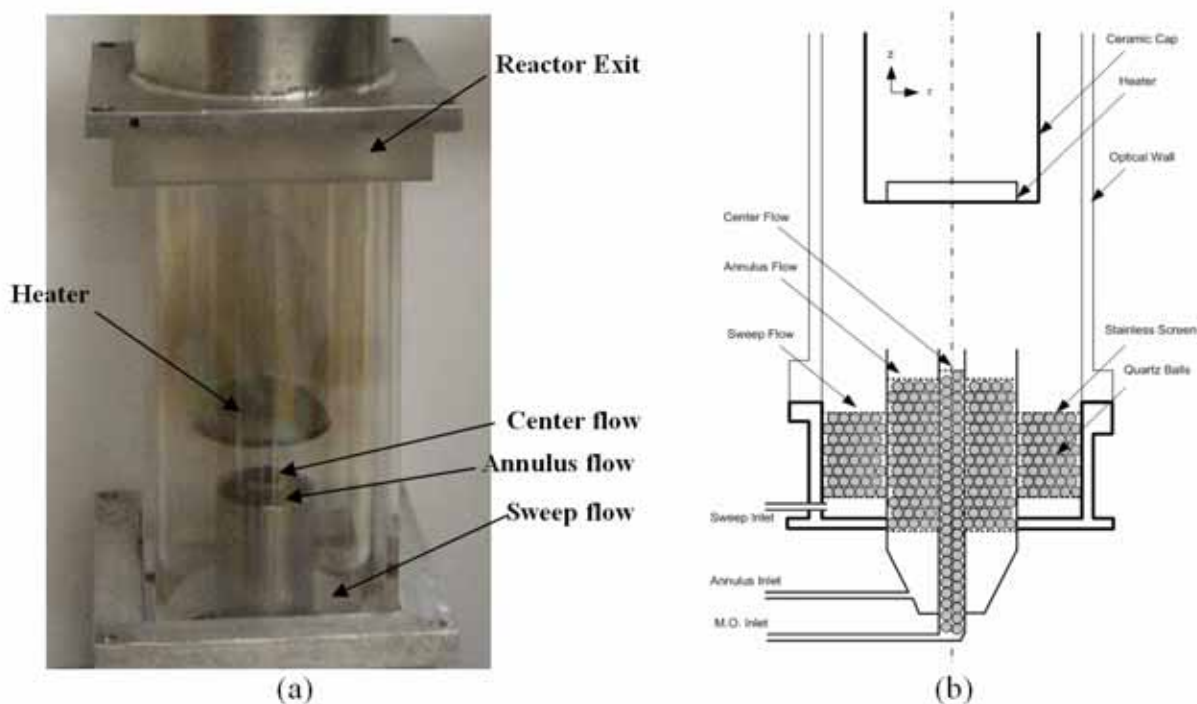


Figure 2-3. MOCVD reactor along with a photograph of the experiments (a) and a schematic diagram of the reactor (b).

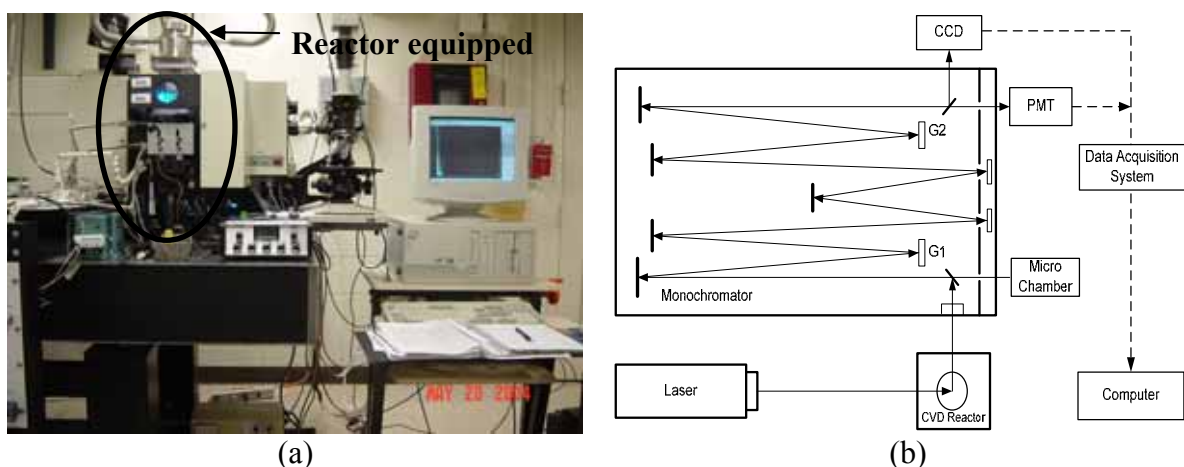


Figure 2-4. Photograph of experimental system (a) and schematic of optical path (b).

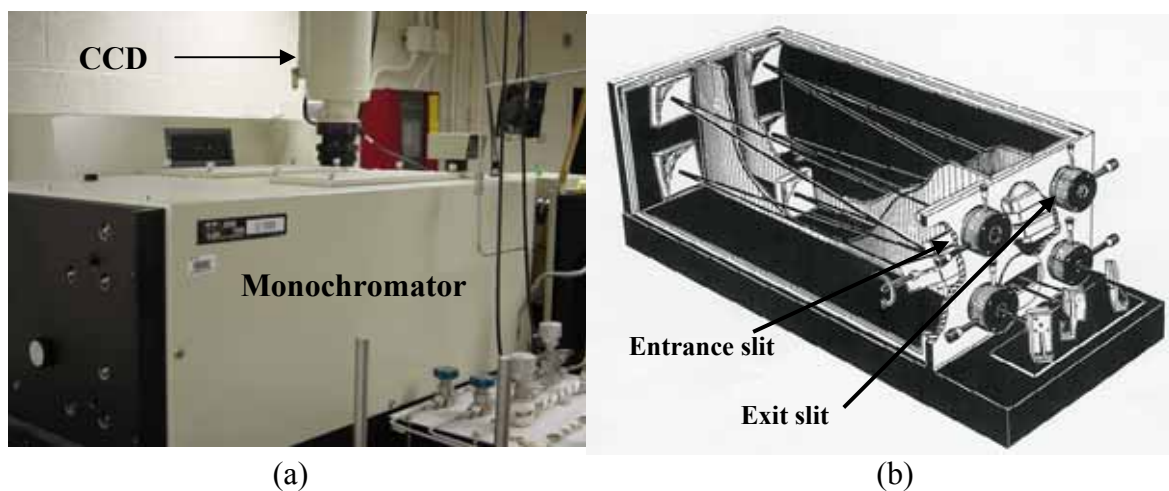


Figure 2-5. Photograph of double additive monochromator (a) and schematic of the inside (b).

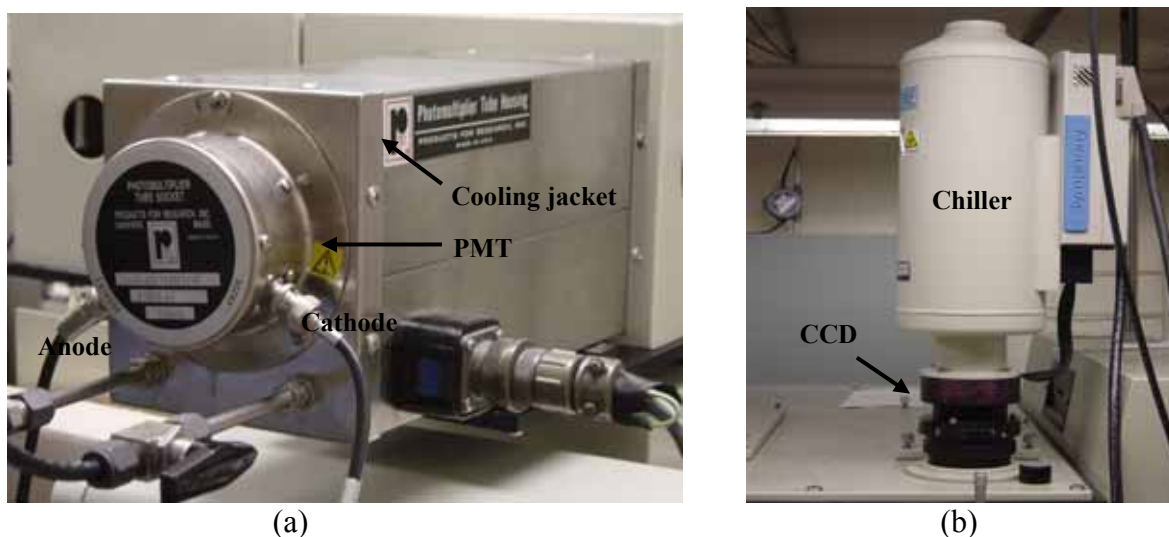


Figure 2-6. Photographs of detectors used in the experiments, PMT (a) and CCD (b).

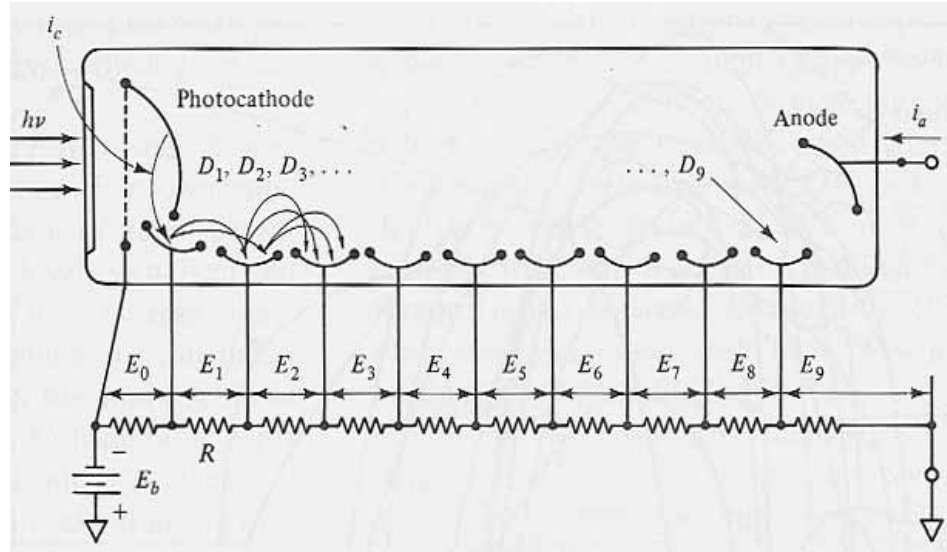


Figure 2-7. Schematic of circuit diagram for a photomultiplier tube (PMT).

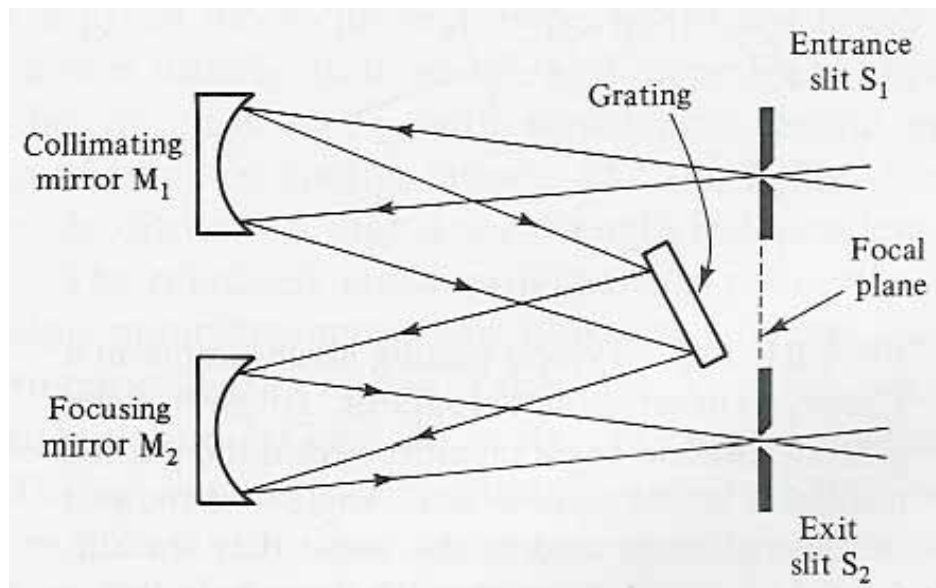


Figure 2-8. Czerny-Turner plane grating monochromator. The grating spatially disperses the spectral components of the incident radiation.

Table 2-3. Dispersions of the monochromator ( $\text{\AA}/\text{mm}$ ).

$\lambda(\text{nm})$ Gr/mm	200	300	400	500	600	700	800	900	1000
1800	2.66	2.58	2.46	2.32	2.15	1.94	1.68	1.34	0.88

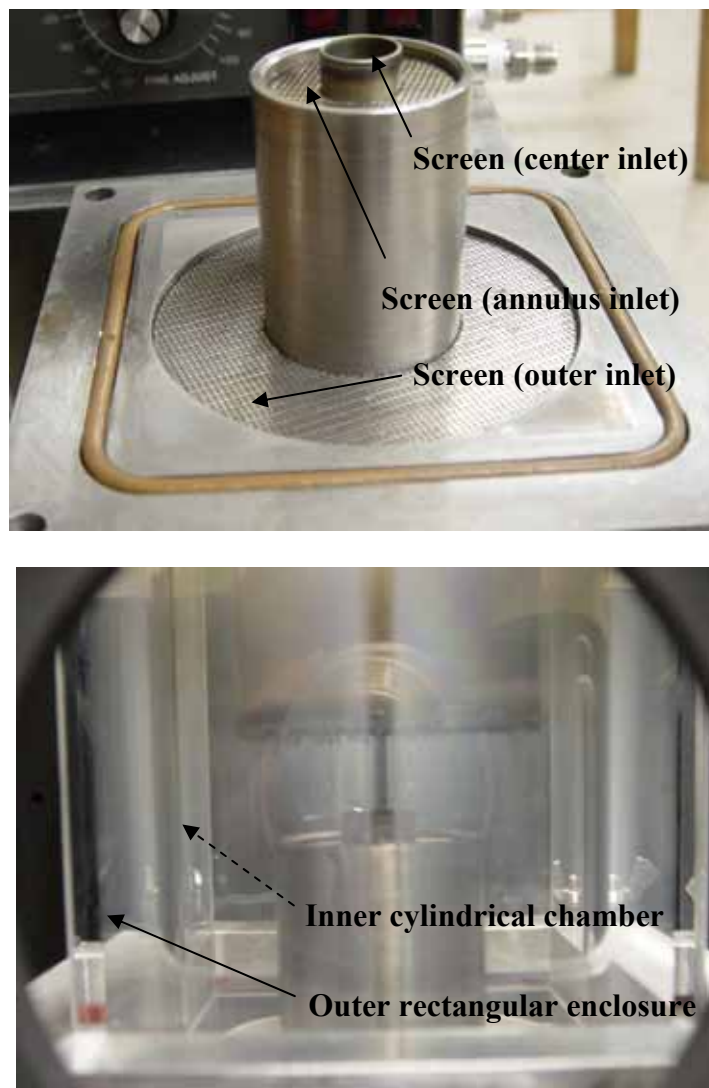
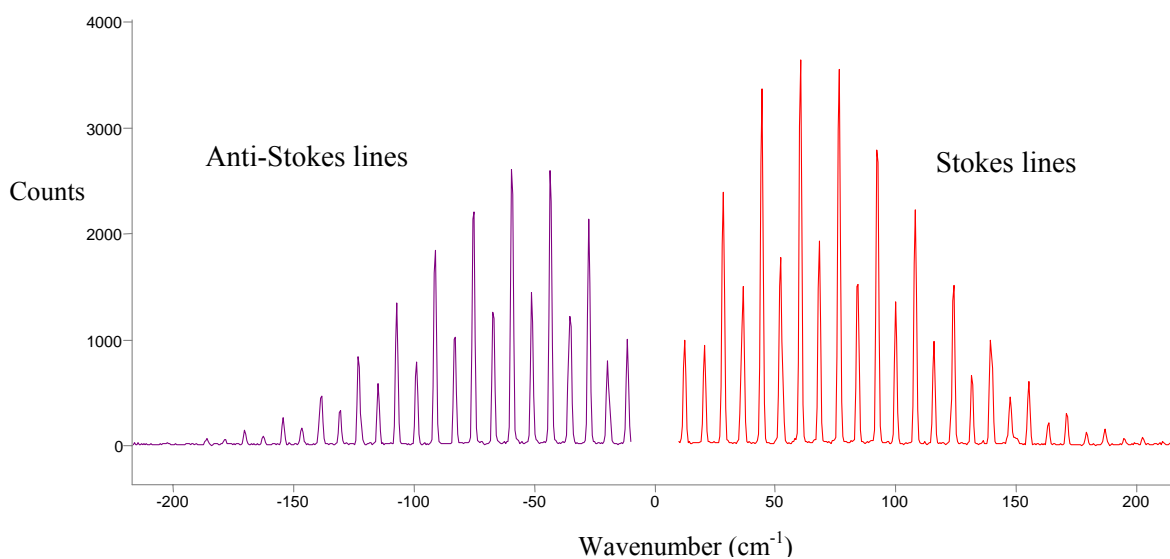


Figure 2-9. Photographs of the delivery system showing the three inlets (center, annulus, and outer). The precursor molecule is introduced via carrier gas through the center line, a second reactant (i.e.,  $\text{H}_2\text{O}$ ) through the annulus inlet, and an inert ‘sweep’ gas through the outer inlet.

Table 2-4. Selected properties of some metal organic precursors.

	Metal Organics	Formula	Molecular weight	Density (g/cc)	Hazard	Vapor pressure Log P(mmHg)=B-A/T	
						B	A
Zn	Dimethylzinc	(CH <sub>3</sub> ) <sub>2</sub> Zn	95.45	1.386	a,b	7.802	1560
	Diethylzinc	(C <sub>2</sub> H <sub>5</sub> ) <sub>2</sub> Zn	123.50	1.182	a,b	8.280	2109
Cd	Dimethylcadmium	(CH <sub>3</sub> ) <sub>2</sub> Cd	142.88	1.985	a,c	7.764	1850
In	Trimethylindium	(CH <sub>3</sub> ) <sub>3</sub> In	159.93	1.568	a,b,d	10.52	3014
	Triethylindium	(C <sub>2</sub> H <sub>5</sub> ) <sub>3</sub> In	202.01	1.260	a,b,d	8.93	2815
Ga	Trimethylgallium	(CH <sub>3</sub> ) <sub>3</sub> Ga	114.83	1.100	a,b	8.07	1703
	Triethylgallium	(C <sub>2</sub> H <sub>5</sub> ) <sub>3</sub> Ga	156.91	1.058	a,b	8.083	2162
Al	Trimethylaluminum	(CH <sub>3</sub> ) <sub>3</sub> Al	72.09	0.750	a,b	8.224	2134.83
	Triethylaluminum	(C <sub>2</sub> H <sub>5</sub> ) <sub>3</sub> Al	114.17	0.835	a,b	8.999	2361.2
Sb	Trimethylantimony	(CH <sub>3</sub> ) <sub>3</sub> Sb	166.86	1.528	b	7.707	1697
	Triethylantimony	(C <sub>2</sub> H <sub>5</sub> ) <sub>3</sub> Sb	208.94	1.324	b	7.904	2183
	Triisopropylantimony	(C <sub>3</sub> H <sub>7</sub> ) <sub>3</sub> Sb	251.02	1.200	a	9.268	2881
Se	Dimethylselenide	(CH <sub>3</sub> ) <sub>2</sub> Se	109.03	1.408	c,d	7.98	1678
	Diethylselenide	(C <sub>2</sub> H <sub>5</sub> ) <sub>2</sub> Se	137.08	1.230	c	7.905	1924
	Diisopropylselenide	(C <sub>3</sub> H <sub>7</sub> ) <sub>2</sub> Se	165.14	1.100	c	-	-
Te	Dimethyltelluride	(CH <sub>3</sub> ) <sub>2</sub> Te	157.68	1.960	c,d	7.97	1865
	Diethyltelluride	(C <sub>2</sub> H <sub>5</sub> ) <sub>2</sub> Te	185.72	1.599	c,d	7.99	2093
	Diisopropyltelluride	(C <sub>3</sub> H <sub>7</sub> ) <sub>2</sub> Te	213.77	1.365	c,d	8.288	2309

a. moisture sensitive, b. pyrophoric, c. air sensitive, d. heat sensitive

Figure 2-10. Pure room temperature rotational spectrum of N<sub>2</sub>.

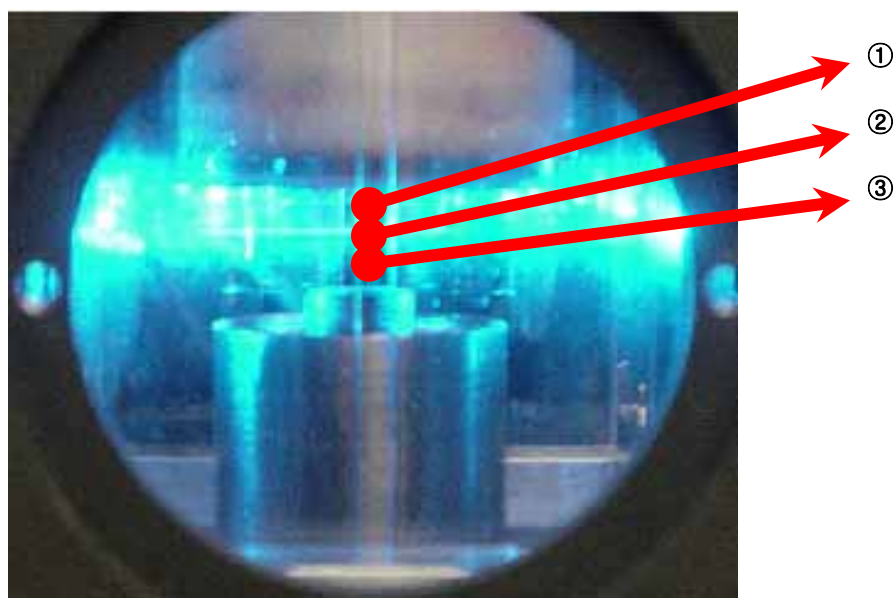


Figure 2-11. Measurement positions for temperature determination.

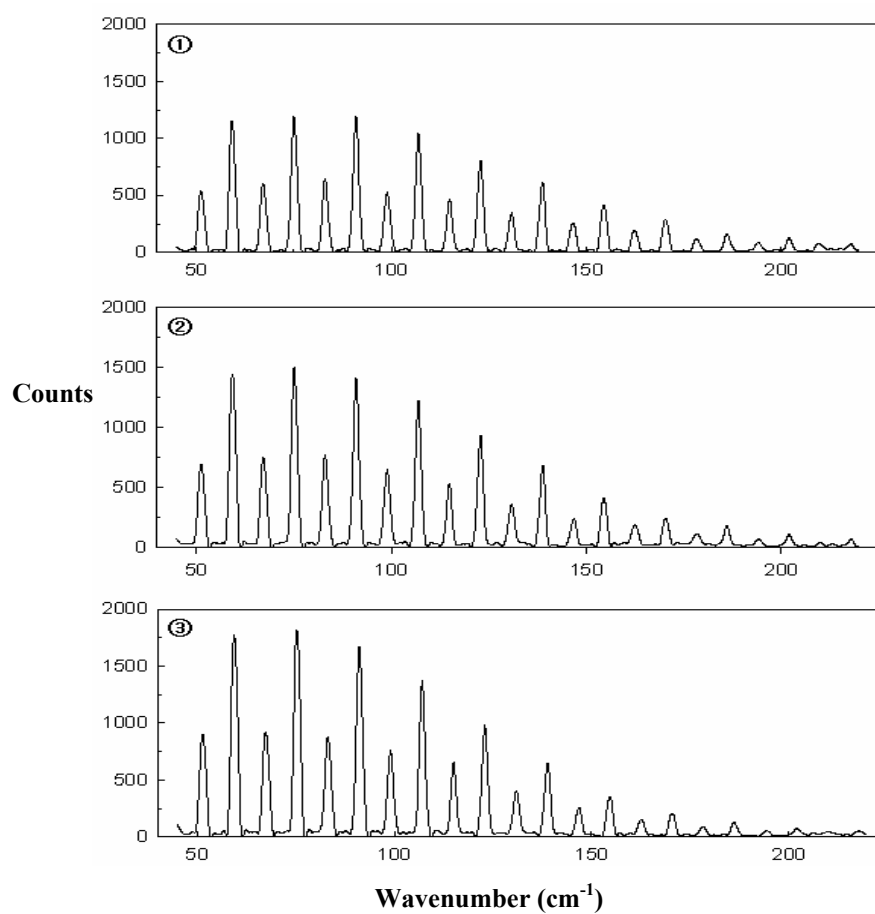


Figure 2-12. The  $N_2$  rotational spectra taken at the three different in Fig. 2-11.

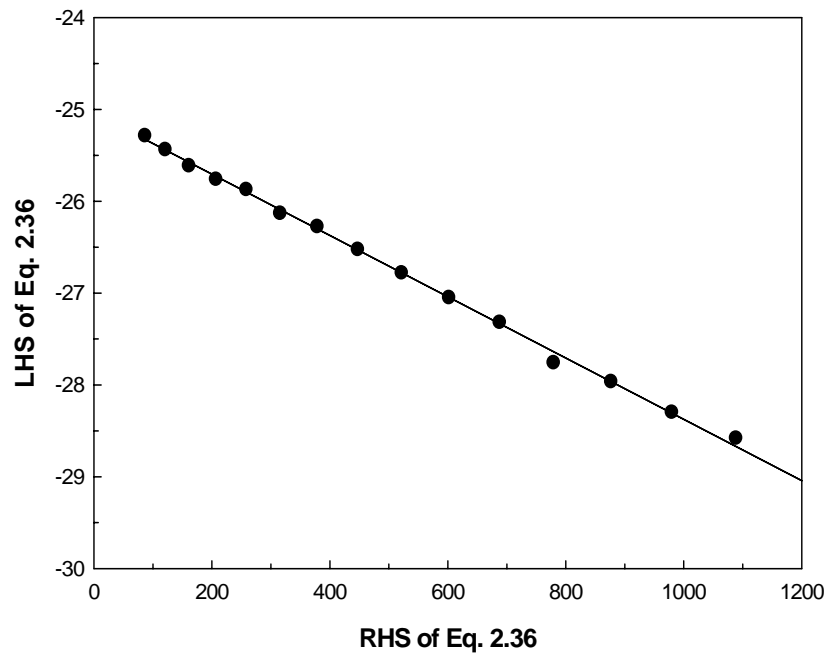


Figure 2-13. Temperature extraction at a single position using Equation 2-36.

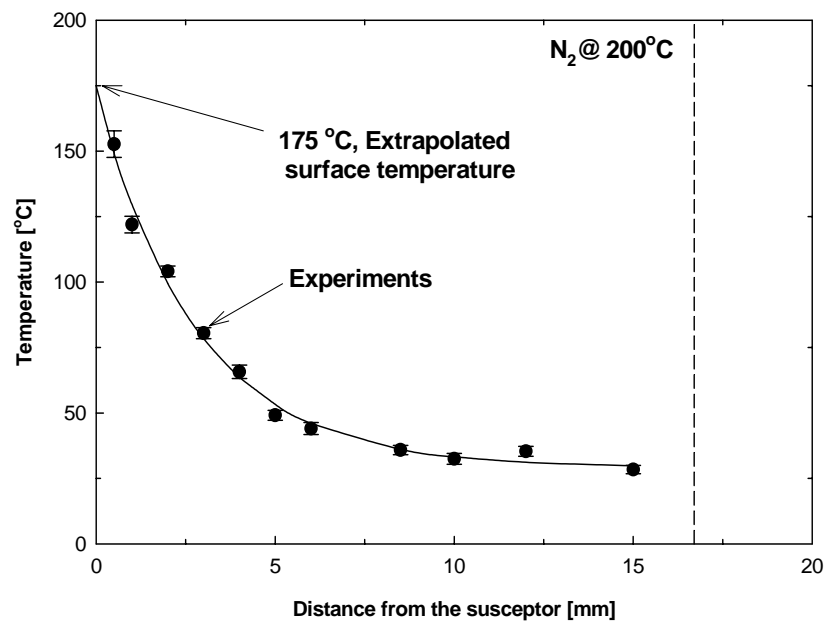


Figure 2-14. The measured temperature profile in the MOCVD reactor. The heater temperature was set at 200°C. The points were obtained by experiments and the line was simulated from the detailed model.



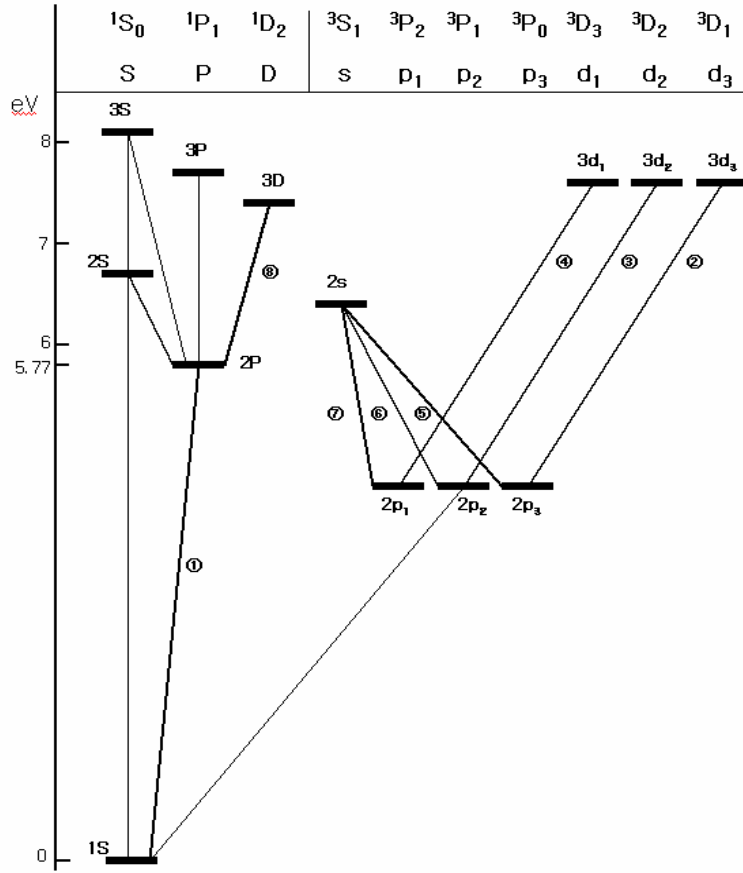


Figure 2-15. Emission lines of Zn atoms with respect to its electronic energy state.

Table 2-5. Expected emission wavelengths of Zn atom and their lifetime.

Wavelength [ $\text{\AA}$ ]	Energy Levels [K]	gA [ $10^8/\text{sec}$ ]
2138.56	0 – 46745	19.0
3282.33	32311 – 62769	4.0
3302.59	32501 – 62772	18.0
3345.02	32890 – 62777	28.0
4680.14	32311 – 53672	5.8
4722.16	32501 – 53672	4.9
4810.53	32890 – 53672	7.2
6362.35	46745 – 62458	2.8

## CHAPTER 3 FIRST PRINCIPLES CALCULATIONS

### 3.1 Introduction

Materials with the II-VI compound thin film (e.g., ZnSe) are of considerable technological importance with various applications, such as narrow and wide band-gap semiconductors, optoelectronics, thermal-imaging devices, and light emitting diodes [Bac99, Wag04, Wan05]. Despite intense experimental study for gas-phase homogeneous II-VI MOCVD kinetics, there is a large gap in understanding the reaction pathways of MOCVD precursors. In reality, there has been no detailed computational modeling of chemical processes that occur as discrete precursors are converted into extended II-VI materials even though there has been an enormous amount of comparison between computational calculations and alternative methods based on the molecular wave function. In fact, various computational methods have been fast developing over the past few years, so it is expected that the first principles calculation will be remarkably used for understanding reaction chemistry and molecular design for metal organic precursors.

There are several computational calculation methods, such as Hartree Fork (HF), density functional (DFT) theory, and molecular orbital (MO) theory calculations [Sim97, Cra02]. For a molecule, its quantum states are described by wave functions of the following eigenvalue problem:

$$\begin{aligned}\hat{H}(\vec{R}, \vec{r})\Psi(\vec{R}, \vec{r}) &= i\hbar \frac{\partial \Psi(\vec{R}, \vec{r})}{\partial t} && \text{(Time - dependent formula)} \\ &= E \Psi(\vec{R}, \vec{r}) && \text{(Time - independent formula)}\end{aligned}\tag{3-1}$$

where  $\hat{H}$ ,  $\Psi$  and  $E$  are the Hamiltonian operator of the molecule, its wave function and energy, which is an eigenvalue of the Hamiltonian, respectively. Each calculation method has its own way to define Hamiltonian. For example, DFT optimizes molecular geometry and obtain

electron density in advance. Then each term in Hamiltonian, such as electron-electron repulsion can be directly estimated. On the other hand, MO theory optimizes a wave function while HF counts the average interaction force between one electron and nucleus. Among these methods, the DFT calculation is widely accepted as a good computational solution for metal containing molecules, such as MOCVD precursors, since quantum mechanical properties strongly depend on how density distribution is accurately calculated. This implies that DFT makes a reasonable quantum mechanical operator.

The first principles calculations were performed using the Gaussian 03 program package [Fri04]. Bond formation and dissociation energies were calculated mainly using Becke's three parameters hybrid exchange functional combined with the Lee-Yang-Parr gradient-corrected correlation functional (B3LYP) with pertinent basis set for the molecule. The method and basis set specified the model chemistry used to calculate molecular optimized geometry. The calculation also gave a way to search reaction transition states and thermo-chemistry calculations. The free energy changes were used to determine whether reactions are likely or not to occur in gas phase. Therefore, in principle, a lot more information including, Raman-active shift, its intensity and thermodynamic property of the molecule can be precisely calculated in view of computational chemistry and its applications to estimate whether the reaction rate constant and equilibrium constant are also available. In addition, the first principles calculation can also be used in surface reaction study, such as adsorption or desorption on metal surfaces.

### **3.2 Estimation of Vibrational Frequency**

#### **3.2.1 Numerical Estimation**

An important advantage from the first principles calculation is the Raman frequency assignment. According to molecular symmetry, all the normal modes of vibrational motions can be defined and every specific vibrational motion can be judged to see if it is Raman-active or

Infrared-active motion and whether its intensity can be estimated. This is because of the fact that every atom in a molecule is constantly moving around its equilibrium position, and motions in a molecule are characterized with normal modes of the vibrations and they are useful in identifying chemical species. Each normal mode frequency can be calculated from the shape of the potential energy surface corresponding to the vibration. Raman intensity, however, are more difficult to compute than IR intensity, as a mixed third derivative is required to approximate the change in the molecular polarizability with respect to the vibration that is measured by the experiment. The sensitivity of Raman intensity to basis set and correlation is even larger than it is for IR intensity. However, large basis set, such as valence-triple-zeta basis set, has been developing very fast and its application with frequency scaling factors enables it to be used in estimation of most likely Raman shift and its intensity. Therefore, the software package, Gaussian 03, can provide numerical solutions for Raman-active frequency calculations for specific molecules if pertinent model chemistry is provided. It is, however, noted that the calculated frequency should be compared to literature or experimental results to verify whether the basis set really describes the molecular system well at a confident level. In fact, irrelevant model chemistry could give erroneous frequency values. In the case of MOCVD precursors, more careful verification is required since they contain metal atoms inside, which normally contain d- and f- orbital.

### 3.2.2 Analytical Estimation

Metal-carbon symmetrical vibration for MOCVD precursors can also be estimated analytically with the Morse potential, i.e.,  $V(r) = D(1 - e^{-\beta(r-r_e)})^2$  where  $D$ ,  $r_e$  and  $\beta$  represent dissociation energy, equilibrium distance, and a constant, respectively [Tow75, Sch95]. The Morse potential is based on the fact that the atoms are independent at large distances. At this time, the force between them is negligible so their energy is just the sum of the energies of the

individual atoms. At a very small distance, however, atoms must repel each other. The radial equation of the Schrödinger equation is, then, analytically solvable and the solution can be expressed as

$$\frac{E}{hc} = G(v) = \omega_e \left( v + \frac{1}{2} \right) - \omega_e \chi_e \left( v + \frac{1}{2} \right)^2 + \dots \quad (3-2)$$

where  $\omega_e = \frac{\beta}{2\pi} \sqrt{\frac{2D}{\mu}}$  and  $\chi_e = \frac{h\omega_e}{4D}$ . This implies that the analytical estimation of Raman shift

can be available since the above equation is a function of vibrational frequency. As an example, vibrational frequency between Zn and C in diethylzinc was estimated using B3LYP/6-311G(d) model chemistry. Before the atoms are close enough, they keep connecting a bond so that the whole molecule is in Singlet state; however, as the distance between Zn and C is elongated enough to be broken out, each part of two products (i.e.,  $\bullet\text{C}_2\text{H}_5$  and  $\bullet\text{ZnC}_2\text{H}_5$ ) becomes a radical so that the whole molecule becomes a triplet molecular state. The calculated potential scan is represented (Figure 3-1). The scan was accomplished with arbitrary change in distance between two atoms, Zn and C. The surface potential curves calculated from B3LYP/6-311G(d) with Singlet and Triplet multiplicities gave the dissociation energies of the molecule (D) as 0.1191178 Hartree and constant  $\beta = 1.4416062 \text{ \AA}^{-1}$ . Therefore, the harmonic term ( $\omega_e$ ) was obtained as  $477.09 \text{ cm}^{-1}$  and anharmonic term ( $\omega_e \chi_e$ ) was turned out  $1.201 \text{ cm}^{-1}$ .

### 3.2.3 Hot-band Transition Estimation

As temperature increases, the Raman shift tends to shift from its original place since more electrons jump up to higher excited states. Therefore, the contribution of temperature to the vibrational partition functions can account for population redistribution. This is called the band transition. In fact, based on information in the previous section, the hot band transition can be calculated using the relation of  $\Delta G(v) = \omega_e - 2\omega_e \chi_e (v+1)$  (Table 3-1). Beside the Morse

potential, however, computational calculation can be independently used in hot band estimations.

The general non-linear N atomic molecule has 3N-6 vibrational degrees of freedom and characteristic vibrational temperature for vibrational mode, K, can be written as [McQ76]:

$$\Theta_{v,K} = \frac{h \nu_K}{k_B} \quad (3-3)$$

Given vibrational mode, the contribution to the partition function is:

$$q_{v,K} = \frac{e^{-\Theta_{v,K} / 2T}}{1 - e^{-\Theta_{v,K} / T}} \quad (3-4)$$

Moreover, the contribution to internal thermal resulting from molecular vibration is:

$$E_v = R \sum_K \Theta_{v,K} \left( \frac{1}{2} + \frac{1}{e^{\Theta_{v,K} / T} - 1} \right) \quad (3-5)$$

As an example of diethylzinc, experimentally, symmetrical vibrational stretching between Zn and C atoms appear at 480 cm<sup>-1</sup>. From the Equation 3-3, it is easy to calculate vibrational partition functions to figure out Equation 3-4. If the zero reference point of the vibration is set as the first vibration level, it is obvious that ground state has energy of 240 cm<sup>-1</sup>. Moreover, the harmonic oscillation approximation tells us that energy difference is coherent for higher levels of excited states (in this case 480 cm<sup>-1</sup>). Table 3-2 shows the calculated Raman frequencies and vibrational temperatures. Therefore, the hot band transitions between 0→1, 1→2, 2→3, and so on can be graphically illustrated (Figure 3-2).

The relative electron population of each excited state compared with ground state can be calculated using the equation below:

$$\frac{P_{excited}}{P_{ground}} = e^{-\Delta E_{thermal}} \quad (3-6)$$

where  $P$  is the population density of electrons at specific energy level. Since the MOCVD using diethylzinc decomposition is generally carried out less than 500 °C, the population changes of each transition along with the temperature were examined below the temperature. Table 3-3 shows the calculated population changes. It is obvious that more electrons occupy higher excited states at higher temperature; as a result, portion of the lowest transition,  $P(0) \rightarrow P(1)$ , decreases. Therefore, the total shape of Zn-C symmetrical vibrational stretching looks like shifting to the left from the original frequency, 480 cm<sup>-1</sup>. To see this phenomena graphically, the fraction on ground state and excited states have been evaluated using the following equations. The transition energy can be expressed as:

$$E_v = (\nu + \frac{1}{2})h\nu \quad \nu = 0, 1, 2 \dots \quad (3-7)$$

The vibrational partition function  $q_{vib}$  becomes;

$$q_{vib}(T) = \sum_{\nu} e^{-\beta E_{\nu}} = \sum_{\nu=0}^{\infty} e^{-\beta(\nu+\frac{1}{2})h\nu} = e^{-\beta h\nu/2} \sum_{\nu=0}^{\infty} e^{-\beta h\nu \nu} \quad (3-8)$$

The summation over the equation can be evaluated easily with  $\sum_{\nu=0}^{\infty} x^{\nu} = \frac{1}{1-x}$ , therefore;

$$q_{vib}(T) = \frac{e^{-\beta h\nu/2}}{1 - e^{-\beta h\nu}} = \frac{e^{-\Theta_{vib}/2T}}{1 - e^{-\Theta_{vib}/T}} \quad (3-9)$$

In the  $\nu^{\text{th}}$  vibrational state, the fraction is:

$$f_{\nu} = \frac{e^{-\beta h\nu(\nu+\frac{1}{2})}}{q_{vib}} = (1 - e^{-\beta h\nu}) e^{-\beta h\nu \nu} = (1 - e^{-\Theta_{vib}/T}) e^{-\nu \Theta_{vib}/T} \quad (3-10)$$

In the case of diethylzinc, the calculated frequency (B3LYP/6-311G(d)) is 486 cm<sup>-1</sup> and the corresponding vibrational temperature is 841.52 K. Table3-4 shows the calculated fractions at different temperatures and Figure 3-3 represented the overall peak shapes based on the data in

Table 3-4. The graph shapes followed the Doppler formula and blue shift is obvious as the temperature increases.

### 3.3 Thermodynamic Properties

Since thermodynamics determines the energetic driving force for the overall growth process of MOCVD reactions, explicit reactor dynamics can be explained if energy states of the reactants and intermediates are known. Knowledge of the decomposition mechanism of metal organic complexes, particularly the sequence of the bond dissociation in the ligand, is important for two reasons. Firstly, it provides fundamental information to design or modify metal organic chemicals in order to maximize the process efficiency. For example, a ligand can be substituted to heavier or lighter structures based on its purpose. Secondly, process optimization is possible. For instance, the reaction temperature can be decided or heat and mass transfer characteristics with carrier gas can be preliminary examined [Wol03, MaQ76].

Computational calculations can provide accurate thermodynamic properties based on statistical thermodynamics. Once optimum structural geometry is found, computational calculations examine all the molecular motions, including translational, electronic, rotational and vibrational contributions. Each partition function for all motions is then summed up for the final results. Therefore, it is necessary to know how each partition function  $q(V,T)$  contribute in thermodynamic property.

- **Contributions from translational motion:** For ideal gas  $PV = NRT = (\frac{n}{N_A})N_A k_B T$  and

$$V = \frac{k_B T}{P}; \text{ therefore,}$$

$$q_t = \left( \frac{2\pi k_B T}{h^2} \right)^{3/2} \frac{k_B T}{P} \quad (3-11)$$



- **Contributions from electronic motion:** The usual electronic partition function is:

$$q_e = \omega_0 e^{-\varepsilon_0 / k_B T} + \omega_1 e^{-\varepsilon_1 / k_B T} + \omega_2 e^{-\varepsilon_2 / k_B T} + \dots \quad (3-12)$$

Since there are no temperature dependent terms in the partition function, the electronic heat capacity and the internal thermal energy due to electronic motion are both zero.

- **Contributions from rotational motion:** There are three cases,

a. For a single atom,  $q_r = 1$ . (3-13)

b. For a linear molecule,

$$q_r = \frac{1}{\sigma_r} \left( \frac{T}{\Theta_r} \right) \quad (3-14)$$

where  $\Theta_r = \frac{h^2}{8\pi^2 I k_B}$  and  $I$  is the moment of inertia.

c. For the general case for a nonlinear polyatomic molecule,

$$q_r = \frac{\pi^{1/2}}{\sigma_r} \left( \frac{T^{3/2}}{(\Theta_{r,x} \Theta_{r,y} \Theta_{r,z})^{1/2}} \right) \quad (3-15)$$

- **Contributions from vibrational motion:** There are two ways to calculate the partition function, depending on where the zero of energy to be: either the bottom of the internuclear potential energy well, or the first vibrational level.

This contribution is composed of a sum of the contributions from each vibrational mode,  $K$ . Each of  $3N-6$  (or  $3N-5$  for linear molecules) mode has a characteristic vibrational temperature,

$$\Theta_{v,K} = \frac{h \nu_K}{k_B}.$$

(a) If the zero reference point is to be the bottom of the well,

$$q_{v,K} = \frac{e^{-\Theta_{v,K} / 2T}}{1 - e^{-\Theta_{v,K} / T}} \quad (3-16)$$

The overall vibrational partition function is the sum of all vibrational modes.

$$q_v = \prod_K \frac{e^{-\Theta_{v,K}/2T}}{1 - e^{-\Theta_{v,K}/T}} \quad (3-17)$$

(b) If the first vibrational energy level is to be the zero of energy ( $V=0$ ),

$$q_{v,K} = \frac{1}{1 - e^{-\Theta_{v,K}/T}} \quad (3-18)$$

The overall vibrational partition function is:

$$q_v = \prod_K \frac{1}{1 - e^{-\Theta_{v,K}/T}} \quad (3-19)$$

The overall motions should be considered to complete the thermodynamic property.

### 3.4 Rate Constant Estimation

One of the great applications of the first principles calculation is to estimate of thermodynamics and, as a result, kinetics information such as reaction rate constant or equilibrium constant can be calculated [Cra02, McQ76, Sim97]. This useful information helps to understand many chemical processes. Among them, MOCVD can take advantage since it involves gas-phase decomposition reactions of metal-containing molecules [Irv97, Ras98]. With most likely decomposition mechanisms and additional reaction steps for intermediate formation [Smi03, Won06], the most probable molecule which participates in thin film formation on the substrate might be elucidated and even specific reaction pathways might be found. The heterogeneous surface reactions, however, can be understood in details after gas-phase information is known.

Taking advantage of the density functional theory (DFT) calculation, trials to predict reaction rate constants have been attempted. Rate constant calculations are based on transition state theory and all the results were compared to experimentally obtained data in the literature.

As examples, diethylzinc  $\text{Zn}(\text{C}_2\text{H}_5)_2$  and dimethylcadmium  $\text{Cd}(\text{CH}_3)_2$  were selected because these molecules are very common MOCVD precursors in II-VI compound semiconductor processes and actually their importance have been emphasized recently [Waa04, Li03, Bae02]. After the reasoning was discussed with the other example of trimethylindium,  $\text{In}(\text{CH}_3)_3$ , which most likely has kinetics data proved by *in-situ* Raman spectroscopy and validated hydrodynamic simulation [Hua93, Hwa05b].

### 3.4.1 Unimolecular Reaction

The quantum chemical calculations were performed using the Gaussian 03 program package [Fri04]. To estimate the reaction rate constant using the first principles calculation, Zn-C bond homolytic fission in diethylzinc,  $\text{Zn}(\text{C}_2\text{H}_5)_2$ , was selected as an example. The B3LYP/6-311G(d) model chemistry was employed to calculate geometry optimization, thermodynamic property and rate constant estimation. The obtained values were, then, compared with reported experimental data [Kos76, Jac89b, Dum92, Dum93]. The best advantage of this calculation is that the rate constant information, i.e., activation energy and frequency factor, can be used as a key initial guess directly to reactor design or optimization processes. Moreover, it can even be used to describe gas-phase reaction chemistry in hydrodynamic simulations for chemical and process engineers. In fact, if the rate constant is not known in the literature but needed to be known, this calculation would give the critical ideal. It will be a useful estimation of reaction steps, whose species detection is not easy due to the short lifetime or the fast participation into other reactions. Therefore, the importance of first principles calculation should be emphasized. Figure 3-4 shows the schematics of the Zn-C homolytic bond dissociation of  $\text{Zn}(\text{C}_2\text{H}_5)_2$  (DEZ).

The reported activation energies are agreed well in the ranges from 50 to 56 kcal/mol and the frequency factors are below  $\sim 10^{16}$  /s. Generally, thermodynamical property is calculated as the difference between the reactant and the products, as shown in Equation 3-20:

$$\text{Thermodynamical property} = \sum \text{products} - \sum \text{reactant} \quad (3-20)$$

Consequently, the summation of two products, i.e., monoethylzinc and ethyl radical, and one reactant, i.e., DEZn, should be considered. Using B3LYP/6-311G(d) model chemistry, all the partition functions were evaluated and enthalpy, entropy, and free energy were obtained under experimental temperature. Table 3-5 shows the calculated results as well as the estimated rate constants. However, it should be noted that the calculated rates are quite faster than the reported values. This disagreement of experimental reports was caused from the erroneous calculation-domain concepts. In fact, two important things should be considered in this case. These are pertinent multiplicity and calculation domains. When Zn and C atoms are connected, i.e., before the decomposition occurs, the proper multiplicity of DEZn is 1; however, as the distance between Zn and C is elongated and when it is finally disrupted, two products,  $\bullet\text{ZnC}_2\text{H}_5$  and  $\bullet\text{C}_2\text{H}_5$ , exist in the same space, which makes the stable multiplicity to 3.

To correct the frequency factor, the calculation domain for geometry optimization and thermodynamical property for these two products should be considered in the same frame, i.e., two molecules should be treated as one molecule considering a long enough imaginary bond between  $\bullet\text{ZnC}_2\text{H}_5$  and  $\bullet\text{C}_2\text{H}_5$  (Figure 3-5). Moreover the multiplicity of product, i.e., right side of Figure 3-5, should be corrected to 3 because the molecules are radicals even though they exist apart from each other. For schematic understanding, the potential energy scans along with Zn-C distance were carried out (Figure 3-1). Two multiplicities of 1 and 3 were considered and calculations were performed by the same model chemistry of B3LYP/6-311G(d). It is obvious that the singlet state is stable until the bond is disrupted at around 3.5 Å, on the other hand, the triplet state is much more stable when two molecules are separated with the distance of longer than 3.5 Å. Therefore, triplet state should be considered when thermodynamic calculations are

performed for products. In addition, it is also noted that the potential curve with singlet status itself gives higher ionization energy. It brings inevitable over-estimated activation energy (Table 3-6). Therefore, it should be noted that likely kinetics information can be obtained from considerations of proper calculation domain as well as stable multiplicity.

The best explanation why the general calculation method is not appropriated can be started from the concept of the degree of freedom (DOF). Dissociation of a molecule into two products means that the number of moles is changed from 1 to 2. Since it is an entropy increased reaction, it is a thermodynamic favored reaction. However, this brings a serious domain error with the missing 6 vibrational degrees of freedom. Since the vibrational degree of freedom is  $3N-6$  for general nonlinear N-atoms polyatomic molecules, the reaction can be analyzed as:

$$\bullet \text{ DOF of reactant: } 3 \times 15 - 6 = 39 \quad (3-21)$$

$$\bullet \text{ DOF of two products: } (3 \times 8 - 6) + (3 \times 7 - 6) = 33 \quad (3-22)$$

where 15 was used in the first calculation since diethylzinc composed of 15 atoms and 8 and 7 were used in the second row to account for the mono-ethylzinc and the ethyl radical, respectively. The missing 6 DOF in products are from doubly counted translational and rotational motions. Therefore, the number of vibrational DOF is different between the reactant and the product. This is very important since this gives us totally over-estimated frequency (Reported  $\sim 10^{16}$ /s, Calculation  $\sim 10^{24}$ /s). However, if the suggested calculation domain in Figure 3-5 is used, the number of DOF for each side would be the same. This means that the constraint for imaginary bond between two products should be considered for proper initial guess. For example, DFT calculations with fixed imaginary distance between Zn and C at 5 and 10 Å were carried out (Table 3-6). In calculations, the same model chemistry of B3LYP/6-311G(d) was used. With the fixed imaginary bond between Zn and C atoms, 6 vibrational DOF were not missing and

reasonable bond dissociation energy and frequency factors were obtained when proper multiplicity of 3 was used. Figure 3-6 shows the comparison of reaction rates. Rate constants reported by Dumont *et al.* and obtained in this study made a good agreement near the reaction temperature  $\sim 600^\circ\text{C}$  [Dum93]. However, the obtained results will be totally different if much lower or much higher temperature is considered based on this kinetic information. This discrepancy could be caused by various experimental uncertainties, such as a chemical impurity level, detector calibration, or even operator's measurement skills. Therefore, the practical estimation method is important and experimental confirmation is necessary.

Another example, dimethylcadmium,  $\text{Cd}(\text{CH}_3)_2$  (DMCd), can be considered. This molecule is also popular as a MOCVD precursor for Cd-containing compound semiconductors [Ni97, Chu92], and it has very similar characteristics with DEZn, since they are on the same column in the periodic table. Unlike DEZn, however, the quantum calculation is not trivial since the Cd atom is more complicated than the Zn atom, i.e., Cd has the closed outer shell with  $5s^2 4d^{10}$  orbital configuration. For better results, effective core potential (ECP) should be considered and among the reported basis set, SDD is known as a good basis for describing Cd atoms. Therefore, the model chemistry for DMCd was a combination set of SDD for Cd and 6-311G(d) for C and H. The reported information for the first  $\bullet\text{CH}_3$  and  $\bullet\text{CdCH}_3$  homolytic fission is in good agreement on activation energy between 43.5 and 56 and its frequency factors of  $10^{11.9} \sim 10^{13.1}$ . This reaction can also be evaluated from statistical thermodynamics and, in fact, the general calculation method gives much faster kinetic data again as shown in DEZn case. However, the suggested calculation method gives reasonable kinetics information (Table 3-7), and the rates under actual MOCVD reaction temperature are compared in Figure 3-7. Again, the calculated rate is well matched up to  $\sim 400^\circ\text{C}$ ; however, a large discrepancy is expected as

temperature increases. Therefore, it is interesting to see how likely activation energy and frequency factor can be calculated in the next section with a final example of the trimethylindium (TMIn) molecule. The reason for the TMIn example is that In-C bond dissociation kinetics is most likely reliable since it was determined by *in-situ* Raman spectroscopy and its validated reactor modeling [Hua93, Hwa05b].

Regardless of whether the fact that transition state exists or not, general decomposition reaction involves bond dissociation. For general homolytic bond fission, it is regarded that there is no activation energy, i.e., no energy barrier between the reactant and product, and only bond dissociation energy is required for one mole of reactant to produce two moles of products. If a transition state certainly exists during decomposition, such as  $\beta$ -hydration reaction, a transition state must be considered.



Even though severe geometry deformation has not occurred during the homolytic fission, the transition state of  $TS^{\ddagger}$  can be assumed for better understanding. The reactant, A, is in equilibrium with transition state of  $TS^{\ddagger}$  and the reaction rate constant forward to the product, B and C, was assumed as  $k'$ . The rate of product formation can be expressed:

$$rate = \frac{d[B + C]}{dt} = k[A] = k'[TS^{\ddagger}] \quad (3-24)$$

The rate constant  $k'$  can be expressed using the equilibrium constant,

$$K_{eq}^{\ddagger} = \frac{[TS^{\ddagger}]}{[A]} \quad (3-25)$$

Substitution (3-25) into (3-24) gives,

$$rate = \frac{d[B + C]}{dt} = k[A] = k'[TS^{\ddagger}] = k'K_{eq}^{\ddagger}[A] \quad (3-26)$$

Another equation to reach the complete form is the relationship between free energy and the equilibrium constant, which is expressed  $\Delta G^\ddagger = -RT \ln K_{eq}^\ddagger$ . Applying this to equation 3-26;

$$\ln K_{eq}^\ddagger = \Delta G^{0,\ddagger} / RT = -\Delta H^{0,\ddagger} / RT + T\Delta S^{0,\ddagger} / RT = -\Delta H^{0,\ddagger} / RT + \Delta S^{0,\ddagger} / R \quad (3-27)$$

And

$$K_{eq}^\ddagger = \exp(\Delta S^{0,\ddagger} / R - \Delta H^{0,\ddagger} / RT) = \exp(\Delta S^{0,\ddagger} / R) \exp(-\Delta H^{0,\ddagger} / RT) \quad (3-28)$$

Therefore, the overall rate of Equation 3-26 becomes:

$$rate = k^\ddagger \exp(\Delta S^{0,\ddagger} / R) \exp(-\Delta H^{0,\ddagger} / RT) \quad (3-29)$$

The last step is introducing the statistical thermodynamic relation in order to eliminate  $k^\ddagger$ .

$$G = U + PV + k_B T \ln Q \quad (3-30)$$

where Q is the partition function. Combining the Equations of 3-27 and 3-30 gives:

$$\begin{aligned} K_{eq}^\ddagger &= \exp\left\{\frac{(U_A + PV_A + k_B T \ln Q_A^\ddagger) - (U_{TS}^\ddagger + PV_{TS} + k_B T \ln Q_{TS}^\ddagger)}{k_B T}\right\} \\ &= \frac{Q_{TS}^\ddagger}{Q_A} \exp\left\{\frac{-(U_{TS}^\ddagger - U_A)}{k_B T}\right\} \exp\left\{\frac{-P(V_{TS} - V_A)}{k_B T}\right\} \\ &\approx \frac{Q_{TS}^\ddagger}{Q_A} \exp\left\{\frac{-(U_{TS}^\ddagger - U_A)}{k_B T}\right\} \end{aligned} \quad (3-31)$$

Assuming that PV changes are negligible in activation energy of A leads to the final line of Equation 3-31. Here,  $Q_{TS}^\ddagger$  is the partition function of the activated complex which has  $3N-7$  degrees of freedom since the activated complex has one minus frequency which indicates the saddle point. This missing frequency is from the bond rupture so it should be considered from the previous reaction coordinate. Therefore, the Equation 3-29 becomes:

$$rate = k^\ddagger \frac{Q_{TS}^\ddagger}{Q_A} \exp\left\{\frac{-(U_{TS}^\ddagger - U_A)}{k_B T}\right\} \quad (3-32)$$



For the vibrational motion, it is necessary to separate the partition function for the reaction coordinate degree of freedom

$$\begin{aligned}
 rate &= \frac{k'}{1 - e^{-h\omega^\ddagger/k_B T}} \frac{Q_{TS}^\ddagger}{Q_A} \exp\left\{-\frac{(U_{TS}^\ddagger - U_A)}{k_B T}\right\} \\
 &= \frac{k' k_B T}{h \omega^\ddagger} \frac{Q_{TS}^\ddagger}{Q_A} \exp\left\{-\frac{(U_{TS}^\ddagger - U_A)}{k_B T}\right\} \\
 &\approx \frac{k_B T}{h} \frac{Q_{TS}^\ddagger}{Q_A} \exp\left\{-\frac{(U_{TS}^\ddagger - U_A)}{k_B T}\right\}
 \end{aligned} \tag{3-33}$$

For the second line of the equation, power series expansion for the exponential function of  $\omega^\ddagger$  has been used. In this case, the vibrational frequency  $\omega^\ddagger$  should not be thought of as the imaginary frequency that derives from the standard harmonic oscillator analysis, but rather the real inverse time constant associated with motion along the reaction coordinate. However, it is the exact motion along the reaction coordinate that converts the activated complex into products. That is,  $k' = \omega^\ddagger$  in the third line of the equation. Therefore, the reaction rate can be expressed with the free energy form again:

$$rate = \frac{k_B T}{h} \exp(\Delta S^\ddagger / R) \exp(-\Delta H^\ddagger / RT) \tag{3-34}$$

In consequence, two moles of products should be considered as a whole molecule with long enough imaginary bonding to eliminate the possibility of increasing entropy effect, i.e., the total mole of reactant and product should be considered as the same. This is important, as shown in Equation 3-34, since the frequency factor is a function of entropy change. Moreover, the activation energy will be from the proper information of the lowest state when a bond is broken.

To give another support data, the other kinetics information of In-C bond dissociation in trimethylindium (TMIn) was examined. TMIn is considered as a most popular MOCVD precursor for InN thin film and more various applications in MOCVD or atomic layer deposition

(ALD) have been attempted [But86, Kol98, Par02a]. For the homogenous gas-phase reaction, the sequential In-C bond dissociation is a widely accepted mechanism and, as a result, dimethylindium, monomethylindium and indium atom release as decomposition products. Table 3-8 shows the reported kinetics information with various carrier gases [Hwa04, Jac64, Lar86].

Recently, Hwang *et al.* [Hwa04] reported kinetics data using an *in-situ* probing and validated hydrodynamics simulation. After TMIn was introduced through the gas inlet using N<sub>2</sub> carrier gas, the gases underwent thermal decomposition due to the heated radiation. Since TMIn was perfectly surrounded by environmental gas N<sub>2</sub> and isolated from any surface, the decomposition reaction was purely from homogenous gas reaction. Therefore, probing with *in-situ* Raman spectroscopy most likely gave kinetics information. Based on experimental results, simulated data were compared to them and Hwang *et al.* could successfully extract kinetics information for TMIn decomposition. Figure 3-8 shows how kinetics information is correlated with data from other researchers. For higher temperature reaction, it is noted that kinetics data from Hwang *et al.* and Jacko & Price [Jac64] are mostly reliable. For the same carrier gas of N<sub>2</sub>, the rates at around 300~500 °C by Hwang *et al.*, Larsen and Stringfellow, and Jackco and Price made a good agreement even though experimental uncertainty made somewhat different slopes. Rate determinations from different carrier gases, such as H<sub>2</sub>, D<sub>2</sub>, and He were also shown [Lar86, Buc88] and the decomposition was somehow affected by carrier gas; however, no severe difference was found and all the rates are in good agreement considering MOCVD reaction temperature. With given reference, DFT calculations were again carried out with LanL2DZ for In and 6-311++G(2d,2p) for C and H model chemistry. The BSSE was considered in Ea calculation giving the value 61.5 kcal/mol and frequency factor was  $4.45 \times 10^{17} \text{ s}^{-1}$ . Frequency

factor is well matched with reported values; however, the activation energy is somehow higher than references. In fact, the same thing happened in previous examples of DEZn and DMCd.

Even though the calculated activation energy is not much higher than the reported values, it is obvious that the calculation somehow gives an over-estimated activation energy. Figure 3-9 shows the electron density contour for TMI<sub>n</sub>, DMI<sub>n</sub>, and methyl molecules. As mentioned earlier, bond dissociation energy is obtained from Equation 3-20, which is the difference in thermodynamic properties between the reactant and the products. Therefore, DFT calculation first searches for optimum geometry, which is most stable with molecular electronic energy, and based on that, electron density is obtained (Figure 3-9). Finally B3LYP DFT obtained a relevant electron-electron repulsion term in the Hamiltonian operator from the density distribution. However, after the bond dissociation, each product molecule tried to minimize its own electronic energy through structural deformation; as a result, the basis-set domains between products and reactant are not really the same. The uncertainty in energy calculation from this basis-set can be corrected from basis set superposition error (BSSE) calculation and, in fact, the bond dissociation energy can be dramatically approximated. Table 3-9 shows the examples for TMI decomposition calculated various basis sets. In the case of 6-311++G(2d,2p) basis set, the calculated BSSE is not much higher since it is already flexible enough to cover all the geometry deformations of DMI<sub>n</sub> and Methyl radicals. However, if a stiffer basis set is used, then BSSE will be seriously increased.

On the other hand, if activation energy is considered from the calculation domain (Figure 3-10), the story will be changed. Even though two product molecules were separated with a long enough imaginary bond, electron density distribution would be expanded. In other words, more overlapped orbital would exist between two separated molecules and, as a result, the probability

of finding electrons is higher than that of Figure 3-11. Therefore, the whole domain of electron density will be widely distributed and over-estimated activation energy is inevitable. Since it is not trivial to correct the error caused by this over-estimated density distribution, activation energy is better to be calculated from the concept in Figure 3-10. In fact, BSSE plays a key role to correct it and the result is quite reliable.

Combing results of activation energy and frequency factor give good enough estimation as shown in Figure 3-12. All the reference data were considered the carrier gas as N<sub>2</sub>. Since the rate could be estimated with a suggested calculation method, it is regarded as a possible calculation method for rate constant, especially when the experiments are not possible to detect reaction products or intermediates.

### 3.4.2 Bimolecular Reaction

Bimolecular reaction can be thought of as a reverse pathway of unimolecular reaction.



The rate equation is, therefore,

$$rate = \frac{d[C]}{dt} = k[A][B] = k'[TS^{\ddagger}] \quad (3-36)$$

The equilibrium constant can be expressed as shown in the previous section so that the rate equation can be restated in Equation 3-38.

$$K_{eq}^{\ddagger} = \frac{[TS^{\ddagger}]}{[A][B]} \quad (3-37)$$

$$\frac{d[C]}{dt} = k[A][B] = k'[TS^{\ddagger}] = k'K_{eq}^{\ddagger}[A][B] \quad (3-38)$$

The equilibrium constant can be expressed with partition functions with an assumption that volume change is negligible.

$$\begin{aligned}
K_{eq}^{\ddagger} &= \exp\left\{\frac{(U_A + PV_A + k_B T \ln Q_A^{\ddagger}) + (U_A + PV_A + k_B T \ln Q_A^{\ddagger}) - (U_{TS}^{\ddagger} + PV_{TS} + k_B T \ln Q_{TS}^{\ddagger})}{k_B T}\right\} \\
&= \frac{Q_{TS}^{\ddagger}}{Q_A Q_B} \exp\left\{\frac{-(U_{TS}^{\ddagger} - U_A - U_B)}{k_B T}\right\} \exp\left\{\frac{-P(V_{TS} - V_A - V_B)}{k_B T}\right\} \\
&\approx \frac{Q_{TS}^{\ddagger}}{Q_A Q_B} \exp\left\{\frac{-(U_{TS}^{\ddagger} - U_A - U_B)}{k_B T}\right\}
\end{aligned}
\tag{3-39}$$

Therefore, the rate equation becomes:

$$\begin{aligned}
rate &\approx \frac{k_B T}{h} \frac{Q_{TS}^{\ddagger}}{Q_A Q_B} \exp\left\{\frac{-(U_{TS}^{\ddagger} - U_A - U_B)}{k_B T}\right\} \\
&= \frac{k_B T}{h} \frac{Q_{TS}^{\ddagger}}{Q_A Q_B} \frac{Q_A^0 Q_B^0}{Q_{TS}^{\ddagger,0}} \exp\left\{\frac{-(U_{TS}^{\ddagger} - U_A - U_B)}{k_B T}\right\} \\
&= \frac{k_B T}{h} \frac{RT^0}{P^0} \exp\left\{\frac{-\Delta G^{\ddagger,0}}{RT}\right\}
\end{aligned}
\tag{3-40}$$

However, it is necessary to pay attention to the unit because it is different from unimolecular reaction. In the case of unimolecular reaction, i.e., homolytic dissociation has a unit as  $\text{sec}^{-1}$ ; however, the bimolecular rate constant has a unit of  $\text{concentration}^{-1}\text{sec}^{-1}$ . Therefore, the third statement in Equation 3-40 was introduced to give standard state volume units. Here, the  $Q^0$  stands for the translational partition function and has the value of one. This volume is expressed with  $RT^0 / P^0$  with the ideal gas assumption. The unit generation factor here, i.e.,  $RT^0 / P^0$ , is 24.45 l/mol at 298K and atmospheric pressure conditions.

### 3.5 Equilibrium Constant Estimation

Another important application of first principles calculation is the calculation of equilibrium constants in terms of molecular parameters. The general homogeneous gas phase chemical reaction at equilibrium can be expressed as;



where  $\nu$ 's are stoichiometric coefficients for reactants and products. If  $\lambda$  is defined as  $dN_j = \nu_j d\lambda$ , where  $j=A, B, C, \text{ or } D$  and where  $\nu_j$  is taken to be positive for products and negative for reactants,  $(dG/d\lambda)_{T,V} = 0$  is the necessary condition for the equilibrium state since the free energy must be a minimum with respect to all possible changes. In other words, the condition for chemical equilibrium is;

$$\sum_j \nu_j j = \nu_C C + \nu_D D - \nu_A A - \nu_B B = 0 \quad (3-42)$$

In a mixture of ideal gases, the species are independent and distinguishable, and so the partition function of the mixture is a product of the partition functions of the individual components.

Thus,

$$\begin{aligned} Q(N_A, N_B, N_C, N_D, V, T) &= Q(N_A, V, T) Q(N_B, V, T) Q(N_C, V, T) Q(N_D, V, T) \\ &= \frac{q_A(V, T)^{N_A}}{N_A!} \frac{q_B(V, T)^{N_B}}{N_B!} \frac{q_C(V, T)^{N_C}}{N_C!} \frac{q_D(V, T)^{N_D}}{N_D!} \end{aligned} \quad (3-43)$$

The chemical potential of each species is given by an equation such as

$$\mu_A = -kT \left( \frac{\partial \ln Q}{\partial N_A} \right)_{N_j, V, T} = -kT \ln \frac{q_A(V, T)}{N_A} \quad (3-44)$$

where Stirling's approximation has been used. Substitution of Equation 3-44 into 3-42 gives,

$$\frac{N_C^{\nu_C} N_D^{\nu_D}}{N_A^{\nu_A} N_B^{\nu_B}} = \frac{q_C^{\nu_C} q_D^{\nu_D}}{q_A^{\nu_A} q_B^{\nu_B}} \quad (3-45)$$

For an ideal gas, the molecular partition function is of the form  $f(T)V$ , so that  $q/V$  is a function of temperature only. This allows writing,

$$K_C(T) = \frac{\rho_C^{\nu_C} \rho_D^{\nu_D}}{\rho_A^{\nu_A} \rho_B^{\nu_B}} = \frac{(q_C/V)^{\nu_C} (q_D/V)^{\nu_D}}{(q_A/V)^{\nu_A} (q_B/V)^{\nu_B}} \quad (3-46)$$

where  $K_C(T)$  is the equilibrium constant of the reaction. For an ideal system,  $K_C$  is only a function of temperature. Another commonly used equilibrium constant  $K_p(T)$ , which is expressed in terms of partial pressures rather than concentrations. It can be derived the equation for by substituting  $p_j = \rho_j kT$  into Equation 3-46.

$$K_p(T) = \frac{P_C^{\nu_C} P_D^{\nu_D}}{P_A^{\nu_A} P_B^{\nu_B}} = (kT)^{\nu_C + \nu_D - \nu_A - \nu_B} K_C(T) \quad (3-47)$$

For example, Zn or Cd containing a MOCVD process involves a metal-carbon bond breaking and, as a result, the first reaction product is a radical. Because the radicals tend to dimerize easily, it is important to know the equilibrium constant using derived expressions above. Instead of a metal-containing radical, a simpler  $\text{Na}_2$  molecule would be better understood at this point. The reaction involving two Na atoms can be expressed:



According to the Equation 3-47, the equilibrium constant can be written as

$$K_p(T) = \frac{P_{\text{dimer}}}{P_{\text{monomer}}^2} = (kT)^{-1} \frac{(q_{\text{Na}_2}/V)}{(q_{\text{Na}}/V)^2} \quad (3-49)$$

$$\text{with } q_{\text{Na}}(T, V) = \left( \frac{2\pi m_{\text{Na}} kT}{h^2} \right)^{\frac{3}{2}} V q_{\text{elec}}(T) \quad (3-50)$$

$$q_{\text{Na}_2}(T, V) = \left( \frac{2\pi m_{\text{Na}_2} kT}{h^2} \right)^{\frac{3}{2}} V \left( \frac{T}{2\Theta_r} \right) (1 - e^{-\Theta_v/T})^{-1} e^{D_0/kT} \quad (3-51)$$

where  $q_{\text{elec}}$  denotes electronic partition function and  $\Theta_r$ ,  $\Theta_v$  and  $D_0$  are rotational temperature, vibrational temperature and ionization energy, respectively. Therefore, the equilibrium constant can be calculated with the partition functions of a monatomic ideal gas and a diatomic molecule, which are calculated by the first principles calculation.

### 3.6 Summary

Computational calculations estimate Raman-active vibrational frequency as well as thermodynamic properties. Specially, the estimation method for kinetics information including activation energy and frequency factor was introduced using B3LYP DFT calculation. Using proper model chemistry, the activation energy could be estimated. However, the BSSE correction should be considered to reduce calculation uncertainty. For frequency factor estimation, it was suggested to use the same calculation domain as the reactant calculation. A fixed imaginary bond between two broken products made it possible not to lose 6 vibrational degrees of freedom and, in addition, stable multiplicity was examined using potential surface scanning. As a result, the calculated activation energy and frequency factor were well matched with experimental reports. Therefore, it is regarded that first principles calculation can be applied in the estimation rate constant and it will be useful in kinetics mechanism, especially in experiments whose detections are impossible. As another example, the equilibrium constant was expressed with the partition functions which can be obtained from computational calculations.



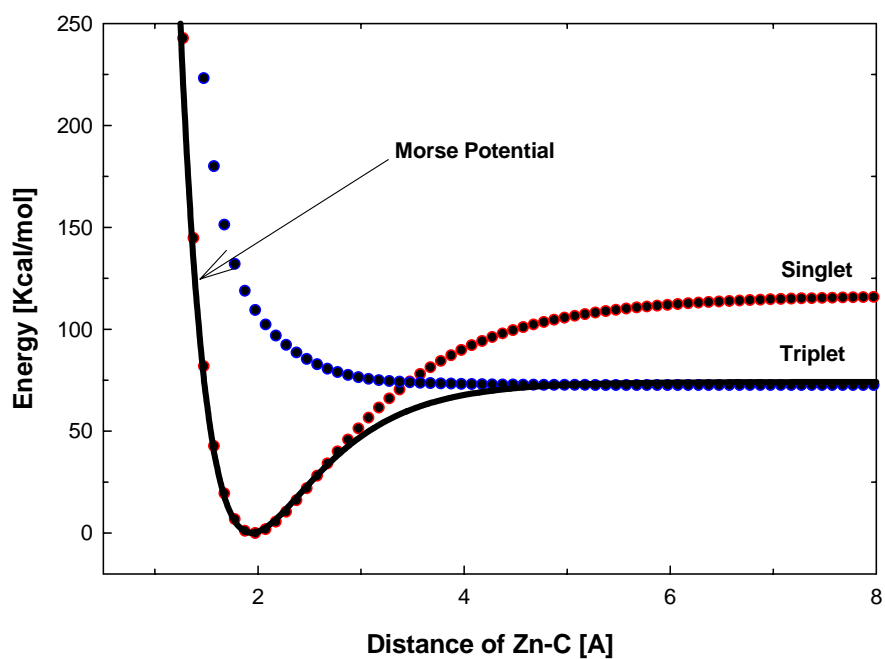


Figure 3-1. Potential surface scan along with Zn-C distance in diethylzinc.

Table 3-1. Calculated Raman shift between various vibrational states.

Ground $\rightarrow$ 1	480.0
1 $\rightarrow$ 2	477.6
2 $\rightarrow$ 3	475.1
3 $\rightarrow$ 4	472.7

Table 3-2. Calculated vibrational temperatures regarding to possible frequencies between Zn-C.

Frequency [ $\text{cm}^{-1}$ ]	Vibrational temperature [K]
240	349.81
480	699.62
960	1399.24
1920	2098.86
3840	4197.72
7680	6296.58

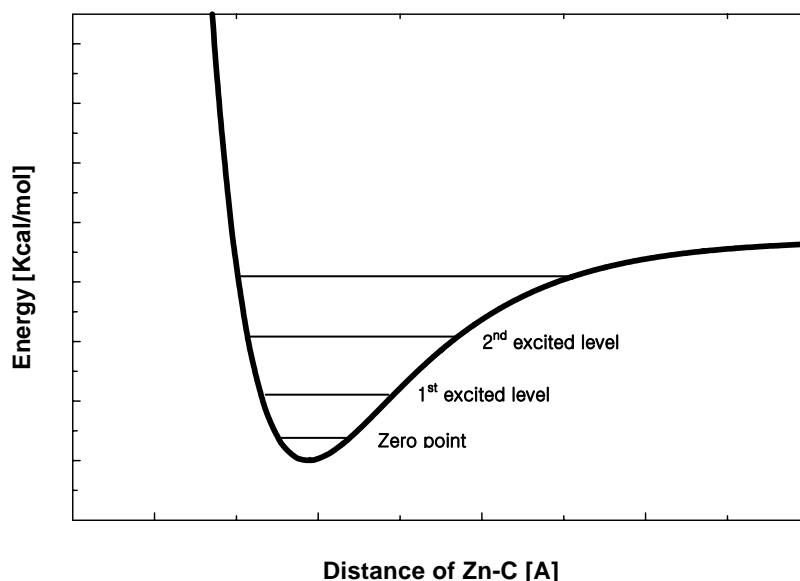


Figure 3-2. Energy difference between ground state and excited states explaining equal energy split. Hot band transition can be analytically calculated based on this concept.

Table 3-3. Contributions of hot band transition for overall peak shift with temperature increase.

Temperature [°C]	Transition	Relative energy	Normalized percent
200	$P(0) \rightarrow P(1)$	32.4620	48.9940
	$P(0) \rightarrow P(2)$	20.8074	31.4040
	$P(0) \rightarrow P(3)$	11.3831	17.1802
	$P(0) \rightarrow P(4)$	1.4328	2.1625
	$P(0) \rightarrow P(5)$	0.1718	0.2593
300	$P(0) \rightarrow P(1)$	33.7013	43.8421
	$P(0) \rightarrow P(2)$	24.4161	31.7629
	$P(0) \rightarrow P(3)$	15.4150	20.0535
	$P(0) \rightarrow P(4)$	2.8522	3.7105
	$P(0) \rightarrow P(5)$	0.4850	0.6309
400	$P(0) \rightarrow P(1)$	34.4871	40.0292
	$P(0) \rightarrow P(2)$	27.0562	31.4041
	$P(0) \rightarrow P(3)$	18.9000	21.9373
	$P(0) \rightarrow P(4)$	4.6812	5.4335
	$P(0) \rightarrow P(5)$	1.0304	1.1959
500	$P(0) \rightarrow P(1)$	35.0119	37.0968
	$P(0) \rightarrow P(2)$	28.9943	30.7208
	$P(0) \rightarrow P(3)$	21.7846	23.0818
	$P(0) \rightarrow P(4)$	6.7689	7.1720
	$P(0) \rightarrow P(5)$	1.8200	1.9285

Table 3-4. Probability changes of existing photons at each excited state with respect to temperature increase.

Temp. [K]	$f_0$	$f_1$	$f_2$	$f_3$
298.15	0.940541	0.055923	0.003325	0.000198
498.15	0.815349	0.150555	0.027800	0.005133
698.15	0.700415	0.209834	0.062863	0.018833
898.15	0.608178	0.238297	0.093370	0.036584

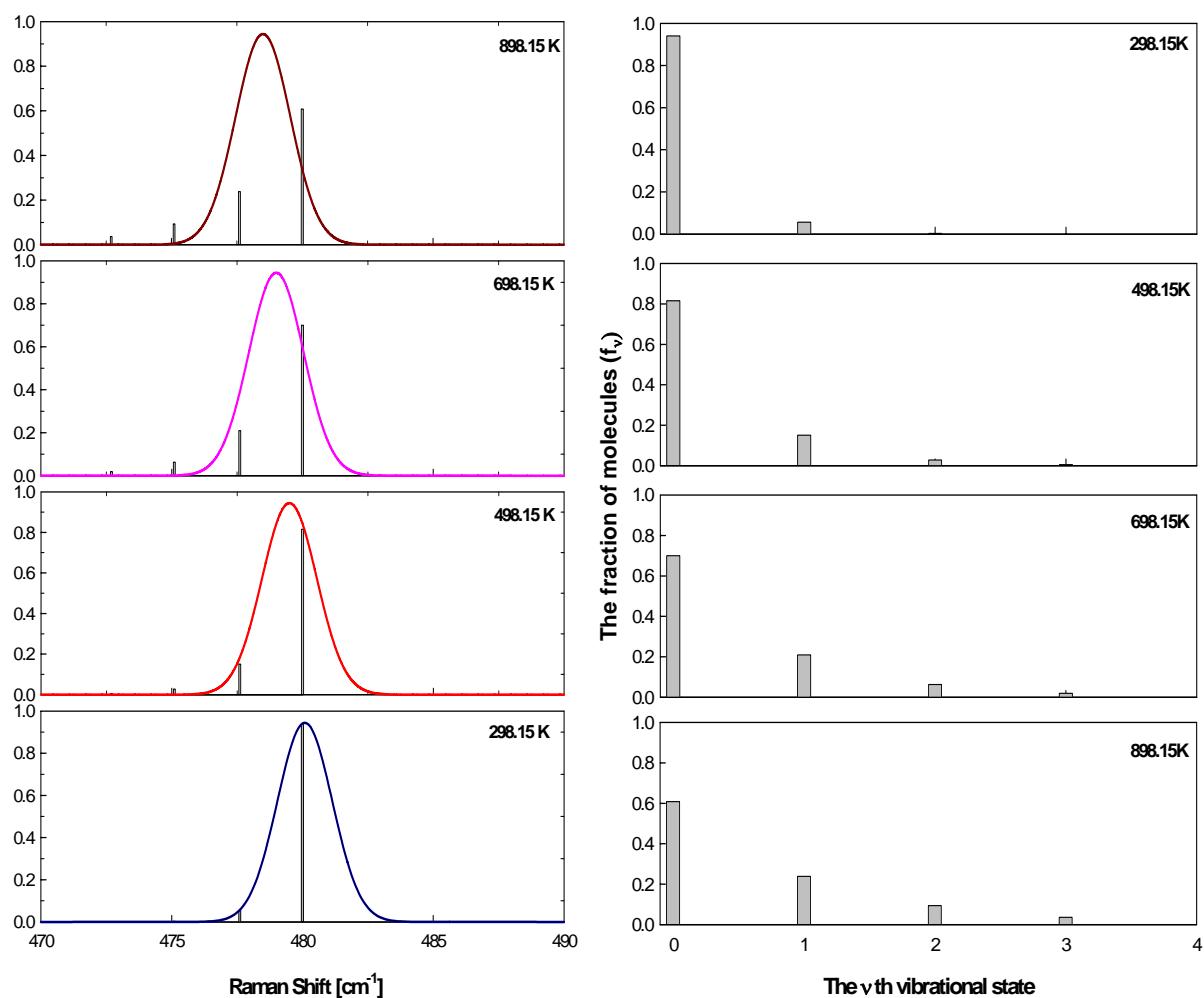


Figure 3-3. Peak shift of Zn-C stretch due to population changes at each vibrational excited state.

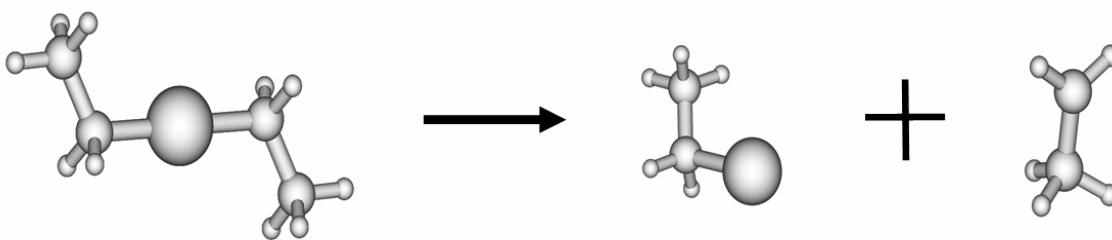


Figure 3-4. Reaction scheme of homolytic fission in Zn-C bond.

Table 3-5. Thermodynamic properties and according rate constants calculated from B3LYP/6-311G(d) model chemistry.

	$\Delta H$	$\Delta G$	$\Delta S$	Rate	Ea	A
398.15	69.782	49.474	0.051	5.75E-15	70.57269	$3.171 \times 10^{24}$
498.15	69.921	44.357	0.051	3.583E-07	70.91069	$4.645 \times 10^{24}$
598.15	69.989	39.217	0.051	0.058285	71.17779	$5.948 \times 10^{24}$
698.15	70.002	34.071	0.051	313.60571	71.38967	$7.017 \times 10^{24}$
798.15	69.933	28.926	0.051	199443.38	71.55574	$7.850 \times 10^{24}$
Unit: kcal/mol					<b>71.12132</b>	<b><math>5.726 \times 10^{24}</math></b>

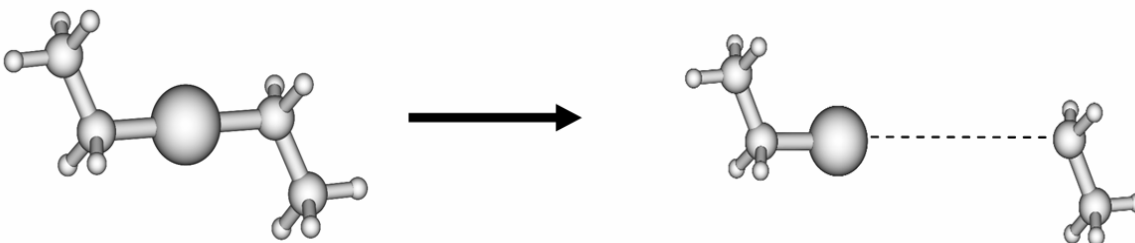


Figure 3-5. Suggested calculation domain with an imaginary bond between Zn-C to correct entropy calculation.

Table 3-6. Thermodynamic properties and estimated rate constants calculated from B3LYP/6-311G(d) model chemistry (Unit: kcal/mol). 10 Å bond length with triplet multiplicity could reproduce plausible reaction rate.

T[K]	Multiplicity: 1				Multiplicity: 3							
	Distance Zn-C: 5 Å				Distance Zn-C: 5 Å				Distance Zn-C: 10 Å			
	$\Delta H$	$\Delta G$	$\Delta S$	A	$\Delta H$	$\Delta G$	$\Delta S$	A	$\Delta H$	$\Delta G$	$\Delta S$	A
398.15	85.3	78.3	0.0176	$1.6 \times 10^{17}$	89.6	81.9	0.0192	$3.6 \times 10^{17}$	55.2	47.8	0.0186	$2.6 \times 10^{17}$
498.15	85.3	76.5	0.0177	$2.1 \times 10^{17}$	89.4	80.0	0.0190	$3.9 \times 10^{17}$	54.9	46.0	0.0179	$2.3 \times 10^{17}$
598.15	85.3	74.7	0.0177	$2.5 \times 10^{17}$	89.3	78.1	0.0186	$4.0 \times 10^{17}$	54.5	44.2	0.0172	$1.9 \times 10^{17}$
698.15	85.3	73.0	0.0176	$2.9 \times 10^{17}$	89.0	76.3	0.0183	$3.9 \times 10^{17}$	54.1	42.6	0.0165	$1.6 \times 10^{17}$
798.15	85.2	71.2	0.0175	$3.1 \times 10^{17}$	88.8	74.5	0.0179	$3.7 \times 10^{17}$	53.6	40.9	0.0159	$1.4 \times 10^{17}$
$2.5 \times 10^{17}$				$3.8 \times 10^{17}$				$2.0 \times 10^{17}$				

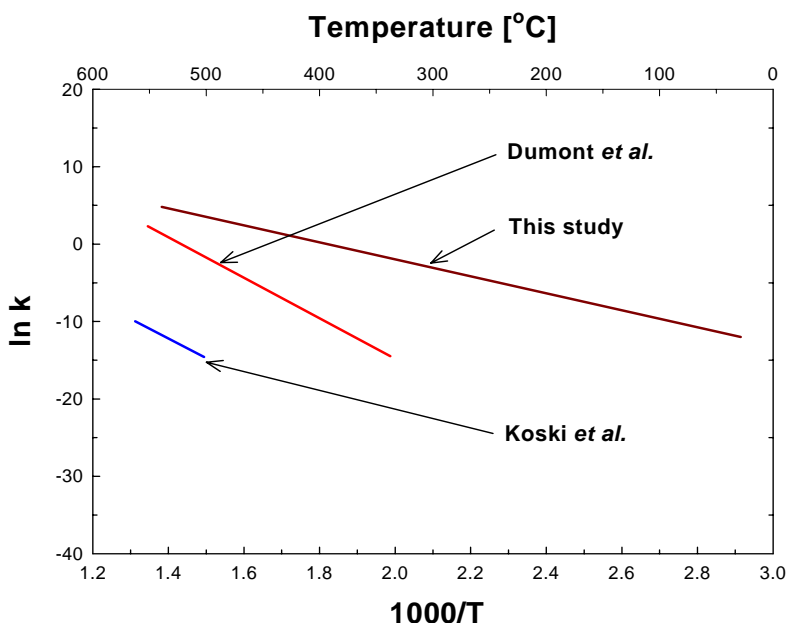


Figure 3-6. Comparison of reaction rates for Zn-C homolytic bond fission. The calculated rate seems reasonable the same with the result from Dumont at 550°C.

Table 3-7. Decomposition mechanisms of DMCd and their calculated rate information.

Reaction / Initial guess	Ea [kcal/mol]	A [s <sup>-1</sup> ]
$\text{Cd}(\text{CH}_3)_2 \rightarrow \bullet\text{CdCH}_3 + \bullet\text{CH}_3$	53.0	$2.061 \times 10^{13}$
$\bullet\text{CdCH}_3 \rightarrow \text{Cd} + \bullet\text{CH}_3$	10.5	$3.854 \times 10^{14}$
$2\bullet\text{CdCH}_3 \rightarrow (\text{CdCH}_3)_2$	0	$2.985 \times 10^{10}$
$(\text{CdCH}_3)_2 \rightarrow 2\bullet\text{CdCH}_3$	33.51	$1.926 \times 10^{19}$

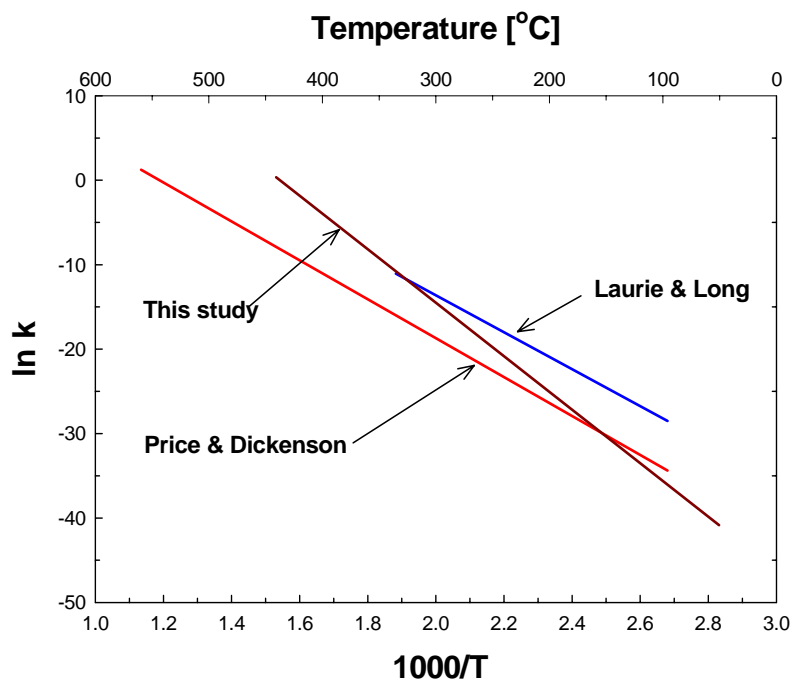


Figure 3-7. Comparison of reaction rates for Cd-C homolytic bond fission. The calculated rate matched well with Laurie and Long at the temperature 300 °C and with Price and Dickenson at 150 °C. However, it should be noted that actual reaction temperature should be around 500 °C.

Table 3-8. Reported kinetics data for TMIn decomposition with various carrier gases.

	$k_0$ ( $s^{-1}$ )	$E_a$ (kcal/mol)	Carrier
Hwang	$10^{17.9}$	56.1	N <sub>2</sub>
Jacko & Price	$10^{15.7}$	47.2	Toluene
Larsen & Stringfellow	$10^{12.6}$	40.5	N <sub>2</sub>
	$10^{12.0}$	35.9	H <sub>2</sub>
Buchan <i>et al.</i>	$10^{17.9}$	54.0	He
	$10^{13.4}$	39.8	D <sub>2</sub>
	$10^{15.0}$	42.6	H <sub>2</sub>

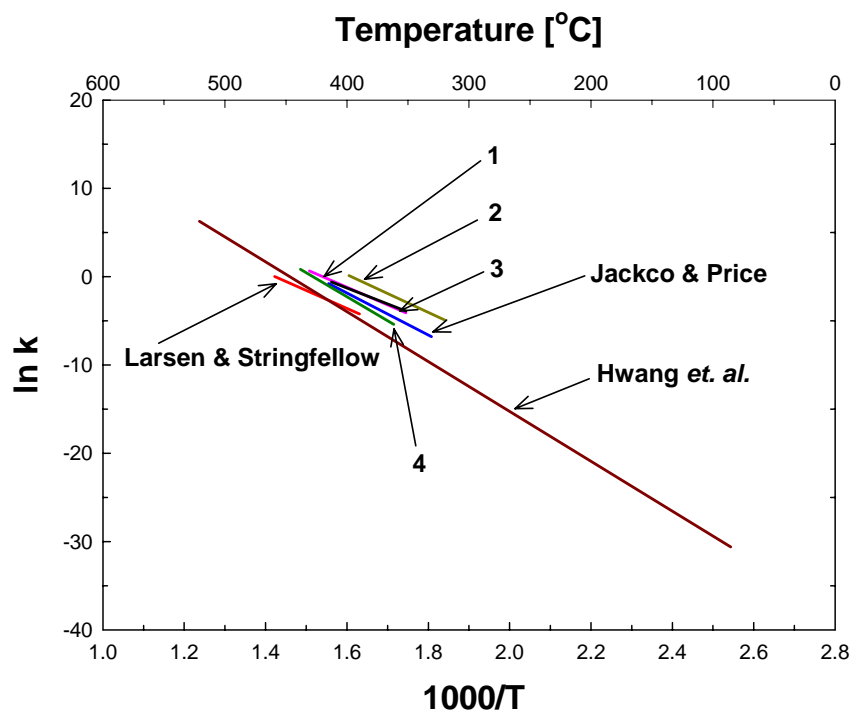


Figure 3-8. Comparison of reaction rates for In-C homolytic bond fission of TMIn with carrier gas, N<sub>2</sub>. Numbered references were reported with different carrier gases: (1) D<sub>2</sub>, (2) H<sub>2</sub>, (3) H<sub>2</sub> and (4) He.

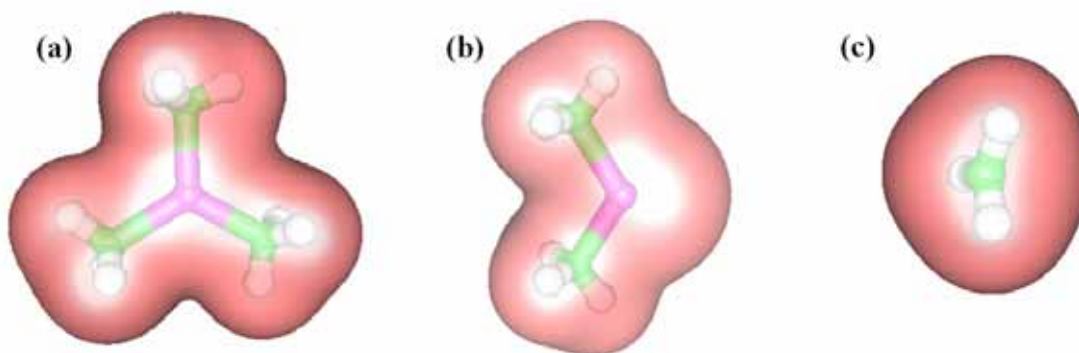


Figure 3-9. Electron density contour for TMIn, DMIn, and Methyl radical. A combination of basis set was used (LanL2DZ for TMIn and 6-311++G(2d,2p) for C and H) with B3LYP calculation method. (a) TMIn, (b) DMIn, (c) Methyl.

Table 3-9. Calculated  $\Delta H$  and  $\Delta G$  with different basis-set combinations (kcal/mol).

Model Chemistry*	BSSE	$\Delta H$	$\Delta G$
B3LYP/(6-311++G(2d,2p) + LanL2DZ)	-0.43	61.5	45.1
B3LYP/(6-311++G(2d,2p) + SDB-cc-pVTZ)	-0.26	64.8	50.8
B3LYP/(6-311++G(2d,2p) + SDB-aug-cc-pVTZ)	-0.26	64.4	50.9

\*Basis set: the first basis set was used for H and C and the second was for In.

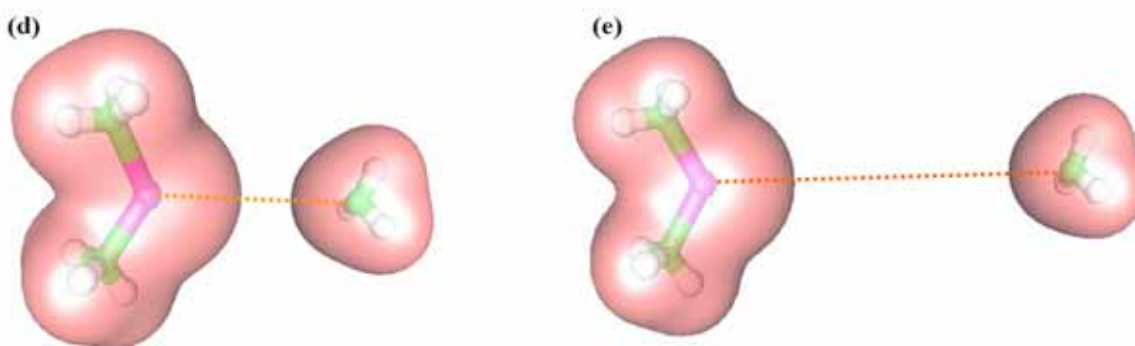


Figure 3-11. Elongated molecular geometries for TMIn decomposition. Two products were connected by an imaginary bond, which has length of (d) 5 Å and (e) 10 Å.

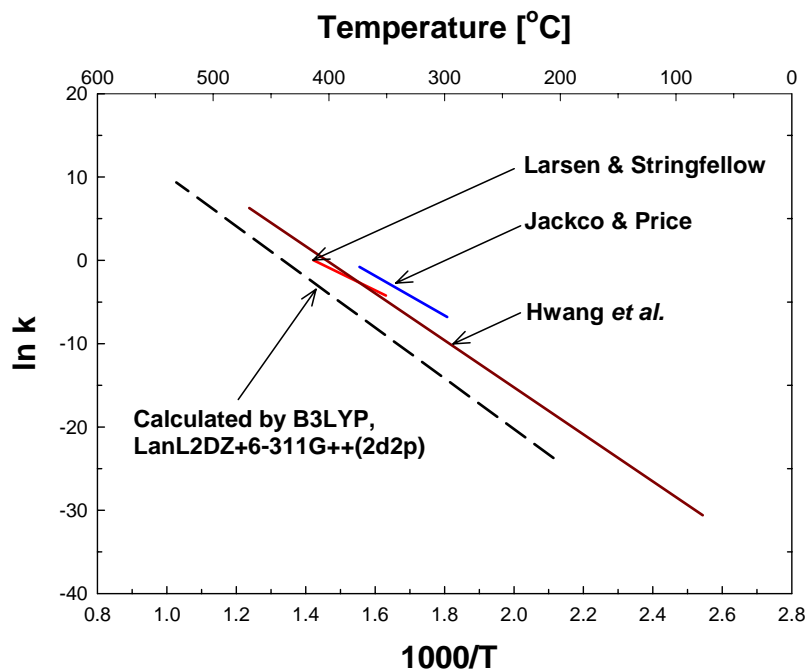


Figure 3-12. The comparison of reaction rates for In-C homolytic bond fission of TMIn.



## CHAPTER 4 REACTOR MODELING AND PARAMETER EXTRACTION

### 4.1 Introduction

Metal Organic Chemical Vapor Deposition (MOCVD) is being applied to the growth of an expanding list of materials. In parallel with experiments, theoretical simulations help to elucidate reaction chemistry and operating conditions. Moreover, the calculated reaction dynamics eventually contribute to optimal reactor design: The lack of understanding of the gas-phase molecular chemistry, however, limits the ability to accurately model MOCVD deposition. Therefore, an understanding of the gas-phase dynamics is the starting point to modeling the MOCVD process.

Modeling a real MOCVD process requires solving the balance equations for momentum, energy and species simultaneously. The momentum equation can be solved independently from the species balance equations because metal organic reactants are generally diluted in carrier gas, typically  $H_2$  or  $N_2$ . Using these hydrodynamic equations, a two-dimensional, axisymmetric reactor model was developed for the purpose of data analysis. In the model, the assumption of ideal gas behavior at the elevated temperature and reduced pressure typical of MOCVD is employed. In addition, thermal diffusion and radiation heat transport are incorporated in the reactor model with multi-component thermal diffusion coefficients calculated from molecular properties of the constituent components. Radiation heat transfer between solid surfaces is considered in the model, but not for the gas domain since radiation effects are negligible for the path lengths of the reactor. Since the explicit presence of the incompressibility constraint in the problem brings numerical difficulties with matrix manipulations [Gru89, Red93], a penalty function formulation was used. The pressure term and the continuity constraint are explicitly removed and momentum transport is efficiently calculated. In this formulation, pressure is

calculated by the relationship  $\mathbf{p} = -\epsilon \nabla \cdot \vec{\mathbf{v}}$  after the velocity field is obtained. The incompressibility constraint is more strictly enforced with a larger value of the penalty parameter  $\epsilon$ . In the following section, the model equations are given, the property value estimated, the algorithm described and validation results presented.

## 4.2 Mathematical Description

Atmospheric MOCVD is usually carried out under conditions of dilute concentrations of metal organic reactants in a carrier gas at sufficient high temperature to prevent condensation on the walls in the delivery manifold. Therefore, the ideal gas law is a good assumption for the system behavior. The following sets of conservation equations describe the steady state transport processes [Bir60, Cur99]:

- **Equation of State:**  $\rho = \frac{PM}{RT}$  (4-1)

- **Continuity:**  $\nabla \cdot \rho \vec{\mathbf{v}} = 0$  (4-2)

- **Momentum:**  $\rho \vec{\mathbf{v}} \cdot \nabla \vec{\mathbf{v}} = -\nabla p + \nabla \cdot \mu (\nabla \vec{\mathbf{v}} + (\nabla \vec{\mathbf{v}})^T) + \rho \vec{\mathbf{g}}$  (4-3)

- **Energy:**  $\rho C_p \vec{\mathbf{v}} \cdot \nabla T = \nabla \cdot k \nabla T$  (4-4)

- **Species k:**  $\rho \vec{\mathbf{v}} \cdot \nabla w_k = \nabla \cdot \left\{ \sum_{i=1}^{\lambda-1} L_{ki} \nabla w_i + G_k \nabla \ln T \right\} + r_k$ ,  $k = 1, \dots, \lambda-1$  (4-5)

where  $\rho$ ,  $\mu$ ,  $C_p$  and  $M$  are the density, viscosity, heat capacity, and molecular weight of the gas mixture, respectively. Moreover,  $P$ ,  $R$ ,  $k$ ,  $T$  and  $\vec{\mathbf{g}}$  are the nominal pressure, gas constant, thermal conductivity, temperature, and gravitational constant, respectively.  $\vec{\mathbf{v}}$  and  $p$  are the velocity vector and pressure within the gas region.

#### 4.2.1 Boundary Conditions

Since the reactor has axisymmetry, half of the region was considered for the modeling domain. Figure 4-1 shows the schematic of the modeling domain and basic variables used in the simulation [Ego98, Vor02]. To complement the governing equations stated above, proper boundary conditions are necessary. First, it was assumed that gases introduced through the glass bead bed exited the bed with parallel flow with initial velocities of  $V_C$ ,  $V_A$ , and  $V_S$  at the center, annulus, and sweep inlets, respectively. No slip conditions were assumed on solid-block surfaces and natural boundary conditions were used along the centerline of the reactor for all transport phenomena: to satisfy the Galerkin condition (equation 4-6), firstly the non-vanishing term is searched and the other term is regarded as the vanishing term. This mathematics condition is the natural boundary condition. On the other hand, there are essential boundary conditions. A constant temperature ( $T_{\text{Heater}}$ ) was maintained at the heater surface, which was placed underneath the ceramic cap (Figure 4-1). Because of conduction and radiation from the heater, a temperature gradient was generated in the gas phase region as heat was being lost by Newton's cooling to the ambient at the reactor wall, conduction through the walls and convection out of the reactor. A constant temperature ( $T_{\text{Bottom}}$ ) was specified at the bottom surface of the reactor, which was experimentally determined by nitrogen rotational spectra. Therefore, conductive heat was only considered inside the quartz envelope.

#### 4.2.2 Encoding

A residual of the equation can be defined as the value of which is the difference between calculated and exact solution in the calculation domain. The given problem of the Galerkin method is to find out the solution ( $u, v, p$ ) that makes the residuals null in the domain  $\Omega$ . This can be restated as a necessary condition as following [Bur87, Hug79, Pla84]:

$$\int_{\Omega} \mathbf{R} w \, d\Omega = 0 \quad (4-6)$$

where  $\mathbf{R}$  represents the residual from the exact solution and  $w$  is a weight function. A weight function can be expressed as a linear combination of independent functions, i.e., basis functions. For a more accurate solution, an infinite set of basis functions should be used. This is not, however, always possible. Therefore, a finite number of basis functions are inevitable in a real calculation. As a result, the obtained solution is only an approximation to the true solution. The main procedure of the finite element method (FEM) simulation is to obtain coefficients of the basis functions which are already substituted into the Equation 4-6. Trial (or shape function) and weight functions are not necessarily made up of the same set of basis functions. If the same basis function is used, the solution method is called the Galerkin method, which is used here.

$$u = \sum_{i=1}^M u_i \psi_i, \quad v = \sum_{i=1}^M v_i \psi_i, \quad p = \sum_{i=1}^N p_i \varphi_i \quad (4-7)$$

where  $\psi_i$  and  $\varphi_i$  are linearly independent basis functions for momentum vector and pressure, respectively, and  $u_i$ ,  $v_i$ , and  $p_i$  are constants to be determined. With constructed basis functions, solutions can be obtained for the sub-region of the developed mesh. Therefore, the finite element method is a feasible method that can easily handle the complex MOCVD reactor geometry.

### 4.3 Physical Property Estimation

In FEM simulation studies, the necessary gas phase transport properties were estimated from the Chapman-Enskog theory [Bir60], which is based on simple collision theory. For example, the binary diffusivity, viscosity, and thermal conductivity are given by the Equation 4-8 through 4-10:

$$D_{12} = 2.2680 \times 10^{-7} \frac{\sqrt{T^3 (M_1 + M_2) / 2 M_1 M_2}}{p \sigma_{12}^2 \Omega_{12}^D} \quad [\text{m}^2/\text{s}] \quad (4-8)$$

$$\mu = 2.6693 \times 10^{-6} \frac{\sqrt{MT}}{\sigma^2 \Omega^\mu} \quad [\text{Pa}\cdot\text{s}] \quad (4-9)$$

$$k = 2.6693 \times 10^{-3} \frac{\sqrt{T/M}}{\sigma^2 \Omega^\mu} \left( C_p + \frac{5}{4} R \right) \quad [\text{J}/\text{m}\cdot\text{s}\cdot\text{K}] \quad (4-10)$$

The values  $\sigma$  and  $\Omega$  are the collision diameter and appropriate collision potentials. The collision integrals are analytically obtained from the 12-6 Lennard-Jones potential and then the above physical properties are estimated with the collision diameter ( $\sigma$ ) and characteristic energy ( $\varepsilon/k_B$ ) of interaction between molecules. The following regression of collision integrals were mostly used for estimations [Neu72]:

$$\Omega^D = \frac{1.06036}{T_*^{0.15610}} + \frac{0.19300}{e^{0.47635T_*}} + \frac{1.03587}{e^{1.52996T_*}} + \frac{1.76474}{e^{3.89411T_*}} \quad (4-11)$$

$$\Omega^\mu = \frac{1.16145}{T_*^{0.14874}} + \frac{0.52487}{e^{0.77320T_*}} + \frac{2.16178}{e^{2.43787T_*}} \quad (4-12)$$

where  $T_* = k_B T / \varepsilon$ . The two Lennard-Jones potential parameters ( $\sigma$ ,  $\varepsilon/k_B$ ) were estimated using the empirical equations as shown below. To complete the values, the gas species critical properties and normal boiling point were required [Ste94, Hol92, Pol01].

$$\frac{\varepsilon}{k_B} = 0.77 T_c \quad \text{and} \quad \sigma = 0.841 V_c^{1/3} \quad (4-13)$$

$$\frac{\varepsilon}{k_B} = 1.15 T_b \quad \text{and} \quad \sigma = 1.18 V_b^{1/3} \quad (4-14)$$

where subscripts c and b represent for the critical state and normal boiling point at 1 atm, respectively. Table 4-1 shows the typical values of Lennard-Jones potential parameters calculated in this study.

#### 4.4 Optimization for Parameter Extraction

Given a validated reactor model [Hwa05a], the next step is to extract meaningful physical parameters. In this step the simulated data was matched with the experimental data and based on the result, a detailed comparison was made. In essence, the least square method was employed as shown in Equation 4-15 and the pertinent parameter vector, which minimizes the objective function, was searched using a Genetic algorithm.

$$S(k) = \sum_{i=1}^N \left( \frac{f_i - \hat{f}_i(k)}{\sigma_i} \right)^2 \quad (4-15)$$

where  $f_i$ ,  $\hat{f}_i$ , and  $k$  are experimental data, simulated data, and the parameter vector to be determined, respectively. Given the initial estimate for  $k_j$ , the parameter vector is iteratively updated by;

$$k_{j+1} = k_j + \Delta k_j \quad (4-16)$$

where the increment  $\Delta k_j$  solves the linear least squares problem.

$$\| S(k_j) + J(k_j) \Delta k_j \| \rightarrow \text{minimize} \quad (4-17)$$

with  $J_i(k) = dS_i(k) / dk$ . After the full domain search using Genetic algorithm, the Simplex algorithm was followed to fine-tune this parameter estimation.

**Genetic Algorithm:** The linear least squares Equation 4-17 involves the computation of the generalized inverse matrix of  $J(k_j)$ . Therefore, calculation of the derivatives  $J(k_j)$  is an important step and must be done very efficiently since inaccurate Jacobians are one of the most likely causes for failure in gradient-based methods. Therefore, in practice, it is difficult to accurately estimate the derivatives of the function  $S(k_j)$ . In the Genetic algorithm, the basic steps to estimate the function  $S(k_j)$  are as follows: First, the initial population is randomly

constructed by generating solution vectors within the problem space. If any information about the objective function is available then the initial population should be constructed such that it covers the regions of interest in the solution vector space. After evaluating the initial population, the fitness values are computed for every individual in the population. Next, the pool of offspring is created to generate the children of the new population. Again, the children population is evaluated by computing the fitness values for every individual. By merging the parents' population and the children's population, it is possible to construct the next population of individuals. The central advantage of Genetic algorithm is its robustness and, during the process, it neglects exploration of the search space and provides local optimum values depending crucially on the selection of the starting point.

**Simplex Algorithm:** The purpose of the Simplex algorithm is to obtain an optimal solution in search of the extreme points in its feasible region. The solution is determined by selecting a set of basic variables (BV) and testing its optimality. If some optimality condition is verified, then the algorithm terminates. Otherwise, the algorithm identifies an adjacent BV, with a better objective value. The optimality of this new solution is tested again and the entire scheme is repeated until an optimal BV is found. Since every time a new BV is identified, the objective value is improved and the set of BV's is finite, it follows that the algorithm will terminate in a finite number of steps (iterations).

#### 4.5 Applications

Heat and mass transport phenomena from the developed FEM model were validated by comparison to experimental measurements. Since  $\text{CH}_4$  gas has a large relative Raman cross-section, it was chosen as a trace molecule. The temperature or concentration profiles in the reactor for specific conditions were calculated using the model and compared to experimental

result. The FEM simulation results successfully describe a hydrodynamics behavior as summarized in a previous dissertation [Hwa04].

One of the advantages in FEM simulation is that a numerical specification of a temperature or concentration profile for all given geometry is available without actual measurement. Since this study is focused on the centerline, i.e., z-axis along with the asymmetric line from the gas inlet to the heater, FEM simulation can provide insight into MOCVD reactor performance.

Figure 4-2 gives example profiles of simulated results for N<sub>2</sub> carrier gas.

#### 4.5.1 Gas Phase MOCVD Simulation

After validation of the simulation describing the MOCVD reactions, the reaction chemistry and property values for the actual MOCVD deposition system was input into the simulation code. The binary diffusivity, viscosity, and thermal conductivity were obtained from the Chapman-Enskog theory stated in section 4.3: other properties, however, were needed to be estimated. To this end, DFT B3LYP was again employed to estimate the heat capacity and thermal conductivity. The heat capacity of dimethylcadmium and its first decomposed product, monomethylcadmium, are given below. The ECP model chemistry of SDD and 6-311++G(2d,2p) were used for Cd metal and hydrocarbons, respectively.

$$C_{p_{DMCd}} = -6.7116 \times 10^{-4} \times T^2 + 1.6389 \times 10^0 \times T + 3.5127 \times 10^2 \quad (4-18)$$

$$C_{p_{MCD}} = -2.8127 \times 10^{-4} \times T^2 + 6.7954 \times 10^{-1} \times T + 2.4818 \times 10^2 \quad (4-19)$$

The thermal decomposition reaction was simulated at a fixed temperature of 500 °C and the streamlines of the reactant other species as well and temperature isotherms are shown in Figure 4-3. The experimental results for DECd decomposition and comparison to model predicts are more fully described in Chapter 6. In addition to extracting parameter from measurements along the centerline, the model can also be used to examine flow patterns. This is helpful to check if gas flows are stable or not. Even a closed streamline pattern can be examined so actual operating



conditions can be adjusted to avoid this hydrodynamic condition in experiments. As another example, a transient flow study is introduced in the following section.

#### 4.5.2 Transient Study

Transient flow means that the flow velocity and pressure is changing with time. The only difference is that a time derivative of the velocity appears in the convective terms of the left-hand side Equation 4-3.

$$\rho\left(\frac{\partial \vec{v}}{\partial t} + \vec{v} \cdot \nabla \vec{v}\right) \quad (4-20)$$

Therefore, time dependent problems are governed by hyperbolic equations and their characteristics play a dominant role in their solution. As stated earlier, the Galerkin method uses Taylor-series expansions and it can be applied in this case as well. If heat transfer is not considered, as a simple example, then the Navier-Stokes equations are only different in mathematics considerations. As an example, Figure 4-4 shows the transient flow pattern of N<sub>2</sub> carrier gas in the MOCVD reactor. The temperature was set at 25 °C and the carrier gas was introduced at 2.5 cm/s velocity through the center and annulus inlets. The other inlets, i.e., annular, and sweep, had no gas flow. For convenience, 7 different observation times were selected. In this calculation example, it is shown that N<sub>2</sub> gas reaches steady state within 30 sec after initially introduced into the reactor.

The flow pattern from (a) through (g) shows the development of the N<sub>2</sub> gas flow. The flow has uniform concentration distribution near the substrate and fully developed gas flow through the exhaust. The vortex (or closed streamline flow) appears approximate 1 min after the gas flow is initiated and became fully developed after 6 min. This flow pattern exactly matches the solution from steady state flow (h), the steady state experiment. Therefore, this result gives the guideline that for the metal organic precursor under study should not begin before 6 min.

On the other hand, if the gas inlet velocity is increased, then the reaction condition should be different. For example, Figure 4-5 shows the results of 10 cm/s velocity condition for N<sub>2</sub> carrier gas. In this calculation, all the other conditions were the same as the 2.5 cm/s case (Figure 4-4). The calculated flow patterns for these 2 cases were the same prior 30 sec of initiation of flow. Thus 0.05, 0.5, 5 and 30 sec flow patterns were omitted in Figure 4-5. Unlike the previous case, the flow pattern reaches the steady state around 2 min after flow initiation and two large closed streamline flows appear in gas regions. Newly formed vortex helps more uniform gas distribution near the substrate.

To cover transient heat transfer additional physical terms are required, i.e., time dependent term in Equation 4-4. This situation was not considered in previous examples since the reactions studied in this work are always conducted at steady state. There are, however, some processes in which transient conditions are of interest in heated systems (e.g., as atomic layer deposition (ALD)). In ALD, two or more gases are introduced into the reactor to deposit on a heated substrate. It is important to understand how long it takes to reach the steady state flow pattern. It provides an actual experimental condition, such as gas switching time between two different metal organic chemicals. Therefore, the hydrodynamics simulation provides required information facts for understanding MOCVD or ALD reactions.

#### **4.6 Summary**

A reactor model was developed to describe experimental reactor used to study gas-phase MOCVD reactions. The model will be used along with experimental data to estimate rate parameters and physical properties. Specifically, the centerline data extracted from the experiment and using combined Genetics and Simplex algorithms will be used to estimate properties for DEZn and DMCd in Chapters 5 and 6. The Genetic algorithm is based on the least square method, which is basically minimizing the difference between experimental and

simulated data. This algorithm determines the global minimum, which can be finely tuned using a Simplex algorithm.

The initiation of flow in the experimental reactor was studied. Considering only N<sub>2</sub> flow at room temperature, transient flow pattern for describing two different inlet velocities were examined and from the result, minimum times to reach steady state were computed. This model can be applied to other operating condition, such as ALD; however, additional consideration of the system should be included.





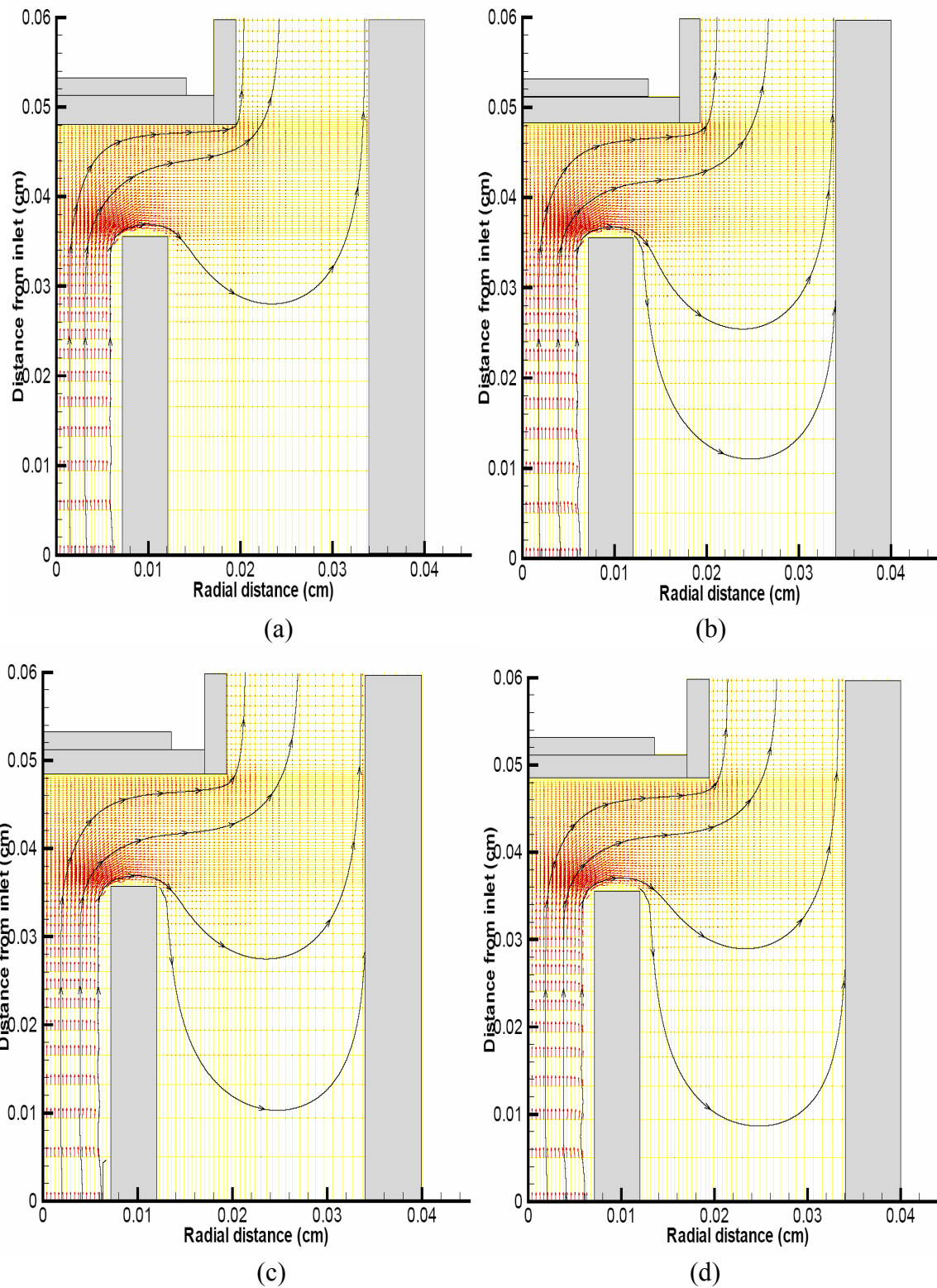


Figure 4-4. Streamlines of  $N_2$  gas at room temperatures ( $25\text{ }^{\circ}\text{C}$ ) after (a) 0.05 (b) 0.5 (c) 5 and (d) 30 sec. (Next page) The flow patterns of  $N_2$  gas at (e) 60 (f) 120 (g) 360 sec and (h) time-independent solution. The gas flow rate was set at  $2.5\text{ cm/s}$ .

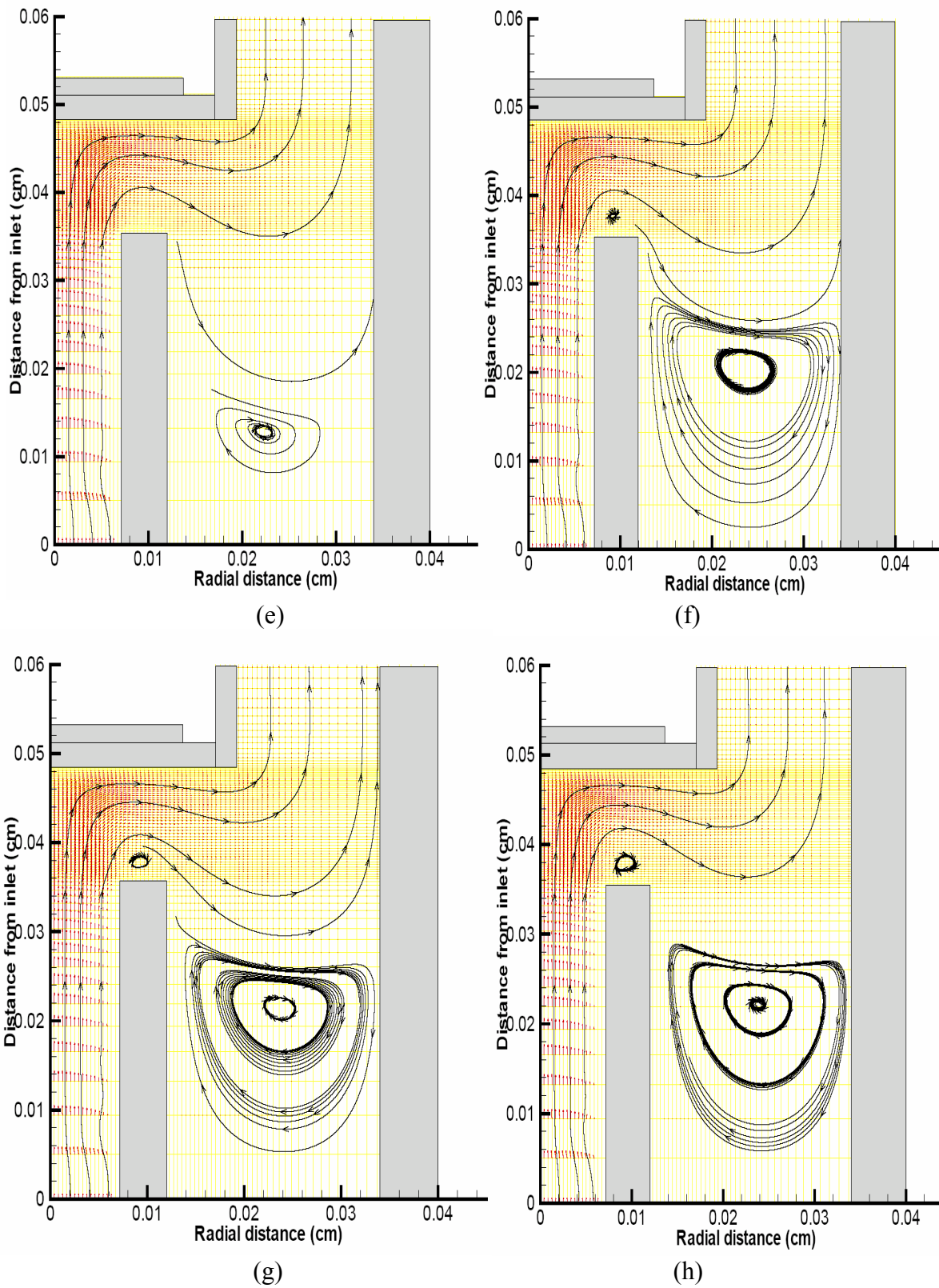


Figure 4-4. Continued.

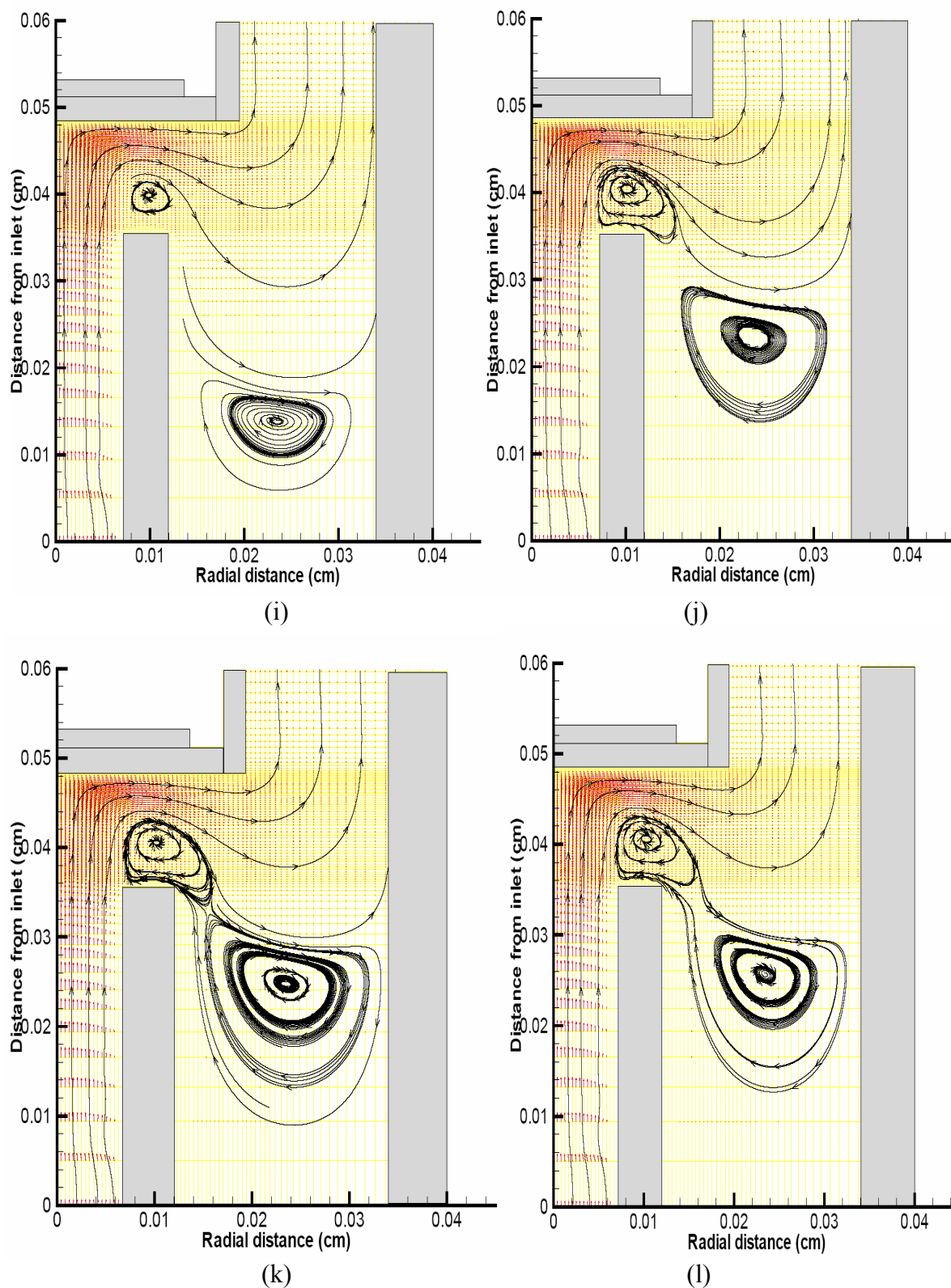


Figure 4-5. Streamlines of  $N_2$  gas at room temperatures (25 °C) after (i) 60 (j) 120 (k) 360 sec and (l) time-independent solution. The gas flow rate was set at 10.0 cm/s.



## CHAPTER 5

### DIETHYLZINC DECOMPOSITION KINETICS AND REACTION CHEMISTRY WITH WATER

#### 5.1 Introduction

Several applications motivate chemical vapor deposition (CVD) of Zn-containing thin films. In particular, the Zn-VI compound semiconductors and alloys with other group II-VI compounds are used as the host semiconductor material in a variety of optoelectronic devices including light emitting devices, photodetectors, and lasers [Wag04, Wan05, Bac99]. Among these compound semiconductors, zinc oxide is commonly used as a transparent conducting material in emissive device applications as well as solar cells [Cho99, Hag99, Myc04, Li03, Gha80]. ZnO can be made highly conductive by adjusting the oxygen vacancy concentration or doping (e.g. Al), while recent reports of p-type conductivity are encouraging for transparent electronics [Loo02, Min97]. Zinc oxide thin films have been deposited by CVD from a variety of organo-Zn precursors including zinc acetate,  $\text{Zn}(\text{CH}_3\text{CO}_2)_2$ , zinc acetylacetonate,  $\text{Zn}(\text{C}_5\text{H}_7\text{O}_2)_2$ , and most commonly from diethylzinc,  $\text{Zn}(\text{C}_2\text{H}_5)_2$  in combination with an oxygen source such as water in the temperature range 350 to 500 °C.

The first detailed study of pyrolysis of  $\text{Zn}(\text{C}_2\text{H}_5)_2$  was reported by Koski *et al.* [Kos76] using the toluene carrier method. They reported that sequential homolytic fission of the metal-carbon bond is the dominant dissociation mechanism. Jackson [Jac89a] subsequently investigated the onset of pyrolysis of diethylzinc in  $\text{H}_2$  and He flows by optical monitoring of the rate of condensation of Zn. Most recently, Dumont *et al.* [Dum92, Dum93] used mass spectroscopic analysis of the output of a metal organic chemical vapor deposition (MOCVD) reactor to study the pyrolysis of  $\text{Zn}(\text{C}_2\text{H}_5)_2$ . These researchers observed ethane and n-butane as the predominant decomposition products. Based on their results as well as those of previous studies, Dumont and co-workers also concluded that decomposition was mainly homolytic in

nature, with the resultant ethyl radicals undergoing either recombination to yield butane (reaction 5-1c), disproportionation, (reaction 5-1a), or decomposition (reaction 5-1e). Subsequent investigations by others have supported the following decomposition mechanism:

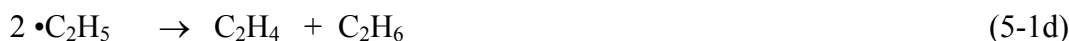


Table 5-1 summarizes the measured apparent activation energy for homogeneous homolytic fission of the first Zn-C bond of DEZn [Kos76, Jac 89, Dum92, Dum93]. It is noted that the measured activation energy in each study is based on direct measurement of the concentration decrease of diethylzinc and indirectly the increase of the  $\bullet\text{C}_2\text{H}_5$  radical concentration. Experimental detection of primary reaction intermediates, including  $\bullet\text{ZnC}_2\text{H}_5$ , however, has not been reported. As listed in Table 5-1, the reported apparent activation energy for breaking the first Zn-C bond is in the range 50 to 56 kcal/mol, which is considered relatively good agreement amongst the different measurements. The only evidence supporting sequential homolysis is the detection of ethane and n-butane in the outlet of a MOCVD reactor

In contrast to the bond homolysis radical mechanism suggested above, Linney and Russel [Lin93] observed a different reaction pathway using FTIR and  $^1\text{H}$  NMR spectroscopy. They detected  $\text{H}_2\text{Zn}$  as the major Zn product of diethylzinc homogeneous pyrolysis in the temperature range 280 to 520 °C and suggested  $\beta$ -hydride elimination as the most probable route for the reaction (reactions 5-2a and 5-2b).





To better understand the homogeneous pyrolysis mechanism of  $\text{Zn}(\text{C}_2\text{H}_5)_2$ , its decomposition was studied by Raman spectroscopy in an inverted impinging jet reactor. Quantum chemical calculations were used to estimate Raman frequencies to assist in the interpretation of the experimental data. The Gibbs energies of intermediate species were also estimated to test the thermodynamic possibility of proposed reaction pathways. Based on experimental observations and computational results reported here, the following additional reaction step of dimer formation is suggested.



## 5.2 Experimental and Calculation Details

A schematic of the experimental reactor used to study the gas phase decomposition of  $\text{Zn}(\text{C}_2\text{H}_5)_2$  is shown in chapter 2. The metal organic precursor in a carrier gas is introduced through a center-lined tube, while a  $\text{N}_2$  sweeping gas flow envelops the metal organic gas to minimize wall deposition of precursors or reaction products. The reactor body is constructed of four optically flat quartz plates fused on edge to produce a square base. This rectangular chamber is inserted into a quartz tube with four vertical slits to permit access of the probe beam to the reactor centerline and detection of the scattered light. The up-flowing gas stream impinges on a resistance-heated pedestal susceptor equipped with a control and measurement thermocouple. Before measuring the concentration and temperature profiles along the centerline of the reactor, a steady-state flow pattern is first established. To ensure that no closed streamlines exist in the reactor, a  $\text{CH}_4$  tracer flow study was performed to delineate suitable conditions [Hwa05a]. This impinging jet reactor was designed to eliminate wall reactions and produce well defined and easily modeled flow region. The temperature and species

concentration gradients that develop along the centerline allow study of reactions over a wide range of conditions in a single steady state experiment. By adjusting the temperature and gas velocity, the reaction mechanism could be programmed for a homogenous decomposition study.

A U-1000 Raman spectrometer (Jobin Yvon) was used to collect and analyze the scattered light. The 488 nm wavelength of an Ar-ion laser or the 532 nm wavelength of a Nd/YAG solid state laser was used as the excitation source and a photomultiplier tube was used as a detector. A maximal laser power of 1~5 W was used, although the actual excitation power was lower due to losses from mirrors and other optical components. A coupled charge device (CCD) was also available in system but the analytical measurements were mainly performed using the PMT.

The theory of Raman scattering based on fundamental molecular motions, including electronic, rotational and vibrational motions is very well developed [Lon77, Sch79, Jac92]. The Raman intensity is proportional to the 4<sup>th</sup> power of the light source wavelength and Raman cross-section. To estimate the mole fraction of a specific molecule from the measured intensity, the ratio of the Raman intensity of the molecular species of interest and the carrier gas (N<sub>2</sub>) is used as shown in Equations 5-3 and 5-4.

$$x_j = \frac{N_j}{N_j + N_Q} \quad (5-3)$$

$$\frac{N_Q}{N_j} = \frac{(\tilde{\nu}_0 - \tilde{\nu}_j)^4}{(\tilde{\nu}_0 - \tilde{\nu}_Q)^4} \frac{1 - \exp(-hc\tilde{\nu}_Q/k_B T)}{1 - \exp(-hc\tilde{\nu}_j/k_B T)} \frac{I_Q}{I_j} \Sigma_j \quad (5-4)$$

where  $N_j$  and  $I_j$  are the number density and measured intensity of component  $j$ , and the subscript 'Q' denotes the Q-branch of N<sub>2</sub> carrier gas.  $\tilde{\nu}_0$ ,  $\tilde{\nu}_j$  and  $\tilde{\nu}_Q$  are the wave number of the incident light, molecular vibration and Q-branch of N<sub>2</sub> carrier gas. The term  $\Sigma_j$  is the relative Raman cross-section for vibration mode  $j$ . The Raman intensity of the molecular species of

interest is compared to that of N<sub>2</sub> since N<sub>2</sub> is at high concentration and known to have stable rotational and vibrational motions at reaction conditions. In addition to the vibrational frequency, the relative Raman cross-section,  $\Sigma_k$ , is required. In practice, cross-sections are usually reported relative to that of the Q-branch of N<sub>2</sub> since N<sub>2</sub> has sufficient stability to be an internal standard [Sch79].

$$\Sigma_k = \frac{C_k \tilde{\nu}_Q}{C_Q \tilde{\nu}_k} = \frac{(\partial\sigma/\partial\Omega)_k (\tilde{\nu}_0 - \tilde{\nu}_Q)^4}{(\partial\sigma/\partial\Omega)_Q (\tilde{\nu}_0 - \tilde{\nu}_k)^4} \frac{1 - \exp(-hc \tilde{\nu}_k/k_B T)}{1 - \exp(-hc \tilde{\nu}_Q/k_B T)} \quad (5-5)$$

where  $C_k$  is a constant, which contains specific information on the  $k^{\text{th}}$  vibration mode. The relative Raman cross-section shown above is calculated using the Q-branch of the N<sub>2</sub> vibrational motion of  $\tilde{\nu}_Q$ , which appears at 2331 cm<sup>-1</sup>. The Raman cross-sections for metal organic precursors, however, are generally not known.

In a preliminary experiment, the Raman cross-section of DEZn was measured in a commercial flow-cell reactor. In this measurement a steady stream of DEZn (10 mol % in N<sub>2</sub>), nominally at atmospheric pressure, was introduced into the flow-cell reactor at 3.0 cm/s velocity and sufficient time was allowed for the reactor to reach steady state. The contents of the cell were then excited with the 532.08 nm line at 1~3 W and the scattered intensity of the Zn-C stretch at 480 cm<sup>-1</sup> was recorded. With repeated measurements at room temperature, the value of the relative Raman cross-section of DEZn was estimated to be 4.2. It is noted that the estimated value of the relative Raman cross-section did not change in the laser measured power range 1 to 3 W. At higher power, however, decomposition products were observed as discussed in section 5.3.1. Although the cross-section of this molecule is lower than that of the group III alkyls (e.g.  $\Sigma_{\text{TMIIn}} = 22.3$ ), the signal to noise ratio at this concentration was sufficient to quantify the Zn(C<sub>2</sub>H<sub>5</sub>)<sub>2</sub> concentration from the measured intensity of the 480 cm<sup>-1</sup> line.

Coupling the experimental observations with the computational calculations enabled identification of reaction intermediates and thus suggestion of a decomposition mechanism. The quantum chemical calculations were performed using the Gaussian 03 package [Fri04]. Bond dissociation energies were calculated using Becke's three-parameter hybrid exchange functional combined with the Lee-Yang-Parr gradient-corrected correlation functional (B3LYP) and the 6-311G(d) basis set. This method and basis set specify the model chemistry used to calculate molecular optimized geometries, and atomic or molecular properties for the reaction species, i.e. Zn-containing molecules [Sim97, Smi03]. This model chemistry was also used to calculate the Raman active frequencies along with the symmetrical vibrational motions between zinc and carbon or zinc and hydrogen atoms in selected intermediate species. Calculated values of the rotational or vibrational frequencies allowed their partition functions to be evaluated to yield Gibbs energies of possible intermediates to judge which reactions are thermodynamically favored. In identifying reaction intermediates, multiple combinations of different fragments, i.e. reaction intermediates, were tested.

### 5.3 Decomposition Mechanism of Diethylzinc

The two gas-phase decomposition reaction pathways reported in the literature can be distinguished by their Zn intermediates. The species Zn and  $\bullet\text{ZnC}_2\text{H}_5$  are produced from homolytic fission, while  $\text{HZnC}_2\text{H}_5$  and  $\text{ZnH}_2$  result from  $\beta$ -hydride elimination. The first set of experiments was designed to promote the decomposition of  $\text{Zn}(\text{C}_2\text{H}_5)_2$  to a sufficient extent that the Zn intermediates could be detected by Raman scattering. To this end photolysis of  $\text{Zn}(\text{C}_2\text{H}_5)_2$  was carried out using the incident laser at high power in the flow cell. To assist in the peak assignment, first principles calculations were performed to identify vibrational frequencies of candidate reaction intermediates.

Several computational approaches were first tested to represent species in the DEZn system. Among them, the B3LYP level calculation with 6-311G(d) basis set was chosen to describe the nature of bond rupture and analyze the thermodynamic properties based on geometry optimization calculations. The products from carbon-carbon dissociation, i.e.  $\text{Zn}(\text{C}_2\text{H}_5)_2 \rightarrow (\text{C}_2\text{H}_5)\text{Zn}(\text{CH}_2) + \text{CH}_3$ , were not included since the carbon-carbon bond strength is considerably greater than the zinc-carbon bond strength. This assertion is supported by an analysis using the Wiberg bond index in the natural bond orbital (NBO): Zn-C:0.4990, C-C:1.0600, C(next to Zn)-H: 0.9362, and C(next to C)-H: 0.9403. Based on the optimal geometries, the symmetry point groups were identified and Raman-active vibrational frequencies in normal modes along with the symmetry groups were obtained [Nag80]. Table 5-2 summarizes the calculated results.

Detection of atomic Zn has not been reported by Raman spectroscopy since the most probable emission radiates from the excited state ( $^1\text{P}_1$ ) to the ground state ( $^1\text{S}_0$ ) with just 1.6 ns lifetime, which is too short to be detected [Cor62]. Therefore, Raman scattering experiments were used to search for the possible decomposition fragments  $\text{ZnC}_2\text{H}_5$ ,  $\text{HZnC}_2\text{H}_5$ , and  $\text{ZnH}_2$ .

### 5.3.1 Laser-Induced Decomposition of $\text{Zn}(\text{C}_2\text{H}_5)_2$ in a Flow Cell

As presented in the experimental section, room temperature scattering experiments were performed in the flow cell on DEZn in  $\text{N}_2$  carrier gas to determine the scattering cross-section of DEZn. The literature has suggested both homolysis of the Zn-C bond and  $\beta$ -hydride elimination as the homogeneous decomposition pathways. No reaction intermediates, however, have been experimentally detected for Zn species. The only products detected have been the sequential  $\beta$ -hydride elimination product  $\text{ZnH}_2$  and hydrocarbons ( $\text{C}_2\text{H}_4$  and  $\text{C}_2\text{H}_6$ ). In an attempt to evaluate the use of Raman scattering to detect intermediates or products, a series of experiments and high

laser power was performed to promote decomposition of DEZn, presumably via photolysis at the 532 nm wavelength of the incident beam, although the preferred photolysis pathway is not expected, to be the same as the pyrolysis one, identification photolysis decomposition products would assist in the interpretation of the subsequent experiments.

Laser induced photolysis of a stream of 10 mol %  $\text{Zn}(\text{C}_2\text{H}_5)_2$  in  $\text{N}_2$  nominally at room temperature was studied in the commercial flow cell operating at steady state. No decomposition of  $\text{Zn}(\text{C}_2\text{H}_5)_2$  is expected at low power but as the power is increased photolytic decomposition of DEZn should activate decomposition sufficient to detect reaction intermediates. Since all anticipated fragments reside in the Raman shift ranges 250 to 700 and 1850 to 1950  $\text{cm}^{-1}$ , only these ranges were scanned. The Raman spectra obtained for laser powers of 2 and 5 W are shown in Figure 5-1. The lower spectrum, which was taken at a laser power of 2 W nominal (1.3 W incident) shows a broad vibration peak around 480  $\text{cm}^{-1}$ . Minimal photolysis is anticipated at this incident power and the observed peak is attributed the Zn-C stretch in  $\text{Zn}(\text{C}_2\text{H}_5)_2$ . The main peak assignment was carried out based on literatures as well as computational calculation results. It should be noted that all the calculation results in Raman shift were also confirmed from literatures.

On the other hand, increasing the laser power to 5 W (3.3 W incident) yields an increase in the intensity of the 480  $\text{cm}^{-1}$  band and introduces an additional sharp feature at 1917.9  $\text{cm}^{-1}$ . This feature is attributed to the Zn-H vibrational stretch of  $\text{H}_2\text{Zn}$ , consistent with the calculated frequency of 1918.9  $\text{cm}^{-1}$  listed in Table 5-2. Incomplete decomposition of DEZn and the higher incident power resulted in a strong peak for DEZn. The higher local temperature also produced a peak shift of  $\sim 1 \text{ cm}^{-1}$  to lower wavelength. A weak scattering signal is detected around at 666.7  $\text{cm}^{-1}$  assigned to the Zn-H symmetrical vibration of  $\text{HZnC}_2\text{H}_5$ . Both of these fragments are



expected for decomposition via  $\beta$ -hydride elimination. The low intensity of the peak corresponding to the  $\text{HZnC}_2\text{H}_5$  suggests the second  $\beta$ -hydride elimination is relatively fast compared to the first  $\beta$ -hydride elimination. It is noted that the peak at  $441.7\text{ cm}^{-1}$  agrees well with the calculated value for Zn-C stretching of the transition state species in the product of the first  $\beta$ -hydride elimination,  $\text{HZnC}_2\text{H}_5$ . In contrast, no peak was detected in the spectrum at the 5 W power level at the frequency calculated for the homolysis intermediate  $\bullet\text{ZnC}_2\text{H}_5$ . It is possible, however, that  $\bullet\text{ZnC}_2\text{H}_5$  radical has too small of a Raman cross-section or its molecular density is too small, as may occur for short lived species, as is generally the case for radicals when compared to uncharged molecules. Identifying hydrocarbon decomposition products would assist in differentiating between the two reaction pathways. The expected hydrocarbon gas molecules, however, have small Raman cross-sectional areas rendering their detection challenging. The results of two preliminary experiments suggest that the  $\beta$ -hydride elimination pathway is active at least by photolysis. The results also lend support to the accuracy of the first principles calculations. These results encouraged a more complete study using the inverted impinging-jet reactor.

### 5.3.2 Diethylzinc Decomposition in an Inverted Impinging Jet Reactor

In the next experiment,  $\text{Zn}(\text{C}_2\text{H}_5)_2$  was introduced into the center line of the probe reactor described in chapter 2 at an inlet concentration 0.5 mol % in  $\text{N}_2$ . The purpose of this experiment was to measure the  $\text{Zn}(\text{C}_2\text{H}_5)_2$  profile along the centerline as well as any other detected reaction products. It is noted that the high temperature reduced the signal to noise level, while transverse and axial diffusion diluted the precursor as well as reaction products. The existence of a validated reactor model [Hwa05b] and rate constants from the computational studies allowed comparison of the experimental profiles to those predicted by the reaction simulation.

The concentration of DEZn was calculated from measured Raman scattering intensities using Equations 5-3 and 4 and the relative Raman cross-section obtained from the preliminary flow-cell experiments. The intensity ratio of DEZn relative to nitrogen was calculated from Equation 5-4 and mole fraction of DEZn in nitrogen carrier gas was obtained using Equation 5-3 along with the measured temperature gradient. Figure 5-2 plots the measured centerline DEZn concentration at selected positions below the heated susceptor (set point 600 °C). Figure 5-2 also shows the temperature profile calculated using a detailed 2-D asymmetrical reactor model. This model is described in greater detail elsewhere, including its validation [Hwa05a, Hwa05b]. Briefly, the simulation uses the finite element method (FEM) to simultaneously solve the steady state momentum, heat, and mass balance equations in a reacting system. It is noted that a ~160 °C difference exists between the set-point temperature and the gas phase temperature extrapolated to the heater surface. This difference is a result of thermal resistances between the central thermocouple embedded in the ceramic heater, the glass envelope, and into the gas phase. It is also noted that the thermal boundary layer thickness is on the order of 6 mm at these conditions.

As previously indicated measurement of the mole fraction of DEZn is challenging since the relative Raman cross-section of the Zn-C stretch is small. It was possible, however, to quantitatively measure the DEZn concentration above a mole fraction of ~0.5 mol %. The onset of DEZn thermal decomposition is seen to occur at ~4 mm below the heated susceptor at a gas phase temperature of ~150°C. The measured profile was compared to that predicted by the reactor model assuming the disappearance of DEZn occurs by homolytic fission using values of  $E_a$  and  $A$  listed in Table 5-1 by either Koski *et al.* [Kos76] or Dumont *et al.* [Dum93].

The comparisons (Figure 5-2) show that the rate constants suggested by Koski *et al.* give a lower decomposition extent than using the constants reported by Dumont *et al.* It is noted that the DEZn profile using the Koski *et al.* constants is almost identical to that assuming no decomposition occurs (calculation not shown in Figure 5-2). This is because transverse diffusion occurs along the axis to decrease the centerline DEZn concentration and the magnitude of the decrease is similar to the extent of homogenous decomposition. It is also obvious from the comparison that the reported homolysis kinetic data do not fully account for the experimentally observed decomposition extent. If the experimental values are correct, then either the rate constants are incorrect or another decomposition pathway is significant. Even more, the rate constants for simple dissociation were also estimated using the model chemistry of B3LYP/6-311G(d), which yielded  $E_a = 71.1$  kcal/mol and  $A = 5.73 \times 10^{24} \text{ s}^{-1}$ . These values, however, are considerably greater than the experimental values listed in Table 5-1 and as a result, the simulated DEZn concentration decreased very rapidly. In fact, the estimation of kinetic data was incorrect since the correction factor of basis set superposition error (BSSE) was not considered. Furthermore, improper multiplicity without considering induced radicals also overestimated the kinetic rate parameters. This calculation result was obtained based on the generally accepted thermodynamic estimation procedure, i.e., the energy difference between the products and reactants. It is suggested, however, that more elaborate corrections should be considered as detailed below. Moreover, detailed quantum chemical calculations were attempted to estimate rate constants for both the homolytic fission and  $\beta$ -hydride elimination routes.

Since no quantitative rate constants have been reported for the  $\beta$ -hydride elimination, they were calculated as outlined below. In this estimate the statistical thermodynamic properties were calculated using the same model chemistry (B3LYP/6-311G(d)) used to estimate the vibrational

frequencies. Based on the optimal geometries for the reactant, a transition state was first postulated to transfer an H atom from the beta position of  $\text{Zn}(\text{C}_2\text{H}_5)_2$  to Zn metal and product. The Gibbs energy and enthalpy changes were then calculated in the reaction temperature range to obtain the activation energy and frequency factor for reaction (5-2a). For  $\beta$ -hydride elimination, the bond dissociation energy is defined as the energy difference between the transition state  $[\text{HZnC}_2\text{H}_5\cdots\text{C}_2\text{H}_4]$  and the reactant  $[(\text{Zn}(\text{C}_2\text{H}_5)_2)]$ . The calculated rate constant for the first order reaction (5-2a) is  $E_g=47.24$  kcal/mol and frequency factor  $A=7.90 \times 10^{14} \text{ s}^{-1}$ . These values for the rate constants, however, predict minimal decomposition along the centerline of the impinging jet reactor, and to a lesser extent than by homolysis using the rate constants of Dumont *et al.* It is apparent from the comparison of the measured DEZn concentrations to the calculated profile assuming  $\beta$ -hydride elimination using the estimated rate constants that this reaction does not fully account for the extent of DEZn disappearance.

In the case of homolytic fission, it is noted that the calculated value of A is significantly greater and suggests a pathway that involves less entropy change. Therefore, the potential energy surface for Zn-C dissociation was scanned quantum chemically along the Zn-C bond distance to better understand the preferred molecular behavior during bond rupture. The same model chemistry of B3LYP/6-311G(d) was used in this scan, but two multiplicities (singlet and triplet) were considered. Figure 5-3 compares the calculated potential energy variation of DEZn dissociation for the singlet and triplet states. It is seen that the singlet state is the lowest energy state in the precursor, but the triplet state is more stable in the dissociated state.

From Figure 5-3, one might expect a reaction enthalpy is  $\sim 71$  kcal/mol. Based on the reports, this value, however, is too high. Since this potential scan used arbitrary bond lengths, the actual geometry optimization was not considered. Therefore, the potential values were

overestimated due to the lack of energy compensation from geometrical structure deformation. It should be noted that the main purpose of this scan is to show that the multiplicity setting is critical in rate estimation. The more stable triplet state at large separation distance along with its lower entropy reduces both the activation energy and frequency factor. Table 5-3 summarizes the calculated reaction rate parameters for both the dissociation and the  $\beta$ -hydride elimination reactions, and Figure 5-4 shows the concentration profiles predicted with these values. The agreement between experimental concentrations and the predicted profile that includes both pathways is very good. Thus both  $\beta$ -hydride elimination and homolytic fission occur, with homolysis the dominant pathway in the temperature range of study.

### 5.3.3 Reaction Intermediates

The evidence supporting simple dissociation as the preferred pathway includes the observation of the expected final hydrocarbon products (butane, ethane, and ethane) and a measured apparent activation energy that is consistent among several investigators and similar to the value suggested by calculations. The primary reaction intermediates,  $\bullet\text{ZnC}_2\text{H}_5$  and  $\bullet\text{C}_2\text{H}_5$ , however, has not been detected experimentally, perhaps due to small molecular densities or scattering cross-sections. In contrast, the observation of solid  $\text{ZnH}_2$  on the cell window during IR laser-powered homogeneous pyrolysis as well as the expected hydrocarbon end products supports the route of double  $\beta$ -hydride elimination. Although the photolysis pathway can be different than the pyrolysis route, it is noted that the single and double  $\beta$ -hydride elimination intermediates  $\text{HZnC}_2\text{H}_5$  and  $\text{H}_2\text{Zn}$  were both observed upon photolysis of  $\text{DEZn}$ . Thus a series of additional reactions were postulated and the likelihood of their existence probed computationally. The same model chemistry of B3LYP/6-311G(d) was used for consistency to calculate Gibbs energies. In particular, reactions that included  $\bullet\text{ZnC}_2\text{H}_5$  or  $\text{ZnH}$  (possible product from Zn-C bond dissociation of  $\text{HZnC}_2\text{H}_5$ ) were considered.

Table 5-4 lists four reactions that involve these intermediates that gave negative calculated values of Gibbs energy changes at a reaction temperature of 798.15 °C. Moreover, these reactions are exothermic so that the reactions may be facile in the gas phase. These reactions include  $2\text{Zn-H} \leftrightarrow \text{Zn}_2\text{H}_2$ ,  $\text{HZn} + \text{ZnC}_2\text{H}_5 \leftrightarrow \text{HZnZnC}_2\text{H}_5$ , and  $2\text{ZnC}_2\text{H}_5 \leftrightarrow (\text{ZnC}_2\text{H}_5)_2$  in both cis and trans conformations. Other reactions examined included formation of  $\text{CH}_3\text{ZnC}_2\text{H}_5$ ,  $\text{HZnCH}_3$ , and  $(\text{ZnH})_3$  but the calculated energy changes were positive.

Based on the results in Table 5-4, the most favorable reactions are the monoethylzinc dimerization reactions to form the cis- and trans- conformations. The distance between the two ethyl groups is sufficiently long (6.27 Å) that there should not be a difference in their stability. Therefore, no energy rotation barrier was evident between the cis- and trans- conformations and the Raman-active vibrational frequencies are identical. Table 5-5 shows the calculated Raman frequencies for each stable reaction intermediate along with the Zn-C symmetrical motions. Given similar Zn-C motions in  $\text{DEZn}$  and the intermediates examined, a scaling factor was introduced based on comparison between the experimental and calculated Zn-C vibrational frequencies for  $\text{DEZn}$  [Sco96]. DFT calculations gave accurate frequency values for the Zn-H stretch, especially for motions containing hydrogen with its symmetrical s orbital.

A second experiment was performed to detect products of reactions between intermediates. In this experiment the susceptor set point temperature was elevated to 600 °C to give more complete decomposition and thus possibly increase the concentration of intermediates. The Ar-ion laser power was 1 W and the concentration of  $\text{DEZn}$  was 0.5 mol% in  $\text{N}_2$  carrier gas. Based on the calculated Raman shifts shown in Table 5-5, scans were taken over the expanded range 200 to 1300  $\text{cm}^{-1}$  (Figure 5-5). The lower scan was obtained 1 mm above the inlet and the upper scan at 2 mm. The multiple scans increased the signal to noise ratio to more confidently extract a

value for Raman shift of the intermediate, which likely has a low Raman cross-section. Comparison of the experimental value of the shift at  $1185\text{ cm}^{-1}$  to those listed in Table 5-5 strongly suggests the presence of the  $(\text{ZnC}_2\text{H}_5)_2$  as a reaction product of the  $\text{ZnC}_2\text{H}_5$  intermediate decomposition. In fact, the Raman shift of  $1185\text{ cm}^{-1}$  is not directly obtained from Zn-C vibrational stretching. The normal mode of vibration was from C-C vibrational stretching. From the calculated result, however, it was noted that the angle of the Zn-C-C bond is around  $116^\circ$  and the direct vibrational motion at this frequency induced the indirect Zn-C bending motion as well as Zn-C vibrational stretching. The broad peak shape definitely says that the motion is related to Zn-C motion. Since it was from secondary induced motion, it showed a small relative Raman cross-section. Therefore, the actual measurement of this peak was not easy since it was similar in intensity to noise levels. The multi-time scanning with elaborating integration time and the noise filtering process, however, made it distinguishable (Figure 5-5). Based on experimental observations and support from first principles calculations, the thermal decomposition of DEZn is suggested to have energies as depicted in Figure 5-6.



In summary, the decomposition pathways of  $\text{Zn}(\text{C}_2\text{H}_5)_2$  were investigated by both Raman spectroscopy and quantum calculations at the B3LYP/6-311G(d) chemistry level. Detection of  $\text{H}_2\text{Zn}$  in photolysis gives support for including  $\beta$ -hydride elimination as one of the reaction paths. The thermal decomposition of DEZn was followed in an up-flow impinging-jet reactor using Raman scattering and using the  $480\text{ cm}^{-1}$  line attributed to symmetrical stretch of the Zn-C bond.

The measured concentration profile was then compared to those predicted by a 2-D hydrodynamic simulation including various rate equations. This comparison indicates that homolytic fission of the Zn-C bond is the dominant initial deposition reaction, although  $\beta$ -hydride elimination also is active. Dimerization of the reaction intermediate  $\text{ZnC}_2\text{H}_5$  was confirmed both experimentally and by first principles calculations.

#### **5.4 Zinc Oxide Film Formation from Diethylzinc and Water Reactions**

The wide band gap energy of ZnO (3.4 eV) makes it useful various optical window applications such as light emitting diodes (LEDs), flat panel displays, and solar cells. ZnO thin films are also used as a transparent conducting oxide (TCO) after replacing the more expensive indium tin oxide (ITO) films [Bac99, Waa04, Zen03, Fen04]. ZnO thin films can be deposited by metal organic chemical vapor deposition (MOCVD) using various metal organic compounds [Wan05, Hag99, Myc04]. MOCVD is especially attractive for fabricating large scale devices due to the possibility of high deposition rate and excellent thickness uniformity.

In the MOCVD, the substrate selection is a critical decision. Although high quality bulk ZnO substrates are now under development, their high cost and limited availability currently preclude their use in mass production environments. Silicon is an attractive substrate as a result of its low cost, good thermal conductivity, high crystalline quality, availability of large size substrates, and a wide range of conductivity. For applications that require transparent substrates, glasses or polymers are often used, particularly for flexible display applications [All01, Cha01]. For these applications, the MOCVD deposition temperature should be lower than the transition temperature of substrate (e.g., glass temperature or melting point).

To design better reactor and optimize deposition conditions, better understanding of the gas-phase reactions in MOCVD is required [All98]. In this study, the reaction of diethylzinc ( $\text{Zn}(\text{C}_2\text{H}_5)_2$ ) with water ( $\text{H}_2\text{O}$ ) to form ZnO has been selected for detailed study. In the previous



section 5.3, it was shown that the homogeneous pyrolysis of diethylzinc produces two reaction intermediates,  $\text{HZnC}_2\text{H}_5$  and  $(\text{Zn}(\text{C}_2\text{H}_5)_2)_2$ . The first species is formed from  $\beta$ -hydride elimination and the second molecule results from homolysis of the Zn-C bond followed by dimerization. Therefore three Zn-containing molecules (i.e., two the reaction intermediates and unreacted diethylzinc) are considered to exist near the substrate in gas phase when the temperature is under 600 °C.

The computational calculations aim to clarify the most likely reaction mechanisms near the substrate surface and suggest other possible reaction pathways when an impurity is added to the system. Since impurity-doped ZnO is becoming widespread in a number of applications, understanding the gas phase dynamics as well as the heterogeneous surface reactions is a priority. In fact, it is a rather difficult challenge to process p-type doped ZnO films, while n-type ZnO is available even without any intentional doping [Par02c].

#### 5.4.1 Calculation Methods

The quantum chemical calculations were performed using the Gaussian 03 program package [Fri04]. Bond formation and dissociation energies were calculated using Becke's three parameters. These parameters are a hybrid exchange function, a Lee-Yang-Parr gradient-corrected correlation function (B3LYP), and a 6-311G(d) basis set that, together, specifies the model chemistry used to calculate the molecular optimized geometry. This calculation method also enabled the evaluation of likely reaction transition states. Thermo-chemical calculations were also performed with the same model chemistry and the calculated Gibbs energy changes were used to determine the likelihood of the gas phase reactions.

The reaction temperature was assumed to be less than 600 °C to allow the two different reaction intermediates  $\text{HZnC}_2\text{H}_5$  and  $(\text{Zn}(\text{C}_2\text{H}_5)_2)_2$ . First, a reaction with only one mole of water was considered to estimate the most likely reaction product from each Zn-containing molecule.

Then additional reactions involving water were considered since the concentration of water is much higher than that of metal organic species.

## 5.4.2 Computational Reaction Pathways

### 5.4.2.1 Diethylzinc with water

Gas phase decomposition of  $\text{Zn}(\text{C}_2\text{H}_5)_2$  in a nitrogen carrier gas showed that 100% conversion did not occur under the 600 °C. To deposit ZnO at low temperature (e.g., polymer substrate), it is necessary to examine the hydrolysis of unreacted diethylzinc. Figure 5-7 shows a probable reaction pathway of diethylzinc attack by water. This pathway is based on geometry optimizations suggested by the selected model chemistry. Smith and Schlegel reported the reaction path using molecular orbital theory [Smi03], and the calculated reaction pathway shows very similar bond lengths and angles.

Diethylzinc is depicted in (1). It has a linear C-Zn-C structure and the atomic distance between Zn and C is 2.04 Å. The Wiberg bond index in the natural bond orbital (NBO) analysis indicated the most probable bond dissociation takes place between Zn and C atoms. When diethylzinc complex as with  $\text{H}_2\text{O}$  (2), the enthalpy is calculated to be 7 kcal/mol lower than the reactant. The Zn-C bond length slightly decreases to 1.96 Å and the linear arrangement of C-Zn-C changes to an angle of 166.11°. Since Zn has an atomic charge of +2 in diethylzinc, it attracts the lone electron pair of water to give a weak solvation effect that stabilizes the structure. Once water complexed with diehtylzinc, one of the water hydrogen atoms easily reacts with the nearby carbon. The transition state (3) shows a broad angle of 146.74° in the C-Zn-C arrangement with an elongated distance between the zinc and carbon atoms of 2.26 Å. On the other hand, the distance between the zinc and carbon atom shortens to 1.95 Å to eventually lead to a bond length of 1.92 Å as shown in structures (4) and (5). After detachment of  $\text{C}_2\text{H}_6$  from structure (4), the

first important reaction intermediate (5) is formed. Figure 5-8 schematically shows enthalpy changes of these reactions calculated using the B3LYP/6-311G(d) model chemistry.

#### 5.4.2.2 Ethyl Hydrido zinc with water

Unlike diethylzinc, the reaction intermediate ethyl hydrido zinc,  $\text{HZnC}_2\text{H}_5$ , undergoes two possible pathways with water (Figure 5-9). Water was assumed to attach to ethyl hydrido zinc in two ways, depending on the reactivity of the ethyl group or nearby hydrogen. The reaction enthalpies of structures (7) and (10) are approximately the same implying that  $\text{C}_2\text{H}_5$  rotational barrier energy is low. Therefore, it is considered that these structures as identical. Once water forms a weak coordinate covalent bond with zinc, two transition states of (8) and (11) can form with respect to where the hydrogen in water attacks. The hydrogen can first approach the ethyl group to release ethane as shown in (8) to yield hydrido hydroxozinc (9). This molecule has a much shorter Zn-O bond length, since the characteristic bond length has been changed from a coordinated covalent bond to a covalent bond with the release of ethane. On the other hand, structures (7) or (10) are same structure as (5) if the hydrogen in water approaches the hydrogen in ethyl hydrido zinc as shown in the structure (11). In Figure 5-9, two hydrogen atoms form a hydrogen molecule, which is readily released from structure (12). Therefore, the Zn-C distance in structure (12) decreases from 1.97 to 1.90. It is interesting to point out that diethylzinc and the first product from  $\beta$ -hydride elimination give the same reaction intermediate when they combine with water. The corresponding enthalpy changes are represented in Figure 5-10. Comparing the two enthalpies in Figures 5-8 and 5-10, it is obvious that the ethyl hydrido zinc group needs the lower Gibb's energy (7 kcal/mol) to become structure (5) as apposed to diethylzinc.

#### 5.4.2.3 Dimer with water

The dimer of monoethylzinc is shown as structure (13) in Figure 5-11. The Zn-C bond is longer than that of structure (1) and free rotation of ethyl groups is expected since the two

carbons are separated by a large distance, (i.e. 6.28 Å). A molecule of water can approach the zinc atom and, as a result, the C-Zn-Zn angle slightly bends to 158.25° as shown in (16). Then one hydrogen atom approaches the near atom (C or the other Zn). If it approaches carbon, then it undergoes the transition state of structure (14) to release an ethane molecule and form structure (15). This molecule can also react with another water molecule to form a Zn(OH)<sub>2</sub>, which may play a role in formation of ZnO. There is a more favorable reaction pathway, however, instead of (16) to (14). In structure (16), one hydrogen atom in water can react with the nearest Zn atom to form structure (17). The O-Zn bond length decreases due to the formation of a stronger bond, and the distance between the two Zn atoms increases from 2.42 Å to 3.26 Å. This reaction path is favorable by ~ 5 kcal/mol less than the previous path (Figure 5-12). Undergoing a transition state (17), this molecule is divided into molecules (5) and (6). Coincidentally the same structure (5) appears in this reaction path. Moreover, the other product structure, (6), can also react with water to form structure (5) as explained earlier.

Three cases were presented above to illustrate how complex gas-phase pathway for reacting DEZn with water. Each pathway includes ethyl hydroxozinc as a reaction product. Of course this is not an exhaustive search and other pathways are possible. The atomic bond lengths and associated angles are summarized in the Table 5-6. Of course, more than one molecule of water can participate in the reaction with diethylzinc or intermediates. As an example, the farther reaction of structure (5) with water is more energetically favorable (Figure 5-13). It is also noted that, besides the presence of three Zn-containing molecules, it is anticipated H<sub>2</sub>Zn molecule is also present in the gas phase due to a sequence of β-hydride eliminations. This molecule, however, was not considered in this study since this reaction product is predicted to be thermodynamically stable at only temperature over 650 °C. Again in this study the reaction

temperature is assumed to be lower than 600 °C since a number of novel substrates (suitable for transparent displays) requires a relatively low temperature deposition process. Although,  $\text{H}_2\text{Zn}$  exists in the gas phase with water, it is obvious that this molecule will follow a similar reaction pathway to produce the same product (Figure 5-13).

Comparing adsorbed ethyl hydroxozinc and dihydroxozinc, ethyl hydroxozinc is expected to be more reactive than dihydroxozinc. This is due to the  $\text{C}_1$  symmetry of ethyl hydroxozinc and the fact that dihydroxozinc belongs to the  $\text{C}_{2h}$  point group. As a result, it is predicted that the dipole moment of ethyl hydroxozinc is great and this produces stronger physisorption bonding energy to the surface. Dihydroxozinc, however, has two OH groups and because of the strong reactivity of this functional group (lone electron pairs), this molecule is more likely to chemisorb on the surface where dangling bonds are present. Therefore, it is interesting to compare their reactivity from the viewpoint of film formation. Reaction pathways to form a solid structure are next examined assuming there are no other molecules present except dihydroxozinc.

### 5.4.3 Zinc Oxide Film Deposition

Dihydroxozinc,  $\text{Zn}(\text{OH})_2$  (Figure 5-13), is believed to be central to film formation. To study surface reactions, it is interesting to follow how this molecule assembles with other molecules on the substrate surface.

ZnO film has a Wurtzite structure with lattice parameters of  $a=3.250$  and  $c=5.207$  Å. Assuming that dihydroxozinc is present near the surface; it is interesting to examine the rate of its dimer in the formation of the Wurtzite structure. Previously reported ZnO initial structures,  $\text{Zn}_2\text{O}_2$ ,  $\text{Zn}_3\text{O}_3$ , and  $\text{Zn}_4\text{O}_4$  complexes are two-dimensional, but additional Zn and O atoms make solid ZnO structures in three-dimensional complexes [Mat02, Beh94]. Moreover, certain structures were more stable for a given number of atoms. Therefore, dimerizations of two or

three hydroxozinc were calculated with the same computational model chemistry, B3LYP/6-311G(d). Figure 5-14 shows the calculated enthalpy changes when two or three monomers of dihydroxozinc are assembled. Note that this calculation assumes that other molecules are absent.

Primarily pathway (a) represents the dimerization of two dihydroxozinc molecules. Two zinc and two oxygen atoms form a ring structure due to weak solvation effects from the unpaired electrons in oxygen. As a consequence, the calculated distances between the Zn and O atoms in dihydroxozinc elongate slightly from 1.76 to 1.79 Å. The Zn-O bond lengths are not identical in the ring (1.91 and 1.95 Å) since one bond is connected in a coordinated covalent bond and the other bond is formed primarily from electrostatic interactions between Zn and O atoms. This molecule was then allowed to add another  $(\text{Zn}(\text{OH})_2)_2$  molecule to form structure (21) or (23). The distance of a dangling branch from the cubic structure (i.e. distance between Zn and O) is elongated again to 1.80 Å and the bond lengths in the cubic structures are increased to 2.02 and 2.04 Å. Analyzing the (21) structure, the difference in bond length in the cubic segment is reduced since each atom of Zn or O is interacting with 3 neighboring atoms. Therefore the energy is dispersed the three directions. Near the substrate surface, it is predicted that any structure in Figure 5-14 can react with the absorption site to initiate film growth and continue to self-assembly reactions. This dimerization, however, does not explain formation of the Wurtzite structure.

On the other hand, ring formation with 3 monomers of dihydroxozinc has a lower enthalpy (-49.2 vs -87.9 kcal/mol). Figure 5-14 (b) shows this assembly. Although other structures can form from 3 monomers, this ring is reported to have an energy at a global minimum. The Zn-O bond length increase in dangle branches has the same pattern shown in pathway in (a). As trimerization proceeds, the bond length elongates. The Zn-O length in the ring is longer than that

of the dimer shown in (a). The second structure (21) is two-dimensional; however, as dimerization continues the products are three-dimensional as shown in structure (22) and (23). Structure (23) has two layers of the second molecule, and three Zn atoms in the first layer make bonds with three O atoms in the second layer or vice versa. The bond length between the two layers is 2.18 Å and the Zn-O bond length in the upper layer or lower layer is slightly elongated relative to structure (22). This pattern in bond elongation increases as dimerization continues. Therefore, it is predicted that the Wurtzite structure showed have a longer Zn-O bond length by a crystal. The experimentally reported lattice parameters are a: 3.250 and c: 5.207. In fact, Behrman reported that the ZnO cluster has the stable spheroid structure when the numbers of Zn and O atoms is greater than 11 [Beh94]. Therefore, more calculations with increased numbers of Zn and O atoms will give closer values to the experimentally measured bond lengths.

Table 5-7 shows the Gibbs energy change for the reactions given in Figure 5-14 at 600 °C along with the standard state enthalpy change at 25 °C. The negative signs in the free energy changes indicate that those reactions are spontaneous and the values further indicate that trimerization is more favorable than dimerization. Both pathways, however, are spontaneous. The free energy changes give a clue as to which reactions occur during MOCVD. In reaction (18)→(19), the free energy is negative, which implies that the reaction path is stable. Other steps can be explained by the location of where this reaction is carried out: gas phase or along the surface. The positive Gibbs energies indicated that dimerizations of (21) → (22) and (22) → (23) do not really occur in gas phase; however, there is a possibility that these reactions occur on the surface: Once the structure of (21) is formed, which has a more stable pathway than (18) → (19), this (21) molecule undergoes dimerization on the surface to form the (23) Wurtzite structure. If structure (18) or (21) comes into contact with the surface, surface reactions would

encourage dimerization due to the lower heterogeneous activation energies as compared to the homogenous activation energies present in gas phase reactions. Therefore, solid state ZnO film formation is explained by trimerization in the gas phase and additional dimerizations on the substrate surface.

It is interesting to compare the dipole moments of the various species. Dimerization ((18)  $\rightarrow$  (19)) or trimerization ((18)  $\rightarrow$  (21)) are thermodynamically spontaneous and the dipole moment increases but more dramatically for the trimer. In the case of the second reaction step in dimerization ((19)  $\rightarrow$  (20)) the dipole moment decreases because the molecule loses its symmetric plane and lies three dimensional space, which is a more symmetrical structure. A large dipole moment increases the adsorption bonding energy to a MOCVD substrate depending on its polycrystallinity. Therefore, the larger increase in the dipole moment for the trimerization reaction increases the deposition rate of the absorbed species compared to the dimer. Additionally a larger dipole moment in structures (22) and (23) will attract gas phase molecules to increase collision cross-section and likely increases the rate of dimerization. One more interesting feature of this structure is that the dangling branches outside of the hexagonal structure can form additional sections of the Wurtzite structure to minimize of the structure's electronic energy.

In summary, molecular reaction studies of three different Zn-containing reactants (i.e.,  $\text{Zn}(\text{C}_2\text{H}_5)_2$ ,  $\text{HZnC}_2\text{H}_5$ , and  $(\text{Zn}(\text{C}_2\text{H}_5)_2)_2$ ) with water have been covered out. The B3LYP/6-311G(d) model chemistry was employed to optimize molecular structures and calculate transition states. These three molecules were reacted with one molecule of water and each underwent a similar reaction pathway to become or release ethyl hydrido zinc,  $\text{ZnC}_2\text{H}_5\text{OH}$ . Subsequent reaction with an additional water molecule produced dihydrido zinc,  $\text{Zn}(\text{OH})_2$ .



Therefore, this molecule is considered to important in the formation of the Wurtzite structure ZnO thin films. To better understand deposition pathways, self-assembly reactions on a substrate were investigated. Ring formation of three monomers was more likely to occur than dimerization for Wurtzite structure. The ring shaped molecule,  $(\text{Zn}(\text{OH})_2)_3$ , is expected to form after repeated dimerization.

### 5.5 Reaction Intermediate Identification from the Diethylzinc/Water System

Important experiments probing the decompositions of DEZn with Raman spectroscopy revealed the decomposition products ( $\text{ZnH}_2$ ,  $(\text{Zn}(\text{C}_2\text{H}_5)_2)$ ). Based on these observed species, computational calculations were performed to evaluate likely reaction pathways between the Zn-containing species and water. These calculations suggest that dihydroxozinc likely forms near the heated substrate. Thus, experiments were conducted to detect this species. In the experiment, 0.1 mol% of diethylzinc was diluted in a  $\text{N}_2$  carrier gas and introduced through the center line of the MOCVD reactor. In this experiment, an equal amount of water (0.1 mol%) was also introduced into the same gas inlet. The two different gases were mixed just prior to the reactor inlet. The other gas inlets, annular and sweep inlets, contained only carrier gas. The reaction was brought to steady state and the centerline was probed by Raman in search of the reaction intermediates. It is noted that both axial and transverse diffusion occur along the centerline in addition to homogenous reaction. The flow velocities were matched to avoid recirculation flows. Figure 5-15 shows the Raman spectra in the ranges of the expected peak for each chemical. The upper spectrum shows two distinguishable Raman peaks of water, including the OH bending and OH symmetrical vibrational motions. The values for each motion are in reasonable agreement with the reported values, indicating appropriate operating conditions and accurate calibration of the measuring devices. The lower spectrum is that expected for diethylzinc (including  $\text{CH}_2$  and  $\text{CH}_3$  stretches) along with the Zn-C stretch. In the figure, it can be noted that  $1556$  and  $3656\text{ cm}^{-1}$

frequencies were contributed by water and the 480, 2900, and 2952  $\text{cm}^{-1}$  frequencies were supplied from diethylzinc.

Several unassigned peaks were detected by Raman scattering as shown in Figure 5-16, which was taken at a possible range of calculated intermediates shown in section 5.4 below the heated substrate (600  $^{\circ}\text{C}$ ). Four dominant peaks were found in the range 290 to 420  $\text{cm}^{-1}$  and one strong peak was observed at 1579  $\text{cm}^{-1}$ . The temperature denoted on each spectrum was estimated the simulated from temperature results based on the distance from the heater to the observation point ( $\sim 7.5$  mm).

First, there are three dominant peaks near the substrate, which began to appear at around 300  $^{\circ}\text{C}$ . A formed peak was detected at 311  $\text{cm}^{-1}$ , but only at the position with an estimated temperature of 315  $^{\circ}\text{C}$ . Although the signal for these peaks was low, they provide indirect evidence of the reaction pathways. Figure 5-17 shows possible peak assignments for detected species calculated based on the B3LYP/6-311G(d) model chemistry. The first peak at 280  $\text{cm}^{-1}$  can be assigned as OH bending motion (Figure 5-17). This molecule is the probable reaction product from all three different reaction pathways shown in Figures 5-7, 5-9, and 5-11. The notable difference is that an additional reaction with water is considered in Figure 5-17. The second peak at 288  $\text{cm}^{-1}$  may be assigned to either one of two molecules. One is the asymmetrical OH bending and stretching when water is reacted with the reaction product from dimerization of two monoethylzinc molecules (Figure 5-11). This peak might be also assigned to the C-Zn-C bending mode in diethylzinc when two more water molecules are associated. These results suggest that the reactions illustrated in Figures 5-11 or 5-7 are possibly represented. The peak at 295  $\text{cm}^{-1}$  can be assigned to the symmetrical OH vibrational stretch of water in a dimer product. This molecule is the same as previously stated but the motion is different. The

other possibility is the Zn-O-H symmetrical bending motion as shown the case (3) in Figure 5-17. Finally, the peak at  $311\text{ cm}^{-1}$  can be assigned to Zn-C molecular vibrational motion, which can be from a fragment from any unstable molecule. Another possibility is the C-H vibrational stretching motion in  $\text{C}_2\text{H}_6$ . The calculation considered dihydroxozinc molecule with two  $\text{C}_2\text{H}_6$  (case (4)). These results support the reaction step shown in Figure 5-9.

Of course, there may be other pathways to explain the observed spectra. Unfortunately, the relative Raman cross-section of diethylzinc is too low for quantitative results. Therefore, reaction intermediates may also have small cross-sections. This likely explains the difficulty of detection and therefore direct revealing the reaction pathways. There is another peak at  $1579\text{ cm}^{-1}$  (Figure 5-16). Because this peak is intense relative to other peaks, it is unlikely related to Zn-based species and may be related to a stable hydrocarbon, such as benzene ( $1580\text{ cm}^{-1}$ ). This species, however, has never been reported in this system. The peak may represent an O-containing stable molecule. Due to the lack of sufficient information, the peak was not assumed to a species.

## 5.6 Surface Adsorption

Besides the application of computational calculations to gas-phase thermodynamics, used to determine rate and equilibrium constants, the calculation can also give physical and chemical insight in regards to the surface. Of course the best way to examine the substrate surface would be experimentally confirming theoretical calculations. However, it is true that not too many methods have been developed to evaluate surface science and it is expected that quantum calculations combined with statistical thermodynamics will help in understanding MOCVD of thin film formation.

As an example, ZnO film formation can be considered in a MOCVD reactor. The detailed decomposition kinetics and reaction pathways are introduced in Chapter 6. In the diethylzinc

and water chemical system, dihydroxozinc( $\text{Zn}(\text{OH})_2$ ) molecules are mostly considered as abundantly present on the substrate surface. Therefore, it is interesting to take note of the detailed adsorption phenomena.

### 5.6.1 System Description

With an assumption of an ideal gas, dihydroxo zinc molecules are presented in a volume  $V$  at the initial concentration  $N$  (initially). This gas is exposed to a clean surface, with no particles bound to the surface (initially). Both the surface and the gas are free to exchange energy at a substrate temperature,  $T$ . The surface has  $M$  distinguishable non-interacting sites, which can bind a gas molecule by a *van der Waals* interaction. The gas bounds as a harmonic oscillator on the surface. A grand canonical ensemble describes the whole system, including the following conditions.

$$\sum a_{N_j} = A \quad (5-6)$$

$$\sum a_{N_j} \cdot E_{N_j} = E \quad (5-7)$$

$$\sum a_{N_j} \cdot N = N \quad (5-8)$$

Therefore a total number of particles and energies in the system is conserved. For fixed  $N$  particles in the system, the grand canonical ensemble can be written as (5-9), where  $u$  is chemical potential.

$$\begin{aligned} \Xi(T, V, u) &= \sum_N \sum_j e^{-\beta E_{N_j}(V)} e^{\frac{u}{kT} N} \\ &= \sum_N Q(T, V, u) e^{\frac{u}{kT} N} \end{aligned} \quad (5-9)$$

Introducing absolute activity,  $\ln \lambda = \frac{u}{kT}$ , Equation 5-9 becomes quite simple.

$$\begin{aligned}
\Xi(T, V, u) &= \sum_N \sum_{\{n_k\}} e^{-\beta \sum n_k \varepsilon_k} \lambda^N \\
&= \sum_{N=0}^{\infty} \sum_{\{n_k\}} e^{-\beta \sum n_k \varepsilon_k} \lambda^{\sum n_k} \\
&= \sum_{N=0}^{\infty} \sum_{\{n_k\}} \prod_k (e^{-\beta \varepsilon_k} \cdot \lambda)^{n_k} \\
&= \sum_{n_1=0}^{n_{1,\max}} \sum_{n_2=0}^{n_{2,\max}} \sum_{n_3=0}^{n_{3,\max}} \cdots \prod_k (e^{-\beta \varepsilon_k} \cdot \lambda)^{n_k} \\
&= \sum_{n_k=0}^{n_{k,\max}} \prod_k (\lambda \cdot e^{-\beta \varepsilon_k})^{n_k}
\end{aligned} \tag{5-10}$$

For fermions,  $n_k$  can be 0 or 1 which makes Equation 5-10 more simple form in Equation 5-11

$$\begin{aligned}
\Xi(T, V, u) &= \prod_k [(\lambda \cdot e^{-\beta \varepsilon_k})^0 + (\lambda \cdot e^{-\beta \varepsilon_k})^1] \\
&= \prod_k (1 + \lambda \cdot e^{-\beta \varepsilon_k})
\end{aligned} \tag{5-11}$$

Equation 5-11 has a Fermi-Dirac statistic distribution.

### 5.6.2 Statistics for Unbound (Ideal Gas) and Bound (Fermi-Dirac Statistics) Molecules

The partition function of an indistinguishable ideal gas (Equation 5-12) is expressed with its translational motion.

$$Q = \frac{1}{N!} \left( \frac{2\pi m k_B T}{h^2} \right)^{\frac{3}{2}N} \cdot V^N \tag{5-12}$$

Activation energy is determined primarily by the energy required to break the bond of the leaving group. The complex accumulates enough energy to completely break the M-X bond, leaving an intermediate; in turn this intermediate reacts with Y (which could be solvent) from the second coordination sphere.

$$\begin{aligned}
\Xi &= \sum_N Q e^{-rN} \\
&= \sum_N \frac{1}{N!} \left( \left( \frac{2\pi m k_B T}{h^2} \right)^{\frac{3}{2}} \cdot V^N \right) e^{-rN} \\
&= \sum_N \frac{1}{N!} \left( \left( \frac{2\pi m k_B T}{h^2} \right)^{\frac{3}{2}} \cdot V e^{-r} \right)^N
\end{aligned} \tag{5-13}$$

This canonical ensemble can be evaluated using integral relation of  $\sum_{m=0}^{\infty} \frac{a^m t^m}{m!} = e^{at}$  therefore;

$$\ln \Xi = \left( \frac{2\pi m k_B T}{h^2} \right)^{\frac{3}{2}} V e^{-r} \tag{5-14}$$

Bound molecules are described in Fermi statistics in Equation 5-11, and for  $M$  molecules all energies should be summed over its harmonic oscillator states.

$$\ln \Xi = M \left( 1 + \sum_{\epsilon_k} e^{-\beta(\epsilon_k - \mu)} \right) \tag{5-15}$$

where the relationship between the chemical activity and potential,  $\ln \lambda = \frac{u}{kT}$ , was used.

### 5.6.3 Equilibrium Analysis

Average number of molecules in gas phase and bound states can be obtained using partition functions given in Equations 5-14 and 5-15.

#### a. Unbound molecules

$$\langle N_{ub} \rangle = kT \left( \frac{\partial \ln \Xi}{\partial u} \right)_{v, T} = \left( \frac{2\pi m k_B T}{h^2} \right)^{\frac{3}{2}} V e^{\frac{u}{kT}} \tag{5-16}$$

#### b. Bound molecules

$$\langle N_b \rangle = kT \left( \frac{\partial \ln \Xi}{\partial u} \right)_{v, T} = kT \cdot M \frac{\frac{1}{kT} \sum_{\epsilon_k} e^{-\beta(\epsilon_k - \mu)}}{1 + \sum_{\epsilon_k} e^{-\beta(\epsilon_k - \mu)}} = M \frac{1}{\sum_{\epsilon_k} e^{\beta(\epsilon_k - \mu)} + 1} \tag{5-17}$$

At the equilibrium state, the adsorption rate and desorption rate are equivalent thus making the chemical potentials of unbound particles and bound molecules also equivalent. In order to apply this equivalency, Equation 5-17 can be modified as follows,

$$\sum_{\varepsilon_k} e^{\beta(\varepsilon_k - \mu)} + 1 = \frac{M}{\langle N_b \rangle} \quad (5-18)$$

Also noting the surface has a greater number of sites than bound particles,  $M \geq \langle N_b \rangle$ , this equation can be further simplified.

$$\sum_{\varepsilon_k} e^{\beta(\varepsilon_k - \mu)} = \frac{M}{\langle N_b \rangle} \quad (5-19)$$

Therefore,  $e^{\beta\mu} = \frac{\langle N_b \rangle}{M} \sum_{\varepsilon_k} e^{\beta\varepsilon_k}$  and applying into (5-16) and finally the ratio of two states can be rearranged.

$$\frac{\langle N_{ub} \rangle}{\langle N_b \rangle} = \left( \frac{2\pi m k_B T}{h^2} \right)^{\frac{3}{2}} \frac{V}{M} \sum_{\varepsilon_k} e^{\beta\varepsilon_k} = \left( \frac{2\pi m k_B T}{h^2} \right)^{\frac{3}{2}} \frac{1}{\rho_s} \sum_{\varepsilon_k} e^{\beta\varepsilon_k} \quad (5-20)$$

The fraction of bound particles on the surface is

$$\begin{aligned} \frac{\langle N_b \rangle}{N} &= \frac{\langle N_b \rangle}{\langle N_{ub} \rangle + \langle N_b \rangle} \\ &= \frac{1}{1 + \frac{\langle N_{ub} \rangle}{\langle N_b \rangle}} \\ &= \frac{1}{1 + \left( \frac{2\pi m k_B T}{h^2} \right)^{\frac{3}{2}} \frac{1}{\rho_s} \sum_{\varepsilon_k} e^{\beta\varepsilon_k}} \end{aligned} \quad (5-21)$$

### 5.6.4 Vibrational Energy Calculations

The most probable molecule that exists near the substrate surface is dihydroxozinc ( $\text{Zn}(\text{OH})_2$ ). When one mole of dihydroxozinc is adsorbed on the substrate (i.e. Si surface) two different adsorption characteristics can be initially estimated (Figure 5-18). It is obvious the Zn

metal atom ( $-3d^{10}4s^2$ ) has greater likelihood to adhere to the surface, since it involves p and d hybrid orbitals. It is shown as (a) in Figure 5-18. Moreover, case (b) can be estimated due to the oxygen atom having unpaired electrons and, in fact, this causes a strong bond formation. However, adsorption with hydrogen was not considered because it would bring about results that will be explained after this analysis.

**a. Gas phase:** The frequency calculations were carried out based on an optimized structure with the model chemistry of B3LYP/6-311G(d). Dihydroxozinc belongs to the  $C_{2h}$  point group; therefore, vibrational normal modes can be expressed with its irreducible representatives. Since there are five atoms, the vibrational degrees of freedom is 9. Table 5-8 shows the calculated properties including Raman-active or IR-active frequency values and their vibrational temperatures. Moreover, the mass and force constants are also listed.

**b. Bound state:** Unlike gas-phase calculation, the bound state is not easy to calculate since the computational calculation does not really include liquid or solid state calculations. However, the adsorption can be estimated with an understanding of the physical phenomena. Considering a silicon substrate, two possible adsorptions are shown in Figure 5-19. However, frequency calculations for *a* and *b* are not simple due to the consideration of solid state Si clusters. The cluster calculation requires an extensive calculation time due to the number of heavy atoms, such as Si, at the same time. So, the configuration of a cluster was too time consuming to be calculated. Therefore, an alternative calculation method was introduced in this study. In this study an observation was made on the frequency of chance that a Zn-Si bond would form with an increasing effective mass of a Si atom. For example, in case *a* one Si atom was arbitrarily added to a Zn atom in  $Zn(OH)_2$  and the vibrational frequency was examined using B3LYP/6-311G(d) model chemistry. Next, the mass of Si was arbitrarily increased to 50, 100, 200, and so forth.



Figure 5-19 shows the Zn-Si frequency change in the case of  $a$  and  $b$ , respectively. The Einstein model was used in the frequency estimation and the results were clear that the calculated frequencies converged to certain values of  $75\text{ cm}^{-1}$  and  $596\text{ cm}^{-1}$ .

As a result, Equation 5-21 was solvable; however, one variable - site density  $\rho_s$ , which is defined as  $M/V$  - was not determined. For the calculation, it turns out that the site density should be between  $10^{31} \sim 10^{34}$  for 1 mole of adsorbent ( $10^{23}$  number density) to satisfy the assumption,  $M \gg N$  and is depicted in Figure 5-20. In the case of  $10^{34}$  order of site density and at low temperature, almost all particles are in a bound state and as the temperature increases particles start to desorb to remain in the unbound gas state. However, the number of desorbed particles is not that large. In the case of  $10^{31}$  order of site density, it is noted that adsorption was not favorable. Therefore, as site density decreases, the number of adsorbed particles would be diminished as well. If  $600^\circ\text{C}$  is selected, for example, it is obvious how the ratio decreases.

However, it should be noted that  $\text{Zn}(\text{OH})_2$  can be adsorbed on the surface with different orientations or different structural forms. For example, there is a possibility that an H atom can play a role as an adsorption site. However, in this case, other surface reactions, such as molecular decomposition or migration will occur in order to compensate the Si-H bond formation. Moreover, it should be noted that there should be additional reaction intermediates beside  $\text{Zn}(\text{OH})_2$ . For example, a certain mole fraction of reactant, undecomposed  $\text{Zn}(\text{C}_2\text{H}_5)_2$ , or intermediates from decompositions,  $\text{HZnC}_2\text{H}_5$  or  $\bullet\text{ZnC}_2\text{H}_5$ , can exist near the surface and therefore, there are possibilities for various surface reactions. These surface reactions are, complicated and difficult to understand due to direct experimental observation tools not being readily available. Introducing a Si cluster model, which is mentioned before, can be a good candidate for observing surface reactions for specific adsorptive molecules. The  $\text{Si}_9\text{H}_{12}$  model is

depicted in Figure 5-21. This is a unit cell of a solid state substrate of Si (111) that has two dangling bonds on top.

According to the detailed mechanism,  $\text{HZnC}_2\text{H}_5$  is a product from  $\beta$ -hydride elimination and under a mild reaction temperature it is expected to exist near the substrate. Using the cluster, if  $\text{HZnC}_2\text{H}_5$  approaches the Si substrate (Figure 5-22), this molecule is actually not just adsorbed on the surface, but undergoes bond dissociation between Zn and H because of the H and Si cluster bond formation. As a result, adsorption can be examined using quantum calculations but it should be noted that not just molecular adsorption, molecular deformation or bond dissociation should be considered for a better understanding. Further frequency calculations for various possible molecules were terminated because of a lack of computer capacity.

## 5.7 Summary

ZnO is one of the most popular II-VI compound semiconductors in various electronic fields, such as light emitting devices, photodetectors, and lasers. Therefore, it is worthwhile to understand its formation kinetics in MOCVD reaction. As an example, the most popular chemical system of diethylzinc/water was chosen. First, decomposition kinetics of diethylzinc was revealed using in-situ Raman spectroscopy and supported by computational calculations. The energetic and kinetics research approaches suggested the most likely reaction pathways including the  $\beta$ -hydride elimination and homolytic fission between Zn-C bond. Furthermore, dimerization of two monoethylzinc molecules were detected as a reaction intermediate and it was the first time this molecule was reported as an intermediate. The computational calculation helped to assign peaks.

Secondly, the reaction pathways between Zn-containing molecules and water was suggested based on B3LYP/6-311G(d) model chemistry. The most reaction probable intermediate turned out to be dihydroxozinc, and trimerization of this molecule has plausible

reaction pathways to form the Wurtzite structure of ZnO film. Therefore, this molecule was considered as a key molecule to compose the film and experimental detection was attempted.

The detection experiments simulated with introducing diethylzinc and water to the centerline of the reactor. The molecules were mixed just before they went through the reactor inlet and in-situ Raman observation was examined. However, the direct evidence of dihydroxozinc was not possible because of a fast enough reaction speed and relatively low Raman cross-sections. However, some reaction intermediates were detected and from the computational study, an indirect interpretation was made possible in order to understand gas-phase reaction pathways.

The calculation also gives ideal conditions for surface adsorption. Based on the grand canonical ensemble, adsorption phenomena were described mathematically. The computational calculations used again to estimate adsorptive frequencies with assumptions of a harmonic oscillator and Born-Oppenheimer approximation. Then, adsorption of  $\text{Zn(OH)}_2$  was examined.

Table 5-1. Reported activation energy for the homogeneous dissociation of the first Zn-C bond of diethylzinc.

Activation Energy [kcal/mol]	Frequency Factor [s <sup>-1</sup> ]	Temperature [°C]	Analytical Method	Reference
50	10 <sup>9~10</sup>	396~489	Gas chromatography	Koski (1976)
52.4	-	270*	Mass spectroscopy	Jackson (1989)
56	-	280~520	Mass spectroscopy	Dumont (1992)
52	2×10 <sup>16</sup>	230~470	Mass spectroscopy using D <sub>2</sub>	Dumont (1993)

\*range not reported, only average measurement temperature.

Table 5-2. Calculated Raman shift (cm<sup>-1</sup>) of ν[Zn-C] and ν[Zn-H] for selected Zn-containing molecules.

	Zn(C <sub>2</sub> H <sub>5</sub> ) <sub>2</sub>	ZnC <sub>2</sub> H <sub>5</sub>	HZnC <sub>2</sub> H <sub>5</sub>	H <sub>2</sub> Zn
Calculation	486.00	313.13	666.49	1918.90

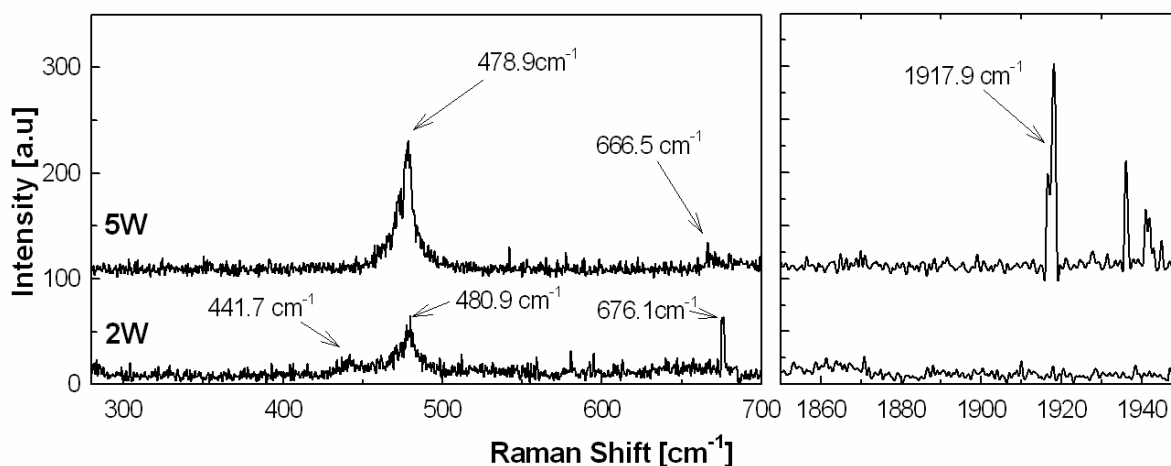


Figure 5-1. Laser induced Raman shifts of DEZn at room temperature. The lower spectrum was obtained at 1.3 W incident laser power and upper line was obtained at 3.3 W incident laser power.

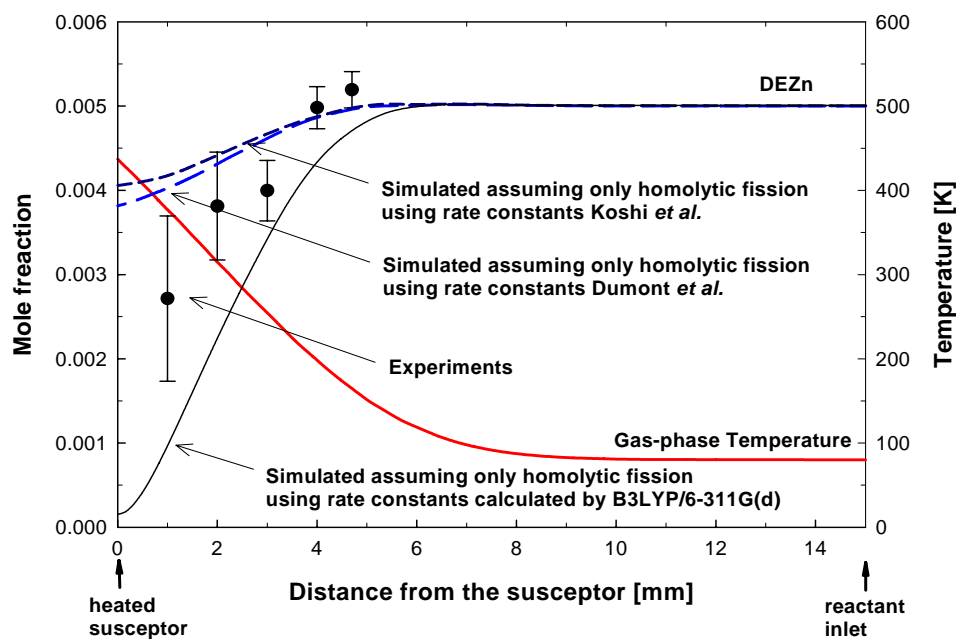


Figure 5-2. Measured DEZn centerline profile along with simulated profile assuming only homolytic fission using rate constants: ----, Koski *et al.*, — — —, Dumont *et al.* and solid line, computational calculation in this study. The simulated temperature profile is also shown.

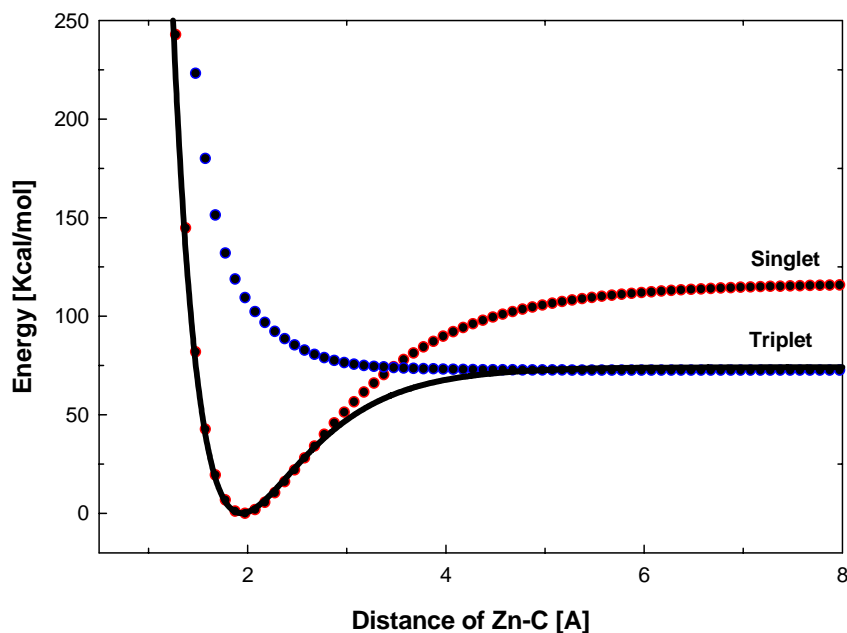


Figure 5-3. The potential energy surface for DEZn along the Zn-C bond length for two multiplicities. The solid line represents a Morse potential fit.

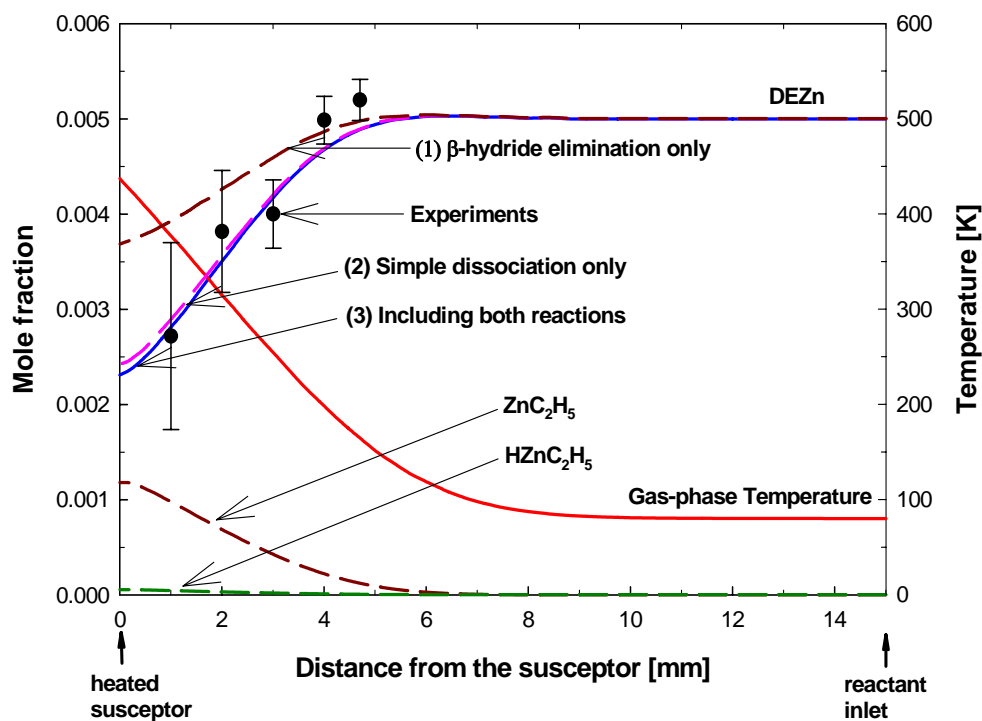


Figure 5-4. Comparison of measured DEZn centerline profile (symbol) to simulated profile assuming only  $\beta$ -hydride elimination (dash line(1)) or only homolysis (dash line(2)) using the rate constants shown in Table 5-3. The solid line includes both reactions. The computed profiles of  $\text{ZnC}_2\text{H}_5$  and  $\text{HZnC}_2\text{H}_5$  are also shown with both pathways included.

Table 5-3. Calculated reaction rate constants.

	$E_a$ [kcal/mol]	$A$ [ $\text{s}^{-1}$ ]
Homolytic dissociation	52.0	$2.40 \times 10^{17}$
$\beta$ -hydride elimination	47.24	$7.90 \times 10^{14}$

Table 5-4. Favorable reactions involving intermediates calculated from B3LYP/6-311G(d) model chemistry. Thermodynamic properties are derived from the same theory level.

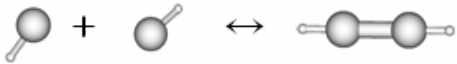
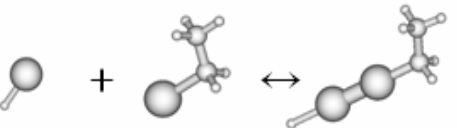
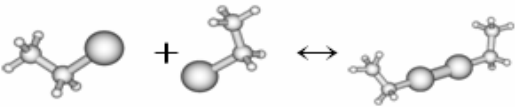
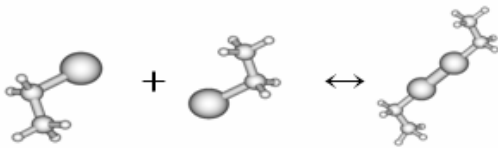
(1) $2\text{Zn-H} \leftrightarrow \text{Zn}_2\text{H}_2$		
		
Raman frequency [Zn-H]: 428.22 $\text{cm}^{-1}$		
	T(K)	$\Delta\text{H}(\text{kcal/mol})$ $\Delta\text{G}(\text{kcal/mol})$
	398.15	-31.05   -13.18
	498.15	-31.05   -8.69
	598.15	-31.03   -4.20
	698.15	-31.00   0.29
	798.15	-30.94   4.76
(2) $\text{HZn} + \text{ZnC}_2\text{H}_5 \leftrightarrow \text{HZnZnC}_2\text{H}_5$		
		
Raman frequency [Zn-H]: 434.50 $\text{cm}^{-1}$		
		$\Delta\text{H}$ $\Delta\text{G}$
	398.15	-35.50   -21.25
	498.15	-35.39   -17.68
	598.15	-35.25   -14.14
	698.15	-35.09   -10.62
	798.15	-34.90   -7.13
(3) $2\text{ZnC}_2\text{H}_5 \leftrightarrow (\text{ZnC}_2\text{H}_5)_2 : \text{cis}$		
		
Raman frequency [Zn-C]: 555.84, 1203.65 $\text{cm}^{-1}$		
		$\Delta\text{H}$ $\Delta\text{G}$
	398.15	-40.01   -25.48
	498.15	-39.75   -21.86
	598.15	-39.46   -18.29
	698.15	-39.14   -14.78
	798.15	-38.81   -11.31
(4) $2\text{ZnC}_2\text{H}_5 \leftrightarrow (\text{ZnC}_2\text{H}_5)_2 : \text{trans}$		
		
Raman frequency [Zn-C]: 555.84, 1203.65 $\text{cm}^{-1}$		
		$\Delta\text{H}$ $\Delta\text{G}$
	398.15	-40.01   -24.93
	498.15	-39.75   -21.18
	598.15	-39.46   -17.48
	698.15	-39.15   -13.82
	798.15	-38.82   -10.22

Table 5-5. Symmetrical Raman-active Zn-C stretching of Zn-containing intermediates and estimated Raman shifts (cm<sup>-1</sup>) with a scaling factor applied.

$\nu[\text{Zn-C}]$	$\text{Zn}(\text{C}_2\text{H}_5)_2$	$\text{ZnH}_2$	$\text{HZn-ZnC}_2\text{H}_5$	$(\text{ZnC}_2\text{H}_5)_2$
Calculation	486.0	428.2	434.5	1203.7
Experiment	480.0			
Scaling factor	0.986		→	
Corrected	480.0	428.2	428.4	1186.3

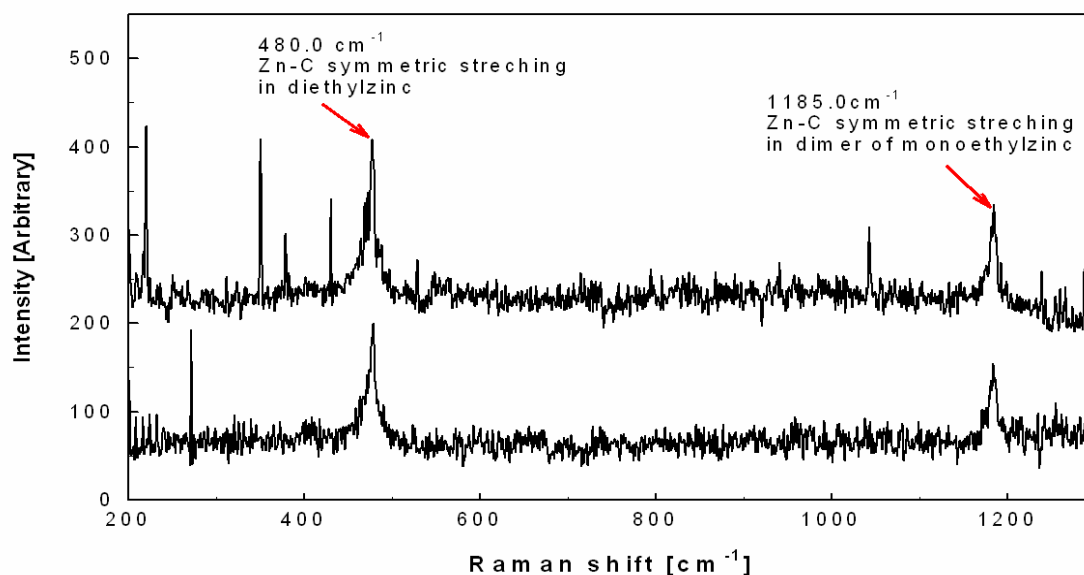


Figure 5-5. Raman spectra at two positions in the reactor (1 and 2 mm above the inlet) indicating presence  $(\text{ZnC}_2\text{H}_5)_2$ .

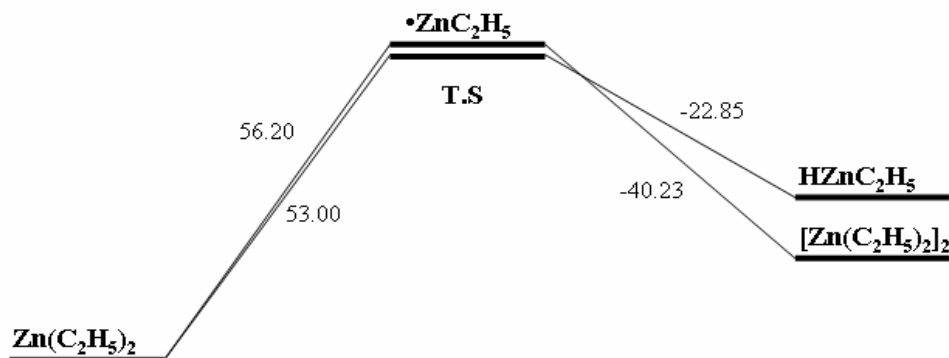


Figure 5-6. Schematic diagram of two suggested competing reactions with reaction enthalpies [kcal/mol] listed.



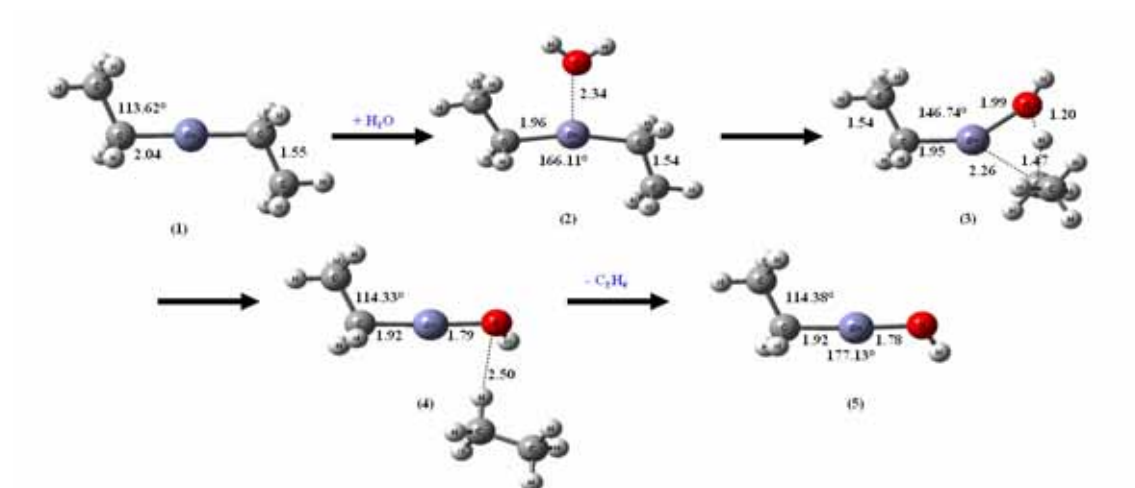


Figure 5-7. Possible reaction pathway of diethylzinc reaction with one mole of water.

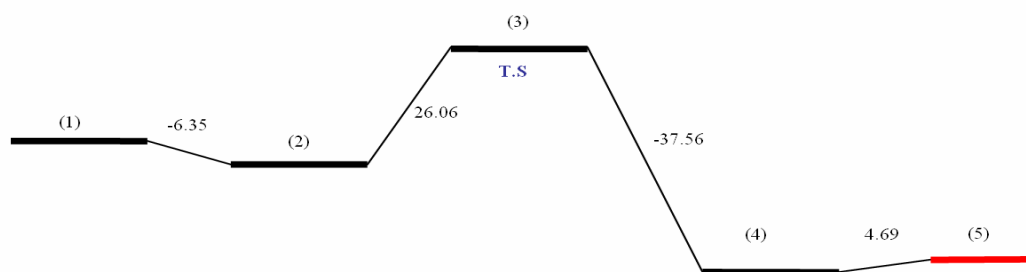


Figure 5-8. Enthalpy changes [kcal/mol] in reactions of diethylzinc and water represented in Fig. 5-7.

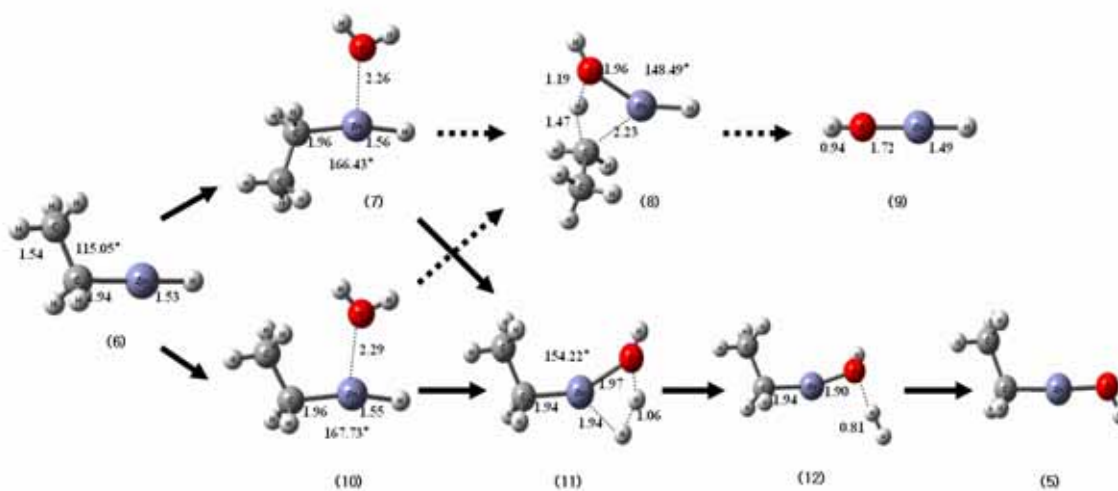


Figure 5-9. Likely reaction pathways of ethyl hydrido zinc with water. Dashed arrow indicate relatively unfavorable reaction pathway.

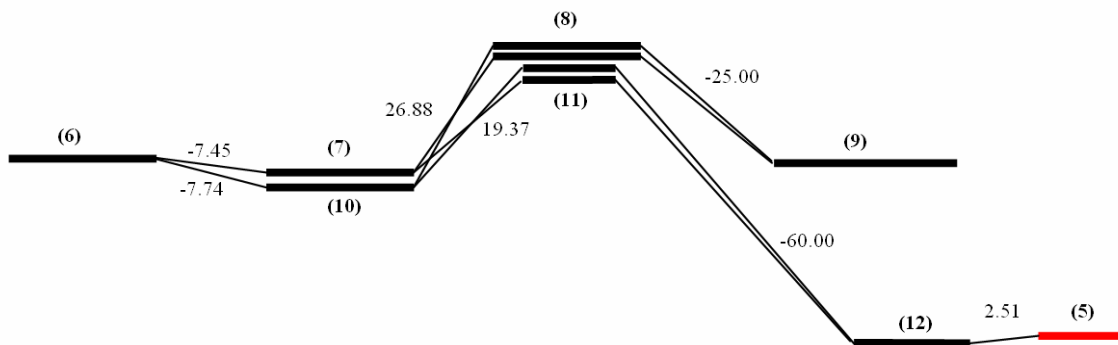


Figure 5-10. Enthalpy changes [kcal/mol] in reaction of ethyl hydridozone and water shown in Fig. 5-9.

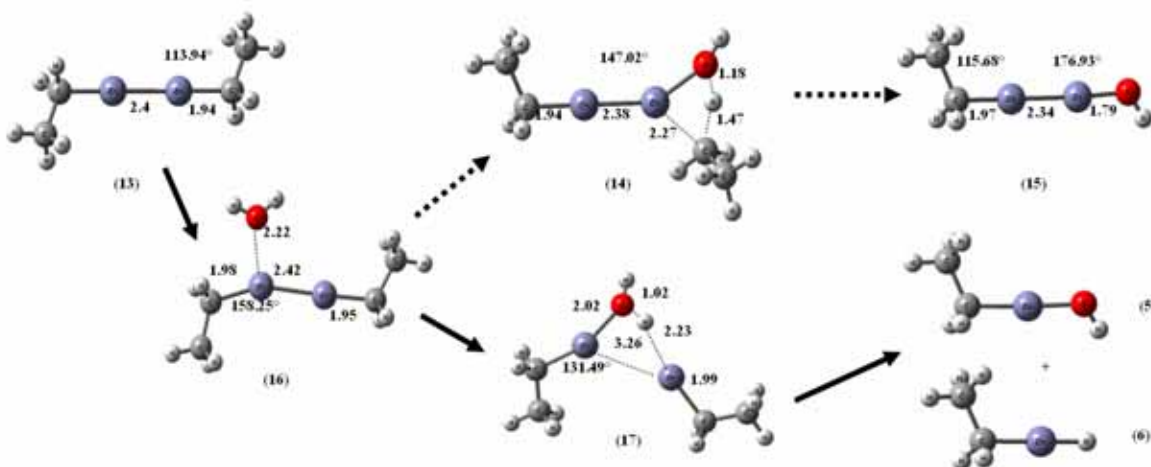


Figure 5-11. Likely reaction pathways of ethyl hydridozone with water. Dashed arrow indicate relatively unfavorable reaction pathway.

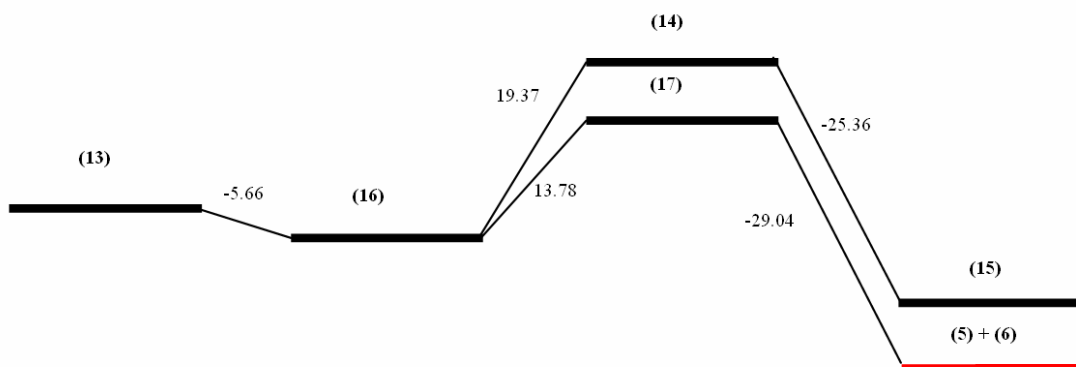


Figure 5-12. Enthalpy changes [kcal/mol] in reactions of ethyl hydridozone and water given in Fig. 5-11.

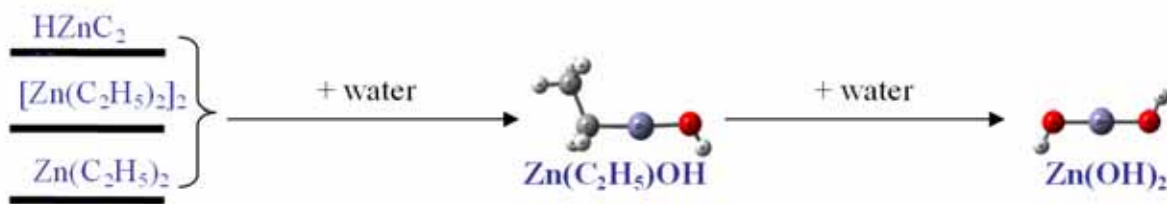


Figure 5-13. Proposed reaction pathways between three Zn-containing molecules and water.

Table 5-6. Structural information of reaction species shown in Figure 5-7, 9, and 11 calculated by B3LYP/6-311G(d) theory level.

Structure	Bond Length (Å)				Angle (°)
	Zn-O	Zn-C	Zn-H	Zn-Zn	
1	-	2.04	-	-	C-Zn-C: 180
2	2.34	1.96	-	-	C-Zn-C: 166
3	1.99	1.95	-	-	C-Zn-O: 147
4	1.79	1.92	-	-	C-Zn-O: 177
5	1.78	1.92	-	-	C-Zn-O: 177
6	-	1.94	1.53	-	C-Zn-H: 180
7	2.26	1.96	1.56	-	C-Zn-H: 166
8	1.96	2.23	1.53	-	O-Zn-H: 148
9	1.72	-	1.49	-	O-Zn-H: 179
10	2.29	1.96	1.55	-	C-Zn-H: 168
11	1.97	1.94	1.94	-	C-Zn-O: 154
12	1.90	1.94	-	-	C-Zn-O: 159
13	-	1.94	-	2.40	C-Zn-Zn: 180
14	1.99	1.94	-	2.38	C-Zn-Zn: 180
15	1.79	1.97	-	2.34	Zn-Zn-O: 177
16	2.22	1.98	-	2.42	C-Zn-Zn: 158
17	2.02	1.99	2.23	3.26	C-Zn-Zn: 131

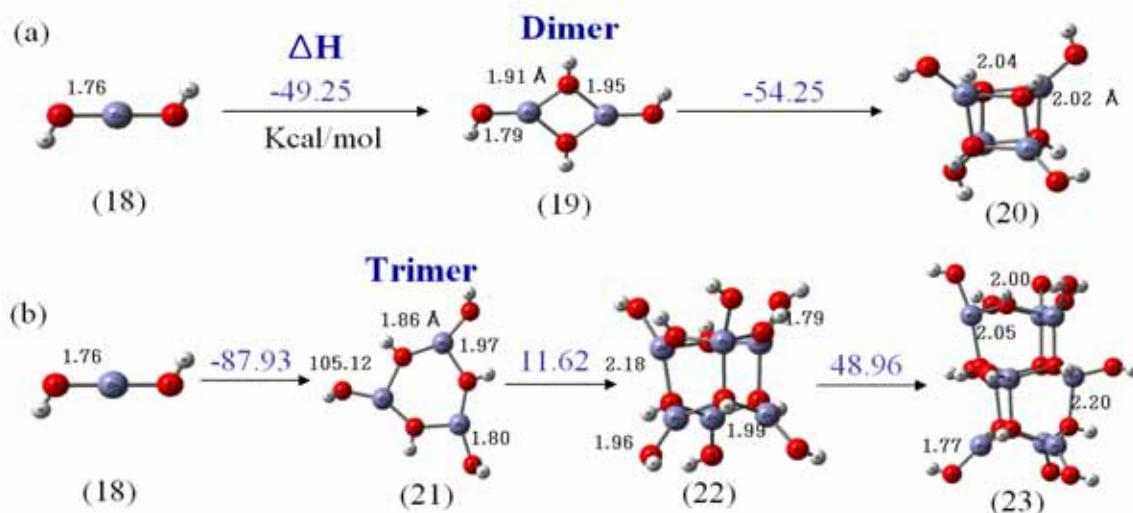


Figure 5-14. Proposed reaction pathways of dihydroxozinc (a) dimerization from two molecules and (b) trimerization from three molecules. In energetic comparison, trimerization reaction (b) is more likely feasible. However, this reaction seems not likely continuously happening in gas-phase but on solid surface.

Table 5-7. Gibbs energy and enthalpy of reactions shown in Figure 5-14 along with the computed dipole moments calculated by B3LYP/6-311G(d) theory model chemistry.

Reactions	$\Delta H_{298}$	$\Delta G_{898}$	Calculated dipole moment	
			(18)	0.00
(18)→(19)	-49.25	-15.99	(19)	0.19
(19)→(20)	-54.25	-12.73	(20)	0.02
(18)→(21)	-87.93	-24.56	(21)	3.90
(21)→(22)	11.62	94.35	(22)	8.87
(22)→(23)	48.96	137.83	(23)	26.51

Units:  $\Delta H_{298}$ ,  $\Delta G_{898}$  [kcal/mol] and dipole [Debye]

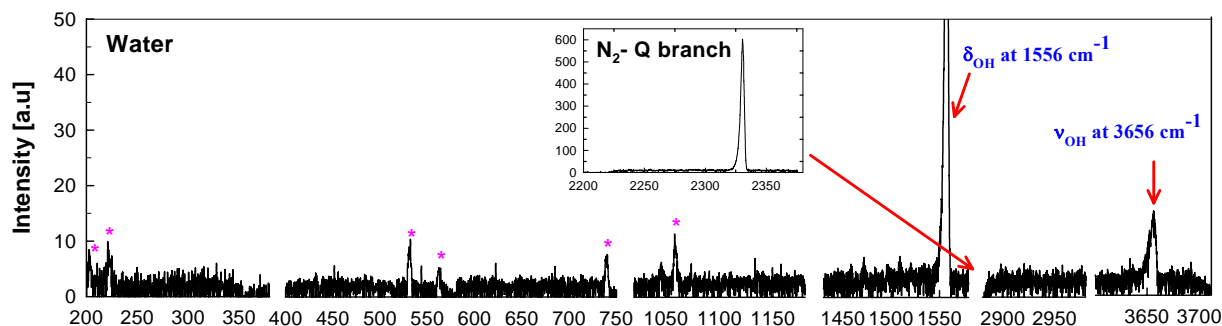


Figure 5-15. Measured Raman shifts for water (upper) and diethylzinc (lower). The peaks labeled with a star are plasma peaks from Ar<sup>+</sup> laser probe.

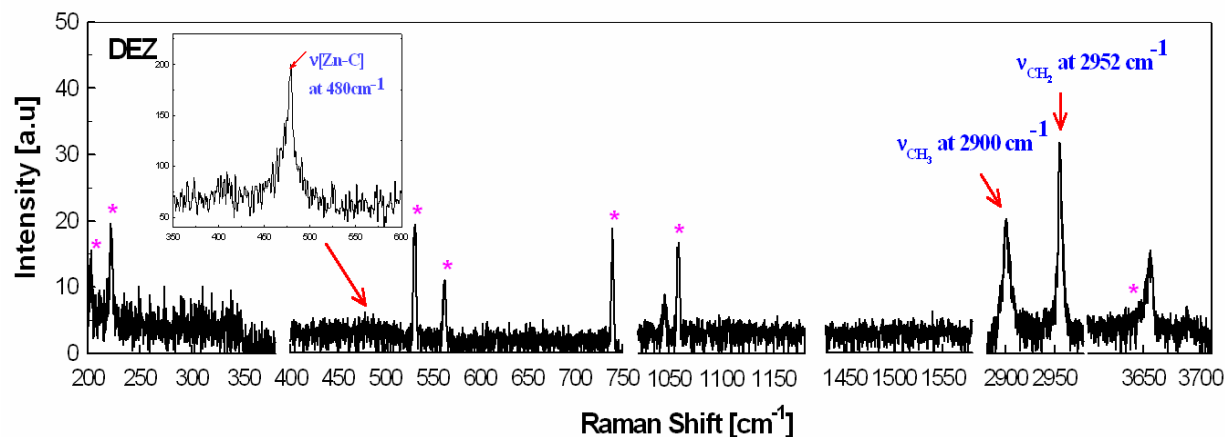


Figure 5-15. (Continued).

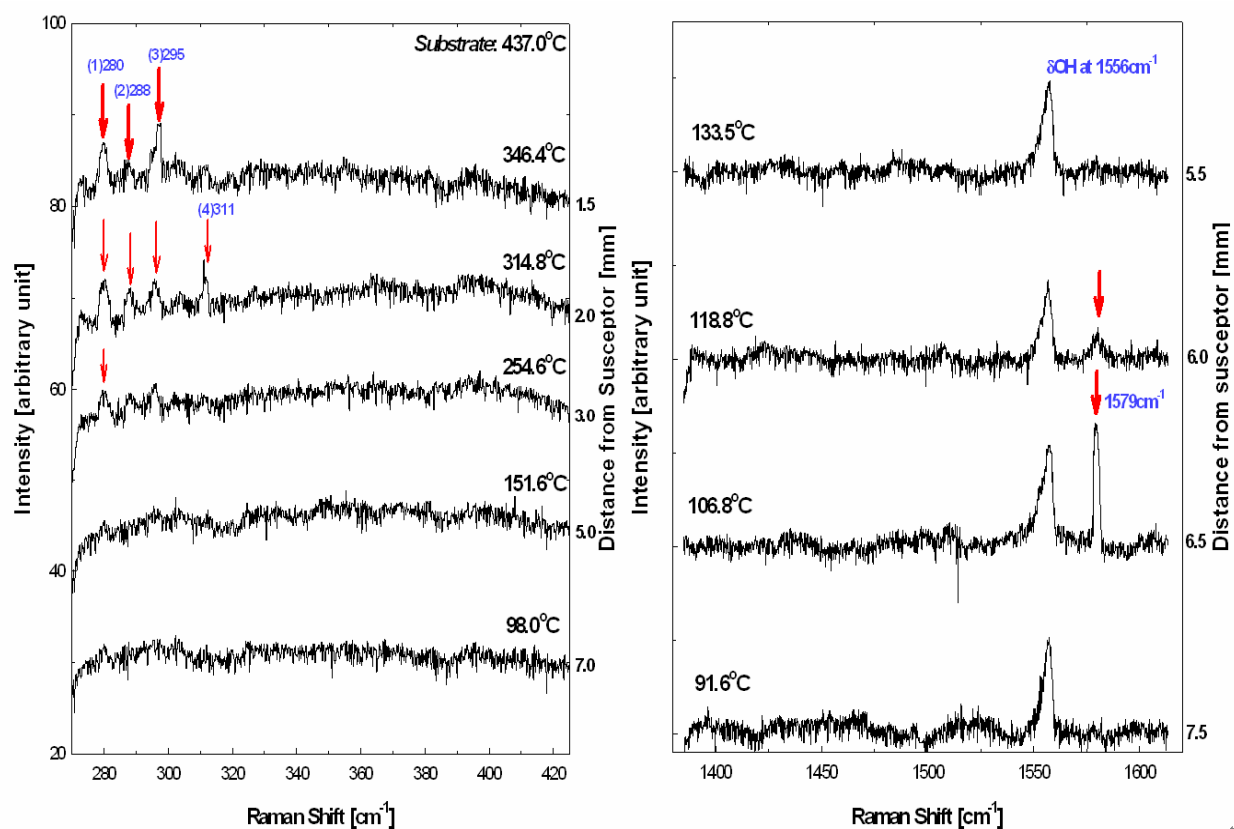


Figure 5-16. Raman spectra taken at various positions (temperatures) along the centerline of the reactor. The heater temperature was set at 600 °C.

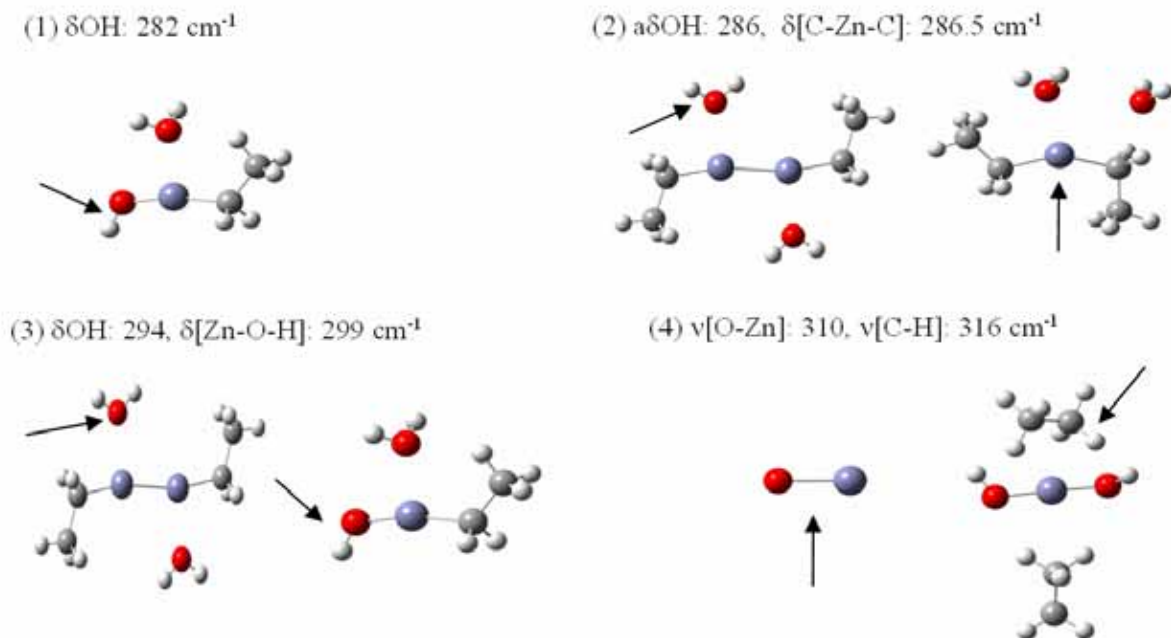


Figure 5-17. Possible peak assignments of the four detected peaks in Fig. 5-16.

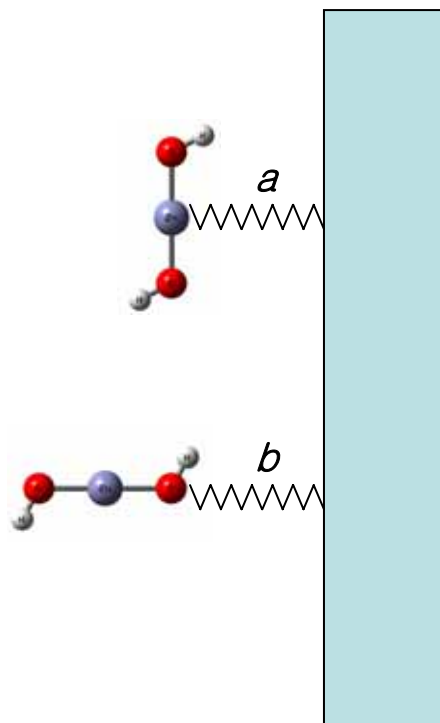


Figure 5-18 Two different adsorption mechanisms according to molecular orientation onto the surface. The first case, *a*, Zn atom was bound with a dangling bond on Si substrate; on the other hand, lone pair of oxygen participated in bond formation in the case of *b*. Harmonic oscillation was assumed in frequency estimations for both cases.

Table 5-8. Vibrational normal modes of dihydroxozinc. Each motion was assigned to proper irrepresentative of  $C_{2h}$  point group, and subsidiary information was obtained.

	1	2	3	4	5	6	7	8	9
Motion	Au	Bu	Au	Ag	Bu	Ag	Bu	Ag	Bu
Frequency	33.1	190.8	297.3	613.8	772.0	866.6	897.7	3851.1	3851.8
Mass	1.0668	6.2905	12.2014	12.7091	13.6403	1.0679	1.1506	1.0672	1.0669
k	0.0007	0.1349	0.2799	2.8212	4.7892	0.4725	0.5463	9.3250	9.3261
Vibrational Temperature	47.69	274.49	283.90	884.14	1110.67	1246.81	1291.63	5540.88	5541.85
IR Intensity	361.05	40.82	53.32	0	122.14	0	120.0	0	14.11
Raman Intensity	0	0	0	37.39	0	7.38	0	265.24	0

\*Harmonic frequencies ( $\text{cm}^{-1}$ ), Force constants ( $\text{mDyne/\AA}$ ), Vibrational temperature (K), IR intensities ( $\text{KM/Mole}$ ), Raman scattering activities ( $\text{\AA}^4/\text{AMU}$ ).

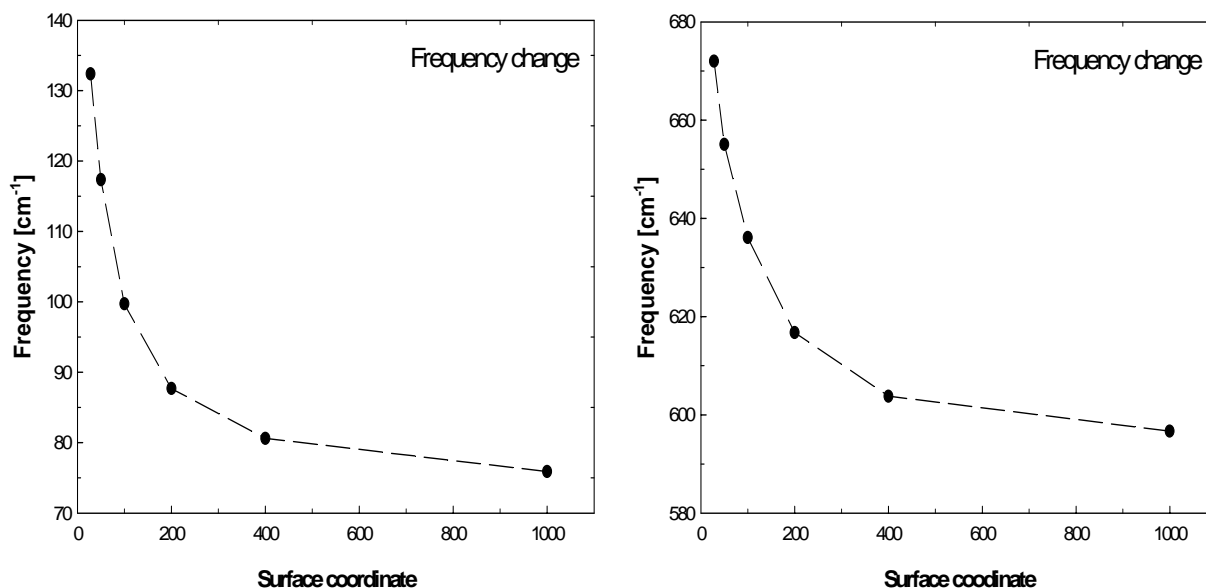


Figure 5-19. Zn-Si or O-Si vibrational frequency estimation (*a* and *b* motions in Fig 5-18). Structure optimization and frequency calculation were carried out using B3LYP/6-311G(d) model chemistry to keep the consistency. The mass of Si was arbitrary increased to realize the solid surface and it turned out that the vibrational motions converged to certain wavenumber of frequency.

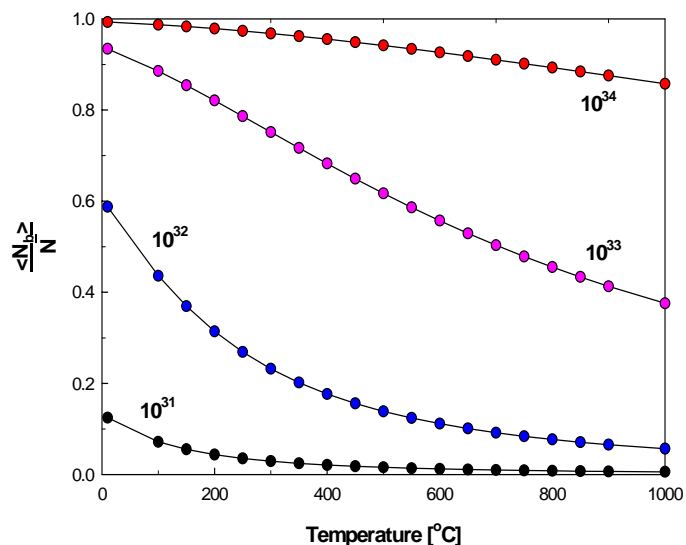


Figure 5-20. The adsorption behavior of dihydrozinc on Si surface. The adsorbed portion of gas molecules is a function of the site density, and it was examined from  $10^{31}$  to  $10^{34}$  with assumption of one mole of adsorbent ( $10^{23}$ ).

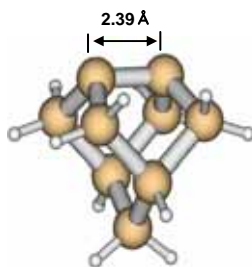


Figure 5-21. The  $\text{Si}_9\text{H}_{12}$  silicon substrate model. 12 H atoms were used for each Si atoms on second and third row to terminate the available bond formation and strong enough force constants in Si-H vibration were assumed to keep proper geometry. The geometry optimization was carried out using B3LYP/6-311G(d).

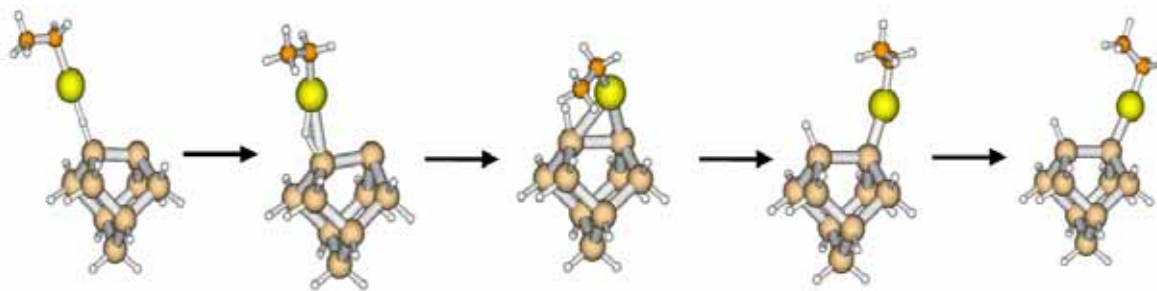


Figure 5-22.  $\text{HZnC}_2\text{H}_5$  adsorption on Si cluster. Due to strong interaction between Zn and Si, original Zn-H bond was broken and the fragment migrated to neighbor Si site.



## CHAPTER 6

### DIMETHYLCADMIUM DECOMPOSITION KINETICS AND PARAMETER EXTRACTION

#### 6.1 Introduction

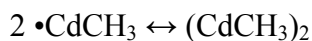
Another example, decomposition kinetics of dimethylcadmium,  $\text{Cd}(\text{CH}_3)_2$ , (DMCd) was examined using computational calculations and Raman scattering experiments. In the experiments, a Raman spectrometer (Jobin Yvon, U-1000) was used to collect and analyze the scattered light. The 532 nm wavelength of a Nd/YAG solid state laser was used as the excitation source at a laser power of 1W and a photomultiplier tube (PMT) or coupled charge device (CCD) was used as the detector. In this measurement, a stream of dimethylcadmium (1.3 mol% in  $\text{N}_2$ ) was introduced into an inverted impinging-jet reactor at a velocity of 2.5 cm/s. The reactor included a resistance heater placed at the top of the reactor with an upward reactant flow. Since the DMCd/ $\text{N}_2$  was introduced at room temperature, the flow expanded as the gas stream was heated. Since the reactor height is adjustable, the focal point of the laser source could be scanned along the reactor center-line to follow reactions.

DMCd is a common precursor for deposition of Cd-containing compound semiconductors. The homogeneous decomposition of DMCd becomes significant at a relatively low temperature ( $\sim 500^\circ\text{C}$ ) and thus homogeneous reactions are important at conditions commonly used in MOCVD of Cd-containing compounds. Unfortunately, there has been little study of the decomposition mechanism and associated reaction rate constants. There is, however, general agreement that gas-phase decomposition occurs by sequential homolytic fission of the Cd-C bond [Bae02, Lau57, Pri57, Jac89b]:



The activation energy of these two reactions has been suggested by experimental measuring, such as mass spectrometry. The values of the activation energy for reactions (6-1) and (6-2) are summarized (Table 6-1).

Although this pathway is likely the dominant one, comparison with suggested pathways for other group II alkyls suggest that additional reactions may also contribute to the deposition process [Ban77]. In experimental observations of species in a reacting system band, quantifying their concentration variations can be challenging. Thus, there is motivation to use computational chemistry to assist in designing and interpreting experiments, as well as exploring variety pathways. Compared to Zn metal organics, however, the greater number of electrons in Cd makes these calculations more difficult. In this study, the Cd-C vibrational frequencies are predicted using two methodologies, including DFT and HF, and the results are compared to values measured by Raman scattering experiments at elevated temperature. It is expected in the computation chemistry that selection of the basis set is important to provide sufficient information on the molecular system. To select a reasonable basis set for DMCD, calculations using ECP basis sets for atomic Cd with various basis sets for C and H were first performed for better understand the bond dissociation behavior and explore possible formation of selected intermediates. Furthermore, the Raman active vibrational frequencies between Cd and C atoms in Cd-containing molecules were calculated and the best basis set of various molecular species was selected based on comparison to reported bond dissociation energies [Ban77, Coa94]. The selected basis set was then used to estimate the vibrational frequencies and the likely reaction intermediates. The calculated frequencies and predicted intermediate reactions were then compared to observations using gas-phase Raman scattering experiments. In particular, the dimerization of monomethyl cadmium is suggested based on the following reaction:



(6-3)

## 6.2 Decomposition Mechanisms of Dimethylcadmium

The objective of the effective core potential (ECP) in quantum chemical calculations is to construct potentials which depend on the coordinates of the valence electrons, but considering the influence of the inert core electrons. The ECP calculation for the heavy elements, in special, is a rather distinctive challenge for the molecular-orbital theory since they have large numbers of electrons with an associated requirement to use a large number of basis functions to describe them [Kra84, Tit96]. It should be noted that ECP calculation carries out nothing more than reduce the scale of the electronic structure problem. In fact, more electrons mean more energy associated with electron correlation, too. So-called ‘large-core’ ECP includes everything but the outermost valence shell, while ‘small-core’ ECP scales back to the next lower shell. Because polarization of the sub-valence shell can be chemically important in heavier metals, it is usually worth the extra cost to explicitly include that shell in the calculations. Thus, the most robust ECP for the elements Sc-Zn, Y-Cd, and La-Hg employ [Ne], [Ar] and [Kr] cores respectively and it would still give good enough calculation results.

ECP quantum calculations are very useful in thermodynamic estimations, such as bond dissociation energy, enthalpy and free energy changes [Pan02, Ant00, Wan04, Kau94]. Moreover, IR frequency or vibrational and rotational Raman shift can be calculated theoretically to assign experimentally obtained unknown peaks. Therefore, various methods and basis sets have been reported to describe the nature heavy atom containing molecules.

### 6.2.1 Bond Dissociation Energy

For the calculations, the Gaussian 03 software package was used [Fri04]. As shown in Table 6-1, the activation energy for the first gas-phase Cd-C bond fission is in the range 43.5 to 56.0 kcal/mol and this range was used as a criterion to select the basis set. Among reported

ECPs for the Cd atom, five different basis sets, CRENBS, CRENBL, SDD, LanL2DZ, and SBKJC, were compared as they are reported to provide an acceptable description of the Cd atom. For the H and C atoms, two different chemistries, B3LYP and HF, were used with a conjugated basis set of 6-311++G(2d,2p) or 3-21G. The two basis sets for H and C were studied to determine if the calculated thermodynamic properties are really influenced by the ligand basis set.

A preliminary set of calculations was performed to define an acceptable level of calculation accuracy. Table 6-2 summarizes the enthalpy and Gibbs energy changes calculated for reaction (6-1) using the two different calculation sets. Calculations set (1) shows B3LYP or HF calculations results combined with a higher accuracy basis set for the ligands, while calculation set (2) is different only in use of the lower basis set for the ligand. In the calculation, the basis set superposition error (BSSE) was estimated to judge the efficacy of the ligand basis set [Dui94]. If the BSSE is small, then the error from the geometry deformation or optimization is judged to be small. This is the reason why a higher order of basis set with diffuse and polarization options is generally accepted as a better basis set although it takes more calculation time. In the first calculation set, it is obvious that B3LYP theory calculation gives similar values of  $\Delta G$  to the reported activation energies (43.5 to 56 kcal/mol) better than Hartree-Fock approach. The BSSE is also seen to be very small and thus it is regarded that the B3LYP calculation does count into error that could be caused by geometry deformation during the bond-rupture calculations. The HF calculation, however, gives considerably lower values of  $\Delta G$  to the reported range. This is not surprising since HF calculations do not consider electron-electron correlation when it builds up the Hamiltonian operator. The lower accuracy ligand chemistry (calculation set 2 in Table 6-2) did not change the conclusion of the comparison on the B3LYP vs. HF chemistries. However, it did give a higher BSSE correction factor. Therefore, the

accurate BSSE should be considered if lower accuracy basis set is used in thermodynamic calculations. This is from the fact that accurate BSSE value dose correct over-estimated calculation errors reasonably.

### **6.2.2 Raman-Active Frequency**

All the selected basis-set combinations gave plausible bond dissociation energies compared to reported values. However, it turned out that it is not always true for estimations in Cd-containing intermediates because Cd has to be stated using ECP theory calculations. Since the Cd-C symmetric stretch has larger Raman scattering cross-sectional areas compared to diethylzinc stated in chapter 5, stronger peak intensity in experimental detection was expected and computational calculations were first performed to estimate the vibrational frequencies of this stretch in both DMCD and the first intermediate, monomethylcadmium (MCd). The reported vibrational frequencies, which were mainly determined by atomic absorption/emission spectroscopy, are summarized in Table 6-3.

Based on reported frequencies, trials for finding the best basis set combining ECP for the Cd atom and various ligand basis sets were attempted with B3LYP and HF calculation methods. Even though HF could not make good guesses of bond dissociation in Table 6-2, it was attempted to find a specific vibrational motion. In fact, the thermodynamic values in Table 6-2 were calculated with consideration of all the vibrational motions and the summation gave the enthalpy changes. Therefore, it should be noted that the frequency of Cd-C stretching is just one of total degrees of freedom in vibrational normal modes. Of course, HF would be unlikely to give a reliable result, however it is regarded that the basis set selection has more influence on the value of specific vibrational motion rather than calculation methodology. Table 6-4 shows the calculation results using the B3LYP model chemistry with five different ECPs for the Cd atom. In this case, five different basis sets, including STO-3G, 3-21G, 6-31G(d), 6-311G(d) and 6-

311++G(2d,2p) were selected for the C and H ligands to check the basis set effect on the calculated frequency. The calculations were repeated with replacing the B3LYP model chemistry with the HF approach, and the results are listed in Table 6-5.

The Raman experiments in this study detect the Cd-C vibrational motion in  $\text{Cd}(\text{CH}_3)_2$  at  $473\text{ cm}^{-1}$ , which agrees well with the calculated value of Miles *et al.* [Mil68]. The symmetric stretch was also experimentally observed in  $\text{CdCH}_3$  at  $350\text{ cm}^{-1}$ , which is also in the range of values listed in Table 6-3. The calculated frequencies in Tables 6-4 and 6-5 were compared with this experimental value and a scaling factor using the experimental shift ( $473\text{ cm}^{-1}$ ) was applied to each calculated frequency for both  $\text{Cd}(\text{CH}_3)_2$  and  $\text{CdCH}_3$ . This attempt was to find out the best basis set, which can describe the specific vibrational frequency as well as the thermodynamic estimation of specific bond dissociation. In other words, the basis set should be chosen to correct and reproduce the symmetrical motion of Cd-C stretching motion in MCd as the experimental value of  $350\text{ cm}^{-1}$ . The likely basis set from the preliminary works in Table 6-4 turned out the B3LYP model chemistry with SDD/STO-3G, which gave a frequency of  $344.25\text{ cm}^{-1}$ . It is noted that all calculated frequencies were less than this value. Thus, the higher accuracy basis set did not give the better result. It does, however, make sense since Cd-C vibration is just one of 30 vibrational degrees of freedom. Therefore, calculation results indicate that stiff basis set gives better solution when an ECP basis set is used for the metal atom. This is reasonable in a sense that ECP actually considers electrons at the outermost shell, as a result, smaller electrons would be used to describe the metal atom. Therefore, basis sets for the ligands that were much larger and more flexible than metal gave an unbalanced distribution of electron density.

On the other hand, HF calculation with SBKJC VDZ/3-21G and SDD/3-21G basis sets also give a value of the Cd-C stretch frequency for intermediates close to the experimental (Table 6-5). This suggests that electron correlation is not a significant factor in determining the Raman frequencies for a specific motion. Therefore, these HF calculations are also considered reasonable basis sets and further trials to detect unknown reaction intermediates were attempted.

Experiments were performed to measure or detect and establish the Raman shifts for both DMCD and MCD using *in-situ* Raman spectroscopy with the charge coupled detector array (CCD) detector. Figure 6-1 shows the Raman spectra of them. Two strong peaks are evident at positions expected for Cd(CH<sub>3</sub>)<sub>2</sub> and CdCH<sub>3</sub>. Their intensity decreases as the temperature increases would be coming along in actual measurements because of the results from expanding convection and diffusion. In the case of PMT detector, the intermediate, MCD, was not detected due to high reactivity of the species. However, the longer exposure time in CCD measurement made it possible to catch the evidence of the intermediate.

To further probe why the stiffer basis set produced a better estimation of the Cd-C stretch frequency, the molecular orbital levels were examined for both the restricted B3LYP and HF calculations. Figures 6-2 and 6-3 show the orbital levels for Cd(CH<sub>3</sub>)<sub>2</sub> and CdCH<sub>3</sub>, followed by Tables 6-6 and 6-7 listing the energy values for each state. From these results it is seen that the B3LYP results have no significant energy difference in each level with respect to the ligand basis set. As the basis set becomes stiffer and less accurate (or inexpensive), the energy of each orbital increases and HF has the same tendency. It is noted that the small increase in orbital energy yielded gave better frequency value.

The molecular orbital levels in CdCH<sub>3</sub>, on the other hand, show somewhat obvious different energy values. B3LYP calculations with a stiff basis set, e.g., 3-21G and STO-3G,

show energy increases especially in (8) to (15) orbital levels, which are relevant to the Cd-C overlapped orbital. Therefore, it is clear that the stiff basis set favors higher energy values, while the flexible basis set made a lower energy estimation in the Cd-C orbital. Since ECP calculations only consider valence electrons in its wave function, the number of primitives in the calculations seems to be well matched with a stiff basis set, which also has a similar number of primitives.

To provide a more practical basis set, complex combinations of basis sets were considered next. More trials with three different basis sets for each atom were attempted, and the vibration frequencies in Cd-C bond were estimated. Table 6-8 shows the result using the B3LYP and HF model chemistries. Based on the results in Tables 6-4 and 6-5, the SDD ECP for B3LYP calculation and SBKJC VDZ and SDD ECPs for HF calculations were performed. In these calculations, STO-3G and 3-21G were used for C and H, respectively. First, the B3LYP calculations were performed for two cases as shown in Table 6-8 with the SDD, STO-3G and 3-21G basis set combination for Cd, C and H atoms to reproduce the Cd-C vibrational frequency of CdCH<sub>3</sub>. Moreover, the HF calculations with SDD/3-21G/6-31G(d), SBKJC VDZ/3-21G/STO-3G and SBKJC VDZ/STO-3G/3-21G basis sets also gave frequency values close values. It should be noted, however, that the HF calculation does not consider electron correlation so that the accuracy is less than the DFT calculations.

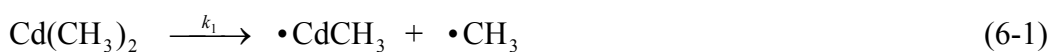
### **6.2.3 Reaction Intermediates**

The basis sets which were consistent with the measured shifts were then used to suggest additional reaction intermediates. They were then sought in subsequent Raman scattering experiments. In particular, dimerization of two CdCH<sub>3</sub> radicals was a possible reaction. The quantum calculation supports its evidence; therefore, those two reactions, including homolytic fission and dimerization, actually exist at the same time but the rates should be different. As a



result, only homolytic fission between Cd and C atoms was reported experimentally. However, electronic Raman detection of Cd atom, which is an evidence of the sequential homolytic fission, was not possible since Cd has a closed outer shell and lifetime for the transition between the ground state and the first excited state is too short. Therefore, experimental detection of the second Cd-C bond fission is not possible. Table 6-9 shows the calculation results, including Cd-Cd vibration and Cd-C stretching, and the same scaling factor listed in Tables 6-4 and 6-5 applied to the Cd-C vibrational frequencies.

The B3LYP calculation suggests that the dimer peak should be observed at  $\sim 482\text{ cm}^{-1}$ . There is also a Raman active Cd-Cd stretching motion around  $154\text{ cm}^{-1}$ , but the calculated Raman shift might contain an error since the exact scaling factor was not based on experimental Cd-Cd vibrations. Furthermore the Cd-Cd stretch has a very small calculated Raman cross-section and thus was not expected to be detected. Based on the results in Table 6-9, *in-situ* Raman experiments were carried out in the transparent reactor with the sensitive PMT detector at a reactor position having a higher temperature than shown in the spectra in Figure 6-1. Figure 6-4 shows the results of scans at 3 positions with gas temperatures of  $\sim 25$ ,  $300$ , and  $500\text{ }^{\circ}\text{C}$ . As expected, only one peak representing the Cd-C vibrational stretch at  $473\text{ cm}^{-1}$  exists at room temperature. An additional peak at  $482\text{ cm}^{-1}$ , however, appears as the temperature is increased, indicating decomposition of dimethylcadmium coupled with dimerization. At the highest temperature  $\sim 500\text{ }^{\circ}\text{C}$ , almost all dimethylcadmium is decomposed giving a strong dimer peak. Therefore, the overall decomposition mechanism can be written as below in three steps with reaction rate constants;





where  $K$  is equilibrium constant defined as  $K = k_3 / k_4$ , i.e.  $k_3 = K \cdot k_4$ . However, the new species of  $(\text{CdCH}_3)_2$  has not been reported from any other experiments in literature, even though it was found in this study of the first principles calculations and supported experiments. This molecule might be impossible to be detected due to a short lifetime or other researchers used experimental detectors with short detection limits, such as gas chromatography or mass spectrometry. Therefore, it is interesting to use the first principles calculation once again to verify the propriety of the reaction step. Using statistical thermodynamics, the equilibrium constant of reaction (6-3) can be expressed with frequency analysis [McQ76];

$$K(T) = K_p(T) = K_c(T) = \frac{P_{\text{dimer}}}{P_{\text{monomer}}^2} = (kT)^{-1} \frac{(q_{\text{dimer}}/V)}{(q_{\text{monomer}}/V)^2} \quad (6-4)$$

The partition functions are given by

$$\frac{q_{\text{dimer}}}{V} = \left( \frac{2\pi m_{\text{dimer}} kT}{h^2} \right)^{3/2} \cdot \frac{\pi^{1/2}}{\sigma} \cdot \left( \frac{T^3}{\Theta_A \Theta_B \Theta_C} \right)^{1/2} \cdot \left\{ \prod_{j=1}^9 \frac{e^{-\Theta_{vj}/2T}}{(1 - e^{-\Theta_{vj}/T})} \right\} \omega_{el} e^{D_0/kT} \quad (6-5)$$

$$\frac{q_{\text{monomer}}}{V} = \left( \frac{2\pi m_{\text{monomer}} kT}{h^2} \right)^{3/2} \cdot \frac{\pi^{1/2}}{\sigma} \cdot \left( \frac{T^3}{\Theta_A \Theta_B \Theta_C} \right)^{1/2} \cdot \left\{ \prod_{j=1}^{24} \frac{e^{-\Theta_{vj}/2T}}{(1 - e^{-\Theta_{vj}/T})} \right\} \omega_{el} e^{D_0/kT} \quad (6-6)$$

where  $\sigma$  is the symmetry number of rotational motion,  $\Theta_{A,B,C}$  and  $\Theta_{vj}$  are rotational and vibrational temperatures, respectively. And  $\omega_{el}$  and  $D_0$  are degeneracy of the electronic partition function and zero-point vibrational energy, respectively. All the necessary variables in Equations 6-4, 6-5, and 6-6 can be calculated from the first principles calculations. Here, it should be noted that the separated basis sets do not really make a difference in thermodynamic properties since all the frequency values are used in the calculation and in fact the final value is the summation of all values. Table 6-10 shows the necessary values calculated from B3LYP/6-

311G(d) level theory calculations. Moreover, Table 6-11 shows the calculation results after applying the values in Table 6-10 to Equations 6-4 through 6-6. The temperature ranges were chosen for actual MOCVD conditions.

On average, it turned out that  $K = 8.26 \times 10^{-8}$  and therefore reaction constants for forward and backward could be obtained as follows;  $k_4 = 1.07 \times 10^9$  /s and  $k_3 = K \cdot k_4 = 88.382$  /s.

Therefore, it is obvious that the reverse path is kinetically much faster than forward and it is natural for previous researchers not to observe the species even though it is a thermodynamically stable intermediate.

### 6.3 Kinetics Parameter Extraction

Once proper model chemistry including method and basis set was developed, reaction mechanisms could be established. Then, rate constant for each step was evaluated based on thermodynamic properties. Those values were calculated from optimized geometry calculations and followed frequency analysis. All the data were compared to the reported values and they made good agreements. The big advantage of computational calculation is, therefore, the ability to estimate rate constant even for experimentally undetectable reaction steps.

The next step, which is going to be shown in this section, is a parameter extraction from the comparison between experimental and simulated data. Since the main purpose of the research was focused on kinetics information, firstly the rate constant was evaluated. Generally, the Arrhenius equation is widely used to describe kinetics of reaction; however, it was not appropriate equation form in Genetic algorithm because the Arrhenius equation is actually a non-linear equation, i.e., unknown variable (frequency factor,  $k_0$ ) multiply by unknown variable (activation energy,  $E_a$ ). Therefore, if any other relationship between  $k_0$  and  $E_a$ , which makes it

linear equation, can be utilized, then it can be used in Genetic algorithm. Fortunately, the rate equation could be reparameterized according to the following empirical equation:

$$k = \exp \left[ p_1 - \frac{10p_2}{R} \left( \frac{1}{T} - \frac{1}{T_m} \right) \right] \quad (6-7)$$

where  $p_1 = \ln(k_0) - E_a/RT_m$  and  $p_2 = E_a/10$ . In the new equation,  $T_m$  denotes the mean temperature of measurement. Moreover, the relative Raman cross-section for dimethylcadmium was also evaluated by minimizing the difference between experimental and simulated data.

Figure 6-5 shows how the objective functions were converged upon. A maximum of 25 iterations was attempted for Genetic algorithm and from the obtained point Simplex algorithm tuned the value finely. The relative Raman cross-section of dimethylcadmium turned out 20.97, which is very reasonable compared to other group III metal organic precursors. For example,  $\Sigma_{TMIn}$  is 22.3. However, this is a much higher value than diethylzinc. In fact, spectroscopic detection for group II materials is very difficult because of the small relative Raman cross-section.

In the case of rate constant, converged  $P_1$  and  $P_2$  made  $k_0 = 5.01 \times 10^{13} \text{ s}^{-1}$ ,  $E_a = 55.98$  kcal/mol. This value is actually not quite different from a computational initial guess (in Chapter 3,  $k_0 = 2.06 \times 10^{13} \text{ s}^{-1}$ ,  $E_a = 53.0$  kcal/mol). Therefore, the computational guess is quite good and it turns out that more physical parameters can be extracted from parameter optimization procedures very accurately not just even kinetics data.

#### 6.4 Homogeneous Reactions with Water

Similar to diethylzinc in section 5.4, reactions between Cd-containing species and water have been considered to understand CdO film formation. This reaction study suggested likely homogeneous reactions occurring before certain surface reactions take place on the substrate.

Based on examined basis sets in previous sections, SDD ECP was selected to describe Cd atom and 6-311G(d) was employed to explain C, H, and O atoms. Then, thermodynamics properties were estimated to evaluate each reaction step. Figure 6-6 shows the energetic diagram of reactions between one mole of dimethylcadmium and water.

Similar to diethylzinc, the first reaction (1) was a spontaneous reaction with -5.48 kcal/mol enthalpy due to a lone pair of electrons in a water molecule. Then one hydrogen reached carbon due to vibrational motion of the water and it underwent transient state shown as structure (3). Releasing methane from its structure occurred very fast with -38.81 kcal/mol and meta-stable structure of (4) formed. However, this molecule might not survive longer since more water molecules could exist near this molecule. In step (b), therefore, one more addition of water was introduced. Another transient state of (7) formed with additional water and methane was released from it. Again, it was a spontaneous reaction of -35.23 kcal/mol. Therefore, dihydroxocadmium of the structure (8) became a final product. This molecule has the same structure which was made from reactions between diethylzinc and water. The metal atom is located at the center and two OH groups are connected. Therefore, dihydroxocadmium may undergo trimerization reactions in gas phase as well as on the surface and due to the dipole moment interactions and finally Wurtzite structure CdO film is expected to be formed as shown in the previous chapter.

## 6.5 Summary

A reasonable selection in the basis sets is important in a computational calculation, because it yields more valuable information. As an example, a basis set selection for dimethylcadmium using ECP was shown based on the reported data in the literature. Two calculation results, bond dissociation energy in Cd-C bond and its Raman active stretching motions were examined using different combinations of various basis sets; five different basis

sets for Cd atom, i.e., CRENBS, CRENBL, SDD, LanL2DZ and SBKJC and five different basis sets for C and H atoms, i.e., STO-3G, 3-21G, 6-31G(d), 6-311G(d) and 6-311++G(2d,2p).

Among the possible candidates, B3LYP level theory calculations with SDD/STO-3G/3-21G basis set combinations for Cd, C and H atoms could reproduce the experimentally reported Cd-C vibrational stretching of  $\text{Cd}(\text{CH}_3)_2$  and  $\text{CdCH}_3$ ; therefore, this basis set was also utilized to find the most likely reaction intermediate, i.e.,  $(\text{CdCH}_3)_2$ , and its frequency was also calculated.

Based on calculated information, gas-phase Raman scattering experiments in certain temperature gradient were carried out in an inverted impinging-jet reactor and the existence of  $(\text{CdCH}_3)_2$  was confirmed. The forward reaction of dimerization was turned out much slower than backward; however, longer integration time setting in Raman spectroscopy was enabled to detect the species. Therefore, the computational calculation is very useful to predict Raman active frequencies. However, the criteria for choosing basis sets should be set up first. Moreover, a stiff basis set for C and H atoms gives better results if an ECP is used for metal atoms, and it doesn't really affect any other property calculation, such as thermodynamics.

Then parameter estimation was carried out using Genetic and Simplex algorithms. The obtained experimental data was compared to simulations and, as a result, decomposition kinetics data of dimethylcadmium were obtained. The relative Raman cross-section turned out 20.97 and the rate constant consists  $k_0 = 5.01 \times 10^{13} \text{ s}^{-1}$ ,  $E_a = 55.98 \text{ kcal/mol}$ .

Table 6-1. Reported activation energies for the homogeneous dissociations of the first and second Cd-C bonds of dimethylcadmium.

Activation Energy [kcal/mol]		Temp. [°C]	Analytical Method	Author/Year
Reaction (1)	Reaction (2)			
43.5/10 <sup>13.1</sup>	21.4/10 <sup>11.9</sup>	~258	Gas Calorimetry	Laurie and Long (1957)
45.8/10 <sup>11.9</sup>	21.0	~608	Gas Chromatography (Toluene-carrier flow)	Price and Trotman-Dickenson (1957)
56.0	15.2	~550	RKKM theory calculation	Jackson (1989)

Table 6-2. Calculated thermodynamic properties of first Cd-C homolytic fission in DMCd. (1) ECP for Cd and higher accuracy basis set for ligands as specified, (2) ECP for Cd and lower accuracy basis set for ligands as specified

Calculation set (1): ECP for Cd and higher accuracy basis set for ligands as specified

B3LYP/Ligand Basis Set	BSSE [kcal/mol]	$\Delta H$ [kcal/mol]	$\Delta G$ [kcal/mol]
CRENBS + 6-311++G(2d,2p)	0.48	46.50	35.61
CRENBL + 6-311++G(2d,2p)	0.43	53.77	42.91
SDD + 6-311++G(2d,2p)	0.29	53.99	42.18
LanL2DZ + 6-311++G(2d,2p)	0.27	46.49	35.10
SBKJC + 6-311++G(2d,2p)	0.15	53.40	42.52
HF/Ligand Basis Set	BSSE [kcal/mol]	$\Delta H$ [kcal/mol]	$\Delta G$ [kcal/mol]
CRENBS + 6-311++G(2d,2p)	0.61	29.45	18.48
CRENBL + 6-311++G(2d,2p)	0.61	29.60	19.08
SDD + 6-311++G(2d,2p)	0.30	29.92	20.54
LanL2DZ + 6-311++G(2d,2p)	0.39	30.29	17.62
SBKJC + 6-311++G(2d,2p)	0.41	29.92	20.54

Table 6-2. (Continued) The calculated thermodynamic properties of first Cd-C homolytic fission in DMCd.

Calculation set (2): ECP for Cd and lower accuracy basis set for ligands as specified

B3LYP/Ligand Basis Set	BSSE [kcal/mol]	$\Delta H$ [kcal/mol]	$\Delta G$ [kcal/mol]
CRENBS + 3-21G	1.37	45.00	31.41
CRENBL + 3-21G	2.37	55.96	42.12
SDD + 3-21G	2.43	57.39	44.20
LanL2DZ + 3-21G	2.04	48.06	34.49
SBKJC + 3-21G	2.24	54.93	41.16
HF/Ligand Basis Set	BSSE [kcal/mol]	$\Delta H$ [kcal/mol]	$\Delta G$ [kcal/mol]
CRENBS + 3-21G	3.08	24.13	13.28
CRENBL + 3-21G	3.28	31.44	17.65
SDD + 3-21G	3.38	30.97	18.26
LanL2DZ + 3-21G	2.98	31.28	18.57
SBKJC + 3-21G	2.79	31.18	17.45

\* The first basis set is for Cd atom and the other is for the ligand, C and H.

Table 6-3. Reported  $\nu[\text{Cd-C}]_{\text{sym}}$  vibrational frequencies ( $\text{cm}^{-1}$ ).

Molecules		Authors	Ref.
$\text{Cd}(\text{CH}_3)_2$	$\text{CdCH}_3$		
-	356	E.S.J. Robles (1991)	Rob91
-	355	A.M. Ellis (1992)	Ell92
-	330	C.J Chen (1984)	Che84
459	-	K. Cabanagh (1969)	Cav69
472(Cal), 465(Exp)	-	M.G. Miles (1968)	Mil68



Table 6-4. The calculated frequencies for the symmetric Cd-C stretching motion in Cd(CH<sub>3</sub>)<sub>2</sub> and CdCH<sub>3</sub> using the B3LYP model chemistry.

B3LYP/Model chemistry		Calculated $\nu[\text{Cd-C}]_{\text{sym}}$		Scaling factor	Corrected	
		Cd(CH <sub>3</sub> ) <sub>2</sub>	CdCH <sub>3</sub>		Cd(CH <sub>3</sub> ) <sub>2</sub>	CdCH <sub>3</sub>
LanL2DZ	STO-3G	442.98	306.99	1.0614		325.87
	3-21G	479.90	298.86	0.9856		294.56
	6-31G(d)	417.73	266.27	1.1323		301.50
	6-311G(d)	412.31	272.86	1.1472		313.02
	6-311++G(2d,2p)	408.03	272.87	1.1592		316.32
CRENBS	STO-3G	381.23	228.49	1.2407		283.49
	3-21G	435.53	281.62	1.0860		305.85
	6-31G(d)	410.93	231.21	1.1510		266.13
	6-311G(d)	392.41	207.62	1.2054		250.26
	6-311++G(2d,2p)	420.73	281.33	1.1242		316.28
CRENBL	STO-3G	483.92	343.65	0.9774		335.90
	3-21G	461.49	314.52	1.0249		322.36
	6-31G(d)	455.04	291.10	1.0395		302.59
	6-311G(d)	448.22	291.24	1.0553		307.34
	6-311++G(2d,2p)	449.78	286.58	1.0516		301.37
SBKJC VDZ	STO-3G	463.29	313.78	1.0210		320.36
	3-21G	456.66	314.61	1.0358		325.87
	6-31G(d)	452.32	297.07	1.0457		310.65
	6-311G(d)	448.85	298.76	1.0538		314.83
	6-311++G(2d,2p)	449.23	294.77	1.0529		310.37
SDD	STO-3G	495.12	360.35	0.9553		344.25
	3-21G	471.84	323.92	1.0025		324.72
	6-31G(d)	462.38	300.56	1.0230		307.46
	6-311G(d)	458.25	299.36	1.0322		309.00
	6-311++G(2d,2p)	456.54	293.32	1.0361		303.90

Table 6-5. The calculated frequencies for the symmetric Cd-C stretching motion in Cd(CH<sub>3</sub>)<sub>2</sub> and CdCH<sub>3</sub> using the HF model chemistry.

HF/Model chemistry		Calculated $\nu[\text{Cd-C}]_{\text{sym}}$		Scaling factor	Corrected	
		Cd(CH <sub>3</sub> ) <sub>2</sub>	CdCH <sub>3</sub>		Cd(CH <sub>3</sub> ) <sub>2</sub>	CdCH <sub>3</sub>
LanL2DZ	STO-3G	500.01	287.06	0.9460		271.55
	3-21G	479.90	346.59	0.9856		341.61
	6-31G(d)	465.50	305.96	1.0161		311.89
	6-311G(d)	459.33	317.45	1.0305		327.13
	6-311++G(2d,2p)	457.90	320.82	1.0330		331.40
CRENBS	STO-3G	420.84	104.68	1.1239		117.65
	3-21G	471.28	198.89	1.0036		199.62
	6-31G(d)	432.92	Not converged	1.0926		-
	6-311G(d)	414.30	Not converged	1.1417		-
	6-311++G(2d,2p)	458.92	306.27	1.0307		315.67
CRENBL	STO-3G	504.83	293.35	0.9369		274.85
	3-21G	473.96	339.25	0.9979		338.56
	6-31G(d)	464.27	291.90	1.0194	473.00	297.56
	6-311G(d)	457.29	299.99	1.0344		310.30
	6-311++G(2d,2p)	459.88	300.12	1.0285		308.68
SBKJC VDZ	STO-3G	479.50	216.17	0.9864		213.24
	3-21G	469.06	342.96	1.0084		345.84
	6-31G(d)	462.73	305.67	1.0222		312.45
	6-311G(d)	459.05	316.65	1.0304		326.27
	6-311++G(2d,2p)	459.51	311.70	1.0294		320.85
SDD	STO-3G	506.84	348.28	0.9332		325.03
	3-21G	480.02	366.83	0.9854		361.47
	6-31G(d)	470.03	316.35	1.0063		318.35
	6-311G(d)	466.39	315.99	1.0142		320.47
	6-311++G(2d,2p)	465.60	310.52	1.0159		315.46

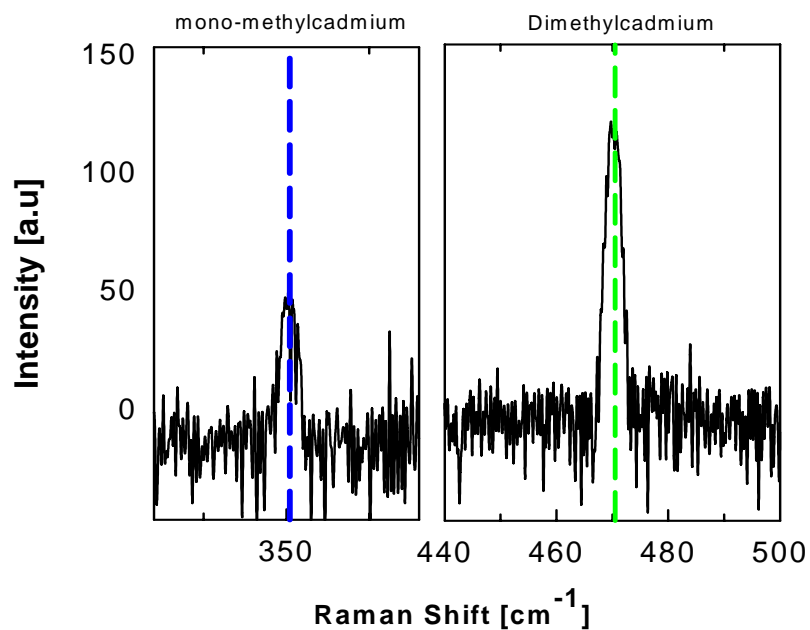


Figure 6-1. Raman shift of  $\text{Cd}(\text{CH}_3)_2$  and its first dissociated product,  $\text{CdCH}_3$ , observed at different positions using the inverted, impinging-jet reactor.

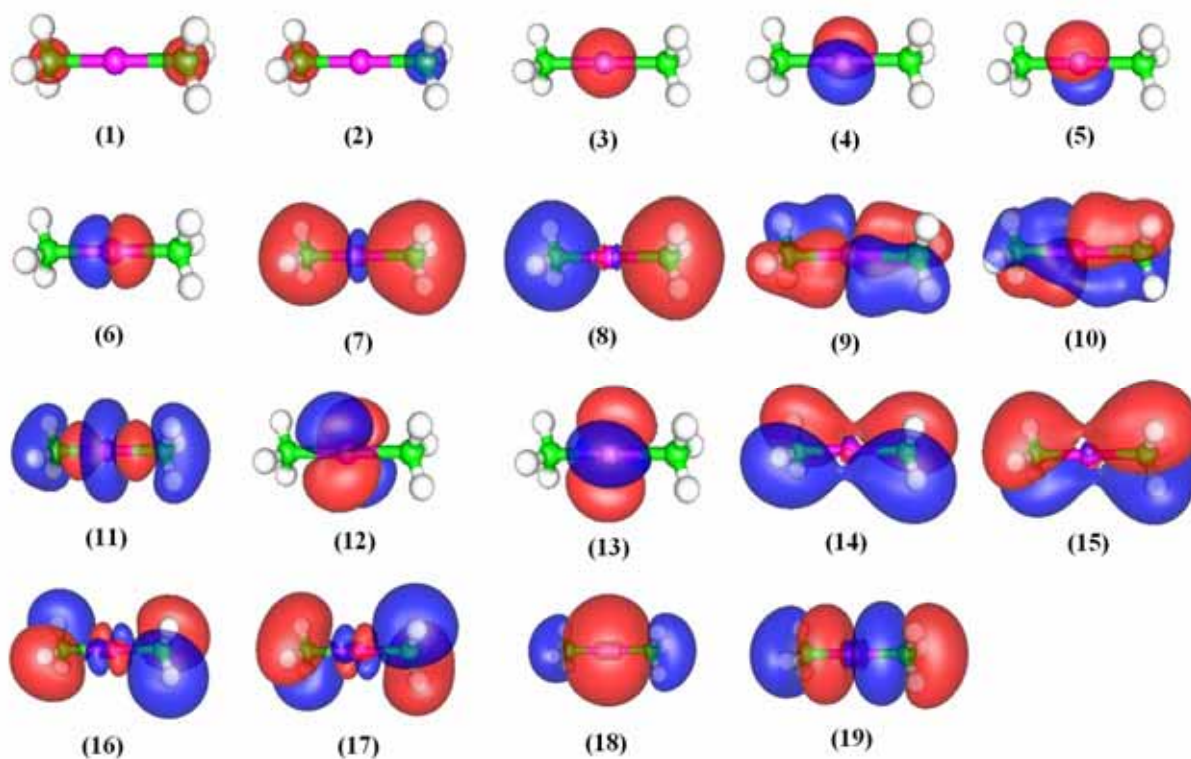


Figure 6-2. Molecular orbital contours of  $\text{Cd}(\text{CH}_3)_2$ . The energy values are listed in Table 6-6.

Table 6-6. Molecular orbitals of Cd(CH<sub>3</sub>)<sub>2</sub> and their energy values in Hartree obtained by (A) B3LYP and (B) HF level theory calculations.

(A) B3LYP	(1)	(2)	(3)	(4)	(5)	(6)	(7)	(8)	(9)	(10)
6-311++G(2d,2p)	-10.145	-10.137	-4.161	-2.667	-2.667	-2.661	-0.675	-0.659	-0.514	-0.514
6-311G(d)	-10.144	-10.136	-4.160	-2.666	-2.666	-2.660	-0.673	-0.658	-0.513	-0.513
6-31G(d)	-10.153	-10.145	-4.155	-2.660	-2.660	-2.654	-0.669	-0.653	-0.507	-0.507
3-21+G	-10.104	-10.096	-4.160	-2.666	-2.666	-2.660	-0.676	-0.660	-0.513	-0.513
STO-3G	-10.011	-10.004	-4.135	-2.641	-2.641	-2.634	-0.657	-0.641	-0.489	-0.489
	(11)	(12)	(13)	(14)	(15)	(16)	(17)	(18)	(19)	
6-311++G(2d,2p)	-0.513	-0.513	-0.513	-0.387	-0.387	-0.373	-0.373	-0.302	-0.243	
6-311G(d)	-0.512	-0.512	-0.512	-0.385	-0.385	-0.371	-0.371	-0.301	-0.242	
6-31G(d)	-0.506	-0.506	-0.506	-0.381	-0.381	-0.367	-0.367	-0.296	-0.236	
3-21+G	-0.512	-0.511	-0.511	-0.388	-0.388	-0.374	-0.374	-0.301	-0.242	
STO-3G	-0.489	-0.488	-0.486	-0.369	-0.369	-0.354	-0.354	-0.279	-0.216	
(B) HF	(1)	(2)	(3)	(4)	(5)	(6)	(7)	(8)	(9)	(10)
6-311++G(2d,2p)	-11.184	-11.184	-4.817	-3.180	-3.180	-3.172	-0.908	-0.894	-0.738	-0.738
6-311G(d)	-11.185	-11.185	-4.817	-3.181	-3.181	-3.173	-0.907	-0.893	-0.738	-0.738
6-31G(d)	-11.183	-11.183	-4.814	-3.177	-3.177	-3.170	-0.905	-0.891	-0.735	-0.735
3-21+G	-11.132	-11.132	-4.818	-3.181	-3.181	-3.174	-0.910	-0.896	-0.739	-0.739
STO-3G	-11.025	-11.025	-4.789	-3.151	-3.151	-3.144	-0.891	-0.876	-0.709	-0.709
	(11)	(12)	(13)	(14)	(15)	(16)	(17)	(18)	(19)	
6-311++G(2d,2p)	-0.734	-0.734	-0.722	-0.526	-0.526	-0.518	-0.518	-0.397	-0.339	
6-311G(d)	-0.734	-0.734	-0.723	-0.525	-0.525	-0.516	-0.516	-0.399	-0.341	
6-31G(d)	-0.731	-0.731	-0.720	-0.523	-0.523	-0.515	-0.515	-0.396	-0.338	
3-21+G	-0.735	-0.735	-0.724	-0.526	-0.526	-0.517	-0.517	-0.399	-0.341	
STO-3G	-0.706	-0.706	-0.694	-0.510	-0.510	-0.501	-0.501	-0.378	-0.316	

\*Basis set: SDD for Cd and listed basis sets for C and H

\*Unit: Hartree

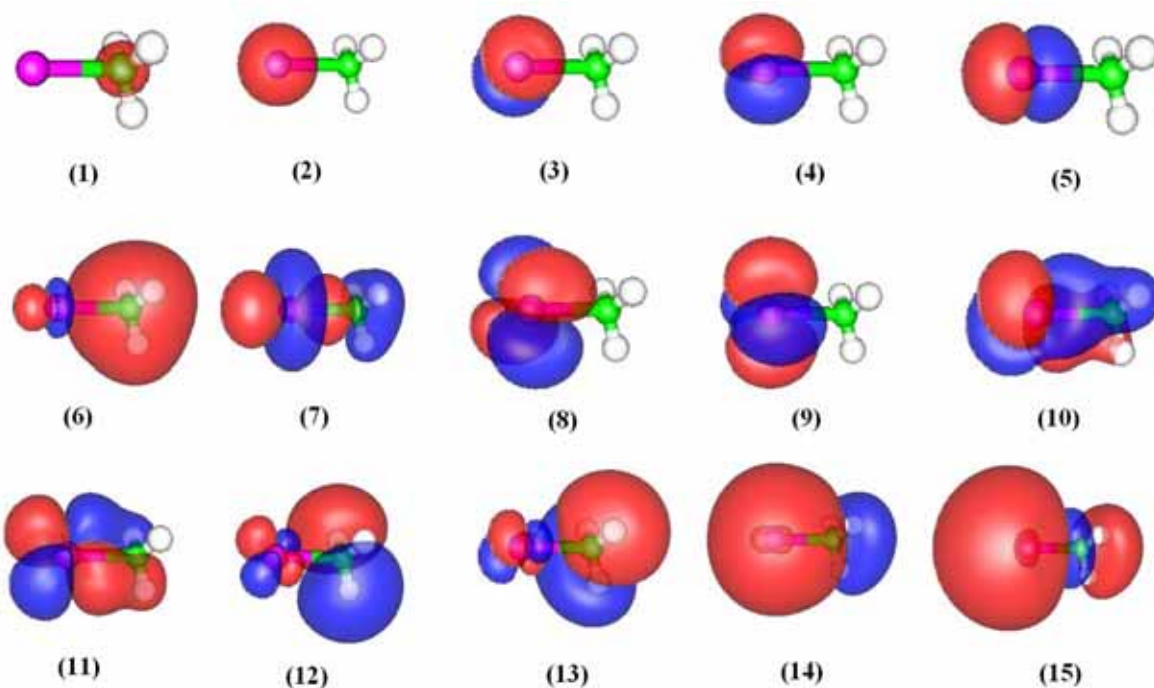


Figure 6-3. Molecular orbital contours of  $\text{CdCH}_3$ . The energy values are listed in Table 6-7.

Table 6-7. Molecular orbitals of  $\text{CdCH}_3$  and their energy values in Hartree obtained by (A) B3LYP and (B) HF level theory calculations.

(A) B3LYP	(1)	(2)	(3)	(4)	(5)	(6)	(7)	(8)	(9)	(10)
6-311++G(2d,2p)	-10.158	-4.148	-2.653	-2.653	-2.649	-0.677	-0.500	-0.500	-0.500	-0.499
6-311G(d)	-10.161	-4.153	-2.659	-2.659	-2.655	-0.681	-0.506	-0.505	-0.505	-0.505
6-31G(d)	-10.173	-4.150	-2.655	-2.655	-2.652	-0.679	-0.503	-0.502	-0.502	-0.501
3-21+G	-10.116	-4.148	-2.653	-2.653	-2.649	-0.679	-0.500	-0.500	-0.500	-0.499
STO-3G	-10.039	-4.141	-2.646	-2.646	-2.642	-0.678	-0.495	-0.493	-0.493	-0.493
	(11)	(12)	(13)	(14)	(15)					
6-311++G(2d,2p)	-0.499	-0.398	-0.398	-0.290	-0.173					
6-311G(d)	-0.504	-0.400	-0.400	-0.296	-0.180					
6-31G(d)	-0.501	-0.398	-0.397	-0.293	-0.176					
3-21+G	-0.499	-0.398	-0.398	-0.290	-0.172					
STO-3G	-0.493	-0.394	-0.394	-0.287	-0.163					

Table 6-7. Continued

(B) HF	(1)	(2)	(3)	(4)	(5)	(6)	(7)	(8)	(9)	(10)
6-311++G(2d,2p)	-11.206	-4.817	-3.179	-3.179	-3.176	-0.923	-0.737	-0.737	-0.733	-0.733
6-311G(d)	-11.206	-4.818	-3.180	-3.180	-3.176	-0.922	-0.737	-0.737	-0.733	-0.733
6-31G(d)	-11.205	-4.816	-3.178	-3.178	-3.174	-0.922	-0.735	-0.735	-0.731	-0.731
3-21+G	-11.148	-4.820	-3.182	-3.182	3.178	-0.922	-0.739	-0.739	-0.735	-0.735
STO-3G	-11.060	-4.803	-3.165	-3.165	-3.162	-0.919	-0.722	-0.722	-0.720	-0.719
	(11)	(12)	(13)	(14)	(15)					
6-311++G(2d,2p)	-0.733	-0.543	-0.543	-0.407	-0.263					
6-311G(d)	-0.733	-0.541	-0.541	-0.408	-0.263					
6-31G(d)	-0.731	-0.540	-0.540	-0.407	-0.262					
3-21+G	-0.735	-0.538	-0.538	-0.406	-0.263					
STO-3G	-0.719	-0.538	-0.538	-0.403	-0.249					

\*Basis set: SDD for Cd and listed basis sets for C and H

\*Unit: Hartree

Table 6-8. The Cd-C symmetric frequency calculated from different basis-set combinations.

Model chemistry				Calculated $\nu[\text{Cd-C}]_{\text{sym}}$		Scaling factor	Corrected	
		Cd	C	H	Cd(CH <sub>3</sub> ) <sub>2</sub>	CdCH <sub>3</sub>	Cd(CH <sub>3</sub> ) <sub>2</sub>	CdCH <sub>3</sub>
B3LYP	SDD		3-21G	STO-3G	479.69	334.93	473.00	330.26
			STO-3G	3-21G	489.87	360.59		348.17
HF	SDD		3-21G	STO-3G	489.34	381.35		368.62
			STO-3G	3-21G	500.74	387.00		365.56
			3-21G	6-31G(d)	478.52	358.31		354.18
			6-31G(d)	3-21G	471.33	316.60		317.72
	SBKJC VDZ		3-21G	STO-3G	475.92	351.33		349.17
			STO-3G	3-21G	490.72	354.66		341.85

Table 6-9. Expected Raman active frequency for the dimer,  $(\text{CdCH}_3)_2$ .

Model chemistry				Calculated $\nu[\text{Cd-C}]_{\text{sym}}$		Scaling factor	Corrected
Method	Cd	C	H	$[\text{Cd-Cd}]_{\text{sym}}$	$[\text{Cd-C}]_{\text{sym}}$		$[\text{Cd-C}]_{\text{sym}}$
B3LYP	SDD	STO-3G	3-21G	154.91	498.32	0.9656	481.18
		3-21G	6-31G(d)	147.12	494.97	0.9885	489.28
HF	SBKJC VDZ	3-21G	STO-3G	146.85	495.10	0.9939	492.08
		STO-3G	3-21G	145.12	504.69	0.9639	486.47

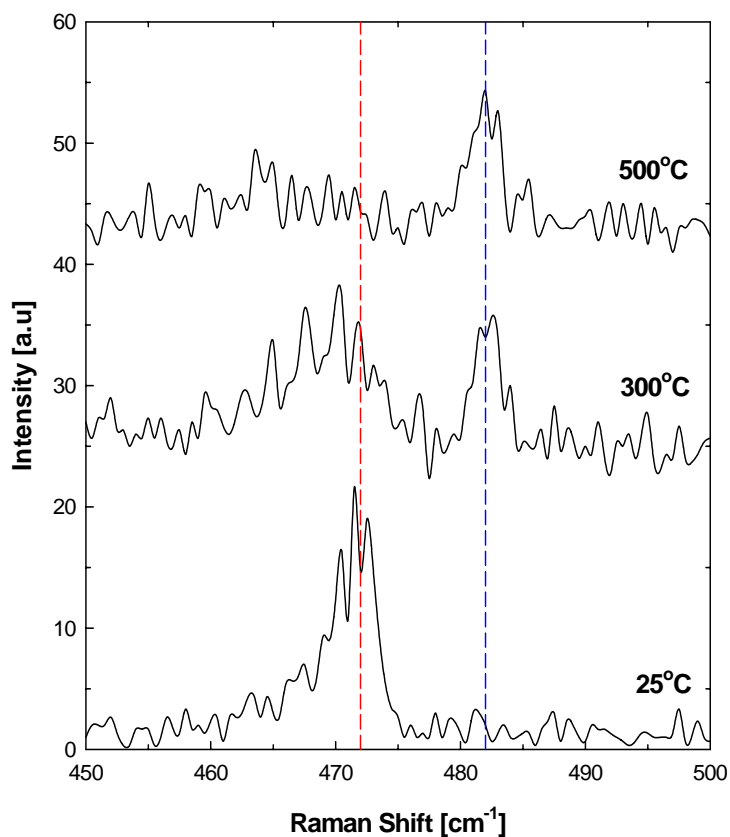


Figure 6-4. Detection of reaction intermediate during dimethylcadmium decomposition. The bottom spectrum was taken at room temperature and the most upper spectrum was scanned at around 500 °C, while the middle spectrum was taken around 300 °C.

Table 6-10. Partition functions for monomer and dimer species (Equation 6-3). The B3LYP/6-311G(d) level theory calculation was performed for each molecule.

	CdCH <sub>3</sub>			(CdCH <sub>3</sub> ) <sub>2</sub>		
Rotational Temp. (K)	7.38	0.32	0.32	3.83	0.03	0.03
Zero-point energy (Kcal/mol)	21.16			43.99		
Vibrational Temp. (K)				34.01	90.70	90.91
				144.05	144.17	218.58
				655.75	669.50	933.42
	429.63	849.73	852.25	933.49	952.47	952.53
	1501.99	2092.27	2092.44	1717.43	1722.60	2127.59
	4381.47	4547.01	4547.59	2127.62	2128.33	2128.35
				4341.07	4343.10	4453.95
				4453.98	4454.00	4454.03

Table 6-11. Calculated equilibrium constants for Equation 6-3.

Temp. [K]	373.15	473.15	573.15	673.15	773.15
K	$1.29 \times 10^{-7}$	$8.79 \times 10^{-8}$	$7.14 \times 10^{-8}$	$6.39 \times 10^{-8}$	$6.04 \times 10^{-8}$

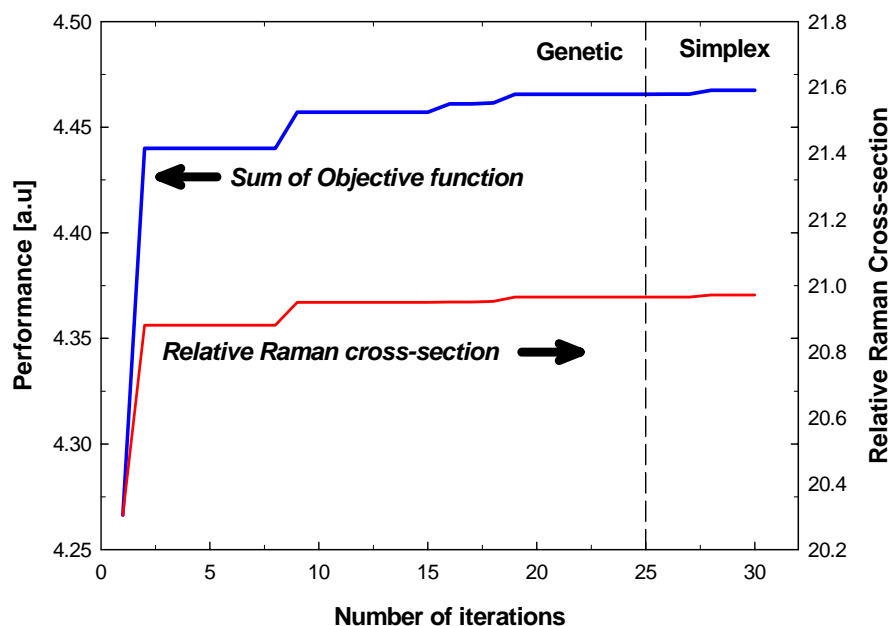


Figure 6-5. Convergence of rate constant and relative Raman cross-section for dimethylcadmium using Genetic and Simplex algorithms.



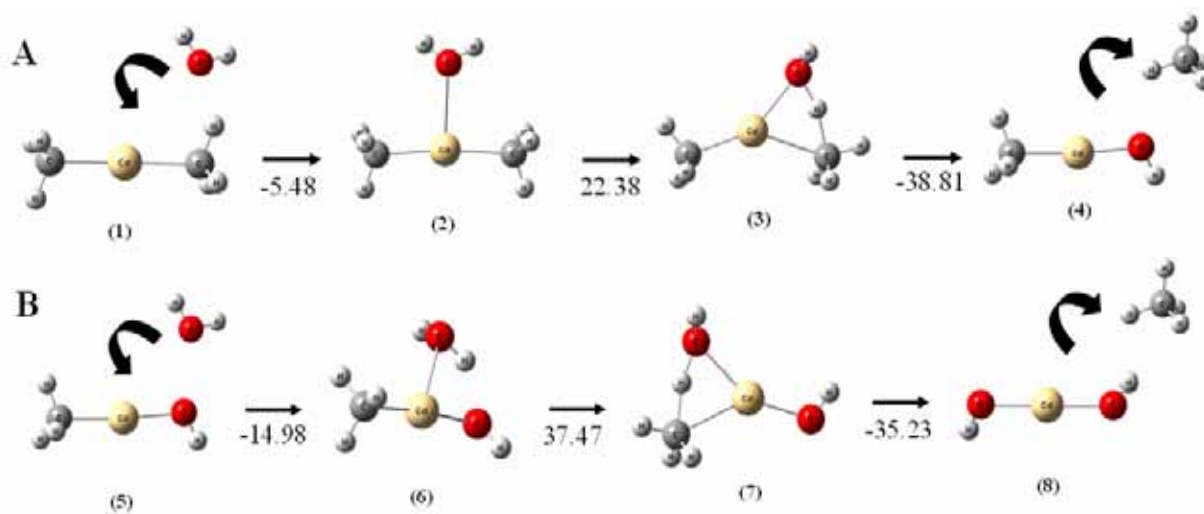


Figure 6-6. Enthalpy of reactions. A) Between one mole dimethylcadmium and water. B) With additional water molecule. The unit of heat of reaction is kcal/mol.

## CHAPTER 7

### CONCLUSIONS AND RECOMMENDATIONS

A methodology to quantitatively understand the physical and chemical behavior of precursors used in group II-VI MOCVD was established. The methodology consists of *in-situ* Raman scattering signals analysis, modeling the process, and extracting unknown parameters from the experimental data. Raman scattering can simultaneously provide temperature and species information with good spatial resolution and therefore it is a viable tool to study chemical reactions. With this apparatus it was possible to obtain more detailed information about the II-VI MOCVD process, e.g., temperature and/or concentration profiles inside the reactor. In addition, hydrodynamics modeling assisted in interpreting the MOCVD reaction system. From the simulated results, the centerline data could be extracted to compare with experimentally obtained data. This comparison enabled parameter extractions using Genetics and Simplex algorithms. The Genetic algorithm is based on a least squares method, which basically minimizes the difference between experimental and simulated data. During the procedure the lowest minimum point, i.e., the global minimum, could be found, and from that point the Simplex algorithm helped to finely tune the result.

To assist both experimental and modeling studies, a computational chemistry software packet Gaussian 03 was utilized. Computational calculations estimate Raman-active vibrational frequencies as well as thermodynamical properties. Specially, the likely estimation method for kinetics information including activation energy and frequency factor was introduced using B3LYP DFT calculation. Using proper model chemistry, the activation energy could be estimated; however, the BSSE correction should be considered to reduce calculation uncertainty. In the case of frequency factor estimation, it was suggested to use the one-domain calculation concept. A fixed imaginary bond between two broken products made it possible not to lose 6

vibrational degrees of freedom and, in addition, stable multiplicity turned out to be important from potential surface examination. As a result, the calculated activation energy and frequency factor were well matched with experimental reports. Therefore, it is regarded that the first principles calculation can be applied in estimation of kinetics information. In particular, it is supposed to be useful in mechanism study which involves reaction steps whose detections are difficult or impossible. This calculation was also utilized for the surface adsorption study based on the grand canonical ensemble, harmonic oscillator and Born-Oppenheimer approximation theory. The DFT calculation was used to estimate adsorptive binding energy of the most likely molecule onto MOCVD substrate.

As the first example molecule, decomposition kinetics of diethylzinc was elucidated using *in-situ* Raman spectroscopy and supported computational calculations. The energetic and kinetics research approaches suggested most likely reaction pathways including  $\beta$ -hydride elimination and homolytic fission between the Zn-C bond. Furthermore, dimerization of two monoethylzinc was detected as a reaction intermediate and this was the first time this molecule has been reported as an intermediate. The computational calculation helped to assign peaks. Then, the reaction pathways between Zn-containing molecules and water was suggested based on B3LYP/6-311G(d) model chemistry. The most probable reaction intermediate near to the substrate turned out to be dihydroxozinc from energetic analysis of all possible reaction pathways. The most plausible reaction of this molecule turned out to be trimerization to complete the Wurtzite structure of solid ZnO films. Therefore, this molecule was considered as a key molecule to deposit the film and experimental detection was attempted to support it. In experiments, two molecules were mixed just before they went through the reactor inlet and *in-situ* Raman scattering examination was carried out. However, the direct evidence of

dihydroxozinc was not obtained. Possibly the species has too small relative Raman-cross section or short lifetime with low enough activation energies in each step. Nevertheless, some reaction intermediates were successfully detected and from the computational calculations, indirect interpretation of the detected peaks was made to understand gas-phase reaction pathways.

As the second example, decomposition kinetics of dimethylcadmium was examined. It is emphasized that reasonable selection in basis sets is very important in computational calculation because it brings more precious information. As an example, basis set selection for dimethylcadmium using ECP was shown based on reported data in literature. Two calculation results, bond dissociation energy in Cd-C bond and its Raman active stretching motion, were examined using different combinations of various basis sets; five different basis sets for Cd atom, i.e. CRENBS, CRENBL, SDD, LanL2DZ and SBKJC and five different basis sets for C and H atoms, i.e. STO-3G, 3-21G, 6-31G(d), 6-311G(d) and 6-311++G(2d,2p). Among the possible candidates, B3LYP level theory calculation with SDD/STO-3G/3-21G basis set combination for Cd, C and H atoms could reproduce the experimentally reported Cd-C vibrational stretching of  $\text{Cd}(\text{CH}_3)_2$  and  $\text{CdCH}_3$ ; therefore, this basis set was utilized to find out if additional reaction intermediates existed. Thermodynamically, the most probable intermediate is  $(\text{CdCH}_3)_2$  and its Raman active frequency was obtained based on selected model chemistry information. Then gas-phase Raman scattering experiments in a certain temperature gradient were carried out in an inverted impinging-jet reactor and the existence of  $(\text{CdCH}_3)_2$  was confirmed experimentally. However, the forward reaction of dimerization turned out to be much slower than the backward reaction. Therefore, the computational calculation is very useful to describe the molecular system and to predict Raman active frequencies. However, the criteria for choosing basis sets should be reasonable.

Finally, the obtained experimental data was compared to simulations. As a result, decomposition kinetics data of dimethylcadmium were successfully extracted using parameter estimation procedures with Genetic and Simplex algorithms. The relative Raman cross-section turned out to be 20.97 and rate constant for the first Cd-C bond breaking is  $k_0=5.01 \times 10^{13} \text{ s}^{-1}$  and  $E_a=55.98 \text{ kcal/mol}$ .

## REFERENCES

- Abr91 P. Abraham, A. Bekkaoui, V. Souliere, J. Bouix and Y. Monteil, *J. Cryst. Growth*, **107** (1991) 21.
- Aki99 O.O.Akinwunmi, M.A.Eleruja, J.O. Olowolafe, G.A. Adegboyega and E.O.B. Ajayi, *Opt. Mat.*, **13** (1999) 255.
- All01 M.D. Allendorf, *Thin Solid Films*, **392** (2001) 155.
- All98 M.D. Allendor and C.F. Melius, *Sur. Coat. Tech.*, **108** (1998) 191.
- Alm92 M.J. Almond, C.E. Jenkins and D.A. Rice, *J. Organomet. Chem.*, **439** (1992) 251.
- Ant00 J. Antony, B. Hansen, L. Hemmingsen and R. Bauer, *J. Phys. Chem. A*, **104** (2000) 6047.
- Bac99 E. M. Bachari, G. Baud, S. B. Amor and M. Jacquet, *Thin Solid Films*, **348** (1999) 165.
- Bae02 A.K. Baev, *Russian. J. Appl. Chem.*, **75**(1) (2002) 159.
- Ban77 G.M. Bancroft and D.K. Creber, *J. Chem. Phys.*, **67**(11) (1977) 4891.
- Beh94 E. C. Behrman, R. K. Foehrweiser, J. R. Myers, B. R. French and M. E. Zandler, *Phys. Rev. A*, **49** (1994) R1543.
- Bir60 R.B. Bird, W.E. Stewart and E.N. Lightfoot, *Transport Phenomena*, John Wiley & Sons, New York (1960).
- Bre02 S.H. Brewer and S. Franzen, *J. Alloy. Com.*, **338** (2002) 73.
- Buc88 N.I. Buchan, C.A. Larsen and G.B. Stringfellow, *J. Cryst. Growth*, **92** (1988) 591.
- Bur87 D.S. Burnett, *Finite Element Analysis*, Addison-Wesley, Sydney, (1987).
- Bus96 G. Busca, *Cat. Today*, **27** (1996) 323.
- But86 J.E. Butler, N. Bottka, R.S. Sillmon and D.K. Gaskill, *J. Cryst. Growth*, **77** (1986) 163.
- Cav69 K. Cavanagh and D.F. Evans, *J. Chem. Soc. (A)*, (1969) 2890.
- Cha01 R. Chandrasekhar and K.L. Choy, *Thin Solid Films*, **398** (2001) 59.
- Che84 C.J. Chen and R.M. Osgood, *J. Chem. Phys.*, **81**(1) (1984) 327.
- Cho03 J.B. Choi, J.H. Kim, K.A. Jeon and S.Y. Lee, *Mat. Sci. Eng.*, **102** (2003) 344.
- Cho99 S. Cho, J. Ma, Y. Ki,, Y. Sun, G. K. L. Wong and J. B. Ketterson, *Appl. Phys. Lett.*, **75**(18) (1999) 2761.

- Chu92 T.L. Chu, S.S. Chu, C. Ferekides, J. Britt and C.Q. Wu, *J. Appl. Phys.*, **71**(8) (1992) 3870.
- Coa94 A.M. Coats, D.C. McKean, H.G.M. Edwards and V. Fawcett, *J. Mol. Structure*, **320** (1994) 159.
- Cor62 C. H. Corliss and W. R. Bozman, *Experimental Transition Probabilities for Spectral Lines of Seventy Elements*, National Bureau of Standards monograph, **53** (1962).
- Cra02 C.J. Cramer, *Essentials of computational chemistry*, John Wiley & Sons Ltd, (2002).
- Cur99 C.F. Curtiss and R.B. Bird, *Ind. Eng. Chem. Res.*, **38** (1999) 2515.
- Dav90 D.F. Davison, K. Kohse-Höinghaus, A.Y. Chang and R.K. Hanson, *Int. J. Chem. Kinet.* **22** (1990) 513.
- Dra82 Drake, M.C., C. Asawaroengchai, D.L. Drapche, K.P. Veirs and G.M. Rosenblatt, *Temperature*, **5** (1982) 621.
- Dui94 F.B. Duijneveldt, J.G.C.M. Duijneveldt-van Rijdt and J.H. Lenthe, *Chem. Reviews*, **97**(7) (1994) 1873.
- Dum92 H. Dumont, A. Marbeuf, J. E. Bouree and O. Gorochoy, *J. Mater. Chem.*, **2**(9) (1992) 923.
- Dum93 H. Dumont, A. Marbeuf, J. E. Bouree and O. Gorochoy, *J. Mater. Chem.*, **3**(10) (1993) 1075.
- Ego98 Yu.E. Egorov and A.I. Zhmakin, *Comput. Mat. Sci.*, **11** (1998) 204.
- Ell92 A.M. Ellis, E.S.J. Robles and T.A. Miller, *Chem. Phys. Letters*, **190**(6) (1992) 599.
- Fen04 X. Feng, *J. Phys.: Condens. Matter*. **16** (2004) 4251.
- Fri04 M. J. Frisch, G. W. Trucks, H. B. Schlegel, G. E. Scuseria, M. A. Robb, J. R. Cheeseman, J. A. Montgomery, Jr., T. Vreven, K. N. Kudin, J. C. Burant, J. M. Millam, S. S. Iyengar, J. Tomasi, V. Barone, B. Mennucci, M. Cossi, G. Scalmani, N. Rega, G. A. Petersson, H. Nakatsuji, M. Hada, M. Ehara, K. Toyota, R. Fukuda, J. Hasegawa, M. Ishida, T. Nakajima, Y. Honda, O. Kitao, H. Nakai, M. Klene, X. Li, J. E. Knox, H. P. Hratchian, J. B. Cross, V. Bakken, C. Adamo, J. Jaramillo, R. Gomperts, R. E. Stratmann, O. Yazyev, A. J. Austin, R. Cammi, C. Pomelli, J. W. Ochterski, P. Y. Ayala, K. Morokuma, G. A. Voth, P. Salvador, J. J. Dannenberg, V. G. Zakrzewski, S. Dapprich, A. D. Daniels, M. C. Strain, O. Farkas, D. K. Malick, A. D. Rabuck, K. Raghavachari, J. B. Foresman, J. V. Ortiz, Q. Cui, A. G. Baboul, S. Clifford, J. Cioslowski, B. B. Stefanov, G. Liu, A. Liashenko, P. Piskorz, I. Komaromi, R. L. Martin, D. J. Fox, T. Keith, M. A. Al-Laham, C. Y. Peng, A. Nanayakkara, M. Challacombe, P. M. W. Gill, B. Johnson, W. Chen, M. W. Wong, C. Gonzalez and J. A. Pople, *Gaussian 03*, Revision C.02, Gaussian, Inc., Wallingford CT, (2004).

- Gha80 S. Ghandhi, R. Field and J. Shealy, *Appl. Phys. Lett.*, **37**(5) (1980) 449.
- Gol62 D.M. Golden, B. Crawford, Jr., *J. Chem. Phys.*, **36** (1962) 1654.
- Gor00 R.G. Gordon, *MRS Bulletin*, August (2000) 52.
- Gru89 M.D. Grunzburger, Finite element methods for viscous incompressible flows, Academic Press, NY, (1989).
- Hag99 K. Haga, F. Katahira and H. Watanabe, *Thin Solid Films*, **343** (1999) 145.
- Hol92 W.L. Holster, *Prog. Cryst. Growth Charact.*, **24** (1992) 111.
- Hua93 Z.S. Huang, C. Park and T.J. Anderson, *J. Organomet. Chem.*, **449** (1993) 77.
- Hug79 T.J.R. Hughes, W.K. Liu and A. Brooks, *J. Comput. Phys.*, **30** (1979) 1.
- Hwa04 J.Y. Hwang, Ph.D Dissertation, University of Florida (2004).
- Hwa05a J.Y. Hwang, C. Park, M. Huang and T.J. Anderson, *J. Cryst. Growth*, **279** (2005) 521.
- Hwa05b J. Y. Hwang, C. Park, M. Huang and T.J. Anderson, *J. Electrochem. Soc.*, **152**(5) (2005) C334.
- Hya73 H.A. Hyatt, J.M. Cherlow, W.R. Fenner, S.P.S Porto, *J. Opt. Soc. Am.*, **63** (1973) 1603.
- Ing88 J.D. Ingle and S.R. Crouch, Spectrochemical Analysis. Prentice Hall, (1988).
- Irv97 S.J.C. Irvine, A. Stafford, M.U. Ahmed, P. Prete and R. Berrigan, *Prog. Crystal Growth and Charact.* **35** (1997) 177.
- Jac64 M.G. Jacko and S.J.W. Price, *Can. J. Chem.*, **42** (1964) 1198.
- Jac89a D. A. Jackson Jr, *J. Cryst. Growth*, **94** (1989) 459.
- Jac89b R.L. Jackson, *Chem. Phys. Lett.*, **163** (1989) 315.
- Jac92 R.L. Jackson, *J. Chem. Phys.*, **96**(8) (1992) 5938.
- Kan75 J. Kane and H.P. Schweizer, *Thin Solid Films*, **29** (1975) 155.
- Kau94 M. Kaupp and H.G. Schnering, *Inorg. Chem.*, **33** (1994) 4179.
- Kel69 N.V.P. Kelvin, Kinetics of Pyrolysis of Ammonia in a Fused Silica Reactor, Ph.D. Dissertation, Yale University, (1969).
- Kol98 D.D. Koleske, A.E. Wickenden, R.L. Henry, W.J. Desisto and R.J. Gorman, *J. Appl. Phys.*, **84**(4) (1998) 1998.



- Kop84 Koppitz, M., O. Vestavik, and W. Pletschen, *J. Crystal Growth*, **68** (1984) 136.
- Kos76 A. A. Koski, S. Price and B. C. Trudell, *Can. J. Chem.*, **54** (1976) 482.
- Kra84 M. Krauss and W. J. Stevens, *Annual reviews of Physical Chemistry*, **35** (1984) 357.
- Lar86 C.A. Larsen and G.B. Stringfellow, *J. Crystal Growth*, **75** (1986) 247.
- Lar87 C.A. Larsen, N.I. Buchan and G.B. Stringfellow, *J. Cryst. Growth*, **85** (1987) 148.
- Lau57 C.M. Laurie and L.H. Long, (1957) 1431.
- Li03 X. Li, Y. Yan, T.A. Gessert, C. DeHart, C.L. Perkins, D. Young and T.J Coutts, *Electrochem. Solid State Lett.*, **6**(4) (2003) C56.
- Lin93 R. E. Linney and D. K. Russell, *J. Mater. Chem.*, **3**(6) (1993) 1587.
- Liu03 C. Liu, T. Matsutani, T. Asanuma and M. Kiuchi, *NIM in Phy. Res. B.*, **206** (2003) 348.
- Liu78 S.S. Liu and D.A. Stevenson, *J. Electrochem. Soc.*, **125** (1978) 1161.
- Lon77 D. A. Long, *Raman Spectroscopy*, McGraw-Hill, New York, (1977).
- Loo02 D. C. Look, D. C. Reynold, C. W. Litton, R. L. Jones, D. B. Eason and G. Cantwell, *Appl. Phys. Lett.*, **81**(10) (2002) 1830.
- Luc88 R. Lückcrath, P. Tommack, A. Hertling, H.J. Koss, P. Balk and K.F. Jensen, *J. Cryst. Growth*, **93** (1988) 151.
- Mar90 T. Maruyama and K. Tabata, *Jpn. J. Appl. Phys*, **29**(2) (1990) L355.
- Mar91 T. Maruyama and K. Fukui, *Thin Solid Films*, **203** (1991) 297.
- Mat02 J. M. Matxain, J. E. Fowler and J. M. Ugalde, *Phys. Rev. A*, **62** (2002) 053201.
- Maz89 D. Mazzaresse, A. Tripathi, W.C. Conner, K.A. Jones, L. Calderon and D.W. Eckart, *J. Electron. Mater.* **18** (1989) 369.
- McQ76 D.A. McQuarrie, *Statistical Mechanics*, Chap. 9, Addison-Wesley, (1976).
- Mes98 M. Mesrine, N. Grandjean and J. Massies, *Appl. Phys. Lett.*, **72** (1998) 350.
- Mih98 T. G. Mihopoulos, V. Gupta and K.F. Jensen, *J. Crystal Growth*, **195** (1998) 733.
- Mil68 M.G. Miles, J.H. Patterson, C.W. Hobbs, M.J. Hopper, J. Overend and R.S. Tobias, *Inorganic Chemistry*, **7**(9) (1968) 1721.
- Min00 T.Minami, *MRS Bulletin*, August (2000) 38.

- Min97 K. Minegishi, Y. Koiwai, Y. Kokuchi and K. Yano, *Jpn. J. Appl. Phys.*, **36** (1997) L1453.
- Mon86 Monteil, Y., M.P. Berthet, R. Favre, A. Harris, and J. Bouix, *J. Crystal Growth*, **77**, 172-181 (1986).
- Mor03 M.A. Morales-Paliza, M.B. Huang and L.C. Feldman, *Thin Solid Films*, **429** (2003) 220.
- Myc04 A. Mycielski, L. Kowalczyk, A. Szadkowski, B. Chwalisz, A. Wysmolek, R. stepniewski, J.M. Baranowski, M. Petemski, A. Witowski, R. Jakiela, A. Barcz, B. Witkowska, W. Kaliszek, A. Jedrzejcack, A. Suchocki, E. Lusakowska and E. Kaminska, *J. Alloy. Compd.*, **371** (2004) 150.
- Nag80 V.B. Nagel and W. Bruser, *Z. Anorg. Allg. Chem.* **468** (1980)148.
- Nak91 S. Nakamura, Y. Harada and M. Seno, *Appl. Phys. Lett.*, **58**(18) (1991) 2021.
- Neu72 P.D. Neufeld, A.R. Janzen and R.A. Aziz, *J. Chem. Phys.*, **57** (1972) 1100.
- Ni97 J. Ni and J.J. BelBruno, *J. Cryst. Growth*, **182**(3) (1997) 321.
- Pan02 A.N. Pankratov, *J. Serb. Chem. Soc.*, **67**(5) (2002) 339.
- Par02a C. Park, W.S. Jung, Z. Huang and T.J. Anderson, *J. Mat. Chem.*, **12** (2002) 356.
- Par02b C. Park, J.Y. Hwang, M. Huang and T.J. Anderson, *Thin Solid Films*, **409** (2002) 88.
- Par02c C.H. Park, S. B. Zhang and S. H. Wei, *Phys. Rev. Lett. B*, **66** (2002) 073202.
- Pla84 J.K. Platten and J.C. Legros, *Convection in Liquids*, Ch. 1, Springer-Verlag, New York, (1984).
- Pol01 B.E. Poling, J.M. Prausnitz and J.P. O'Connell, *The Properties of Gases and Liquids*, 5<sup>th</sup> ed., McGraw-Hill, New York, (2001).
- Pri57 S.J.W. Price and A.F. Trotman-Dickenson, (1957) 939.
- Ras98 V.A. Rassolov, J.A. Pople, M.A. Ratner and T.L. Windus, *J. Chem. Phys.* **109**(4) (1998) 1223.
- Red93 J.N. Reddy, *Computers and Structures*, **47** (1993) 857.
- Ric91 W. Richter, P. Kurpas, R. Lückcrath and M. Motzkus, *J. Cryst. Growth*, **107** (1991) 13.
- Rob91 E.S.J. Robles, A.M. Ellis and T.A. Miller, *Chem. Phys. Letters*, **178**(2) (1991) 185.
- Rya82 L.A. Ryabova, V.S. Salun and I.A. Serbinov, *Thin Solid Films*, **92** (1982) 327.
- Saw02 Y. Sawada, C. Kobayashi, S. Seki and H. Funakubo, *Thin Solid Films*, **409** (2002) 46.

- Sch79 H.W. Schrötter and H.W. Klöckner, *Raman Spectroscopy of Gases and Liquids*, A. Weber, Editor, Ch. 4, Springer-Verlag, New York, (1979).
- Sch95 B. Schrader, *Infrared and Raman Spectroscopy: methods and applications*, VCH (1995).
- Sct96 A. P. Scott and L. Radom, *J. Phys. Chem.* **100** (1996) 16502.
- Sim97 H. Simka, B.G. Willis, I. Lengyel and K.F. Jensen, *Prog. Crystal Growth and Charact.*, **35** (1997) 117.
- Smi03 S. M. Smith and H. B. Schlegel, *Chem. Mater.* **15** (2003) 162.
- Ste94 S.E. Stein and R.L. Brown, *J. Chem .Inf. Comput. Sci.*, **34** (1994) 581.
- Sue95 W. Suetaka and J.T. Yates, Jr., *Surface infrared and Raman Spectroscopy*, Plenum Press, New York (1995).
- Suz02 A. Suzuki, T. Matsushita, T. Aoki, A. Mori and M. Okuda, *Thin Solid Films*, **411** (2002) 23.
- Syw91 B.S. Sywe, J.R. Schlup and J.H. Edgar, *Chem. Mater.* **3** (1991) 737.
- Tho96 A. Thon and T.F. Kueth, *Appl. Phys. Lett.*, **69** (1996) 55.
- Tho99 A. Thorne, U. Litzen and S. Johansson, *Spectrophysics*, Springer, New York (1999).
- Tit96 A.V. Titov, *International J. Quan. Chem.*, **57** (1996) 453.
- Tom01 H. Tomonaga and T. Morimoto, *Thin Solid Films*, **392** (2001) 243.
- Tow75 C.H. Townes and A.L. Schawlow, *Microwave Spectroscopy*, Dover, New York, (1975).
- Tsa03 M.S. Tsai, C.L. Wang and M.H. Hon, *Sur. Coat. Tech.*, **172** (2003) 95.
- Vor02 A.N. Vorobev, S.Yu. Karpov, M.V. Bogdanov, A.E. Komissarov, O.V. Bord, A.I. Zhmakin and Yu.N. Makarov, *Comput. Mat. Sci.*, **24** (2002) 520.
- Waa04 A. Waag, Th. Gruber, K. Thonke, T. Sauer, R. Kling, C. Kirchner and H. Röss, *J. Alloy. Compd.*, **371** (2004) 77.
- Wan04 X. Wang and L. Andrews, *J. Phys. Chem. A.*, **108** (2004) 11006.
- Wan05 L. Wang, Y. Pu, Y. F. Chen, C. L. Mo, W. Q. Fang, C. B. Xiong, J. N. Dai and F. Y. Jiang, *J. Cryst. Growth*, **284** (2005) 459.
- Wol03 B. Wolbank and R. Schmid, *Chem. Vap. Deposit.*, **9**(5) (2003) 272.

- Won06 Y.S. Won, Y.S. Kim, T. Anderson and L. McElwee-White, *J. Am. Chem. Soc.*, **128** (2006) 13781.
- Yan03 X. Li, Y. Yan, T.A. Gessert, C. DeHart, C.L. Perkins, D. Young and T.J Coutts, *Electrochem. Solid State Lett.*, **6**(4) (2003) C56.
- Zen03 K. Zeng, F. Zhu, J. Hu, L. Shen, K. Zhang and H. Gong, *Thin Solid Films*, **443** (2003) 60.
- Zho01 Z.B. Zhou, R.Q. Cui, Q.J. Pang, Y.D. Wang, F.Y. Meng, T.T. Sun, Z.M. Ding and X.B. Yu, *Appl. Surf. Sci.*, **172** (2001) 245.

## BIOGRAPHICAL SKETCH

Young Seok Kim was born on December 17, 1972, in Seoul, Korea to Chul Kyu Kim and Se Young Ahn. He received his B.S degree from the Chemical Engineering, Kwangwoon University (Seoul, Korea) in February 1999 and M.S degree from Korea University (Seoul, Korea) in February 2001.

The author then decided to pursue his Ph.D. degree in the University of Florida. In August 2002, he joined Dr. Anderson's research group and devoted himself to chemical kinetics research in semiconductor processing. During his study, he got married to Hae Kyung Ko in July 17, 2006, and they started their new life in Gainesville. His wife was also admitted as a Ph.D. student in the Genetics Department at the University of Florida. During his academic career, he received the Korean Honor Scholarship from the Korean embassy in the USA in 2006, and he also received the Certificate of Chemical Physics from the Chemistry Physics Center at University of Florida in 2007.